

Electron Paramagnetic Resonance Characterization of  
Surface Sites in Metal-Organic Frameworks by Nitric Oxide  
Adsorption

Der Fakultät für Physik und Geowissenschaften

der Universität Leipzig

genehmigte

D I S S E R T A T I O N

zur Erlangung des akademischen Grades

doctor rerum naturalium

Dr. rer. nat.

vorgelegt

von Dipl.-Phys. Matthias Mendt

geboren am 04.05.1982 in Dresden

Gutachter: Prof. Dr. Jürgen Haase  
Assoc. Prof. Dr. Stefan Stoll

Tag der Verleihung: 16.09.2019





---

## Bibliographische Beschreibung:

Mendt, Matthias

Electron Paramagnetic Resonance Characterization of Surface Sites in Metal-Organic Frameworks by Nitric Oxide Adsorption

Universität Leipzig, Dissertation

208 S., 391 Lit.<sup>1</sup>, 14 Tab. (+4 in Anlagen), 56 Abb. (+39 in Anlagen), 6 Anlagen

Das Titelbild zeigt ein NO Molekül vor der enghohrigen Phase des MOFs MIL-53(Al),<sup>[1]</sup> erstellt mit Diamond 3.0 und POV-Ray 3.7.0

## Referat (abstract):

Die Adsorption von Stickstoffmonoxid (NO) in metallorganischen Gerüstverbindungen (MOFs) wird zum ersten Mal mit Elektronen Paramagnetischer Resonanzspektroskopie (EPR) untersucht. Die diesbezügliche Auswahl an Materialien umfasst den flexiblen MOF MIL-53(Al), den MOF MIL-100(Al), welcher koordinative ungesättigte Al<sup>3+</sup> Plätze zur bevorzugten Adsorption besitzt und zwei Varianten des MOFs DUT-8(Ni), wobei eine strukturell flexibel und die andere starr ist. Die Sorption von NO in diesen Materialien wird mittels quantitativer EPR von desorbierten NO Gas charakterisiert, welche zum Teil auf einer ausführlichen Analyse der Linienbreite des NO Gasphasen EPR Signals basiert. Für alle Materialien wird die Physisorption von NO an dem organischen Teil der MOF Oberfläche beobachtet und ausführlich für den MOF MIL-53-(Al) mittels gepulster EPR untersucht. Zusätzlich zur Charakterisierung von anderen NO Adsorptionsspezies wird gezeigt, dass NO bei tiefen Temperaturen am offenen Metallplatz des MIL-100(Al) physisorbiert und die elektronische und geometrische Struktur des entsprechenden Komplexes wird umfassend mittels gepulster EPR und Dichtefunktionaltheorie-Rechnungen bestimmt. Es wird weiter gezeigt, dass NO an defekten Ni<sup>2+</sup> Plätzen des DUT-8(Ni) chemisorbiert und zwei Arten von Defekten werden identifiziert und charakterisiert, welche mit der strukturellen Flexibilität der DUT-8(Ni) Varianten korrelieren.

The adsorption of nitric oxide (NO) on metal-organic frameworks (MOFs) is studied by continuous wave and pulsed electron paramagnetic resonance (EPR) spectroscopy for the first time. The investigated selection of MOFs comprises the flexible MIL-53(Al) material, the MOF MIL-100(Al) which possesses coordinative unsaturated Al<sup>3+</sup> sites for the preferential adsorption and two derivatives of the MOF DUT-8(Ni) where one shows an intrinsic gate-opening responsiveness and the other is rigid. The sorption of NO on this materials is characterized by quantitative EPR of desorbed NO gas, partially based on a thorough analysis of its EPR signal linewidth. The physisorption of NO at the organic part is observed for all materials and is studied in detail for MIL-53(Al) by pulsed EPR. Besides the characterization of minor NO species, it is shown that NO physisorbs at the open metal site of MIL-100(Al) at low temperatures and the electronic and geometric structure of this NO-Al<sup>3+</sup> complex is determined thoroughly by pulsed EPR investigations and density functional theory computations. EPR further reveals the chemisorption of NO at defective Ni<sup>2+</sup> sites of DUT-8(Ni) and two kinds of defects are identified and characterized, which correlate with the kind of the DUT-8(Ni) framework responsiveness.

---

<sup>1</sup>... Lit. (Anzahl der im Literaturverzeichnis ausgewiesenen Literaturangaben)

---

## Acknowledgments

This PhD project was enabled by the support of many people. Most importantly, I want to thank Prof. Andreas Pöpl for the opportunity working on this great project within the spin resonance group of Prof. Jürgen Haase. His kind supervision accompanied me up to now, starting from my first steps in EPR during my diploma thesis. I greatly acknowledge the time and patience he took for countless inspiring discussions, which deepened my understanding of EPR and broadened my perspective on many subjects particularly related to this thesis as well as his detailed advice and teaching of the practical issues related to real-life EPR in a laboratory.

Furthermore, I would like to thank all coworkers, PhD fellows, technicians and students for a very pleasant and cooperative working atmosphere. Particularly, I want to thank Prof. Jürgen Haase for his benevolent support and the opportunity working on my PhD in his group. I am further indebted to my former PhD colleague Bettina Jee who introduces me into the practical and technical aspects of EPR including sample preparation, spectrometer handling and data processing. I would like to thank Prof. Thomas Heine for the opportunity, learning my first steps in DFT calculations under the supervision of Andreas Mavrantakis at the Jacobs University Bremen. I would like to continue to thank Prof. Rolf Böttcher and Prof. Dieter Michel as well as PD Marko Bertmer for fruitful and instructive discussions, my former and current PhD colleagues Stefan Friedländer and Anastasiia Kulstaeva for their pleasant company and helping hands in the lab, our former master student Mantas Šimėnas for providing code of useful MatLab programs for EPR data processing, the former Bachelor student Felix Gutt for his helping hands measuring and processing EPR data of some NO loaded DUT-8(Ni) samples, Gert Klotzsche for all maintenance and support related to computer stuff and technical issues, Stefan Schlayer for the continuous supply of liquid helium as well as advice in technical questions, our former engineer Joachim Höntsch for the patient support in many aspects of EPR instrumentation, Winfried Böhlmann, Lutz Moschkowitz and Kathrin Koch for activating and guest loading samples, Horst Voigt for helpful technical advice, Jörg Lenzner for advice related to the installation of software, our former secretary Sophie Kirchner for all administration issues, Andreas Rost from the computing center of the university of Leipzig for the possibility and advice doing time consuming calculations including DFT on a computer cluster he maintained, Prof. Harald Krautscheid for the possibility using his glovebox for certain samples as well as for his advice in chemical questions, Prof. Reinhard Kirmse for discussions about complex chemistry, my PhD fellow Arafat Hossain Khan for discussions about NO adsorption on the MIL-100(Al) MOF, our former student Michael Mensing for some EPR measurements on NO loaded MIL-100(Al) samples and our trainees Konrad Eisinger, Christian Gahse, Benno Krüger, Tilo Pilling, Sascha Lettmann and Niklas Vetter for all their valuable assistance. I also gratefully acknowledge the support of the glass workers Stephan Eckert and Marko Wende which were involved in the preparation of almost any EPR sample as well as the constant availability of the technical engineers in our machinery shop, who solved almost any technical problem asked for.

From my colleagues in Leipzig I would like to thank further Michael Jurkutat for many discussions about spin physics after work and for proofreading parts of this thesis as well as Nataliya Georgieva and Daniel Schneider for assistance in administrative issues of this PhD work. Furthermore, I would like to thank the people who synthesized and characterized the MOF materials I investigated in this thesis. Dieter Himsl and Benjamin Barth, former members of the Erlangen group of Prof. Martin Hartmann provided samples of the MIL-53(Al) and MIL-53(Al/Cr) material. The MIL-100(Al) and MIL-100(Fe) materials as well as CPO-27 materials were synthesized by Benjamin Barth. The DUT-8(Ni) MOFs we investigated were synthesized by Negar Kavooosi, a former member of the Dresden group

---

of Prof. Stefan Kaskel under supervision of Volodymyr Bon and Irena Senkovska.

Within my PhD time I collaborate with many people, including research which is not part of the thesis but which deepened my general understanding of the subject area. I would like to thank Joscha P. Nehr Korn and Alexander Schnegg for the possibility performing high field EPR measurements on DUT-8 samples at the Helmholtz Zentrum Berlin, although we did not observe any signal of the  $\text{Ni}^{2+}$ . I further acknowledge additional past and ongoing collaborations with Ulf Kempe, Jakob Albert, Franziska Debatin, Prof. Hans-Jürgen Holdt, Katharina Peickert, Prof. Michael Fröba, Felicitas Niekiet, Tim Ahnfeld, Prof. Norbert Stock, Christian Matjeka, Prof. Harald Krautscheid, Herbet Hoffmann, Marcus Rauche, Prof. Eike Brunner, Nicole Klein, Sebastian Ehrling, Mariia Maliuta, Volodymyr Bon, Irena Senkovska, Prof. Stefan Kaskel, Pia Vervoorts, Andreas Schneemann, Prof. Roland A. Fischer, Julian Keupp and Prof. Rochus Schmid.

I greatly acknowledge the financial support by the Deutsche Forschungsgemeinschaft (DFG) in the frames of the priority program SPP 1362 “Poröse metallorganische Gerüstverbindungen” and the research unit 2433 “Switchable Metal-Organic Frameworks”.

Last but not least I would like to thank my parents, my sister Elisa and my brother Jacob for their love and constant support.

**Contents**

|  |           |
|--|-----------|
| <b>Contents</b>  | <b>4</b>  |
| <b>List of Figures</b>   | <b>6</b>  |
| <b>List of Tables</b>  | <b>8</b>  |
| <b>Nomenclature</b>  | <b>10</b> |
| <b>List of samples</b>   | <b>11</b> |
| <b>Frequently used variables</b>   | <b>12</b> |
| <b>1 Introduction</b>  | <b>14</b> |
| <b>2 Materials, methods and theory</b>   | <b>20</b> |
| 2.1 Metal organic frameworks . . . . .   | 20        |
| 2.1.1 General concepts . . . . .   | 20        |
| 2.1.2 MIL-53(Al) . . . . .   | 21        |
| 2.1.3 MIL-100(Al) . . . . .  | 22        |
| 2.1.4 DUT-8(Ni) . . . . .  | 24        |
| 2.2 EPR spectroscopy . . . . .   | 26        |
| 2.2.1 The spin-Hamiltonian approach . . . . .  | 27        |
| 2.2.2 CW EPR spectroscopy . . . . .  | 31        |
| 2.2.3 Pulsed EPR methods . . . . .   | 33        |
| 2.3 EPR related properties of nitric oxide . . . . .   | 42        |
| 2.3.1 The electronic structure of NO . . . . .   | 42        |
| 2.3.2 Angular momenta of the nitric oxide molecule . . . . .   | 43        |
| 2.3.3 The magnetism and EPR signal of the free nitric oxide molecule . . . . .                                     | 45        |
| 2.3.4 The magnetism and EPR signal of nitric oxide adsorbed at closed shell or diamagnetic surface sites . . . . . | 48        |
| 2.3.5 EPR of nitric oxide adsorbed at open shell or paramagnetic surface sites . . . . .                           | 50        |
| 2.4 Density functional theory . . . . .  | 51        |
| <b>3 EPR of desorbed NO gas - a method to characterize the adsorption of NO on MOFs</b>                            | <b>54</b> |
| 3.1 Simulating the EPR signal of NO gas . . . . .  | 55        |
| 3.2 The relation between the NO gas EPR linewidth and the NO gas pressure . . . . .                                | 57        |
| 3.3 EPR of desorbed NO in the MOF samples . . . . .  | 62        |
| 3.3.1 Results . . . . .  | 62        |
| 3.3.2 Discussion . . . . .   | 68        |
| 3.4 Summary of chapter three . . . . .   | 72        |
| <b>4 NO adsorption species in MIL-53(Al), a MOF material without CUS</b>   | <b>74</b> |
| 4.1 CW-EPR . . . . .   | 74        |
| 4.2 Two-pulse ESE field sweep and HYSCORE spectroscopy . . . . .   | 79        |
| 4.3 Summary of chapter four . . . . .  | 91        |

---

|          |   |            |
|----------|---|------------|
| <b>5</b> | <b>NO adsorption species in MIL-100(Al), a MOF material with CUS</b>  | <b>92</b>  |
| 5.1      | CW-EPR  | 93         |
| 5.2      | Two-pulse ESE field sweep EPR   | 97         |
| 5.3      | HYSCORE spectroscopy  | 99         |
| 5.4      | Davies ENDOR spectroscopy   | 106        |
| 5.5      | DFT calculations  | 110        |
| 5.6      | Insights into the low temperature adsorption of NO  | 118        |
| 5.7      | Summary of chapter five   | 125        |
| <b>6</b> | <b>EPR investigation of defect centers in rigid and flexible derivatives of DUT-8(Ni) using NO as a probe molecule</b>  | <b>127</b> |
| 6.1      | Identification and characterization of NO adsorption species by CW EPR  | 128        |
| 6.2      | First pulsed EPR experiments  | 139        |
| 6.3      | Summary of chapter six  | 142        |
| <b>7</b> | <b>Conclusive discussion</b>  | <b>145</b> |
| <b>8</b> | <b>Summary</b>  | <b>149</b> |
| <b>A</b> | <b>Samples</b>  | <b>152</b> |
| A.1      | Synthesis and Characterization  | 152        |
| A.2      | Preparation of EPR experiments  | 152        |
| A.3      | Nomination of the EPR samples   | 152        |
| <b>B</b> | <b>Spectroscopic details</b>  | <b>153</b> |
| B.1      | Experimental setup  | 153        |
| B.2      | Spectral analysis   | 155        |
| <b>C</b> | <b>Supplementary material for chapter two - the primary echo</b>  | <b>156</b> |
| <b>D</b> | <b>Supplementary material for chapter three</b>   | <b>157</b> |
| D.1      | Estimation of the detection limit of the present X-band CW setup for the determination of the EPR signal of NO gas      | 157        |
| D.2      | Insights into the phase composition of the NO loaded Al/Cr-MIL-53 sample by temperature-dependent Cr <sup>3+</sup> -EPR | 158        |
| <b>E</b> | <b>Supplementary material for chapter four</b>  | <b>166</b> |
| <b>F</b> | <b>Supplementary material for chapter five</b>  | <b>169</b> |
| F.1      | HYSCORE spectra of sample Al-MIL-100  | 169        |
| F.2      | Details of the DFT calculations and further calculated structural and magnetic parameters                               | 183        |
|          | <b>Bibliography</b>   | <b>186</b> |

## List of Figures

|    |  |     |
|----|--|-----|
| 1  | Structur of MIL-53, metal-oxygen chain . . . . .   | 21  |
| 2  | Structur of MIL-53, lp and np phase . . . . .  | 22  |
| 3  | Building units of MIL-100(Al) . . . . .  | 23  |
| 4  | Structure of MIL-100(Al) . . . . .   | 24  |
| 5  | Paddle wheel units of DUT-8(Ni) . . . . .  | 25  |
| 6  | Structure of DUT-8(Ni), lp and cp phase . . . . .  | 25  |
| 7  | Schematic scheme of the energy levels . . . . .  | 30  |
| 8  | Principles of CW EPR on powders . . . . .  | 32  |
| 9  | Some pulse sequences . . . . .   | 34  |
| 10 | Principles of pulsed EPR . . . . .   | 35  |
| 11 | Schematic HYSCORE signals . . . . .  | 38  |
| 12 | Blind spots in case of strong hfi . . . . .  | 41  |
| 13 | MO and angular momentum scheme of NO . . . . .   | 43  |
| 14 | EPR spectrum of NO gas . . . . .   | 46  |
| 15 | EPR spectrum of adsorbed NO . . . . .  | 48  |
| 16 | Room temperature CW EPR spectra of NO gas at different pressures . . . . .   | 56  |
| 17 | Room temperature pressure vs. EPR line width of NO gas . . . . .   | 58  |
| 18 | Temperature dependence of the EPR line width of NO gas . . . . .   | 60  |
| 19 | Room temperature density vs. EPR line width at 123 K of NO gas, EPR signal intensity vs. temperature of NO gas . . . . . | 61  |
| 20 | EPR spectra of NO gas in Al-MIL-100 . . . . .  | 63  |
| 21 | EPR spectra of NO gas in F_DUT-8a and F_DUT-8b . . . . .   | 63  |
| 22 | EPR spectra of NO gas in Al/Cr-MIL-53 . . . . .  | 64  |
| 23 | EPR spectra of NO gas in various DUT-8(Ni) samples . . . . .   | 65  |
| 24 | Experimental EPR signal intensities of NO gas . . . . .  | 67  |
| 25 | X-band and Q-band spectrum of adsorbed NO in Al-MIL-53 . . . . .   | 75  |
| 26 | Temperature-dependent EPR intensities of adsorbed and desorbed NO in Al/Cr-MIL-53 . . . . .                              | 76  |
| 27 | EPR line width vs. temperature of adsorbed NO in Al-MIL-53 . . . . .   | 78  |
| 28 | Two-pulsed field sweep spectrum of adsorbed NO in Al-MIL-53 . . . . .  | 79  |
| 29 | Exemplary HYSCORE spectra of sample Al-MIL-53 . . . . .  | 81  |
| 30 | HYSCORE signals of distant $^{27}\text{Al}$ in Al-MIL-53 . . . . .   | 82  |
| 31 | HYSCORE signals of different proton species in Al-MIL-53 . . . . .   | 84  |
| 32 | Simulated proton HYSCORE signals for Al-MIL-53 . . . . .   | 86  |
| 33 | Exemplary simulated adsorption powder spectrum of nitric oxide . . . . .   | 86  |
| 34 | Illustration of possible NO positions in MIL-53 . . . . .  | 88  |
| 35 | Experimental EPR spectrum adsorbed NO in sample Al-MIL-100 . . . . .   | 94  |
| 36 | Temperature-dependent EPR spectra of adsorbed NO in Al-MIL-100 . . . . .   | 95  |
| 37 | Temperature-dependent EPR intensities of adsorbed and desorbed NO in Al-MIL-100 . . . . .                                | 96  |
| 38 | Two-pulse ESE field sweep spectra of adsorbed NO in Al-MIL-100 . . . . .   | 98  |
| 39 | Representative HYSCORE spectrum of sample Al-MIL-100 . . . . .   | 99  |
| 40 | Experimental and simulated HYSCORE signal of Al2a . . . . .  | 102 |
| 41 | Experimental and simulated HYSCORE signal of Al2b . . . . .  | 104 |
| 42 | Experimental and simulated HYSCORE signal of distant $^{27}\text{Al}$ in Al-MIL-100 . . . . .                            | 106 |
| 43 | Davies ENDOR spectra of sample Al-MIL-100 . . . . .  | 107 |
| 44 | Selected Davies ENDOR spectra of sample Al-MIL-100 . . . . .   | 108 |
| 45 | The finally B3LYP/def-2TZVP-optimized cluster models <b>ML</b> and <b>M</b> . . . . .                                    | 112 |
| 46 | Relaxed surface scans of the PES of the cluster models <b>ML</b> and <b>M</b> . . . . .                                  | 114 |
| 47 | HOMO, LUMO, spin and electronic density of cluster model <b>M</b> . . . . .  | 117 |

|      |   |     |
|------|---|-----|
| 48   | Temperature-dependent EPR spectra of the DUT-8(Ni) samples . . . . .  | 129 |
| 49   | Simulated EPR signals of Ni <sup>2+</sup> -NO species in DUT-8(Ni) samples . . . . .                        | 130 |
| 50   | MO diagrams of Ni <sup>2+</sup> -NO species . . . . .   | 133 |
| 51   | Different qualitative structural models proposed for Ni <sup>2+</sup> -NO species in<br>DUT-8(Ni) . . . . . | 134 |
| 52   | Low temperature EPR spectra of rigid DUT-8(Ni) samples . . . . .  | 136 |
| 53   | Temperature-dependent amount of various Ni <sup>2+</sup> -NO species in DUT-8(Ni)<br>samples . . . . .      | 137 |
| 54   | Two-pulse ESE field sweep spectrum of sample F_DUT-8b . . . . .   | 140 |
| 55   | HYSCORE spectrum of sample F_DUT-8b and structural model for NiNOb  | 141 |
| 56   | Three-pulse ESEEM spectrum of F_DUT-8b . . . . .  | 143 |
| C.1  | The primary echo pulse sequence . . . . .   | 156 |
| D.1  | Temperature-dependent Cr <sup>3+</sup> EPR signals of sample Al/Cr-MIL-53 . . . . .                         | 160 |
| D.2  | Selective simulated X-band Cr <sup>3+</sup> EPR signals of sample Al/Cr-MIL-53 . . . . .                    | 161 |
| D.3  | Temperature-dependent amount of the lp phase in Al/Cr-MIL-53 . . . . .                                      | 162 |
| E.1  | HYSCORE spectrum of Al-MIL-53 at field position A . . . . .   | 166 |
| E.2  | HYSCORE spectrum of Al-MIL-53 at field position B . . . . .   | 166 |
| E.3  | HYSCORE spectrum of Al-MIL-53 at field position C . . . . .   | 167 |
| E.4  | HYSCORE spectrum of Al-MIL-53 at field position D . . . . .   | 167 |
| E.5  | HYSCORE spectrum of Al-MIL-53 at field position E . . . . .   | 167 |
| E.6  | HYSCORE spectrum of Al-MIL-53 at field position F . . . . .   | 167 |
| E.7  | HYSCORE spectrum of Al-MIL-53 at field position G . . . . .   | 168 |
| E.8  | HYSCORE spectrum of Al-MIL-53 at field position H . . . . .   | 168 |
| E.9  | HYSCORE spectrum of Al-MIL-53 at field position I . . . . .   | 168 |
| E.10 | HYSCORE spectrum of Al-MIL-53 at field position J . . . . .   | 168 |
| F.1  | HYSCORE spectrum of Al-MIL-100 at field position A . . . . .  | 170 |
| F.2  | HYSCORE spectrum of Al-MIL-100 at field position B . . . . .  | 170 |
| F.3  | HYSCORE spectrum of Al-MIL-100 at field position C . . . . .  | 171 |
| F.4  | HYSCORE spectrum of Al-MIL-100 at field position C . . . . .  | 171 |
| F.5  | HYSCORE spectrum of Al-MIL-100 at field position D . . . . .  | 172 |
| F.6  | HYSCORE spectrum of Al-MIL-100 at field position D . . . . .  | 172 |
| F.7  | HYSCORE spectrum of Al-MIL-100 at field position D . . . . .  | 173 |
| F.8  | HYSCORE spectrum of Al-MIL-100 at field position D . . . . .  | 173 |
| F.9  | HYSCORE spectrum of Al-MIL-100 at field position E . . . . .  | 174 |
| F.10 | HYSCORE spectrum of Al-MIL-100 at field position E . . . . .  | 174 |
| F.11 | HYSCORE spectrum of Al-MIL-100 at field position E . . . . .  | 175 |
| F.12 | HYSCORE spectrum of Al-MIL-100 at field position F . . . . .  | 175 |
| F.13 | HYSCORE spectrum of Al-MIL-100 at field position G . . . . .  | 176 |
| F.14 | HYSCORE spectrum of Al-MIL-100 at field position H . . . . .  | 176 |
| F.15 | HYSCORE spectrum of Al-MIL-100 at field position I . . . . .  | 177 |
| F.16 | HYSCORE spectrum of Al-MIL-100 at field position I . . . . .  | 177 |
| F.17 | HYSCORE spectrum of Al-MIL-100 at field position J . . . . .  | 178 |
| F.18 | HYSCORE spectrum of Al-MIL-100 at field position J . . . . .  | 178 |
| F.19 | HYSCORE spectrum of Al-MIL-100 at field position J . . . . .  | 179 |
| F.20 | HYSCORE spectrum of Al-MIL-100 at field position K . . . . .  | 179 |
| F.21 | HYSCORE spectrum of Al-MIL-100 at field position L . . . . .  | 180 |
| F.22 | HYSCORE spectrum of Al-MIL-100 at field position M . . . . .  | 180 |
| F.23 | HYSCORE spectrum of Al-MIL-100 at field position N . . . . .  | 181 |
| F.24 | HYSCORE spectrum of Al-MIL-100 at field position N . . . . .  | 181 |
| F.25 | HYSCORE signals of distant <sup>27</sup> Al in sample Al-MIL-100 . . . . .                                  | 182 |

**List of Tables**

|     |  |     |
|-----|--|-----|
| 1   | Parameters characterizing the ad/desorption of NO on the MOF samples . . .                                     | 66  |
| 2   | Room temperature line width and amount of desorbed NO in the MOF samples . . . . .                             | 68  |
| 3   | g-tensor principal values of NO adsorbed in Al-MIL-53 . . . . .  | 74  |
| 4   | $^{27}\text{Al}$ nqi parameters for MIL-53(Al) . . . . .   | 82  |
| 5   | Simulation derived hfi parameters for protons in Al-MIL-53 . . . . .   | 85  |
| 6   | Spin Hamilton parameters for NO adsorbed in MIL-100(Al) . . . . .  | 93  |
| 7   | Experimentally derived hfi and nqi parameters for $^{27}\text{Al}$ species in MIL-100(Al)                      | 100 |
| 8   | Structural parameters of the clusters <b>ML</b> and <b>M</b> . . . . .   | 113 |
| 9   | Spin Hamilton parameters as derived by DFT for the B3LYP/def2-TZVP optimized cluster model <b>ML</b> . . . . . | 115 |
| 10  | Reduced spin populations according to Mulliken and Löwdin . . . . .  | 119 |
| 11  | HOMO-LUMO gaps of adsorbed NO species . . . . .  | 122 |
| 12  | Experimental g-tensor principal values of $\text{Ni}^{2+}$ -NO species . . . . .                               | 131 |
| 13  | g-tensor principal values of weakly physisorbed NO . . . . .   | 140 |
| 14  | $\text{Ni}^{2+}$ -proton distances according the HYSCORE spectroscopy . . . . .                                | 142 |
| A.1 | MOF and NO amount in the EPR samples . . . . .   | 153 |
| D.1 | Spin Hamiltonian parameters of $\text{Cr}^{3+}$ in Al/Cr-MIL-53 . . . . .                                      | 159 |
| F.1 | More DFT derived structural parameters for <b>ML</b> an <b>M</b> . . . . .                                     | 184 |
| F.2 | More DFT derived magnetic parameters for <b>ML</b> . . . . .   | 185 |



---

## Nomenclature

|         |  |
|---------|--|
| 1D      | one-dimensional                                |
| 2D      | two-dimensional                                |
| 3D      | three-dimensional                              |
| AO      | atomic orbital                                 |
| bdc     | benzenedicarboxylate                           |
| btc     | benzenetricarboxylate                          |
| COSX    | chain-of-spheres exchange                      |
| cp      | close pore                                     |
| CUS     | coordinative unsaturated metal site            |
| CW      | continuous wave                                |
| dabco   | 1,4-diazabicyclo[2.2.2]octane                  |
| DFT     | density functional theory                      |
| DQ      | double quantum                                 |
| DUT     | Dresden University of Technology               |
| ENDOR   | electron nuclear double resonance              |
| EPR     | electron paramagnetic resonance                |
| ESE     | electron spin echo                             |
| ESEEM   | electron spin echo envelope modulation         |
| fs      | fine structure                                 |
| FWHM    | full width at half maximum                     |
| hfi     | hyperfine interaction                          |
| HKUST   | Hong Kong University of Science and Technology |
| HOMO    | highest occupied canonical molecular orbital   |
| HYSCORE | hyperfine sublevel correlation                 |
| IR      | infrared                                       |
| LCAO    | linear combination of atomic orbitals          |
| lp      | large pore                                     |
| LUMO    | lowest unoccupied canonical molecular orbital  |
| MIL     | Materials of Institut Lavoisier                |
| MO      | molecular orbital                              |

|      |                                |
|------|--------------------------------|
| MOF  | metal-organic framework        |
| MQ   | multi quantum                  |
| MS   | mass spectroscopy              |
| mw   | microwave                      |
| ndc  | 2,6-naphthalenedicarboxylate   |
| NMR  | nuclear magnetic resonance     |
| np   | narrow pore                    |
| nqi  | nuclear quadrupole interaction |
| PES  | potential energy surface       |
| PXRD | powder X-ray diffraction       |
| REI  | rare earth ion                 |
| rf   | radio frequency                |
| RI   | resolution of the identity     |
| SCF  | self-consistent field          |
| SEM  | scanning electron microscopy   |
| shf  | super hyperfine                |
| SQ   | single quantum                 |
| TGA  | thermogravimetric analysis     |
| TMI  | transition metal ion           |
| TQ   | triple quantum                 |
| XAS  | X-ray absorption spectroscopy  |
| zfi  | zero-field interaction         |
| ZIF  | zeolitic imidazolate framework |

---

## List of samples

---

| sample       | chemical formula  | provided by                                     |
|--------------|---|---|
| Al-MIL-53    | Al(OH)[1,4-bdc] - activated, loaded with NO   | M. Hartmann et al.,<br>FAU<br>Erlangen-Nürnberg |
| Al/Cr-MIL-53 | Al <sub>0.98</sub> Cr <sub>0.02</sub> (OH)[1,4-bdc] - activated, loaded with NO                             |   |
| Al-MIL-100   | {Al <sub>3</sub> O(OH)(H <sub>2</sub> O)} <sub>4</sub> [1,3,5-btc] <sub>4</sub> - activated, loaded with NO |   |
| F_DUT-8a     | Ni <sub>2</sub> (2,6-ndc) <sub>2</sub> dabco - flexible, activated, loaded with little NO                   | S. Kaskel et al. TU<br>Dresden                  |
| F_DUT-8b     | Ni <sub>2</sub> (2,6-ndc) <sub>2</sub> dabco - flexible, activated, loaded with much NO                     |   |
| R_DUT-8a     | Ni <sub>2</sub> (2,6-ndc) <sub>2</sub> dabco - rigid, activated, loaded with little NO                      |   |
| R_DUT-8b     | Ni <sub>2</sub> (2,6-ndc) <sub>2</sub> dabco - rigid, activated, loaded with much NO                        |   |

---

## Frequently used variables and constants

|  |   |
|--|---|
| $\mathbf{A}, A_i$                          | hyperfine interaction tensor/principal value  |
| $A$  | secular hyperfine interaction constant  |
| $a_{\text{iso}}$                           | isotropic hyperfine interaction value   |
| $\alpha$                                   | first Euler angle describing the orientation of a tensor  |
| $B$  | pseudo secular hyperfine interaction constant   |
| $\mathbf{B}_0, B_0$                        | external magnetic field vector/magnitude  |
| $B_1$                                      | magnitude of oscillating magnetic field perpendicular to $\mathbf{B}_0$   |
| $\beta$                                    | second Euler angle describing the orientation of a tensor   |
| $C_Q$                                      | quadrupole coupling constant  |
| $\gamma$                                   | third Euler angle describing the orientation of a tensor  |
| $\mathbf{D}$                               | fine structure tensor   |
| $D$  | axial fine structure constant   |
| $\Delta$                                   | energy difference between the ${}^2\Pi_x$ and ${}^2\Pi_y$ molecular states of NO  |
| $\delta B_{\text{pp}}$                     | peak-to-peak EPR linewidth  |
| $E$  | orthorhombic fine structure constant or energy difference between the ${}^2\Pi_y$ and ${}^2\Sigma$ molecular states of NO |
| $E_A$                                      | activation energy   |
| $\eta$                                     | nuclear quadrupole interaction asymmetry parameter  |
| $\mathbf{g}, g, g_i$                       | g-tensor/factor/principal value   |
| $g_e$                                      | free electron g-value   |
| $g_n$                                      | nuclear g-factor  |
| $\hat{H}$                                  | spin Hamiltonian  |
| $h$  | Planck constant   |
| $\hbar$                                    | reduced Planck constant   |
| $I$  | nuclear spin  |
| $\hat{\mathbf{I}}, \hat{I}_i$              | nuclear spin vector operator and its component  |
| $J$  | total angular momentum  |
| $\lambda$                                  | spin orbit coupling constant of NO  |
| $\mathbf{M}$                               | macroscopic Magnetization vector  |
| $m$  | mass  |
| $m_I$                                      | nuclear magnetic quantum number   |
| $m_S$                                      | magnetic quantum number   |
| $\mu$                                      | reduced mass  |
| $\mu_B$                                    | Bohr magneton   |
| $\mu_n$                                    | nuclear magneton  |
| $\hat{\boldsymbol{\mu}}, \boldsymbol{\mu}$ | magnetization vector operator/ vector   |
| $n$  | volumetric number density   |
| $N$  | total amount  |
| $\omega_1$                                 | angular frequency of precession around $B_1$ field  |
| $\omega_{\text{eff}}$                      | nutaton angular frequency   |

---

|                               |  |
|-------------------------------|--|
| $\Omega_S$                    | angular frequency of precession in the rotating frame                                    |
| $\nu$                         | radio frequency (in ENDOR measurements)  |
| $\nu_{\alpha,\beta}$          | nuclear central transition frequencies of the electron spin $m_S = \pm 1/2$ submanifolds |
| $\nu_I$                       | nuclear Zeeman frequency   |
| $\nu_{\text{mw}}$             | micro wave frequency   |
| $\nu_S$                       | electron Larmor frequency  |
| $\omega_S$                    | electron Larmor angular frequency  |
| $\omega_{\text{mw}}$          | micro wave angular frequency   |
| $p$                           | pressure   |
| $\mathbf{Q}$                  | nuclear quadrupole interaction tensor  |
| $\rho$                        | hyperfine interaction asymmetry parameter  |
| $S$                           | electron spin  |
| $\hat{\mathbf{S}}, \hat{S}_i$ | electron spin vector operator and its component  |
| $\sigma$                      | collisional cross section  |
| $\mathbf{T}$                  | dipolar hyperfine interaction tensor   |
| $T$                           | temperature or dipolar hyperfine interaction constant                                    |
| $t, t_1, t_2$                 | time constants in pulse sequences  |
| $\tau$                        | lifetime decay rate or time constant in pulse sequences                                  |
| $\bar{v}$                     | average relative velocity between two NO molecules                                       |
| $V$                           | volume   |

## 1 Introduction

Metal-organic frameworks (MOFs) consist of metal-oxygen clusters, which are connected by organic ligands forming one-dimensional (1D), two-dimensional (2D) or three-dimensional (3D) crystalline and microporous networks.<sup>[2,3]</sup> The large amount of different kinds of organic linker molecules and metal units allow for the design of an enormous number of tailored MOFs, in principle.<sup>[3]</sup> This large variety as well as the permanent porosity and the diverse surface chemistry have prompted extensive studies since the pioneering work in the early 1990s<sup>[4-9]</sup>. The desired applications<sup>[10-17]</sup> cover the storage of molecules like hydrogen,<sup>[18-20]</sup> or carbon dioxide,<sup>[21-25]</sup> separation of molecules<sup>[26-31]</sup> or even isotopes,<sup>[32-34]</sup> catalysis<sup>[35-41]</sup> including photocatalysis,<sup>[42-45]</sup> sensing,<sup>[46-50]</sup> electrochemical energy storage,<sup>[13,51-54]</sup> light-harvesting,<sup>[55-60]</sup> light-emitting,<sup>[61,62]</sup> pollutants removal,<sup>[63-67]</sup> adsorption cooling<sup>[68,69]</sup> or the controlled release of drug molecules.<sup>[70-75]</sup> But also the scientific interest in new phenomena occurring in nanometre-sized space has motivated the research on MOFs.<sup>[3]</sup>

It is evident that a broad range of experimental methods is necessary for the characterization and study of MOFs and their interactions with guest molecules.<sup>[76,77]</sup> Porosity related properties like the geometric surface area, pore volume or the pore size distribution, enthalpy of adsorption, characterization of coordinative unsaturated metal sites (CUS) and kinetics of structural transitions can be investigated by adsorption experiments.<sup>[76,78]</sup> The overall crystal structure is usually determined by X-ray or neutron diffraction<sup>[79-81]</sup>. Further local geometric and electronic as well as dynamic information can be obtained with methods like X-ray absorption spectroscopy (XAS),<sup>[82]</sup> infrared (IR)<sup>[77]</sup> and Raman spectroscopy<sup>[83]</sup> or nuclear magnetic resonance (NMR) spectroscopy.<sup>[84-86]</sup>

Less common in MOF research is the application of electron paramagnetic resonance (EPR) spectroscopy.<sup>[76]</sup> A literature search for the keywords “MOF” and “EPR” on webofknowledge.com in February 2019 results in 64 hits, compared to 399 if one searches for “MOF” and “NMR”. One might think that one reason for the moderate use of this method, in this field, is its restriction to the detection of paramagnetic species with unpaired electrons. Even if a MOF consists of paramagnetic transition metal ions (TMI) or rare earth ions (REI), their high spatial concentration in the MOF structure might prevent the resolution of the most informative spin interactions due to the dominant magnetic dipole and spin exchange couplings among the TMI or REI.<sup>[76]</sup>

However, EPR methods can often provide local information about structural, electronic and dynamic properties of paramagnetic species which are hardly obtainable by other approaches. In particular, EPR has been proven to be a powerful tool for the investigation of paramagnetic centers in inorganic porous materials and on metal oxide surfaces,<sup>[87-96]</sup> with emphasis on subjects like catalytic applications.<sup>[97-99]</sup> A more frequently usage of EPR in the field of MOFs is therefore highly desirable. For that, a respective avoidance of too large concentrations of paramagnetic species is necessary.

The mentioned problem can be often circumvented by doping a diamagnetic host with paramagnetic EPR probes, called paramagnetic dilution. More specifically, some of the framework metal ions of a diamagnetic MOF can be replaced by paramagnetic metal

---

ions.<sup>[100–104]</sup> In that way, comprehensive studies of gas adsorption at the CUS of MOFs have been reported.<sup>[105–109]</sup> The author of this thesis has investigated in detail the structural phase transition of the MOF MIL-53( $\text{Al}_{1-x}\text{Cr}_x$ ) (MIL = Materials of Institute Lavoisier,  $x = 0.01 \dots 0.02$ ) during temperature variation<sup>[110]</sup> and  $\text{CO}_2$  adsorption.<sup>[111]</sup> Those studies were carried out by doping the diamagnetic  $\text{Al}^{3+}$  with a few percent of paramagnetic  $\text{Cr}^{3+}$  ions, which have a  $3d^3$  electron configuration and therefore an electron spin  $S = 3/2$ . Similar studies have been reported for the  $\text{V}^{4+}$  doped MIL-53(Al) where the paramagnetically diluted  $\text{V}^{4+}$  ions act as EPR active probes for structural transitions of the MOF.<sup>[112,113]</sup> Another example for paramagnetic dilution is a recent study of the author where the  $\text{CO}_2$  sorption triggered structural phase transition of the  $\text{Cu}^{2+}$  doped diamagnetic  $\text{Zn}_2(\text{BME-bdc})_2(\text{dabco})$  MOF was probed by the *in situ* EPR detection of the  $\text{Cu}^{2+}$  signals.<sup>[114]</sup> However, even in cases where all metal ions of the MOF material are paramagnetic, its investigation with EPR might be feasible, if the distances between the ions are large enough as shown exemplarily in a recent study of Kultaeva et al.<sup>[115]</sup>

Whereas the previous approach alters the composition of the host material, it is also possible to introduce paramagnetic guest molecules into the MOF structure. Here, the latter can be diamagnetic, in principle. The adsorption characteristics of those guest molecules are mainly determined by their interaction with the MOF surface. This interaction can be characterized by EPR spectroscopy using these molecules as EPR active probes, since their local microscopic environment alters their EPR spectroscopic relevant properties. Information about the pore volume or the local geometric and electronic structure of the respective adsorption sites on the MOF surface can be obtained in this way. Only a few studies applying this method in MOF research have been reported. For example, the mobility of nitroxide radicals adsorbed in MIL-53(Al) were characterized by EPR and information about the structural phase transition of this MOF and the position and orientation of the nitroxide radicals were obtained in this way.<sup>[116,117]</sup> Furthermore, a nitroxide adsorption complex at the CUS in the MOF HKUST-1 (HKUST = Hong Kong University of Science and Technology) was investigated by EPR<sup>[118]</sup> and Lewis acid sites in the aluminum containing MOFs MIL-100 and MIL-110 were characterized by the EPR spectra of adsorbed nitroxide radicals.<sup>[119]</sup> A recent study reports the introduction of a nitroxide probe into the MOF ZIF-8 (ZIF - zeolitic imidazolate framework).<sup>[120]</sup> Its mobility was altered by the adsorption of additional gases as it was monitored by the EPR signal of that probe.

Other kinds of paramagnetic probes are inorganic radicals like superoxide ( $\text{O}_2^-$ ), the presence of which in MOFs was verified by EPR in several cases.<sup>[121–124]</sup> An electronically similar<sup>[125,126]</sup> but more informative EPR probe is the inorganic radical nitric oxide (NO), since it shows distinct and highly instructive EPR signals in its gaseous desorbed as well as adsorbed phase at certain surface sites. This is demonstrated by the large number of EPR studies in the field of NO adsorption on zeolites or metal-oxide surfaces<sup>[92,127–129]</sup> or in biology.<sup>[130–133]</sup> The research presented in this thesis introduces for the first time the study of the EPR response of adsorbed NO into the field of MOFs. Meanwhile, Khan et al. reported two NMR studies of NO adsorption on two MOFs.<sup>[134,135]</sup> But, although the

most abundant nitrogen isotope  $^{14}\text{N}$  has a nuclear spin  $I = 1$ , the paramagnetism of NO had prevented the usage of NO as a direct NMR active probe in these cases.

The investigation of the adsorption of the paramagnetic molecule NO on MOF surfaces by EPR is of great interest for several reasons. The most prominent one is related to the potential development of medical applications. The physiological role of NO was first discovered by Furchgott, Ignarro and Murad in the 1980s,<sup>[136-140]</sup> who independently discovered its vasorelaxing properties. The following research proved the impact of NO on many organic systems in humans, mammals and plants.<sup>[141-143]</sup> It turns out that NO is a physiological messenger in the cardiovascular, neurological and immune systems and shows antimicrobial and cytotoxic activity.<sup>[140,144-150]</sup> Such important roles in biological systems increase the interest for this gas for medical applications like antithrombotic or antibacterial treatment, wound-healing or for therapies against cancer or neurological diseases.<sup>[139,147,149,151-160]</sup> For the development of appropriate medications, materials are needed, which can store NO and release it in an application adapted manner. Respective drug delivery agents like polymers,<sup>[151,161,162]</sup> functionalized silica nanoparticles,<sup>[163-166]</sup> metallic nanoparticles<sup>[163,167]</sup> and zeolites<sup>[168-172]</sup> have been studied in recent years.

In addition, MOFs have been investigated for their usage as medical storage materials for NO, releasing this gas *in vivo* in a controlled manner.<sup>[173-183]</sup> They enable in principle the storage of large amounts of NO over a long time period owing to the presence of CUS which act as strong bonding adsorption sites for this molecule.<sup>[180,184-186]</sup> By the same time the release of NO is possible under physiological conditions,<sup>[175,178,184,186]</sup> since water molecules replace the NO bound to the metal ion.<sup>[178,184]</sup> A light-induced release of NO from MOFs, functionalized with photoactive NO donors like *N*-nitrosamine, is possible<sup>[177]</sup> as well as the chemical storage of NO in MOFs by the reaction of amino functionalized linkers with NO to diazeniumdiolate,<sup>[173,187]</sup> releasing NO under humid conditions.<sup>[176,188]</sup> Recently, the magnetic resonance imaging-guided and near-infrared light triggered release of NO from nanoscale Mn porphyrin MOF systems with integrated heat-sensitive NO donors was reported<sup>[189]</sup> and might promote the way to new possibilities for cancer therapy. Strategies, using more biocompatible ligands in the MOF structure like vitamin B3, might reduce the toxicity of MOFs acting as NO releasing compounds.<sup>[190]</sup> The development of NO releasing composite materials by combining the functionalities of MOFs with others like polymers is feasible<sup>[191,192]</sup> and might promote the way to an NO delivery agent which fulfills all needs of a real life medication. However, further research toward an MOF based drug delivery agent is necessary. The scale-up of the synthesis of MOFs for NO storage and releases is a crucial factor and subject of ongoing research.<sup>[193]</sup> In addition, an understanding of the fundamentals of NO adsorption on MOFs has high significance and might help tailoring the properties of a desired MOF to the needs of an appropriate NO drug delivery agent.

The adsorption of NO on MOFs is also interesting for other reasons. MOFs might be involved in the development of NO sensors<sup>[194]</sup> or in the catalytic production of NO.<sup>[195]</sup> But such NO related applications are not the only matter which motivates the study of the NO adsorption on MOFs. As pointed out, NO can be used as an EPR active



---

probe molecule which can explore the surface properties of these materials. This might include the characterization of adsorption sites at the organic linker molecules as well as at open metal sites.<sup>[92]</sup> Properties like the Lewis acidity of a catalytically active site, and structural or electronic characteristics of the NO molecules local environment might be derived.<sup>[196–200]</sup> The characterization of the Lewis acidity of catalytically active sites like  $\text{Al}^{3+}$  CUS in MOFs is an important task due to its relevance for the search for MOF materials that are suitable for various applications in heterogeneous catalysis.<sup>[119,201–203]</sup> A standard method for the characterization of Lewis acids in MOFs is IR spectroscopy of certain probe molecules.<sup>[202,204–207]</sup> In general, this method does not enable the unambiguous determination of the adsorption sites' nature probed by the IR active molecule. It is a result of the present thesis, exemplified for the MOF MIL-100(Al), that the alternative use of NO as an EPR probe for the Lewis acidity of  $\text{Al}^{3+}$  CUS in MOFs can, in principle, overcome this disadvantage.

Another important and recent topic is the study of defects in MOFs.<sup>[208,209]</sup> Defects might affect properties related to catalysis, gas adsorption, photoluminescence and magnetic, electrical, electronic and mechanical characteristics.<sup>[208,210–216]</sup> Here, the use of NO as an EPR active probe molecule might be particularly interesting for MOFs without any framework CUS in their defining structure. In the real material, some bonds to the framework ions might be broken, producing defective CUS. NO might adsorb at such defective metal ion sites, making such defects accessible for their characterization by EPR on a microscopic scale. This approach is demonstrated in the present thesis for the particular MOF DUT-8(Ni) (DUT = Dresden University of Technology) relating the characterization of its defects to its flexibility.

Flexibility is an important property of certain MOFs. Some MOFs can change their structure reversibly from a narrow pore (np) or non-porous phase (cp for close pore) to a porous large pore (lp) phase triggered by external stimuli like the gas pressure or the temperature.<sup>[217–221]</sup> This makes them extremely interesting for applications like storage, separation or sensing.<sup>[218]</sup> Particularly, the EPR signal of desorbed NO can give specific insights concerning such structural transformations.<sup>[222–224]</sup>

The analysis of the EPR spectra provides spin Hamiltonian parameters, which characterize the spin system in a phenomenological manner. Of great importance is their interpretation on the basis of the local electronic and geometric structure of the corresponding EPR active species. This objective might be achieved in many cases with the aid of quantum chemical calculations based on approaches like density functional theory (DFT). Such methods correlate the EPR parameters of a certain paramagnetic species with parameters of its local electronic and geometric structure.<sup>[225–233]</sup> To realize such calculations for MOFs, one can either apply periodic boundary conditions<sup>[101,234]</sup> or cut those parts out of the framework structure, which define most importantly the local environment of the paramagnetic species. The latter approach, which is based on the computational characterization of a representative molecular cluster, has been used in the field of MOFs for the development of appropriate force fields,<sup>[235]</sup> or for the study of the adsorption of molecules<sup>[34,236,237]</sup> even correlated with magnetic parameters determined by EPR.<sup>[105]</sup>

DFT has been further used to calculate the structure and EPR parameters of NO adsorption species.<sup>[225,228–232]</sup>

The reader hopefully will be convinced that the investigation of the NO adsorption on MOFs by EPR has great significance although it is not established, yet. The first-time application of this approach is outlined in this thesis. The selection of MOFs investigated in this thesis comprises the MIL-53(Al)<sup>[238]</sup> material and its chromium doped variant,<sup>[110]</sup> the MIL-100(Al)<sup>[239]</sup> and flexible and rigid derivatives of the DUT-8(Ni).<sup>[240,241]</sup> It is representative in such a manner that it includes MOFs with and without coordinative unsaturated metal sites (CUS), with closed and open shell metal ions and with and without intrinsic structural flexibility. The leading questions of this thesis are:

- What are the NO sorption characteristics which EPR reveals?
- What are the local geometric and electronic structures of the NO adsorption species in the various MOFs

After introducing some conceptual background in chapter 2, the methodology of EPR of desorbed NO is further developed and applied to exemplary MOFs in chapter 3.<sup>[222–224]</sup> This way it is demonstrated how the amount of desorbed NO can be roughly quantified *in situ* in an EPR experiment at moderate gas pressures. Its temperature dependence allows for a first characterization of the NO adsorption strength for various MOFs and of their flexibility. One can expect that adsorption of NO might be possible at the organic ligands as well as at the CUS of MOFs. Consequently, for the first comprehensive EPR study of the NO adsorption on MOFs, the famous MIL-53(Al) was chosen as a candidate for a MOF without CUS and the MOF MIL-100(Al) was chosen as a model system for a MOF with CUS, as presented in the chapters 4 and 5, respectively.<sup>[223,242]</sup> Both materials have Al<sup>3+</sup> as their framework metal ion, which has a closed shell 2d<sup>2</sup>2p<sup>6</sup> electron configuration. For the MIL-53(Al) material only a weak physisorption of NO at non-metallic sites at the MOF surface could be identified applying continuous wave (CW) EPR and high resolution pulsed EPR experiments. The MOF MIL-100(Al) is a prominent model system for a heterogeneous catalyst with Al<sup>3+</sup> CUS being strong Lewis acid sites.<sup>[202,205,239]</sup> The application of CW and high resolution pulsed EPR methods to the NO loaded MIL-100(Al) material, complemented by DFT calculations, allowed for the complete characterization of the NO-Al<sup>3+</sup> adsorption complex at the framework CUS and characterized its Lewis acidity at the same time.<sup>[242]</sup> For a third extensive CW EPR study presented in chapter 6 the MOF DUT-8(Ni) was chosen.<sup>[224]</sup> It has no framework CUS but its metal ions are Ni<sup>2+</sup> and therefore open shell ions since they have a 3d<sup>8</sup> electron configuration. Depending on the crystal size,<sup>[241]</sup> this MOF occurs in a flexible<sup>[243–245]</sup> as well as a rigid<sup>[241,246]</sup> version which motivated the search for the microscopic reasons of this difference in flexibility by using NO as an EPR active probe molecule.<sup>[224]</sup> As a result, a correlation between the amount and kind of distinct defective paddle wheel units and the kind of flexibility is strongly indicated by the presented EPR results. The chapter 7 relates some aspects of the preceding four to each other and discusses the significance of the results. A conclusive chapter 8 summarizes the present work and is also suited for readers who are only interested in a brief overview

---

of the thesis. Information about the samples, spectroscopic details and further completing information can be found in the appendix sections at the end of the thesis.

## 2 Materials, methods and theory

The first section 2.1 of this chapter introduces general concepts of MOFs as well as the three different materials, which are considered in this thesis. The section 2.2 explains shortly the different EPR methods applied in this thesis and relevant formulas that will be collected. The section 2.3 comments relevant EPR related properties of NO. The last section 2.4 elucidates shortly the basic concept of DFT.

### 2.1 Metal organic frameworks

#### 2.1.1 General concepts

According to the consensus of the 2013 IUPAC recommendations on Terminology of Metal-Organic Frameworks and Coordination Polymers<sup>[247,248]</sup> the definition of a MOF is: “A *metal-organic framework, abbreviated to MOF, is a coordination network with organic ligands containing potential voids.*” This definition derives from the term “coordination network” which is defined in the same paper as: “A *coordination compound extending, through repeating coordination entities, in 1 dimension, but with cross-links between two or more individual chains, loops, or spiro-links, or a coordination compound extending through repeating coordination entities in 2 or 3 dimensions.*” Consequently, the two defining ingredients of MOFs are “coordination entities”, namely metal clusters, and organic ligands, which connect these clusters to 1D, 2D or 3D crystalline porous networks. The voids in the MOFs can be zero-dimensional, 1D, 2D or 3D existing as closed cavities, channels, layers or intersecting channels, respectively.<sup>[3]</sup>

Often transition-metal ions are the connectors of the organic linkers. Different metals and oxidation states can provide coordination numbers ranging from two to seven.<sup>[3]</sup> Lanthanide ions can increase the coordination number up to ten.<sup>[3]</sup> This diversity of coordination numbers and geometries enables the construction of varied network topologies.<sup>[3]</sup> Another feature of the metal ions is the provision of CUS, which can occur at the cationic sites after the removing of solvent molecules in many MOF structures. They often act as preferred adsorption sites for guest molecules providing the fundamentals for applications like adsorption, catalysis or sensors.<sup>[3]</sup>

The number of organic linker molecules, which can be used for the design of MOFs, is considerably large and includes neutral, anionic and cationic moieties.<sup>[3,249]</sup> With the choice of the linker molecules the topology as well as the functionality of the framework can be tuned.<sup>[249]</sup> The former is strongly determined by the size and shape of the linker, especially its number of the connectors, which can reach from two to eight.<sup>[249]</sup> The surface properties can be altered by the linkers decoration with certain functional groups.<sup>[249]</sup>

Another classification categorizes MOFs as belonging to the first, second and third generation.<sup>[2]</sup> MOFs of the first generation exist as porous frameworks only with adsorbed guest molecules. After the removal of the latter the framework structure breaks down. MOFs of the second generation show permanent and stable porosity, whereas MOFs of the third generation have flexible frameworks enabling transformations between different structural phases as a response to external stimuli like temperature, guest molecules, light,

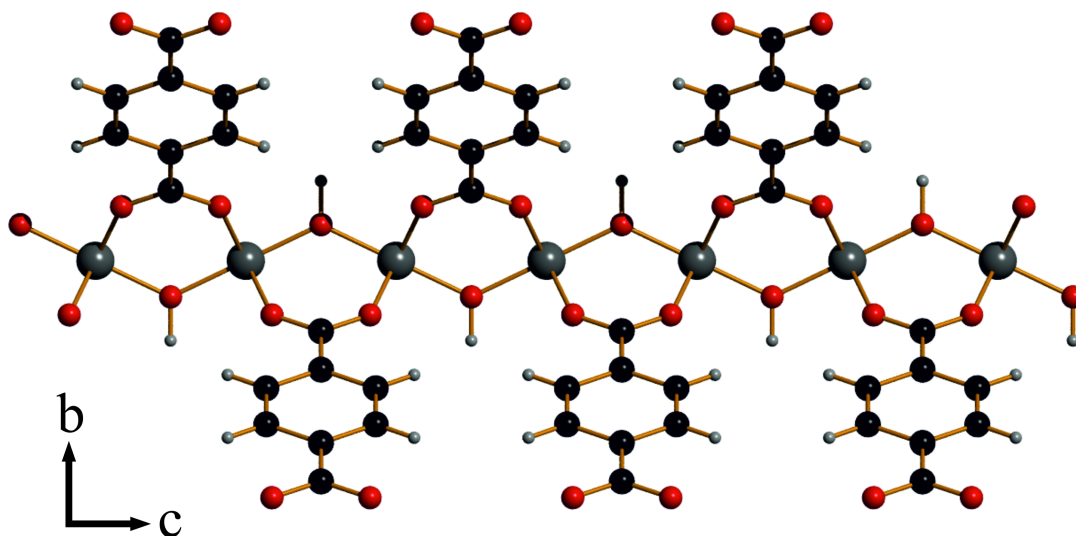


Figure 1: View along the a-direction on a chain of  $\text{AlO}_4(\text{OH})_2$  octahedra with bdc ligands of the empty room temperature lp phase of MIL-53(Al). Atoms are shown in black (carbon), red (oxygen), dark gray (aluminum) and light gray (hydrogen). The structural data were taken from Liu et al.<sup>[1]</sup>

electric or magnetic fields.<sup>[3,219]</sup>

Flexible MOFs can be classified with respect to their stimulated structural transitions including *breathing*<sup>[220]</sup> and *gate pressure*<sup>[221,250]</sup> phenomena.<sup>[219,221,251]</sup> “Breathing” means a structural and reversible transition with a distinct displacement of the framework atoms and a change in the unit cell volume.<sup>[219]</sup> Usually the porosity remains during such a transition whereas the “gate pressure” effect entitles transformations from a non-porous framework structure to a porous one above a certain threshold pressure, namely the “gate-opening” pressure, accompanying with the adsorption of the gas.<sup>[221]</sup> Two MOFs considered in this thesis show the mentioned flexibility. The MOF MIL-53 is a famous example for the “breathing” phenomena,<sup>[238]</sup> whereas DUT-8(Ni) shows the “gate pressure” effect,<sup>[224,241,243–245,252–254]</sup> as outlined in more detail in the following subsections.

### 2.1.2 MIL-53(Al)

The backbone of the famous MOF MIL-53 are 1D chains of  $\text{MO}_4(\text{OH})_2$  octahedra as shown in Figure 1. Here, M is a trivalent cation like  $\text{Cr}^{3+}$ <sup>[255,256]</sup>,  $\text{Fe}^{3+}$ ,<sup>[257]</sup>  $\text{In}^{3+}$ ,<sup>[258]</sup>  $\text{Ga}^{3+}$ <sup>[259]</sup> or  $\text{Al}^{3+}$ <sup>[238]</sup>. Two adjacent metal-oxygen octahedra share a common  $\mu_2$ -(OH) group (Figure 1). These chains are connected with 1,4-benzenedicarboxylate (bdc) ligands forming 1D rhombic channels as is shown in Figure 2. Therefore, the chemical formula of MIL-53 is  $\text{M}(\text{OH})[\text{O}_2\text{C}-\text{C}_6\text{H}_4-\text{CO}_2]$ . In this thesis the aluminum version of MIL-53 as well as its chromium doped version were considered, where about two percent of the framework  $\text{Al}^{3+}$  ions were replaced by  $\text{Cr}^{3+}$  cations. The framework structure of MIL-53(Al) is stable up to a temperature of  $T = 773 \text{ K}$ .<sup>[238]</sup>

The MOF MIL-53(Al) can exist in an lp and an np phase as they are shown in Figure 2a and b.<sup>[1,238]</sup> The empty lp phase has channel dimensions of about  $8.5 \times 8.5 \text{ \AA}^2$  whereas

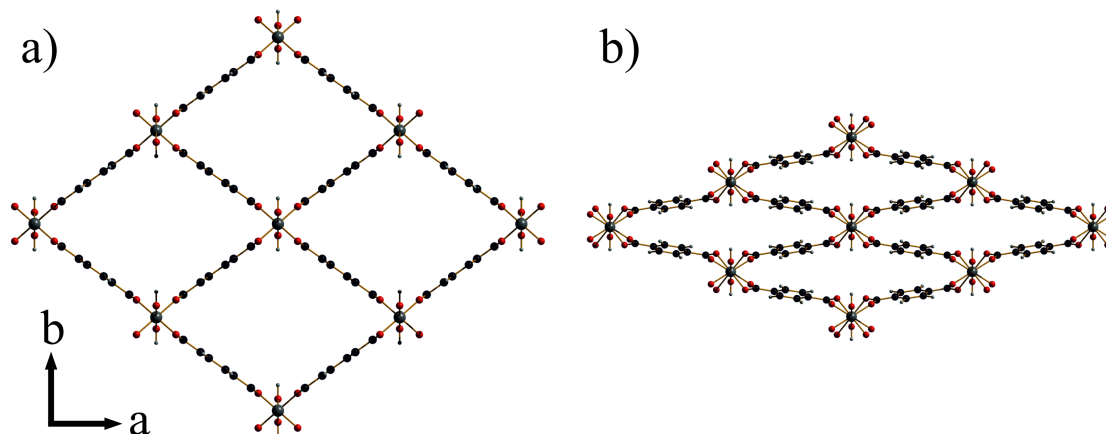


Figure 2: The empty room temperature lp (a) and np (b) phases of MIL-53(Al) as viewed along the  $c$ -axis. The atoms are in black (carbon), red (oxygen), dark gray (aluminum) and light gray (hydrogen). The structural data were taken from Liu et al.<sup>[1]</sup>

the channel dimensions of the hydrated np phase are about  $2.6 \times 13.6 \text{ \AA}^2$  at room temperature.<sup>[238]</sup> The former one has the space group  $Imma$  with an orthorhombic unit cell and a pore volume of  $1430 \text{ \AA}^3$ <sup>[1,260]</sup> whereas the latter has the space group  $C2/c$  with a monoclinic unit cell and a pore volume of about  $864 \text{ \AA}^3$ .<sup>[1,255]</sup> The activated sample exist at room temperature in the lp phase.<sup>[238]</sup> The transformation to the np phase can be triggered reversibly by the adsorption of various guest molecules like water,<sup>[255]</sup>  $\text{CO}_2$ ,<sup>[260]</sup>  $\text{H}_2\text{S}$ ,<sup>[261]</sup> Xe,<sup>[262]</sup> different alkanes<sup>[263,264]</sup> or xylene.<sup>[265]</sup> Also, a temperature change can stimulate the reversible transformation between the lp and np phases, even in the absence of any guest molecules.<sup>[1,110,266]</sup> Starting with the empty lp phase at room temperature, the temperature triggered transformation to the np phase occurs in a temperature range between  $T = 150 \text{ K}$  and  $T = 60 \text{ K}$  during cooling. The back-transformation to the lp phase occurs between  $T = 325 \text{ K}$  and  $T = 375 \text{ K}$  during heating as it has been determined by inelastic neutron scattering, neutron powder diffraction<sup>[1]</sup> and independently by the author with EPR of paramagnetic  $\text{Cr}^{3+}$  probe ions replacing a few percent of the  $\text{Al}^{3+}$  ions.<sup>[110]</sup> This strong hysteresis shows that this temperature driven transformation is of first order. It is accompanied by a coexistence of both phases at all temperatures but most distinct in the temperature ranges where the back- and forward-transitions occur. The reasons of this coexistence are not understood, yet. They might be related to properties like the size of the particles in the powder. For the DUT-8(Ni) material a strong correlation between the framework responsiveness and the particle size was reported<sup>[241]</sup> and a similar correlation may apply to the MIL-53(Al) material.

### 2.1.3 MIL-100(Al)

The structure of the MOF MIL-100(Al) is more complicated than that of MIL-53(Al). The basic metallic building unit is a  $\mu_3$ -oxo-centered trinuclear  $\text{Al}^{3+}$  cluster (Figure 3a) whereas the organic ligand is a 1,3,5-benzenetricarboxylate (btc) ion (Figure 3b). At one  $\text{Al}^{3+}$  ion of each metallic trinuclear cluster one anion like a hydroxyl ion coordinates axially for charge compensation. Water molecules bind to the other two  $\text{Al}^{3+}$  CUS in the non-activated

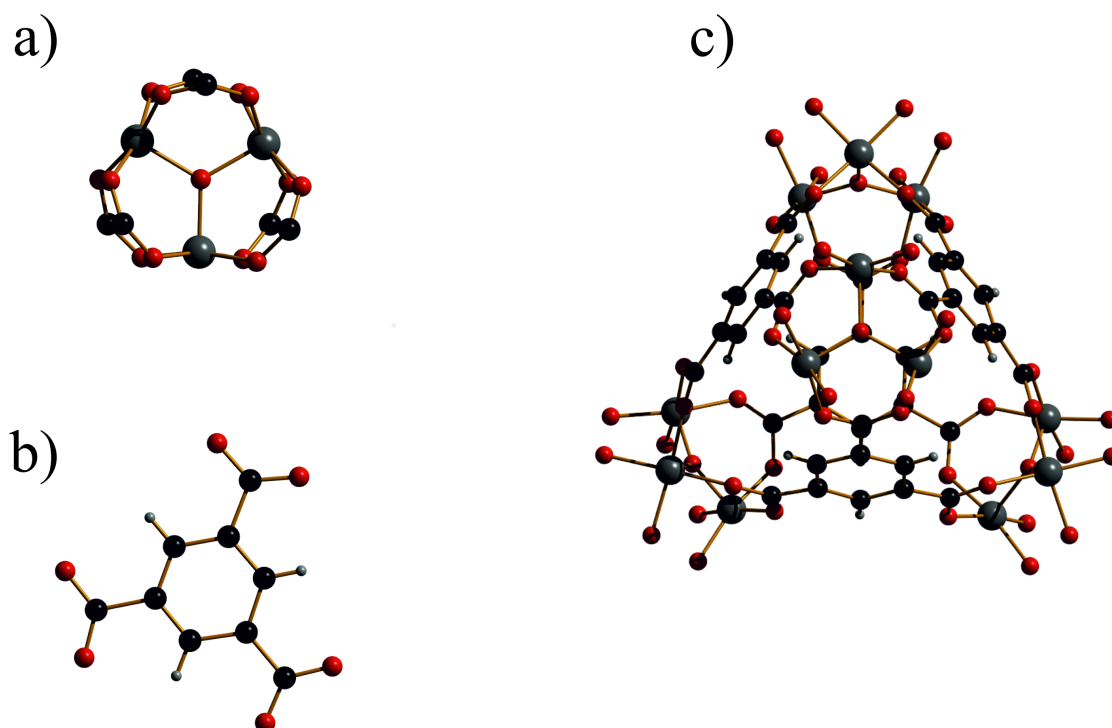


Figure 3: Building units of the MIL-100(Al) structure, namely the trinuclear aluminum cluster (a), the trimesic acid (btc) ligand (b) and the supertetrahedral block (c) with a trinuclear aluminum building unit at each corner and btc ligand at each face. The atoms are carbon (black), oxygen (red), aluminum (dark gray) and hydrogen (light gray). The structural data are from Volkringer et al.<sup>[239]</sup> Water molecules and hydroxyl groups coordinating axially to the aluminum atoms have been omitted.

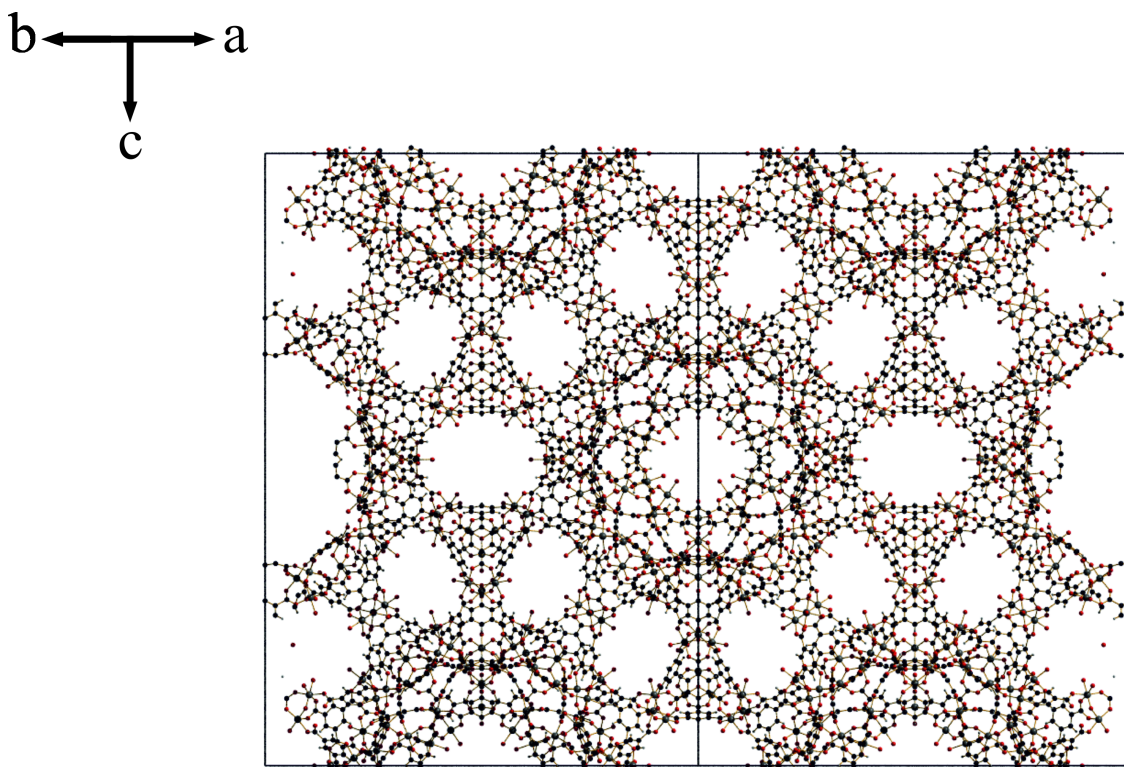


Figure 4: View on one unit cell of the non-activated MIL-100(Al) along the  $[110]$  direction. Only the oxygen atoms of the water and hydroxyl groups coordinating to the aluminum ions are shown. The atoms are black (carbon), red (oxygen), dark gray (aluminum) and light gray (hydrogen). The black lines are the edges for the unit cell. The structural data were taken from Volkringer et al.<sup>[239]</sup>

MOF. These building units form  $\{\text{Al}_3\text{O}(\text{OH})(\text{H}_2\text{O})_2\}_4[\text{btc}]_4$  supertetrahedra with one  $\text{Al}^{3+}$  cluster at each corner and one btc ligand at each face (Figure 3c). The supertetrahedra corresponds to the  $\text{SiO}_4$  units in the zeolite ZSM-39 that also has the MTN topology like MIL-100.<sup>[239,267]</sup> A view of this structure along the  $[110]$  direction is shown in Figure 4. The unit cell of the crystal is cubic with a length  $a = 71.687(3) \text{ \AA}$  and the space group is  $Fd-3m$ .<sup>[239]</sup> This structure has two types of cavities. One is delimited by 12 pentagonal rings with window diameters of  $5.2 \text{ \AA}$  and the other is also delimited by 12 pentagonal rings, but in addition by four hexagonal rings with window diameters of  $8.8 \text{ \AA}$ .<sup>[239]</sup> This structure has seven non-equivalent crystallographic  $\text{Al}^{3+}$  sites.<sup>[239]</sup>

The MOF MIL-100(Al) is thermally stable up to a temperature of  $T = 643 \text{ K}$ .<sup>[201]</sup> During the activation procedure only one water molecule per  $\text{Al}_3$  cluster was indicated to leave the framework leading to only one CUS per  $\text{Al}_3$  trimer.<sup>[201]</sup> Recently, Khan et al.<sup>[135]</sup> reported that the amount of desorbed water during the activation can be even higher.

#### 2.1.4 DUT-8(Ni)

The MOF DUT-8(Ni) has the chemical formula  $\text{Ni}_2(2,6\text{-ndc})_2(\text{dabco})$  where 2,6-ndc stands for 2,6-naphthalenedicarboxylate and dabco stands for 1,4-diazabicyclo[2.2.2]octane.<sup>[244,245]</sup> The metallic building unit is a bimetallic  $\text{Ni}_2$  paddle wheel as shown in Figure 5. Four 2,6-



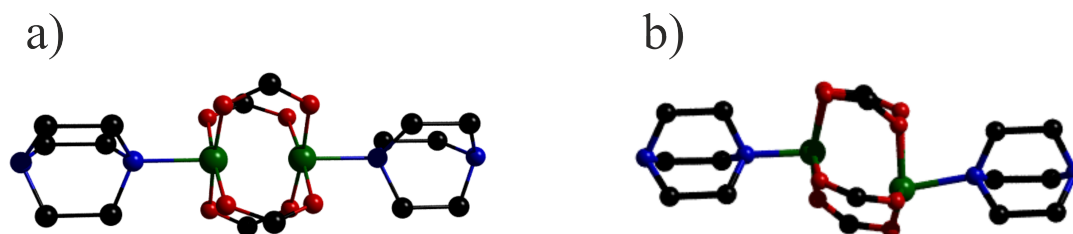


Figure 5: Bimetallic Ni<sub>2</sub> paddle wheel units with coordinating dabco ligands of the lp (a) and cp (b) phase of DUT-8(Ni). The atoms are colored in black (carbon), red (oxygen), blue (nitrogen) and green (nickel). Hydrogen atoms have been omitted. The structural data are from Bon et al.<sup>[240]</sup>

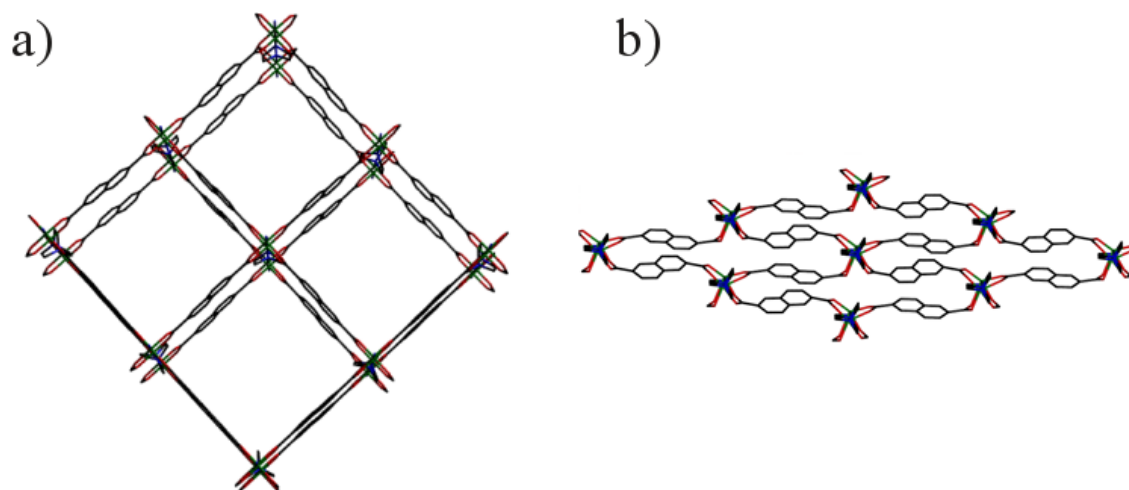


Figure 6: lp phase (a) and the cp phase (b) of DUT-8(Ni). Atoms are colored in black (carbon), red (oxygen), blue (nitrogen) and green (nickel). Hydrogen atoms have been omitted. The structural data are from Bon et al.<sup>[240]</sup>

nde ligands connect each paddle wheel with four other paddle wheels forming square-grid 2D layers in case of the solvent containing lp phase of DUT-8(Ni) as it is shown in Figure 6a. Dabco ligands are coordinating via their nitrogen atoms at the axial sites of the paddle wheels as shown in Figure 5, connecting the 2D layers to a 3D structure (Figure 6). The lp phase of DUT-8(Ni) (Figure 6a) has almost a tetragonal space group  $P4/n$  with the lattice parameters  $a = b = 18.4312 \text{ \AA}$  and  $c = 9.3905 \text{ \AA}$ .<sup>[240,243]</sup> Here, the  $c$ -direction is perpendicular to the 2D layers of DUT-8. The mesh size of the 2D layers is  $9.6 \times 9.6 \text{ \AA}^2$  whereas the smaller channels along the  $a$  and  $b$  directions have approximately  $2.5 \times 7.4 \text{ \AA}^2$  dimensions.<sup>[243]</sup> The diagonals between opposite paddle wheels have lengths of  $18.43 \times 18.43 \text{ \AA}^2$ . After the solvent removal the DUT-8(Ni) structure transforms into a non-porous cp phase with a triclinic  $P1$  space group as it is shown in Figure 6b.<sup>[240]</sup> Now, the diagonals between opposite paddle wheels have changed to the lengths  $23.66 \times 6.95 \text{ \AA}^2$ . Figure 5b illustrates the strong deformation of the  $\text{Ni}_2$  paddle wheels in the cp phase. During the transformation from the lp to the cp phase, the unit cell volume changes drastically from  $1595 \text{ \AA}^3$  to  $647 \text{ \AA}^3$ .<sup>[240]</sup> Also, the color of the powder changes from green to yellow.<sup>[243]</sup>

The reversible transformation between the cp and lp phases of DUT-8(Ni) is an example for the “gate pressure” effect (see subsection 2.1.1). Below a certain threshold gas pressure the MOF stays in its non-porous cp phase. Above this pressure it opens to the porous lp phase to adsorb the corresponding gas. This phenomenon was observed during the adsorption of nitrogen, xenon,  $n$ -butane as well as for carbon dioxide.<sup>[240,243–245]</sup> Both structural phases were further characterized by Raman spectroscopy and distinct low frequency breathing mode bands were identified for both phases.<sup>[253]</sup> The structural responsiveness of the flexible DUT-8(Ni) might become relevant for separation applications. Particularly, it was shown that the flexible DUT-8(Ni) selectively respond with a cp to lp transformation after the exposure to polar aprotic solvents while representative alcohols do not induce this structure transformation, leading to selective adsorption from binary mixtures of such liquids.<sup>[252]</sup>

Interestingly, Lee et al. synthesized a rigid derivative of the DUT-8(Ni),<sup>[246]</sup> modifying slightly the synthesis conditions. This variant stays always in the lp phase even in the absence of any guest molecules. This difference in flexibility of the same MOF materials was correlated to the crystallites sizes.<sup>[241,254]</sup> The DUT-8(Ni) with large crystals ( $> 1 \mu\text{m}$ ) is flexible and adopts the non-porous cp phase in its activated solvent free form whereas the derivative with small crystals ( $< 1 \mu\text{m}$ ) stays in the porous lp phase regardless of whether guest molecules are adsorbed or not.

## 2.2 EPR spectroscopy

EPR spectroscopy can be performed in CW mode, where the sample is irradiated continuously with microwave (mw) radiation of constant frequency or one can choose from a large variety of pulsed EPR methods,<sup>[268]</sup> where sequences of short high power mw pulses are radiated on the sample manipulating the quantum mechanical state of the spin systems. Such spin systems can be described by a spin-Hamiltonian approach which is introduced briefly in the first part of this section. The following subsections discuss the different EPR

methods used in this thesis with a special focus on the needs of the following experiments and analyses.

### 2.2.1 The spin-Hamiltonian approach

Neglecting interactions between electron spins at different spatial positions as well as the magnetic dipole-dipole interactions between different nuclear spins, the energies and corresponding eigenstates of the magnetic sublevels of a magnetic species with electron spin  $S$ , interacting with  $n$  nuclear spins  $I^j$ , can be described in good approximation by the spin Hamiltonian that is

$$\hat{H} = \hat{H}_{\text{EZ}} + \hat{H}_{\text{ZFS}} + \hat{H}_{\text{HF}} + \hat{H}_{\text{NZ}} + \hat{H}_{\text{QI}}, \quad (1)$$

as introduced by Abragam and Pryce in 1951<sup>[268,269]</sup>.

The term:

$$\hat{H}_{\text{EZ}} = \mu_{\text{B}} \mathbf{B}_0^{\text{T}} \mathbf{g} \hat{\mathbf{S}} \quad (2)$$

expresses the electron Zeeman interaction which describes the coupling between the electron spin and the external magnetic field vector  $\mathbf{B}_0$ . Here,  $\mu_{\text{B}}$  is the Bohr magneton and  $\hat{\mathbf{S}}$  the electron spin vector operator. The matrix  $\mathbf{g}$  is the g-tensor with the principal values  $g_x$ ,  $g_y$  and  $g_z$ . As usual, the eigenframe of the g-tensor will define the molecular frame of the considered system throughout this thesis, if nothing else is stated.

The zero-field interaction (zfi) enters in second order into equation (1) as

$$\hat{H}_{\text{ZFS}} = \hat{\mathbf{S}}^{\text{T}} \mathbf{D} \hat{\mathbf{S}}, \quad (3)$$

where the matrix  $\mathbf{D}$  is the traceless zero-field interaction tensor. It has to be considered only for electron spins  $S > 1/2$ . In non-cubic systems, it is responsible for a splitting of the energy levels even at zero magnetic field. It originates from dipolar interactions between electron spins<sup>[270]</sup> as well as from the spin-orbit coupling between the electron spins and their orbital motion.<sup>[271]</sup> It is convenient to express the zfi Hamiltonian as<sup>[268]</sup>

$$\hat{H}_{\text{ZFS}} = D \left[ \hat{S}_z^2 - \frac{1}{3} S(S+1) \right] + E \left( \hat{S}_x^2 - \hat{S}_y^2 \right). \quad (4)$$

Here, the operators  $\hat{S}_u^2$ ,  $u \in \{x, y, z\}$  are the projection of  $\hat{\mathbf{S}}$  on the respective principal axes of the zfi tensor. The parameters  $D$  and  $E$  express directly the symmetry of the zfi tensor. In case of cubic symmetry they are both zero, in case of axially symmetry  $E = 0$  but  $D \neq 0$  and for even lower symmetry they deviate both from zero.

The coupling between the electronic and nuclear spins is described by the hyperfine interaction (hfi) term as follows:

$$\hat{H}_{\text{HF}} = \sum_{j=1}^n \hat{\mathbf{S}}^{\text{T}} \mathbf{A}^j \hat{\mathbf{I}}^j, \quad (5)$$

where the vector operators  $\hat{\mathbf{I}}^j$  describe the nuclear spin  $I^j$  of the  $j$ th nucleus and the matrices  $\mathbf{A}^j$  are the corresponding hfi tensors. Considering the hfi with a single nucleus,

this interaction can be understood as a sum:

$$\hat{H}_{\text{HF}} = \hat{H}_{\text{F}} + \hat{H}_{\text{DD}} \quad (6)$$

consisting of its isotropic part that is:

$$\hat{H}_{\text{F}} = a_{\text{iso}} \hat{\mathbf{S}}^{\text{T}} \hat{\mathbf{I}} \quad (7)$$

and called the Fermi contact interaction and its traceless anisotropic part

$$\hat{H}_{\text{DD}} = \hat{\mathbf{S}}^{\text{T}} \mathbf{T} \hat{\mathbf{I}}, \quad (8)$$

which origin is the dipole-dipole coupling between the electronic and nuclear magnetic moments.<sup>[268]</sup> In its principal value system the dipolar coupling tensor has the following form:

$$\mathbf{T} = T \begin{pmatrix} -(1 + \rho) & 0 & 0 \\ 0 & -(1 - \rho) & 0 \\ 0 & 0 & 2 \end{pmatrix}, \quad (9)$$

with the dipolar coupling constant  $T$  and the asymmetry parameter  $\rho$ . Note that the symbol  $T$  will be also used for the temperature in this thesis, but from the context the usage will be always clear. Consequently, the full hfi tensor calculates as

$$\mathbf{A} = a_{\text{iso}} \mathbf{1} + \mathbf{T}. \quad (10)$$

The Fermi contact interaction is related to the electron spin density  $|\psi(0)|^2$  at the nucleus according to the formula:<sup>[268]</sup>

$$a_{\text{iso}} = \frac{2}{3} \frac{\mu_0}{h} \mu_{\text{B}} \mu_{\text{n}} g_{\text{e}} g_{\text{n}} |\psi(0)|^2, \quad (11)$$

with  $\mu_0$  being the permeability of free space,  $h$  the Planck constant,  $\mu_{\text{n}}$  the nuclear magneton,  $g_{\text{e}} = 2.0023$  the g-factor of the free electron and  $g_{\text{n}}$  the nuclear g-factor.

Assuming that the electronic and nuclear magnetic moments can be considered as point-dipoles, one can estimate from  $T$  the distance  $r$  between the electron and nuclear spins using the relation<sup>[268]</sup>

$$T = \frac{\mu_0}{4\pi h} \mu_{\text{B}} \mu_{\text{n}} g_{\text{e}} g_{\text{n}} r^{-3}. \quad (12)$$

In equation (1) the interaction between the external magnetic field and the various nuclear spins enters as the nuclear Zeeman term

$$\hat{H}_{\text{NZ}} = -\mu_{\text{n}} \sum_{j=1}^n g_{\text{n},j} \mathbf{B}_0^{\text{T}} \hat{\mathbf{I}}^j \quad (13)$$

with the nuclear g-factors  $g_{\text{n},j}$ .

The  $m$  nuclei with nuclear spins  $I^{k_i} > 1/2$ ,  $i = 1, \dots, m$ , where the  $k_i \in \{1, \dots, n\}$ , have an electric quadrupole moment which interacts with the electric field gradient at the site

of the corresponding nucleus. This interaction has to be considered in equation (1) in form of the nuclear quadrupole interaction (nqi) term:

$$\hat{H}_{\text{QI}} = \sum_{i=1}^m \hat{\mathbf{I}}^{k_i \text{T}} \mathbf{Q}^{k_i} \hat{\mathbf{I}}^{k_i}. \quad (14)$$

The matrices  $\mathbf{Q}^{k_i}$  are the nuclear quadrupole interaction tensors. For a single nucleus with spin  $I$  its traceless quadrupole interaction tensor can be expressed in its principal axis system as:<sup>[272]</sup>

$$\mathbf{Q} = \frac{e^2 q Q / h}{4I(2I-1)} \begin{pmatrix} -(1+\eta) & 0 & 0 \\ 0 & -(1-\eta) & 0 \\ 0 & 0 & 2 \end{pmatrix}. \quad (15)$$

Here,  $e$  is the charge of a proton,  $eq$  the largest principal value of the electric field gradient tensor at the nucleus site,  $Q$  the nuclear quadrupole moment and  $\eta$  the biaxiality of the electric field gradient tensor. Often the nqi is described by the quadrupole coupling constant  $C_Q = e^2 q Q / h$ .

Throughout this thesis the energies of the spin-states as well as the zfi, hfi and nqi tensors are given in frequency units. Further, all angular momenta are given in units of 1.

The big advantage of the spin-Hamiltonian approach is that the spatial degrees of freedom of the corresponding wave function are treated as constants that are collected by the few second-rank tensors  $\mathbf{g}$ ,  $\mathbf{D}$ ,  $\mathbf{A}^j$  and  $\mathbf{Q}^{k_i}$  in a phenomenological manner<sup>[268]</sup>. Thus, the dimension of the Hilbert space is drastically reduced to  $d = (2S+1) \prod_{j=1}^n (2I^j+1)$ . The eigenvalues of  $\hat{H}$  are the energies  $E_i$  of the different eigenstates  $|\psi_i\rangle$ . In the high field limit, where the electron Zeeman interaction is large compared to all other terms, each state  $|\psi_i\rangle = |m_S, m_{I_1}, m_{I_2}, \dots, m_{I_n}\rangle$  can be described by the ‘‘almost good’’ magnetic quantum numbers  $m_S = -S, -S+1, \dots, S-1, S$  and  $m_{I^k} = -I^k, -I^k+1, \dots, I^k-1, I^k$  which are the eigenvalues of the  $\hat{S}_z$  and  $\hat{I}_z^k$  operators. The latter are the projections of the  $\hat{\mathbf{S}}$  and  $\hat{\mathbf{I}}^k$  operators on the direction of the magnetic field vector  $\mathbf{B}_0$ . Here, ‘‘almost good’’ means that the Hamiltonian in equation (1) is almost diagonal in the basis consisting of the  $|m_S, m_{I_1}, m_{I_2}, \dots, m_{I_n}\rangle$  states, which means that the  $\hat{S}_z$  and  $\hat{I}_z^k$  operators commute with  $\hat{H}$  (equation (1)) approximately.

For a comprehensive understanding of the following pulsed EPR experiments, it is necessary to collect some information about the energy level spacing of an electron spin  $S = 1/2$  coupled to a nuclear spin  $I$  as derived from equation (1). In the high-field limit each energy level of such a spin system can be characterized by the magnetic quantum numbers  $m_S$  and  $m_I$  as shown schematically in Figure 7. From the spin Hamiltonian in equation (1) one can derive the first order energy of such a level given by:<sup>[268]</sup>

$$\varepsilon(m_S, m_I) = \nu_S m_S + c(m_S) m_I - \frac{1}{2} [I(I+1) - 3m_I^2] Q'_z(m_S), \quad (16)$$

where

$$c(m_S) = \left[ \mathbf{n}^T \left( m_S \frac{\mathbf{g}\mathbf{A}}{g} + \nu_I \mathbf{1} \right) \left( m_S \frac{\mathbf{A}^T \mathbf{g}^T}{g} + \nu_I \mathbf{1} \right) \mathbf{n} \right]^{\frac{1}{2}} \quad (17)$$

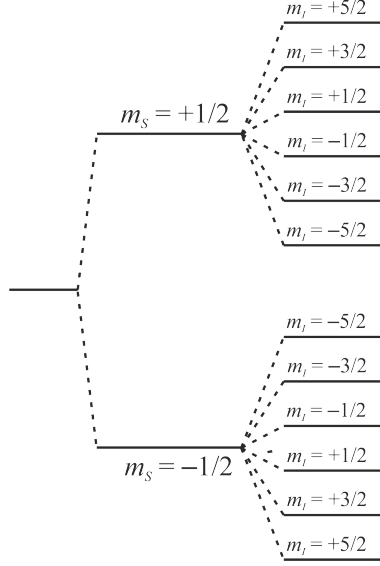


Figure 7: Schematic scheme of the energy levels of an electron spin  $S = 1/2$  coupled to a nuclear spin  $I = 5/2$ . The order of the energy levels corresponds to the case  $A > 0$  and  $A/2 > |\nu_I|$ , where  $A$  is the hfi constant and  $\nu_I = -g_n \mu_n B_0 / h$  the nuclear Zeeman frequency.<sup>[268]</sup>

and

$$Q'_z(m_S) = \frac{1}{c(m_S)^2} \mathbf{n}^T \left( m_S \frac{g\mathbf{A}}{g} + \nu_I \mathbf{1} \right) \mathbf{Q} \left( m_S \frac{\mathbf{A}^T \mathbf{g}^T}{g} + \nu_I \mathbf{1} \right) \mathbf{n} \quad (18)$$

depend only on  $m_S$  but not on  $m_I$ . Here,  $\nu_S = g\mu_B B_0 / h$  is the electron Zeeman frequency,  $\nu_I = -g_n \mu_n B_0 / h$  the nuclear Zeeman frequency,  $B_0 = |\mathbf{B}_0|$  and  $g = \sqrt{\mathbf{n}^T \mathbf{g} \mathbf{g}^T \mathbf{n}}$  the effective g-factor where  $\mathbf{n}^T = (\sin \theta \cos \phi, \sin \theta \sin \phi, \cos \theta)$  is the unit vector describing the direction of  $\mathbf{B}_0$  in the usual spherical coordinates relative to the eigenframe of the g-tensor. The other quantities are the g-, hfi and nqi tensors as defined above.

The nuclear frequencies correspond to the energy differences between levels with different  $m_I$  within the same  $m_S$  submanifold. In the following they are designate as

$$\nu_{m_I, m'_I}^k = \varepsilon(m_S, m_I) - \varepsilon(m_S, m'_I), \quad (19)$$

with  $k = \alpha$  or  $k = \beta$  for  $m_S = +1/2$  or  $m_S = -1/2$ , respectively.

In case of a non-integer nuclear spin, the nuclear frequencies of the nuclear central transitions in each electronic submanifold are called  $\nu_\alpha := \nu_{-\frac{1}{2}, \frac{1}{2}}^\alpha$  and  $\nu_\beta := \nu_{-\frac{1}{2}, \frac{1}{2}}^\beta$ . Neglecting the nqi and assuming small g-anisotropy and an axially symmetric hfi tensor, those frequencies can be expressed in an even more compact form<sup>[268,273]</sup>

$$\begin{aligned} |\nu_\alpha| &= \sqrt{\left(\nu_I + \frac{A}{2}\right)^2 + \frac{B^2}{4}} \\ |\nu_\beta| &= \sqrt{\left(\nu_I - \frac{A}{2}\right)^2 + \frac{B^2}{4}} \end{aligned} \quad (20)$$

with

$$\begin{aligned} A &= a_{\text{iso}} + T(3\cos^2\theta - 1) \\ B &= 3T\sin\theta\cos\theta. \end{aligned} \quad (21)$$

Here,  $A$  and  $B$  describe the secular and pseudo-secular parts of the hfi Hamiltonian in equation (5)<sup>[268,273]</sup> whereas the corresponding non-secular terms, which are proportional to the  $\hat{S}_x$  and  $\hat{S}_y$  operators, are neglected in the derivation of equation (20). Corresponding formulas for the secular and pseudo-secular hfi parameters  $A$  and  $B$  can be obtained if the hf-tensor is orthorhombic.<sup>[268,274]</sup>

A last comment should be made about the electronic transitions, which can be excited by mw radiation. In usual EPR experiments, as considered in this thesis, the transition is induced by the oscillating magnetic field component of the mw radiation which is perpendicular to the external magnetic field. In this case, at magnetic fields which are distinctly larger than the hfi, assuming  $S = 1/2$ , only electronic transitions can be excited which obey the selection rules  $\Delta m_S = \pm 1$  and  $\Delta m_I = 0$ , according to Fermi's golden rule and the conservation of angular momentum.<sup>[275]</sup>

### 2.2.2 CW EPR spectroscopy

The standard and most widely used EPR method is CW EPR spectroscopy.<sup>[275]</sup> Here, electromagnetic waves with constant frequency  $\nu_{\text{mw}}$  in the mw regime are continuously irradiated on the sample. An external magnetic field is applied. Its direction is kept constant but its magnitude is swept over a certain range during an CW EPR experiment. Thus, the most important interaction of those explained in the previous subsection is the electron Zeeman interaction, since it is the only interaction which depends significantly on the magnetic field. Usually, the nuclear Zeeman interaction cannot be resolved in CW experiments. In the simple case of a single electron spin  $S = 1/2$ , the increasing magnetic field would increase the energy separation  $\Delta E$  between the magnetic sublevels that are characterized by the magnetic quantum numbers  $m_S = \pm 1/2$ . This is as an effect of the electron Zeeman interaction (equation (2)). The situation is illustrated in Figure 8a. Since the mw frequency  $\nu_{\text{mw}}$  is constant, the resonance condition  $\nu_{\text{mw}} = \Delta E = g\mu_B B_0/h$  is fulfilled for a single and distinct magnetic field  $B_0^{\text{res}}$ . Therefore, only at this field mw radiation is absorbed by the sample, which is measured in a CW EPR experiment. In the CW setup, the external magnetic field magnitude is superimposed by a small oscillating magnetic field which also modulates the measured EPR response. The corresponding magnitude of the oscillating part of the detected signal gives the typical EPR signal which is consequently the first derivative of the usual adsorption spectrum, as illustrated in Figure 8a.

An increased complication is given, if the sample is a powder, where each molecular orientation occurs with equal abundance in the ideal case. This situation is illustrated in Figure 8b. Here, the simulated EPR powder spectrum of a single electron  $S = 1/2$  with an axially symmetric g-tensor is shown. Its principal values are  $g_{\perp} := g_x = g_y \neq g_z := g_{\parallel}$ . In

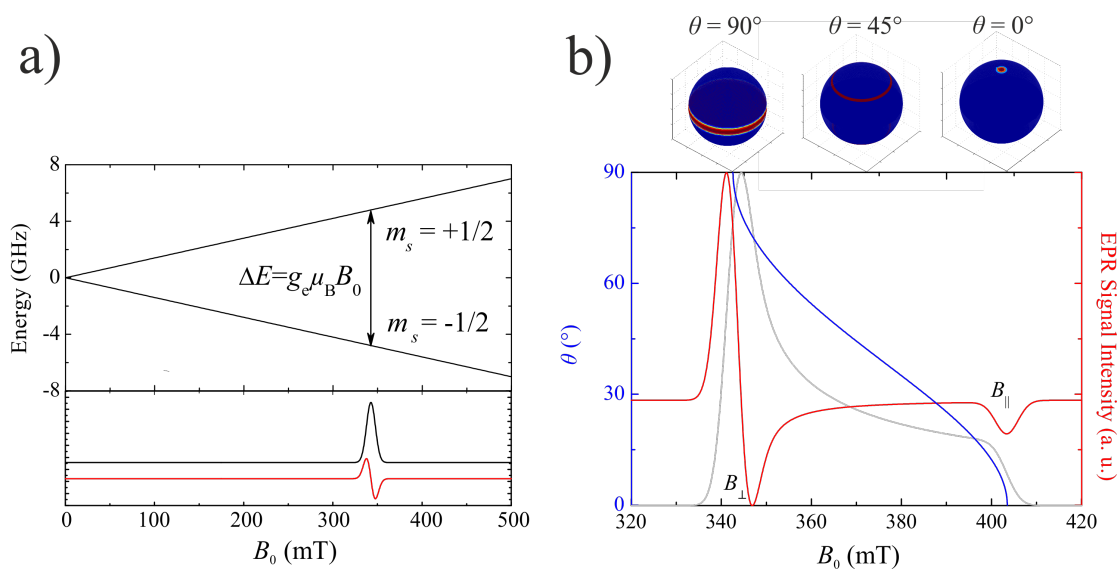


Figure 8: a) Energy levels of an electron spin  $S = 1/2$  with  $g$ -value  $g_e$  as a function of the external magnetic field  $B_0$  (above). The mw absorption spectrum (black) and the corresponding EPR signal which is its first derivative (red) are shown below. The arrow indicates the energy difference  $\Delta E$ , which fulfills at the magnetic resonance field  $B_0$  the resonance condition  $\nu_{\text{mw}} = \Delta E/h$  of a CW EPR experiment, with the mw frequency  $h\nu_{\text{mw}} = 9.6$  GHz. b) The simulated EPR powder spectrum (red) of an electron spin  $S = 1/2$  with an axially symmetric  $g$ -tensor with  $g_{\parallel} = 1.7$  and  $g_{\perp} = 2.0$ . The EPR signal is the first derivative of the corresponding absorption spectrum (light gray). Different orientations of the molecular frame, with respect to the laboratory frame, contribute to the EPR powder signal at different magnetic fields. This is indicated by the magnetic field dependency (blue) of the angle  $\theta$  between the external magnetic field and the axial symmetry axis of the  $g$ -tensor of spin packets, which are in resonance with the mw frequency at the respective magnetic field. Those orientations of the  $g$ -tensor which contribute to the EPR signal at magnetic field positions where  $\theta = 90^\circ$ ,  $45^\circ$  or  $0^\circ$ , are shown on top. The magnetic resonance fields  $B_{\perp}$  and  $B_{\parallel}$  correspond to the resonance positions where  $\theta = 90^\circ$  or  $\theta = 0^\circ$ , respectively.



that case, the resonance field position  $B_0^{\text{res}}(\theta)$  of a micro-crystal with one electron species is fully characterized by the angle  $\theta$  between  $\mathbf{B}_0$  and the principal z-direction of the respective g-tensor. At each magnetic field  $B_0^{\text{res}}(\theta)$ , only those orientations with angle  $\theta$  contribute to the EPR signal, which fulfill the relation:<sup>[275]</sup>

$$B_0^{\text{res}}(\theta) = \frac{h\nu_{\text{mw}}}{\mu_{\text{B}} \sqrt{g_{\perp}^2 \sin^2 \theta + g_{\parallel}^2 \cos^2 \theta}}. \quad (22)$$

In that sense  $\theta = 90^\circ$  defines the resonance field  $B_{\perp}$  where the adsorption signal of the powder has most intensity, since here the largest amount of orientations, namely the full  $x, y$ -plane, contributes to the EPR signal. The angle  $\theta = 0^\circ$  defines the resonance field  $B_{\parallel}$  where the adsorption spectrum has least intensity, since only one orientation parallel to the z-axis of the g-tensor contribute to the EPR signal. The EPR spectrum, which is the first derivative of the absorption signal, has most intense features at the field positions  $B_{\perp}$  and  $B_{\parallel}$  where the principal directions of the g-tensor contribute to the EPR signal (Figure 8b). These features are also called powder edge singularities and they originate from the varied contribution of the g-tensor orientations to different field positions of the EPR spectrum.

As discussed and illustrated in Figure 8b, one can select only a small subset of molecular orientations in the presence of an anisotropic g-tensor, if a distinct magnetic field in an EPR experiment is adjusted. This important technique is called orientation selection and is a powerful tool to determine the relative orientations of hfi or even nqi tensors with high resolution pulsed EPR techniques, even if the sample is a powder and not a single crystal.<sup>[268]</sup> Such pulsed methods will be introduced in the next subsection.

### 2.2.3 Pulsed EPR methods

In this thesis four different pulsed EPR methods were applied to investigate NO species adsorbed in the MOFs, namely two-pulse electron spin echo (ESE) field sweep, hyperfine sublevel correlation (HYSCORE), Davies electron nuclear double resonance (ENDOR) and three-pulse electron spin echo envelope modulation (ESEEM) experiments. Their pulse sequences are summarized in Figure 9.

For the reader, who is not familiar with pulsed EPR, a first understanding of its basic principle will be given in the following. Here, the classical picture of the manipulation of electron spins by short mw pulses will be outlined, as it is described in the textbook of Schweiger and Jeschke.<sup>[268]</sup>

The foundation of pulsed EPR is quantum mechanics. On the other hand, one can describe simple pulsed experiments classically. Here, the macroscopic magnetization vector  $\mathbf{M}$  instead of the microscopic electron spin vector operator  $\hat{\mathbf{S}}$  is considered. As a result of a very fundamental symmetry theorem of quantum mechanics, called *Wigner-Eckart theorem*, each single electron with spin  $S$  has a magnetization that is expressed by the vector operator:<sup>[272]</sup>

$$\hat{\boldsymbol{\mu}} = -g\mu_{\text{B}}\hat{\mathbf{S}}, \quad (23)$$

where  $g$  is the respective g-factor. The macroscopic magnetization vector  $\mathbf{M}$  per unit

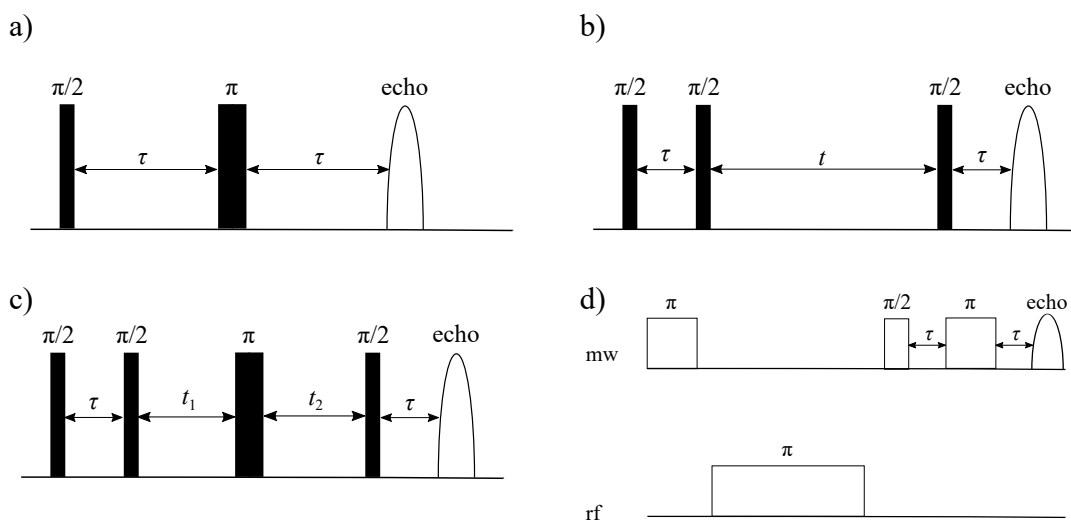


Figure 9: Two-pulse ESE sequence (a) and pulse sequences of the three-pulse ESEEM (b), HSCORE (c) and Davies ENDOR (d) experiments.<sup>[268]</sup> Filled boxes indicate non-selective and empty boxes indicate selective pulses, respectively. In the Davies ENDOR experiment mw pulses as well as radio frequency (rf) pulses are applied in the same sequence.

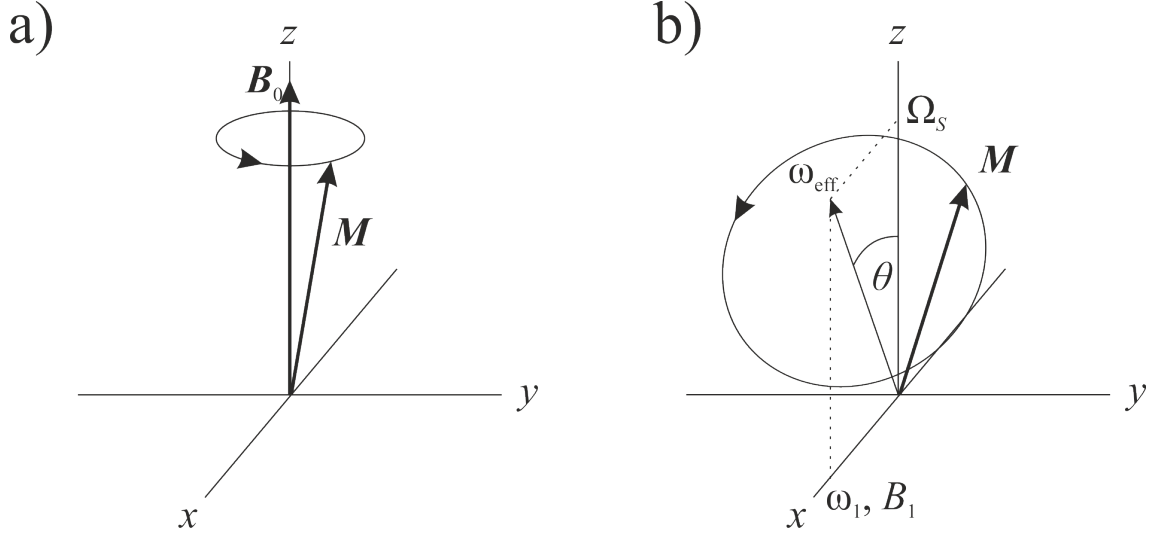


Figure 10: a) Precession of the macroscopic magnetization vector  $\mathbf{M}$  around the magnetic field vector  $\mathbf{B}_0$  with the Larmor frequency  $\omega_S$  in the Laboratory frame and with the frequency  $\Omega_S = \omega_S - \omega_{\text{mw}}$  in the rotating frame.<sup>[268]</sup> b) Nutation of the magnetization vector  $\mathbf{M}$  in the rotating frame in the presence of a magnetic field  $B_1$  along the  $x$ -axis. The nutation frequency is  $\omega_{\text{eff}} = \sqrt{\Omega_S^2 + \omega_1^2}$  where  $\omega_1 = \frac{g\mu_B B_1}{\hbar}$ .<sup>[268]</sup>

volume is related to this microscopic quantity via:<sup>[276]</sup>

$$\mathbf{M} = n \langle \hat{\boldsymbol{\mu}} \rangle, \quad (24)$$

where  $n$  is the density of spins and  $\langle \cdot \rangle$  is the expectation value averaged over all independent sample quantum states. Classically speaking, the magnetization of a single electron is a simple vector  $\boldsymbol{\mu}$  and equation (24) reads as:<sup>[268]</sup>

$$\mathbf{M} = \frac{1}{V} \sum_{i=1}^N \boldsymbol{\mu}_i, \quad (25)$$

where the sum runs over all  $N$  electrons  $i$  within the volume  $V$ . In a static magnetic field  $\mathbf{B}_0$  the equation of motion

$$\frac{d\mathbf{M}}{dt} = \frac{-g\mu_B}{\hbar} \mathbf{M} \times \mathbf{B}_0 \quad (26)$$

holds, where  $\times$  is the cross product between vectors. It follows that  $\mathbf{M}$  precesses about  $\mathbf{B}_0$  with the Larmor frequency:

$$\omega_S = \frac{g\mu_B B_0}{\hbar}, \quad (27)$$

as it is shown in Figure 10a.

In an EPR experiment the oscillating magnetic field component  $B_{1,x}(t) = B_1 \cos(\omega_{\text{mw}}t)$  of the mw radiation pointing along the  $x$ -axis adds to the static magnetic field along the  $z$ -axis, with  $\omega_{\text{mw}} = 2\pi\nu_{\text{mw}}$ . To simplify the situation, one describes the motion of the magnetization in the rotating frame which rotates with the frequency  $\omega_{\text{mw}}$  in the right-hand sense around the external magnetic field. In this frame,  $\mathbf{M}$  still precesses around  $\mathbf{B}_0$  in the absence of any other fields as it is shown in Figure 10a, but now with the frequency

$\Omega_S = \omega_S - \omega_{\text{mw}}$ . If the oscillating field  $B_{1,x}(t)$  is switched on, it can be treated in good approximation as being constant in the rotating frame pointing along the  $x$ -axis as illustrated in Figure 10b. The superposition of both precessions about  $\mathbf{B}_0$  and the  $B_1$  field leads to a nutation around an effective field which axis is inclined by the angle  $\theta = \arctan\left(\frac{\omega_1}{\Omega_S}\right)$  with respect to  $\mathbf{B}_0$  as it is shown in Figure 10b. Here, the frequency of the precession about the  $B_1$  field is  $\omega_1 = \frac{g\mu_B B_1}{\hbar}$  and the nutation frequency calculates to

$$\omega_{\text{eff}} = \sqrt{\Omega_S^2 + \omega_1^2}. \quad (28)$$

If the mw radiation is on-resonant with the Larmor frequency, meaning that  $\omega_S = \omega_{\text{mw}}$ , the nutation occurs completely in the  $y, z$ -plane. If the mw radiation is switched on for the time  $t_{\pi/2}$  defined by the relation  $\pi/2 = \omega_{\text{eff}} t_{\pi/2}$ , the magnetization would point along the  $-y$ -direction in the rotating frame afterwards. If the mw pulse is twice as long,  $\mathbf{M}$  would point along the  $-z$ -axis finally. These two pulses are therefore named  $\pi/2$ - and  $\pi$ -pulses, and they are the cornerstones of all pulse sequences of the different pulsed EPR experiments. Classically speaking, one can use such short pulses to rotate the macroscopic magnetization vector in any direction in the rotating frame, manipulating in that way the spin systems which contribute to  $\mathbf{M}$ .

How do these manipulations of the magnetization matter for the experimentalist? For the detection of a signal an oscillating magnetization is needed emitting mw radiation which can be detected. In thermal equilibrium the macroscopic magnetization  $\mathbf{M}_0$  stays exactly parallel to the external static magnetic field  $\mathbf{B}_0$  and no mw radiation would be emitted. Now, the situation after an on-resonant  $\pi/2$ -pulse shall be imagined. According to the previous considerations, the magnetization  $\mathbf{M}$  would precess in the  $x, y$ -plane at the Larmor frequency immediately after this pulse, emitting a detectable mw signal. In that way a large variety of pulsed EPR experiments<sup>[268]</sup> can be performed with a setup, where distinct sequences of short mw pulses manipulate the spin system and at the end the response of the oscillating macroscopic magnetization is detected, namely as the intensity of an echo which occurs after the pulse sequences as indicated in Figure 9 (see also appendix chapter C for more information).

This illustrative picture holds only for spin systems with two energy levels.<sup>[268]</sup> Systems with more than two levels have to be treated quantum mechanically by the density operator formalism, although for such cases the classical picture might still govern some important aspects.<sup>[268]</sup> Unfortunately, the introduction of this formalism would go beyond the scope of this work, even though it is inevitable to fully understand the advanced HYSCORE and electron nuclear double resonance ENDOR experiments applied in this thesis. Instead, the interpretation of such experiments will be described below without their detailed justifications.

An important technique used for the presented studies is the two-pulse ESE sequence shown in Figure 9a, which induces the primary echo as explained in more detail in the appendix C. It is utilized to measure the magnetic field dependent EPR signal of the sample as an absorption like spectrum. More precisely, the external magnetic field is increased in small time steps over a certain range and at each point the intensity of the integrated pri-

mary echo is recorded after the application of the two-pulse sequence. In that way, spectra of powder samples are recorded, which look qualitatively like the illustrative adsorption signal in Figure 8b. But there might be differences between the spectra determined by two-pulse ESE field sweep or CW experiments. The decay time of the primary echo can be described by the phase-memory time  $T_m$  which includes effects of transverse relaxation as well as spin diffusion.<sup>[268]</sup> Electron spins with short  $T_m$  do not show up in echo experiments but still contribute to the CW EPR spectra. Even if  $T_m$  is long enough to enable the echo detection, it might be field dependent leading to a deviation between the line shapes of the spectra determined by two-pulse ESE or CW experiments.

Two-pulse ESE field sweep experiments have their own merit. For example, if they are conducted with selective pulses, which excite only a small magnetic field range of the powder spectrum, the obtained resolution might be better than in usual CW EPR experiments. They can also detect less intense or broad signals which are not resolved in a CW experiment due to taking the first derivative in the latter case. But a two-pulse ESE field sweep experiment also prepares for continuing studies. After the detection of the EPR spectrum by an ESE field sweep experiment, the proper magnetic field position for further and more advanced experiments like HYSCORE or ENDOR can be selected, to measure nuclear frequencies which are not resolved in the CW or ESE field sweep spectra.

In this thesis nuclear frequency spectra of protons ( $^1\text{H}$   $I = 1/2$ ) and  $^{27}\text{Al}$  ( $^{27}\text{Al}$   $I = 5/2$ ) as well as  $^{14}\text{N}$  ( $^{14}\text{N}$   $I = 1$ ) nuclei have been investigated, which couple to the electron spin  $S = 1/2$  of a certain NO adsorption species. This was mostly achieved by the use of the HYSCORE experiment which is an extension of the three-pulse ESEEM experiment as introduced now.

In a three-pulse ESEEM experiment the echo intensity of the stimulated echo sequence  $\pi/2 - \tau - \pi/2 - t - \pi/2 - \text{echo}$  as shown in Figure 9b is measured in dependence of the incremented time delay  $t$ .<sup>[268]</sup> The later defines the period, where nuclear coherences, created by the first two pulses, can freely evolve, modulating the echo intensity  $t$ -dependently. In an HYSCORE experiment an additional mixing  $\pi$  pulse is applied within this evolution period, interchanging nuclear coherences between different electron spin submanifolds.<sup>[268]</sup> Thus, the HYSCORE pulse sequence is  $\pi/2 - \tau - \pi/2 - t_1 - \pi - t_2 - \pi/2 - \tau - \text{echo}$  as illustrated in Figure 9c.<sup>[268,277]</sup> The echo intensity is recorded while the time variables  $t_1$  and  $t_2$  are varied independently, keeping the duration  $\tau$  constant. In that way a 2D time domain spectrum can be obtained. The application of a 2D Fourier transformation converts this spectrum into a 2D frequency domain spectrum, correlating nuclear frequencies of two different electron spin submanifold for distinct nuclear species and increasing the spectral resolution considerably, compared to 1D methods like three-pulse ESEEM or ENDOR spectroscopy.

The evolution of a single time variable  $t_1$  or  $t_2$  leads to a modulation of the echo intensity oscillating with nuclear frequencies  $\nu_{m_I, m_I'}^{k \in \{\alpha, \beta\}}$  (equation (19)), since the first two  $\pi/2$  pulses generate nuclear coherences.<sup>[268]</sup> This effect is the ESEEM effect. It occurs already with the primary echo. Its origin is explained in detail in the textbook of Schweiger and Jeschke.<sup>[268]</sup>

The  $\pi$  pulse of the HYSCORE sequence mixes nuclear coherences of both electron

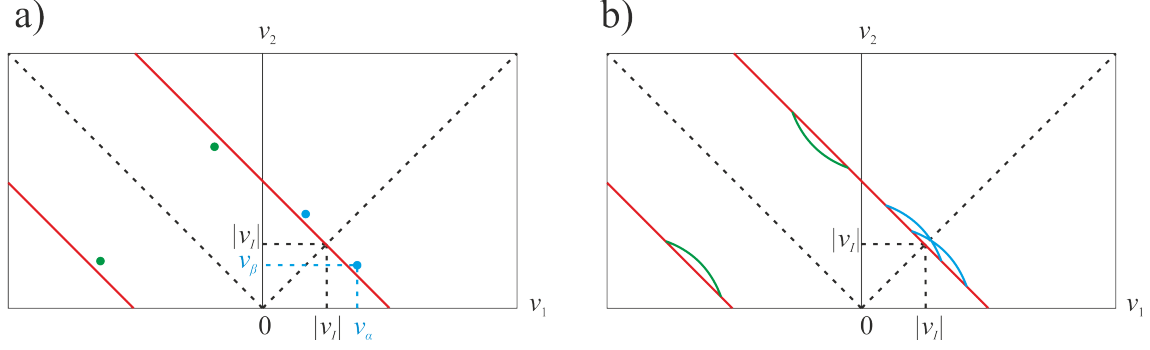


Figure 11: Schematic HYSCORE signals of an electron spin  $S = 1/2$  coupled to a nuclear spin  $I = 1/2$ . a) A single non-canonical orientation of  $B_0$  with respect to the hfi tensor contribute to the signal. b) All non-canonical orientations of  $B_0$  with respect to the hfi tensor contribute to the signal in the case of an isotropic g-tensor and an axially symmetric hfi tensor. Here, green resembles the case of a strong hfi  $|A/2| > |\nu_I|$  whereas blue resembles a weak hfi with  $|A/2| < |\nu_I|$ . The red lines are the functions  $\nu_2 = -\nu_1 \pm 2\nu_I$ .

spin submanifolds and correlates thereby in principle any nuclear frequency  $\nu_{m_I, m_I'}^\alpha$  of the  $\alpha$  manifold with any nuclear frequency  $\nu_{m_I'', m_I'''}^\beta$  of the  $\beta$  manifold. This leads to characteristic cross peaks in the 2D frequency domain spectrum at the eight positions  $\left(\pm\nu_{m_I, m_I'}^\alpha, \pm\nu_{m_I'', m_I'''}^\beta\right)$ ,  $\left(\pm\nu_{m_I, m_I'}^\alpha, \mp\nu_{m_I'', m_I'''}^\beta\right)$ ,  $\left(\pm\nu_{m_I'', m_I'''}^\beta, \pm\nu_{m_I, m_I'}^\alpha\right)$  and  $\left(\pm\nu_{m_I'', m_I'''}^\beta, \mp\nu_{m_I, m_I'}^\alpha\right)$ .<sup>[278]</sup> But due to the symmetry of the HYSCORE signal a restriction to the first and fourth quadrants, as they are shown in Figure 11, is justified. The intensities of those cross peaks in different quadrants can differ from each other already in single crystal spectra and one can assign from that difference ambiguous cross peaks to their nuclear isotopes.<sup>[278]</sup>

A necessary condition for the detection of a HYSCORE signal is that the corresponding spin packets have a non-canonical orientation of  $B_0$  with respect to the hfi tensor, meaning that  $B_0$  is not parallel to a principal direction of that tensor.<sup>[268]</sup> If  $B_0$  would be aligned parallel to a principal direction of the hfi tensor, the pseudo-secular hfi parameter  $B$  (see equations (21)) and as a consequence the depth of the ESEEM modulation would be zero.<sup>[268]</sup> Therefore, the hfi tensor must be anisotropic, otherwise no HYSCORE signal can be detected.

If the HYSCORE experiment is conducted for a powder, extended ridges in the 2D frequency spectrum are usually observed (Figure 11b). Those ridges consists of cross peaks  $\left(\nu_{m_I, m_I'}^\alpha(\Omega), \nu_{m_I'', m_I'''}^\beta(\Omega)\right)$  which depend on the relative orientation  $\Omega$  between the molecular and laboratory frame. The phases of spin packets of adjacent orientations might differ from each other which leads to the suppression of certain ridges by interference effects.<sup>[278]</sup> As a consequence, the HYSCORE signal occurs in case of strong hfi with  $|A/2| > |\nu_I|$  in the fourth quadrant whereas for weak hfi with  $|A/2| < |\nu_I|$  the ridges occur in the first quadrant. The corresponding signals in the other quadrant are suppressed. Both limiting cases are illustrated in Figure 11b. For intermediate hfi, ridges occur in both quadrants.<sup>[268]</sup>

As pointed out, the  $\pi$  pulse correlates any pair of nuclear frequencies from the  $\alpha$  and  $\beta$  manifolds. But in the presence of a small nqi and a shallow modulation of the spin echo, cross peaks between the  $\nu_{m_I, m_I+1}^\alpha$  and  $\nu_{m_I, m_I+1}^\beta$  frequencies are usually most intense.<sup>[268]</sup> According to equation (16) only those of these cross peaks depend on the nqi to first order, for which  $m_I \neq -1/2$ . The cross peaks between the nuclear central transition frequencies  $\nu_\alpha$  and  $\nu_\beta$  or generally between the frequencies  $\nu_{-m_I, m_I}^\alpha$  and  $\nu_{-m_I', m_I'}^\beta$  are in first order independent of the nqi.<sup>[268]</sup> Nevertheless, if the nqi becomes large, it might influence the values of those frequencies in second order.<sup>[268]</sup>

For the given reasons, one often observes in HYSCORE spectra of powder systems with a half integer nuclear spin  $I > 1/2$  only the ridge, correlating the nuclear central transition frequencies  $\nu_\alpha$  and  $\nu_\beta$  since the others are first-order broadened by a distribution of the nqi parameters.<sup>[279]</sup> From the equations (20) it follows that the secular hfi term shifts the orientation dependent  $(\nu_\alpha, \nu_\beta)$  cross peaks along the anti-diagonals

$$\nu_2 = -\nu_1 \pm 2\nu_I \quad (29)$$

in the weak and strong hfi cases, if the pseudo-secular constant  $B$  is small. This is illustrated in Figure 11b. From the equations (20) also follows that the pseudo-secular hfi parameter  $B$  shifts a cross peak to larger magnitudes of the frequencies  $\nu_\alpha$  and  $\nu_\beta$ . Considering only signals extended along the anti-diagonal  $\nu_2 = -\nu_1 + 2|\nu_I|$ , this leads to concave ridges in the first quadrant for weak hfi as shown in Figure 11b. In case of strong hfi, the corresponding ridge in the fourth quadrant has a convex shape (Figure 11b) since the root in equations (20) is a concave function and the values  $(\nu_I + \frac{A}{2})^2$  and  $(\nu_I - \frac{A}{2})^2$  are always different for  $A \neq 0$ .

Only for orientations where the external magnetic field is coaligned with a principal axis of the hfi tensor, the pseudo-secular constant  $B$  becomes zero and the corresponding cross peaks  $(\nu_\alpha, \nu_\beta)$  are located exactly on the lines defined by equation (29). It would be quite easy to determine from those positions the hfi tensor principal values. Unfortunately, the HYSCORE intensity drops to zero at positions where the hfi tensor principal direction contribute, as it was already mentioned.<sup>[268]</sup> Nevertheless, this information can be also obtained from the shape of the extended ridges which do not reach the anti-diagonal. For the determination of the principal values of a hfi tensor with arbitrary symmetry, it is often helpful that the corresponding ridges in a HYSCORE spectrum convert into straight lines in the squared frequency plot.<sup>[274]</sup> Those lines can be easily fitted by the formula:<sup>[274]</sup>

$$\nu_{\alpha(\beta)}^2 = Q_{\alpha(\beta)} \nu_{\beta(\alpha)}^2 + G_{\alpha(\beta)}, \quad (30)$$

where

$$\begin{aligned}
 Q_{\alpha(\beta)} &= \frac{\left(\nu_{u\alpha(\beta)}^2 - \nu_{v\alpha(\beta)}^2\right)}{\left(\nu_{u\beta(\alpha)}^2 - \nu_{v\beta(\alpha)}^2\right)} \\
 G_{\alpha(\beta)} &= \frac{\left(\nu_{v\alpha(\beta)}^2 \nu_{u\beta(\alpha)}^2 - \nu_{v\beta(\alpha)}^2 \nu_{u\alpha(\beta)}^2\right)}{\left(\nu_{u\beta(\alpha)}^2 - \nu_{v\beta(\alpha)}^2\right)}.
 \end{aligned} \tag{31}$$

These equations define three ridges where the symbols  $u$  and  $v$  have to be replaced according to  $(u, v) \in \{(z, x), (z, y), (x, y)\}$ . The corresponding frequencies are defined as:

$$\begin{aligned}
 \nu_{z\alpha(\beta)} &= -\nu_I \pm (a_{\text{iso}} + 2T) / 2 \\
 \nu_{y\alpha(\beta)} &= -\nu_I \pm [a_{\text{iso}} - T(1 - \rho) / 2] \\
 \nu_{x\alpha(\beta)} &= -\nu_I \pm [a_{\text{iso}} - T(1 + \rho) / 2].
 \end{aligned} \tag{32}$$

Those three ridges are the borders of a horn shaped area in the frequency domain spectrum which covers all orientation dependent cross peaks  $(\nu_{\alpha}(\Omega), \nu_{\beta}(\Omega))$ .<sup>[274]</sup> They are usually the most intense features of the signal.<sup>[278]</sup> In case of an axially symmetric hfi tensor, they collapse into one single ridge.

What about the other cross peaks correlating the  $\nu_{m_I, m_I+1}^{\alpha}$  and  $\nu_{m_I, m_I+1}^{\beta}$  nuclear frequencies for  $I > 1/2$  with  $m_I \neq -1/2$ ? As already discussed, they depend in first order on the nqi. Thus, they are shifted orientation dependently perpendicular to the anti-diagonals defined by equation (29).<sup>[268]</sup> Qualitatively, this first-order pattern is symmetric to those anti-diagonals since these shifts have a opposite sign for the  $(m_I, m_I + 1)$  and  $(-m_I + 1, -m_I)$  transitions.<sup>[268]</sup> For powder spectra, this leads to  $2m_I$  ridges aligned qualitatively parallel and symmetric to the anti-diagonals (equation (29)) in the weak and strong hfi cases, small  $B$  and small nqi. Those ridges must cross at some point the anti-diagonal since the nqi tensor  $\mathbf{Q}$  is traceless.

The HYSCORE signal intensity depends also on  $\tau$ .<sup>[280]</sup> This leads to regions in the 2D frequency spectrum, where the signal is suppressed and which are called blind spots. This suppression matters already in three-pulse ESEEM experiments. The intensities of the cross peaks between the  $\nu_{\alpha}$  and  $\nu_{\beta}$  frequencies are proportional to the factor  $|\sin(\pi\nu_{\alpha}\tau)\sin(\pi\nu_{\beta}\tau)|$ .<sup>[268,280]</sup> An exemplary plot is shown in Figure 12, demonstrating the blind spot distribution for strong hfi. Here, it was assumed that the hfi anisotropy is weak and the nuclear frequencies are approximately  $\nu_{\alpha(\beta)} = |\nu_I \pm A|$ . A similar plot for weak hfi can be found in a paper written by Höfer.<sup>[280]</sup> Due to the presence of such blind spots, it is often necessary to conduct HYSCORE experiments with different  $\tau$  values at the same magnetic field, especially if the sample is a powder.

Nevertheless, at this point it should be evident that one gains with the spreading of correlated nuclear frequencies in two dimensions considerably more resolution than one achieves in experiments like 1D ESEEM and ENDOR. For this reason, HYSCORE is often the method of choice to measure hfi and nqi parameters of nuclei neighbored to the electron spin, especially if those couplings are weak.<sup>[268]</sup> On the other hand, the measurement of



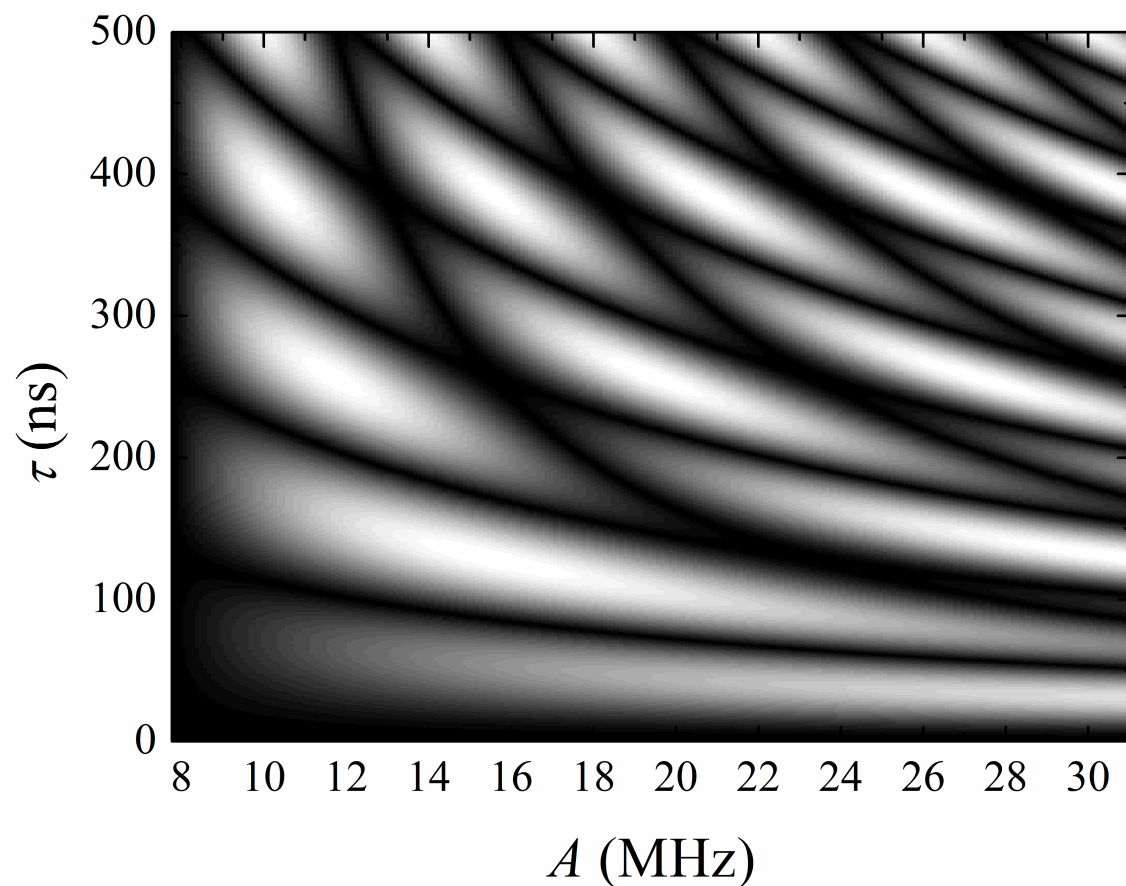


Figure 12: Plot of the factor  $|\sin(\pi\nu_\alpha\tau)\sin(\pi\nu_\beta\tau)|$  which modulates the HYSCORE intensity of cross peaks  $(\nu_\alpha, \nu_\beta)$  in the approximation of weak hfi anisotropy, where these frequencies can be roughly described as  $\nu_{\alpha(\beta)} = |\nu_I \pm A|$ . Here,  $\nu_I$  is the nuclear Larmor frequency of  $^{27}\text{Al}$  at a magnetic field  $B_0 = 350$  mT. In black regions the HYSCORE signal is suppressed whereas in white regions the plotted factor becomes large.

the same nuclear frequency spectrum by other methods can give additional complementary information, which might lead to more reliable results and might have their own merits. In solids, strong hfi are often best measured by Davies ENDOR,<sup>[268]</sup> which will be introduced next.

The pulse sequence of a Davies ENDOR experiment is shown in Figure 9c. It consists of a combination of selective mw pulses and one selective radio frequency (rf) pulse.<sup>[268]</sup> The first mw  $\pi$ -pulse inverses the electron polarization selectively for one allowed EPR transition. The following rf pulse inverses selectively nuclear polarization which modulates the electron polarization of that transition. The latter is read out by a primary echo pulse sequence. The intensity of the resulting echo is measured as a function of the rf frequency. Thus, if the rf frequency is off-resonant with a nuclear frequency as defined by equation (19), the echo magnitude is maximal whereas it is minimal if the rf frequency is on-resonant with such a nuclear transition. This way, the nuclear frequency spectrum can be measured directly with Davies ENDOR. A big advantage of this method, with respect to ESEEM techniques, is the absence of any blind spots.

For some cases like transition metal ions with large hfi or ligand nuclei with small gyromagnetic ratio the nuclear transition amplitudes as measured with ENDOR are modulated by the so called hfi enhancement factor.<sup>[268]</sup> Due to its large Larmor frequency, the electron spin follows the oscillating rf field  $\mathbf{B}_{\text{rf}}(t)$  adiabatically. This modulates the magnetic field  $\mathbf{B}_{\text{hf}}(t)$  which is generated by the electron spin at the nucleus. Therefore, the effective rf field at the nucleus is  $\mathbf{B}_{\text{rf}}^{\text{eff}}(t) = \mathbf{B}_{\text{rf}}(t) + \mathbf{B}_{\text{hf}}(t)$  which might lead to an enhancement or an attenuation of the nuclear transition amplitude.<sup>[268]</sup> As a result the amplitude of nuclear transitions with large frequencies might be enhanced whereas those transitions with small frequencies might become hardly detectable with ENDOR.

## 2.3 EPR related properties of nitric oxide

### 2.3.1 The electronic structure of NO

Nitric oxide (NO) is a heteronuclear diatomic molecule. With the LCAO (linear combination of atomic orbitals) method it can qualitatively be derived that NO has a  $KK(1\sigma)^2(1\sigma^*)^2(2\sigma)^2(1\pi)^4(1\pi^*)^1(2\sigma^*)^0$  electronic ground state configuration (Figure 13a).<sup>[281-284]</sup> Here,  $KK$  denotes the closed  $K$  shell structures formed by the 1s atomic orbitals (AO), of both the nitrogen and the oxygen atoms. The  $1\sigma$  and  $1\sigma^*$  molecular orbitals (MO) are in a first approximation the bonding and antibonding linear combinations of the 2s AOs of the nitrogen and oxygen atoms. The  $2\sigma$  and  $2\sigma^*$  MOs are likewise linear combinations of the  $2p_z$  AOs of both atoms, where  $z$  denotes the direction parallel to the internuclear axis. The  $1\pi$  and  $1\pi^*$  MOs are doubly degenerated by  $1\pi_x, 1\pi_y$  and  $1\pi_x^*, 1\pi_y^*$ , respectively. The latter four MOs are approximately the bonding and antibonding linear combinations of the  $2p_x$  and  $2p_y$  AOs of the nitrogen and oxygen atoms. Here, the  $x$ - and  $y$ -directions are perpendicular to the internuclear axis and to each other and are defined such that the unpaired electron is in the  $1\pi_y^*$  MO. MOs denoted with  $\sigma$  have a projection of the orbital angular momentum along the internuclear axis equal to zero. The  $\pi$  type MOs have a corresponding orbital angular momentum projection equal to  $\pm 1$ .<sup>[282,284]</sup>

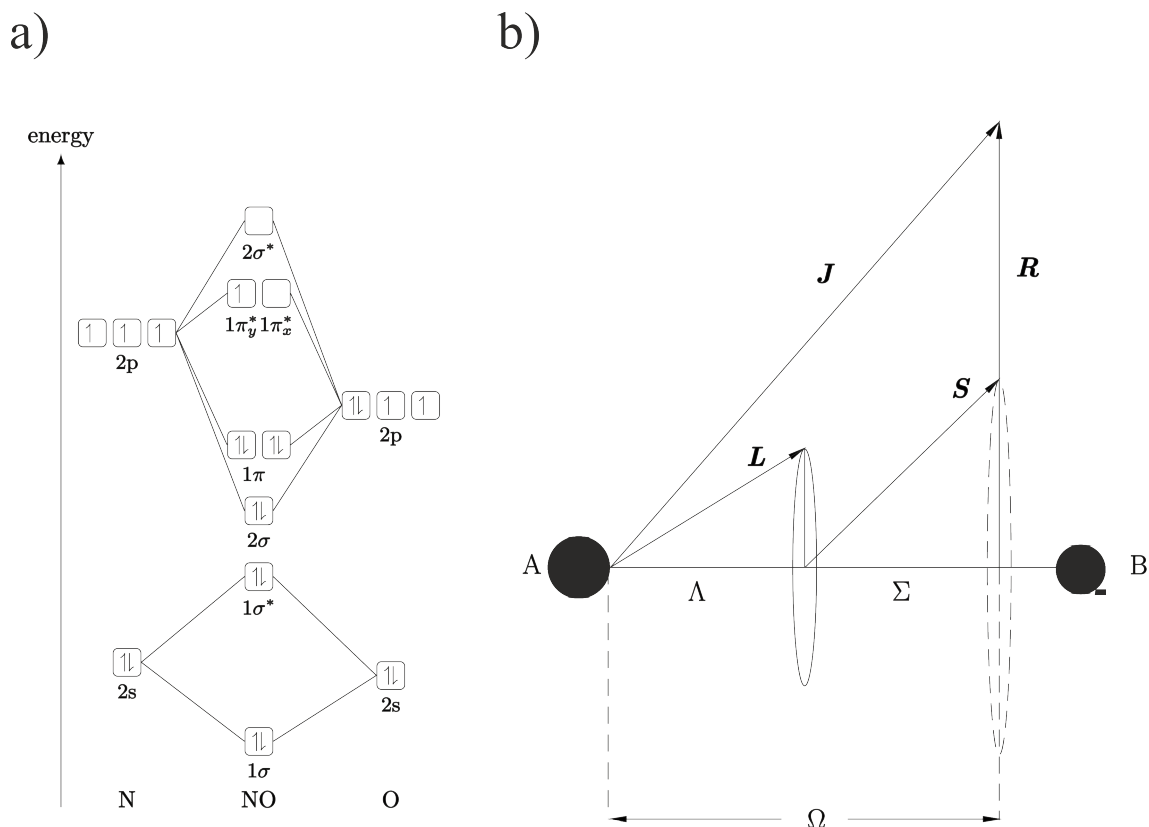
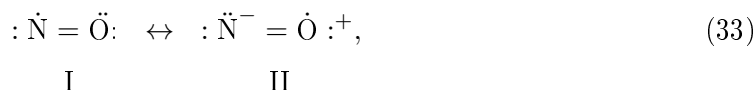


Figure 13: a) Qualitative molecular orbital diagram of NO<sup>[283]</sup>, b) Hund's coupling case (a) of angular momenta in a diatomic molecule with atoms A and B<sup>[281]</sup>

The  $1\pi_y^*$  MO, containing the unpaired electron, is distributed over the whole molecule. Thus, the electronic structure of NO might be understood as a mixture between the two resonance structures<sup>[198,285]</sup>



where the unpaired electron spends approximately half of the time in the  $2p_y$  AO of the nitrogen and half of the time in the  $2p_y$  AO of the oxygen. The corresponding electron pair spends half of the time at the oxygen and half of the time at the nitrogen atom. Accordingly, this interpretation of the electronic structure of the NO molecule motivates the usage of the NO molecule as an EPR active probe for the Lewis acidity of CUS.<sup>[92,198,200,242]</sup> The contribution of both resonance structures to the electronic structure is sensitive to the electron pair acceptor strength of the adsorption site, which can be quantified by the  $^{14}\text{N}$  hfi measured by EPR.

### 2.3.2 Angular momenta of the nitric oxide molecule

The total angular momentum  $\mathbf{J}$  of a diatomic molecule is a sum  $\mathbf{J} = \mathbf{L} + \mathbf{S} + \mathbf{R}$  of the total electronic orbital momentum  $\mathbf{L}$ , the total electronic spin  $\mathbf{S}$  and the angular momentum  $\mathbf{R}$  of the nuclear rotation as it is illustrated in Figure 13b.<sup>[281]</sup> Quantum mechanically,

they are expressed as vector operators. Several coupling modes of these three momenta are possible. For NO, the coupling condition named Hund's case (a) applies.<sup>[281]</sup> Here, the interaction between the nuclear rotation and the electronic spin and orbital motion is very weak. But a strong axially symmetric electrostatic field between the two nuclei is present. This forces the total orbital angular momentum  $\mathbf{L}$  to precess around the internuclear axis as illustrated in Figure 13b. Therefore,  $\mathbf{L}$  is not a constant of motion. But its projection  $\mathbf{L}_z$  along the z-axis (internuclear axis) stays always constant with magnitude  $L_z = m_L$  (note that angular momenta are given in units of one). Here, the magnetic quantum number  $m_L$  can take values  $m_L = L, L - 1, L - 2, \dots, -L$ , where the non-negative integer  $L$  is the quantum number of the total orbital momentum  $\mathbf{L}$ . Reversing the direction of motion of all electrons in an electric field does not change the energy of the system (in contrast to the motion in a magnetic field) but changes  $m_L$  to  $-m_L$ . Therefore, one defines the quantum number

$$\Lambda = |m_L| \quad (34)$$

which describes the projection of the total electronic orbital momentum along the internuclear axis. This number can take values:

$$\Lambda = 0, 1, 2, \dots, L. \quad (35)$$

Molecular states with different  $\Lambda$  have in general different energies, but as long as  $\Lambda > 0$  they are doubly degenerated into states having  $m_L = \pm\Lambda$ . As common, molecular states with  $\Lambda = 0, 1, 2, \dots$  are designated as  $\Sigma, \Pi, \Delta, \dots$ .<sup>[281]</sup> Molecular  $\Sigma$  states are not degenerated.

In Hund's case (a), the relation  $\Lambda > 0$  holds and the electronic orbital motion of the electrons leads to the presence of an internal magnetic field along the internuclear axis. This forces the total electron spin  $\mathbf{S}$  via spin-orbit coupling<sup>[286]</sup> to precess around this axis. Therefore,  $\mathbf{S}$  is not constant but its projection  $\mathbf{S}_z$  with magnitude  $S_z = m_S$  is. Here, the secondary spin quantum number  $m_S$  is denoted by  $\Sigma$  as usual, which should be not confused with the same designation for molecular states with  $\Lambda = 0$ . In contrast to the case of the magnetic quantum number  $m_L$ , states with  $m_S$  and  $-m_S$  have different energies unless  $m_S = 0$ . Therefore,  $\Sigma$  can have following values:

$$\Sigma = S, S - 1, S - 2, \dots, -S, \quad (36)$$

where the non-negative integer  $S$  is the spin quantum number of  $\mathbf{S}$ . The precession of  $\mathbf{L}$  and  $\mathbf{S}$  about the internuclear axis in diatomic Hund's case (a) molecules is much faster than the nutation of the whole molecule around  $\mathbf{J}$ .

One can simply calculate the resultant electronic angular momentum  $\mathbf{\Omega}$  along the internuclear axis by adding  $\mathbf{L}_z$  and  $\mathbf{S}_z$ . The quantum number of  $\mathbf{\Omega}$  is defined as:

$$\Omega = |\Lambda + \Sigma| \quad (37)$$

as illustrated in Figure 13b. For a given  $\Omega$ , the molecule can adopt different rotational

states characterized by the total angular momentum quantum number<sup>[281]</sup>

$$J = \Omega, \Omega + 1, \Omega + 2, \dots \quad (38)$$

Molecular states of diatomic molecules with defined values  $\Lambda$ ,  $\Sigma$  and  $J$  are usually designated as  $^{2S+1}\Pi_{\Lambda+\Sigma}$ .<sup>[281]</sup> Hereby, the last symbol comprises a manifold of states with different values of  $J$  according to equation (38).

### 2.3.3 The magnetism and EPR signal of the free nitric oxide molecule

In the presence of a magnetic field  $\mathbf{B}_0$  with magnitude  $B_0$  the projection of the total angular momentum  $\mathbf{J}$  along the field direction can only have certain values  $m_J$  where<sup>[281]</sup>

$$m_J = J, J - 1, \dots, -J. \quad (39)$$

The  $2J + 1$  quantities  $m_J$  are the eigenvalues of  $\hat{J}_z$  which is the z-component of the vector operator  $\hat{\mathbf{J}}$  describing  $\mathbf{J}$ . The z-direction is assumed to be parallel to the external magnetic field direction. To each specific  $^{2S+1}\Pi_{\Lambda+\Sigma}$  molecular state of NO a magnetic moment is associated. Since NO is a Hund's case (a) molecule, the time average of the component of its magnetic moment in the field direction is in first approximation:

$$\bar{\mu}_B = -\mu_B g_J m_J, \quad (40)$$

where the effective g-factor is the Landé-factor<sup>[281]</sup>

$$g_J = \frac{(\Lambda + 2\Sigma)(\Lambda + \Sigma)}{J(J + 1)}. \quad (41)$$

The coupling of this magnetic moment with the external magnetic field is described by the Zeeman interaction term:<sup>[287]</sup>

$$\hat{H}_Z = \mu_B g B_0 \hat{J}_z. \quad (42)$$

The real g-value  $g$  deviates slightly from the theoretical value  $g_J$  since the magnetic field and nearby states perturb the Hund's case (a) coupling scheme.<sup>[287]</sup>

In the absence of any external electric fields the nitric oxide molecule has a  $^2\Pi_{\frac{1}{2}}$  ground state with  $\Lambda = 1$  and  $\Sigma = -\frac{1}{2}$ , which means that the orbital and spin angular momenta are aligned antiparallel.<sup>[281]</sup> According to the equations (40) and (41), its magnetic moment  $\bar{\mu}_B$  is zero. Therefore, the ground state of a free NO molecule is diamagnetic. But all excited rotational  $^2\Pi_{\frac{3}{2}}$  states of a free NO molecule, where the orbital and spin angular momenta are aligned parallel ( $\Lambda = 1$  and  $\Sigma = +\frac{1}{2}$ ), are paramagnetic including the lowest rotational  $^2\Pi_{\frac{3}{2}}$  state. This state is sufficiently populated at room temperature and shows a nine-line EPR pattern which can be observed at moderate gas pressures at a g-value  $g = 0.777$ .<sup>[222,288,289]</sup> The latter deviates slightly from  $g_J$ .<sup>[222,287,290,291]</sup> Higher rotational  $^2\Pi_{\frac{3}{2}}$  states have much smaller g-values (equation (41)). Consequently, they cannot be observed with conventional X-band EPR spectrometers.

An exemplary X-band EPR spectrum is shown in Figure 14a. If the magnetic moment

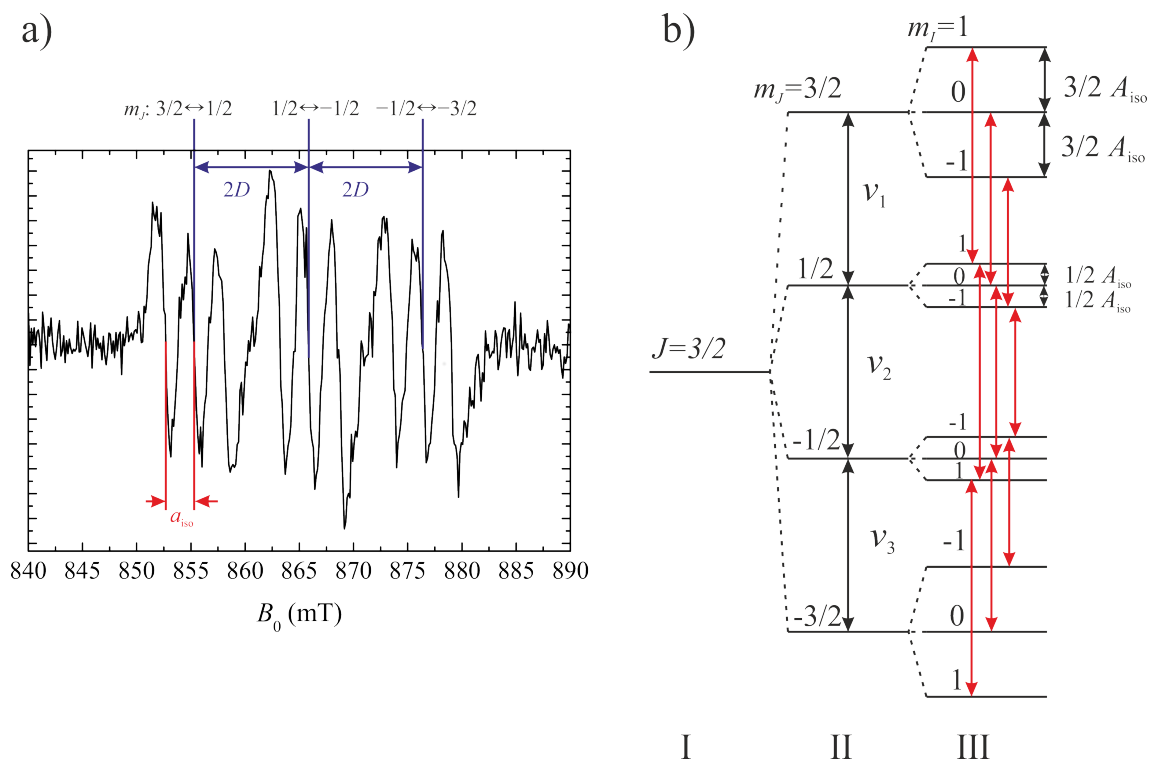


Figure 14: a) Exemplary EPR spectrum of gaseous NO at X-band frequency (room temperature, 1 mbar gas pressure). The fine structure (fs) parameter  $D$ , introduced phenomenologically in section 3.1, as well as the isotropic  $^{14}\text{N}$  hfi splitting constant  $a_{\text{iso}}$  are indicated in blue and red. The three blue vertical lines indicate further the different  $\Delta m_J = \pm 1$  transitions, each of them comprising one hfi triplet. b) Schematic energy level diagram of the lowest rotational  $J = \frac{3}{2}$  level of the  $^2\Pi_{\frac{3}{2}}$  state of NO.<sup>[288]</sup> At stage I any magnetic field and hfi is absent. At stage II a magnetic field is present and the levels are further split due to the hfi in stage III. A further shift of the energy levels due to the  $^{14}\text{N}$  nuclear quadrupole coupling has been omitted in this drawing but is discussed in Beringer and Castle.<sup>[288]</sup> The nine EPR transitions responsible for the nine lines of the EPR signal of free NO (a) are highlighted in red.

of the NO molecule would only be subjected to the Zeeman interaction (equation (42)), one would observe a single line since all allowed  $\Delta m_J = \pm 1$  transitions would be energetically degenerated (see stage (II) in Figure 14b) and would contribute to the EPR signal at the same magnetic field position. But nine lines are observed, three almost equally spaced triplets of three less spaced lines (Figure 14a). The smaller splitting is a consequence of the hfi between the electronic and  $^{14}\text{N}$  nuclear magnetic moments of the NO molecule. This interaction is described by the Hamiltonian operator:<sup>[287]</sup>

$$\hat{H}_{\text{HF}} = a_{\text{iso}} \hat{\mathbf{J}}^T \cdot \mathbf{I}^{14\text{N}}, \quad (43)$$

where  $\hat{\mathbf{I}}^{14\text{N}}$  is the vector operator describing the nuclear spin  $I^{14\text{N}} = 1$  of the  $^{14}\text{N}$  nucleus and  $a_{\text{iso}} = 29.8 \pm 0.3$  MHz<sup>[288]</sup> is the corresponding isotropic hfi constant.

The hfi would explain three EPR lines, each originating from the allowed transition between energy levels with the same magnetic quantum number  $m_I$  of the  $^{14}\text{N}$  nuclear spin  $I^{14\text{N}}$ . But it does not lift the threefold degeneracy of the  $\Delta m_J = \pm 1$  transitions as is also illustrated in Figure 14b. In fact this degeneracy is lifted by the perturbation of the Hund's case (a) coupling scheme through the external magnetic field and nearby states<sup>[287]</sup>.

In the limit of high magnetic fields the electronic spin  $\mathbf{S}$  and the electronic orbital angular momentum  $\mathbf{L}$  would precess independently from each other around the magnetic field axis which is also known as the Paschen-Back effect.<sup>[292,293]</sup> A magnetic field of  $B_0 \approx 860$  mT is not sufficient to reach this limit. But it is still large enough to perturb the Hund's case (a) coupling of the angular momenta to such an extent that the degeneracy of the allowed  $\Delta m_J$  transitions is lifted and all three hfi triplets are well separated from each other at X-band frequencies, meaning that the frequencies  $\nu_1$ ,  $\nu_2$  and  $\nu_3$  in Figure 14b deviate slightly from each other.<sup>[287,288,290,293]</sup> This was a problem for the simulation of the EPR signal of NO gas based on a simple spin Hamiltonian approach, as it was implemented in conventional simulation software like the MatLab toolbox EasySpin<sup>[294]</sup> or XSophe.<sup>[295]</sup> At the time of this work, those programs had no direct implementation of the spin-orbit coupling or the coupling between the electronic spin and rotation preventing the solution of the exact Hamiltonian which considers all couplings between the electronic and rotational angular momenta.<sup>[290]</sup> Recently, the spin-orbit coupling was implemented in EasySpin.<sup>[294]</sup> But it turns out that the X-band EPR signal of gaseous NO can still be simulated by a simple spin Hamiltonian approach, where the occurrence of three well separated hfi triplets is treated phenomenologically by introducing an appropriate fine structure interaction term to the Hamiltonian.<sup>[222,296]</sup> This method will be introduced in section 3.1. There, the homogeneous linewidth of the EPR signal of NO gas is of most interest and can be easily obtained with the proposed simulation procedure.

Since the  $^{14}\text{N}$  nucleus has a nuclear spin  $I^{14\text{N}} > \frac{1}{2}$ , it has a nuclear quadrupole moment which interacts with an electric field gradient at the nucleus site. This nqi is of the order of  $Q = -1.7 \pm 0.5$  MHz which is small but measurable.<sup>[288]</sup> The  $\Lambda$ -doubling (equation (34))<sup>[289,291,297,298]</sup> is often not resolved in a typical X-band EPR experiment. But certain experiments allowed for a measurement.<sup>[289]</sup>

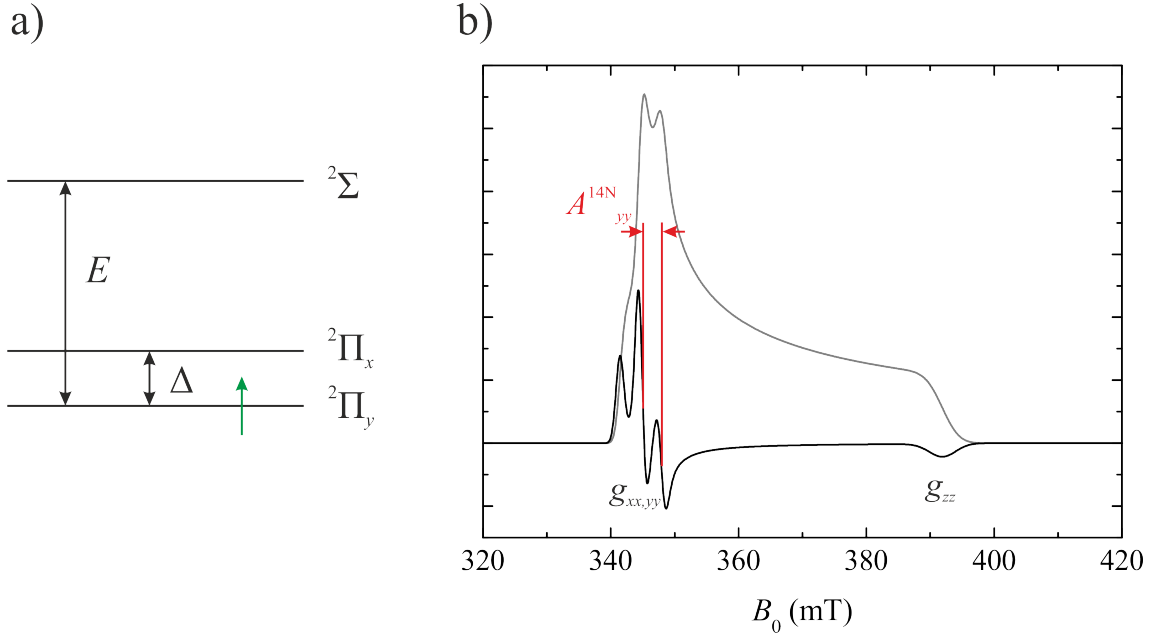


Figure 15: a) Energy level diagram of molecular states of an NO molecule adsorbed on a surface. The occupation by the unpaired electron is indicated by a green arrow. b) A typical simulated X-band CW EPR spectrum of NO adsorbed at a diamagnetic surface site (black) as well as its integrated absorption signal (gray). The parameters are  $g_x = g_y = 1.99$ ,  $g_z = 1.75$ ,  $A_y^{14\text{N}} = 90$  MHz and the spectrometer frequency is  $\nu_{\text{mw}} = 9.6$  GHz.

### 2.3.4 The magnetism and EPR signal of nitric oxide adsorbed at closed shell or diamagnetic surface sites

The previous subsection mentioned that the  ${}^2\Pi_{\frac{1}{2}}$  ground state of a free NO molecule is diamagnetic, since the orbital momentum  $L = 1$  and electron spin  $S = 1/2$  are aligned antiparallel. This situation changes in an external electric field like it exists on metal oxide surfaces or at cations in zeolites where NO can adsorb.<sup>[92]</sup> A field with orthorhombic or lower symmetry quenches the orbital momentum and the  ${}^2\Pi_{\frac{1}{2}}$  state becomes paramagnetic with electron spin  $S = 1/2$ .<sup>[196,299–301]</sup> Then, the degeneracy between the  ${}^2\Pi_x$  and  ${}^2\Pi_y$  states belonging to the  ${}^2\Pi_{\frac{1}{2}}$  state is lifted where the energy difference between both is denoted as  $\Delta$  (Figure 15a). The unpaired electron occupies the lower lying  ${}^2\Pi_y$  state. Since the molecular states  ${}^2\Pi_x$  and  ${}^2\Pi_y$  have electron configurations  $KK(1\sigma)^2(1\sigma^*)^2(2\sigma)^2(1\pi)^4(1\pi_y^*)^0(1\pi_x^*)^1(2\sigma^*)^0$  and  $KK(1\sigma)^2(1\sigma^*)^2(2\sigma)^2(1\pi)^4(1\pi_y^*)^1(1\pi_x^*)^0(2\sigma^*)^0$ ,  $\Delta$  might be seen as the energy difference between the antibonding  $1\pi_y^*$  and  $1\pi_x^*$  MOs where the unpaired electron occupies the former one<sup>[302]</sup>. Further, the energy difference between the  ${}^2\Pi_y$  and  ${}^2\Sigma$  molecular states is denoted as  $E$  (Figure 15a). The state  ${}^2\Sigma$  state has the electron configuration  $KK(1\sigma)^2(1\sigma^*)^2(2\sigma)^2(1\pi)^4(1\pi_y^*)^0(1\pi_x^*)^0(2\sigma^*)^1$ <sup>[302]</sup>. Therefore,  $E$  might be seen as the energy difference between the antibonding  $1\pi_y^*$  and  $2\sigma^*$  molecular states.

According to a derivation of Zeller and Känzig<sup>[125]</sup> for the molecular ion  $\text{O}_2^-$ , the g-tensor principal values of the  ${}^2\Pi_{\frac{1}{2}}$  of NO can be calculated in second order perturbation



theory as follows:<sup>[301]</sup>

$$\begin{aligned}
 g_x &= g_e \frac{\Delta}{\sqrt{\lambda^2 + \Delta^2}} - \frac{\lambda}{E} \left( \frac{\Delta - \lambda}{\sqrt{\lambda^2 + \Delta^2}} - 1 \right) \\
 g_y &= g_e \frac{\Delta}{\sqrt{\lambda^2 + \Delta^2}} - \frac{\lambda}{E} \left( \frac{\Delta + \lambda}{\sqrt{\lambda^2 + \Delta^2}} + 1 \right) \\
 g_z &= g_e - \frac{2l\lambda}{\sqrt{\lambda^2 + \Delta^2}}.
 \end{aligned} \tag{44}$$

Here,  $\lambda = 1.478$  kJ/mol is the NO spin-orbit coupling constant<sup>[286,302]</sup> which is also the energy difference between the  ${}^2\Pi_{\frac{1}{2}}$  and  ${}^2\Pi_{\frac{3}{2}}$  molecular states. The factor  $l$  is the effective g-factor of the orbital contribution<sup>[301]</sup> which is a matrix element of the  $\hat{L}_z$  operator:

$$l = -i \langle {}^2\Pi_y | \hat{L}_z | {}^2\Pi_x \rangle. \tag{45}$$

For the free NO molecule the relation  $l = 1$  holds and deviation of  $l$  from 1 measures the orthorhombic distortion of the corresponding wave functions. The g-tensors  $z$ -principal axis points along the bond between the NO's nitrogen and oxygen whereas the g-tensors  $y$ -axis is aligned parallel to the  $1\pi_y^*$  molecular orbital containing the unpaired electron. All g-tensor principal values of the  ${}^2\Pi_{\frac{1}{2}}$  state of an adsorbed NO species are near but smaller than the free electron g-value  $g_e = 2.0023$  and hold the relations  $g_x > g_y > g_z$ . In X-band experiments the difference between  $g_x$  and  $g_y$  is often not resolved. But it can be resolved at higher mw frequencies like  $\nu_{mw} \approx 34$  GHz (Q-band) or  $\nu_{mw} \approx 94$  GHz (W-band).<sup>[197]</sup> The  $g_z$  value is very sensitive to the energy splitting  $\Delta$  and therefore to the strength of the electric field at the adsorption site of the NO molecule. Especially the non-axial component of the electric field gradient contribute to the magnitude of  $\Delta$ .<sup>[301]</sup> With increasing electric field gradient the  $g_z$  value increases approaching  $g_e$  in the limit of high electric fields, whereas small  $g_z$  values are indicative for weak electric field gradients at the adsorption site of the NO molecule.

A typical X-band CW signal of NO adsorbed at some diamagnetic surface site is also determined by the hfi between the electron spin  $S = 1/2$  and the  ${}^{14}\text{N}$  nuclear spin  $I^{14\text{N}} = 1$ , and sometimes also by the hfi between  $S$  and other neighbored nuclei at the adsorption site<sup>[198]</sup> that can be described by the spin Hamiltonian in equation (1). The tensor  $\mathbf{A}^{14\text{N}}$ , describing the hfi between the electron spin and the  ${}^{14}\text{N}$  nucleus, is usually coaxial to the g-tensor.<sup>[196]</sup> Since most unpaired electron density of the NO molecule is in the  $1\pi_y^*$  MO, the  $\mathbf{A}^{14\text{N}}$  tensor has its largest principal value in the  $y$ -direction. Typically, it has values  $|A_y^{14\text{N}}| \approx 90$  MHz which can be resolved in X-band CW experiments in principle. Unfortunately, this is not the case for the  $A_x^{14\text{N}}$  and  $A_z^{14\text{N}}$  principal values which are such small that they only contribute to the linewidth of the CW EPR signal of adsorbed NO. But, they can be still measured by advance pulsed EPR methods like orientation selective ENDOR spectroscopy. With the latter method it was possible to determine  $|A_x^{14\text{N}}| \approx |A_z^{14\text{N}}| \approx 25$  MHz for an  $\text{Na}^+$ -NO complex in the NaA zeolite.<sup>[200]</sup>

Hfi parameters of neighbored nuclei can be of such size that they are resolved by the CW EPR signal of adsorbed NO as it was observed for  $\text{Al}^{3+}$ -NO or  $\text{AlO}^+$ -NO species

in H-ZSM-5 zeolite<sup>[198]</sup> or for Cu<sup>+</sup>-NO complexes.<sup>[303]</sup> Smaller hfi parameters of neighbored nuclei as well as nuclear quadrupole parameters of neighbored nuclear spins  $I^k > \frac{1}{2}$  might be determined in some cases by high resolution pulse techniques like ENDOR<sup>[200]</sup> or HYSCORE<sup>[304]</sup> spectroscopy.

An exemplary simulated X-band CW signal of NO adsorbed at a diamagnetic surface site is illustrated in Figure 15b. It shows the typical powder spectrum of an  $S = 1/2$  species with an almost axial symmetric g-tensor with principal values  $g_x \approx g_y > g_z$  which are indicated in the figure. The splitting of the  $g_y$  powder edge singularity into three lines originates from the hfi with the <sup>14</sup>N nucleus in  $y$ -direction. Note that for smaller electric surface field gradients at the adsorption site the whole spectrum is shifted to higher magnetic fields whereas for increasing electric field gradients the whole spectrum is shifted to lower magnetic fields approaching  $g_e = 2.0023$  in the limit.<sup>[301]</sup>

### 2.3.5 EPR of nitric oxide adsorbed at open shell or paramagnetic surface sites

NO can also adsorb at a CUS, where the metal ion can be paramagnetic or can have at least an open shell electron configuration. The most prominent examples are complexes with iron ions like they occur in distinct proteins.<sup>[305]</sup> NO can bind to both, iron ions with ferric (Fe<sup>3+</sup>, 3d<sup>5</sup> electron configuration) and ferrous (Fe<sup>2+</sup>, 3d<sup>6</sup> electron configuration) oxidation states.<sup>[141]</sup> Ferrous ions are often EPR silent due to their integer electron spin. Fortunately, NO has the ability to form various paramagnetic nitrosyls with Fe<sup>2+</sup>, making these centers visible for EPR due to their non-integer spin.<sup>[306]</sup>

Another interesting metal ion for the NO adsorption, which can be paramagnetic, is Ni<sup>2+</sup>. It occurs only with integer electron spin including  $S = 0$  or  $S = 1$  and is therefore often not detectable by EPR. Nevertheless, the bonding of NO to the Ni<sup>2+</sup> has been reported, where both entities together form paramagnetic  $S = 1/2$  species like on nickel exchanged zeolites, Ni doped MgO surfaces or on Ni/SiO<sub>2</sub> catalyst.<sup>[307-310]</sup> These signals are comparable to those of Ni<sup>+</sup> or low spin Ni<sup>3+</sup> ions. This was explained by a strong interaction between the  $\pi_y^*$  antibonding MO of the NO and the  $d_{z^2}$  of the Ni<sup>2+</sup> ion, forming a double occupied bonding ( $d_{z^2} + \pi_y^*$ ) MO and an empty antibonding ( $d_{z^2} - \pi_y^*$ ) leaving an unpaired electron in the  $d_{x^2-y^2}$  orbital at the Ni<sup>2+</sup> ion. The resulting effective Ni<sup>+</sup> ground state configuration is  $(d_{z^2} + \pi_y^*)^2 (d_{x^2-y^2})^1 (d_{z^2} - \pi_y^*)^0$  with an electron spin  $S = 1/2$ . The corresponding g-tensor principal values calculate in second order to<sup>[311-313]</sup>

$$\begin{aligned} g_{x,y} &\approx g_e + \frac{2\lambda}{\Delta_1} \\ g_z &\approx g_e + \frac{8\lambda}{\Delta_2}, \end{aligned} \quad (46)$$

with the spin-orbit coupling constant  $\lambda$ , the energy difference  $\Delta_1$  between the  $(d_{x^2-y^2})^1$  ground state and the  $(d_{yz})^1$  and  $(d_{xz})^1$  excited state configurations and the energy difference  $\Delta_2$  between the ground state and the  $(d_{xy})^1$  excited state configuration. Thus, this complex has g-values  $g_{x,y} < g_z$  and shows a typical axially symmetric EPR powder signal

with the  $g_{\perp}$  powder edge singularity at its high field end.

In conclusion, the adsorption of NO on paramagnetic or open shell CUS, where the metal ion has an even number of electrons, might be beneficial, if the EPR silent state of the metal ion is converted into an EPR active nitrosyl complex.

## 2.4 Density functional theory

The theoretical background of the DFT method applied in this thesis is described in detail in a textbook by F. Jensen,<sup>[314]</sup> to which this section refers.

Calculating the ground state energy and wave function  $\Psi(\mathbf{r}, t)$  of a system with  $N_{\text{nuc}}$  nuclei and  $N_{\text{ele}}$  electrons means in principle solving the time-dependent Schrödinger equation:

$$\hat{H}(\mathbf{r}, t) \Psi(\mathbf{r}, t) = i \frac{\partial \Psi(\mathbf{r}, t)}{\partial t}. \quad (47)$$

Here,  $\hat{H}(\mathbf{r}, t)$  is the corresponding Hamiltonian operator,  $\mathbf{r}$  are the particle coordinates and  $t$  is the time. In general  $\hat{H} = \hat{T} + \hat{V}$  where  $\hat{T}$  and  $\hat{V}$  are the kinetic and potential energy operators. If the latter is time-independent as for bound systems, the time dependency can be eliminated and the problem reduces to solving the time-independent Schrödinger equation as

$$\hat{H}(\mathbf{r}) \Psi(\mathbf{r}) = E(\mathbf{r}) \Psi(\mathbf{r}) \quad (48)$$

where  $E$  is the energy of the Hamiltonian's eigenstate  $\Psi$ .

Since the electrons move much faster than the nuclei, the latter are stationary from the electrons point of view and both motions can be separated from each other. This is the Born-Oppenheimer approximation. It allows to describe the system by the electronic wave function alone. This wave function is determined in the center of mass system by the Hamiltonian  $\hat{H}_e = \hat{H} - \hat{T}_n - \frac{1}{2M} \left( \sum_{i=1}^{N_{\text{ele}}} \nabla_i \right)^2$ , where  $M$  is the total mass of all nuclei and the last sum runs over all electronic gradient operators. In  $H_e$  the nuclear positions  $\mathbf{r}_n$  enter just as simple parameters whereas the nuclear kinetic energy operator  $\hat{T}_n$  and consequently the nuclear momenta do not occur anymore. The Schrödinger equation has now the following form:

$$\hat{H}_e \Psi_e(\mathbf{r}_n, \mathbf{r}_e) = E_e(\mathbf{r}_n) \Psi_e(\mathbf{r}_n, \mathbf{r}_e), \quad (49)$$

where  $\Psi_e$  is the electronic wave function and  $\mathbf{r}_e$  are the electronic coordinates. Thus, if the positions  $\mathbf{r}_n$  of the nuclei are once given and fixed, the ground state electronic wave function  $\Psi_e$  and energy  $E_e$  are fully determined by solving equation (49). The same is true for all corresponding excited states of the bound system.

Equation (49) already illustrates the meaning of optimizing the geometry of a system computationally. One just varies the nuclear coordinates  $\mathbf{r}_n$  and solves equation (49) each time, until the global minimum of the function  $E_e(\mathbf{r}_n)$  is found, which defines the energetically optimized structure of the system. But solving equation (49) is highly demanding. Particularly, the degrees of freedom are very large since  $3N_{\text{ele}}$  spatial and  $N_{\text{ele}}$  spin coordinates of the electrons have to be considered. It would be much easier, if the ground state

electronic energy is determined completely by the electron density  $\rho$ , which measures the probability to find a single electron in a confined small volume element and depends only on three spatial coordinates. This is the case indeed, as it has been proven by Hohenberg and Kohn<sup>[315]</sup> in 1964. The corresponding theorem is the basis of DFT. It states that the ground state electronic energy is a functional of the electronic density alone which can be written  $E_e = F[\rho]$ . In detail it has the form:

$$E_e[\rho] = T[\rho] + E_{ne}[\rho] + E_{ee}[\rho], \quad (50)$$

where  $T[\rho]$  is the kinetic energy of the electrons,  $E_{ne}[\rho]$  expresses the attraction between the electrons and nuclei and  $E_{ee}[\rho]$  includes the electron-electron repulsion. The functional  $E_{ee}[\rho] = J[\rho] + K[\rho]$  can be further divided into its Coulomb and exchange parts  $J[\rho]$  and  $K[\rho]$ , respectively.

The problem that has to be faced is the calculation or approximation of the functional defined by equation (50), which existence has been proven but which is still unknown in general. One can try to express all energy contributions to  $E_e$  by functionals depending only on  $\rho$ , which is called orbital-free DFT. For the parts  $E_{ne}[\rho]$  and  $J[\rho]$  one can do this exactly using their classical analytic expressions. But for  $T[\rho]$  and  $K[\rho]$  one needs approximations. The main problem of orbital-free models is their poor approximation of the electrons kinetic energy term  $T[\rho]$ . Thus, modern DFT is usually based on a more accurate method, where orbitals are introduced again as suggested by Kohn and Sham<sup>[316]</sup> in 1965.

For non-interacting electrons the exact solution of the Schrödinger equation would be a Slater determinant of MOs  $\phi_i$  and one can calculate the kinetic energy  $T_S(\phi_i)$  from the orbitals exactly. The idea of Kohn and Sham was to introduce such MOs and approximate the real kinetic energy term  $T(\rho)$  by  $T_S(\phi_i)$ . From the MOs an approximated electron density  $\rho_{\text{approx}} = \sum_{i=1}^{N_{\text{ele}}} |\phi_i|^2$  can be obtained.  $E_e$  in the Kohn-Sham approach is calculated approximately as

$$E_e[\rho_{\text{approx}}] = T_S[\phi_i] + E_{ne}[\rho_{\text{approx}}] + J[\rho_{\text{approx}}] + E_{xc}[\rho_{\text{approx}}], \quad (51)$$

where the first three addends can be evaluated exactly in terms of known formulas. The last term  $E_{xc}[\rho] = (T[\rho] - T_S[\rho]) + (E_{ee}[\rho] - J[\rho])$  is defined such that equation (51) is true. It is the only unknown part in equation (51) for which an approximation has to be found. The Kohn-Sham approach is a big improvement to orbital-free DFT, since  $E_{xc}$  is roughly a factor 10 smaller than  $T_S$ . Consequently, Kohn-Sham DFT is less sensitive to inaccuracies of the energy functional than orbital-free approaches are. But with the orbitals the number of spatial coordinates increases to  $3N_{\text{ele}}$  again.

For the application of the Kohn-Sham DFT to a given problem, a basis set for the various MOs and an approximation of the functional  $E_{xc}$  have to be chosen. These are the common ingredients of each DFT calculation which determine its performance. Unfortunately, there exist no approach to improve the approximation of  $E_{xc}$  systematically, which has lead to a plethora of functionals from which one has to choose. Thus, one should

always cross-check the applicability of a functional with the experiment or bench mark calculations.

After an approximated wave function of the system under consideration in terms of MOs  $\phi_i$  is determined by minimizing equation (51) selfconsistently, different properties which might be accessible by an experiment can be calculated. For EPR this can be hfi or nqi parameters as well as the g-tensor. The Fermi contact interaction describing the isotropic hfi can be calculated from a DFT derived wave function with equation (11) where  $|\psi(0)|^2$  has to be replaced by  $\varrho_{\text{approx}}(\mathbf{r}_n)$ , with  $\mathbf{r}_n$  being the nuclear position.<sup>[317,318]</sup> The spin dipole part of the hfi can be directly calculated from the classical expression of the interaction energy of two magnetic dipoles averaging it over the the spin density matrix and the corresponding MOs  $\phi_i$ .<sup>[317,318]</sup> Similarly, the electric field gradient at a nucleus can be computed and thus its nqi.<sup>[317,318]</sup> Calculating the g-tensor is more demanding since here one has to take second derivatives of the energy with respect to the electron spin and the external magnetic field.<sup>[314,317]</sup> But luckily, for main group radicals such g-tensor calculations are quite insensitive to the choice of the basis-set or the functional.<sup>[318]</sup>

### 3 EPR of desorbed NO gas - a method to characterize the adsorption of NO on MOFs

The EPR signal of desorbed NO gas can be measured easily with EPR at X-band frequency and moderate gas pressures  $p \lesssim 100$  mbar.<sup>[196,222,288,289]</sup> At higher gas pressures the EPR signal becomes so broad that it cannot be detected any more by EPR. This signal originates from the  ${}^2\Pi_{3/2}$  state with the total angular momentum  $J = \frac{3}{2}$  as it is explained in the subsection 2.3.3. EPR is most useful for the study of NO adsorption complexes on MOF surfaces, since in this way information can be obtained which can hardly be achieved with other methods. Typically, EPR of desorbed NO can provide its amount<sup>[196,198,223]</sup> or its gas pressure<sup>[222]</sup> in dependence on parameters like temperature or the kind of the MOF material. But one has to note that the NO gas pressure can be obtained with higher accuracy and over a broader gas pressure range with other methods, e.g. by using a pressure gauge. But typical EPR experiments of NO loaded samples use sealed sample tubes where the pressure of desorbed NO cannot be measured by other methods. This difficulty can be overcome by EPR itself. The gas pressure of desorbed NO can be directly measured in CW EPR experiments by the detection and analysis of the EPR signal of desorbed NO, as it is explained in detail in the present chapter. This way one can relate local and microscopic information obtained by EPR for adsorbed NO species with macroscopic information about the amount of desorbed NO obtained by CW EPR. Hereby, one can relate EPR derived results about adsorbed NO species to results obtained by other methods like volumetric adsorption experiments, in principle.<sup>[76,78]</sup> In this context, the usage of EPR of NO gas as a tool to quantify the amount of desorbed NO is still of high interest.

One can use two properties of the EPR signal of desorbed NO to determine its amount: Its intensity and its linewidth. It is difficult to determine the amount of desorbed NO from its EPR intensity, using a standard sample like ultramarine as a reference. Then, one has to take the population of the lowest rotational  ${}^2\Pi_{3/2}$  state into account. Such kind of analysis is quite complicated since higher rotational states are also populated significantly at ambient temperatures,<sup>[288]</sup> which have to be considered. Therefore, it is more convenient to compare the EPR intensity of NO gas with that obtained for samples with a known amount of pure NO gas. The latter approach has been used by Rudolf et al.<sup>[196,198]</sup> whereas the first approach, using a standard sample as a reference, has not been tried yet so far. Since EPR is quite sensitive for small amounts of NO (see appendix D.1) the temperature dependence of the intensity of the EPR signal of desorbed NO is well suited for the determination of the characteristic temperature where the adsorption or desorption of NO starts.

It has been pointed out that the linewidth of the EPR signal of desorbed NO might be also used to determine the gas pressure of desorbed NO.<sup>[198,288]</sup> For some gases like oxygen<sup>[319,320]</sup> or fluorine<sup>[321]</sup> a linear relation between the gas pressure and the linewidth of the EPR signals of these gases was observed. But as far as known, the linewidth of the EPR signal of NO has been only roughly related to gas pressures  $p \leq 1.33$  mbar.<sup>[288]</sup> At such small pressures all nine lines (see subsection 2.3.3) of the EPR signal of NO gas are well resolved and the peak-to-peak linewidth can be read directly from the spectrum.

This is not possible for higher NO loading where the nine lines have collapsed into three in a medium pressure range or into one line at even higher pressures as it is illustrated in Figure 16. In these cases simulations of the signals becomes necessary to determine their linewidth. With convenient simulation programs like the MatLab toolbox EasySpin<sup>[294]</sup> or XSophe<sup>[295]</sup> an exact simulation of the EPR signal of NO was not possible, since those programs did not have implemented the spin-orbit coupling and the coupling between the spin and rotational angular momenta (see subsection 2.3.3) by the time this subtopic of the thesis was treated.

This chapter will introduce and rationalize in the first section a simulation procedure of the EPR signal of NO gas based on a phenomenological spin Hamiltonian approach, which can be easily performed with EasySpin.<sup>[294]</sup> This method has been already used by other authors<sup>[296]</sup> but without any reasoning. Once established, this approach will be used in the second section to determine experimentally the relation between the EPR linewidth and the room temperature pressure of NO gas. The results will be rationalized by the kinetic gas theory. All these have been published by Mendt and Pöpl.<sup>[222]</sup> The chapter will be completed by the presentation of exemplary studies in the third section where the amount of desorbed NO in EPR samples containing the MOFs MIL-53(Al/Cr), MIL-100(Al) and DUT-8(Ni) has been determined by the proposed EPR linewidth approach. The temperature-dependent intensities of the EPR signal of desorbed NO in the MOF containing samples are also presented and discussed in this section. In a fourth summary section, the main results of the present chapter are reviewed.

### 3.1 Simulating the EPR signal of NO gas

The X-band EPR signal of gaseous NO at low gas pressures has been already discussed in subsection 2.3.3. It consists of three triplets of lines where the smaller splitting of each triplet is determined by the isotropic <sup>14</sup>N hfi constant  $a_{\text{iso}}$  (Figure 14a). The occurrence of three well separated hfi triplets is a consequence of the lifting of the threefold degeneracy of the EPR transitions with  $\Delta m_J = \pm 1$  (Figure 14b). That these transitions occur at different magnetic fields is a consequence of the perturbation of the Hund's case (a) coupling scheme by the external magnetic field and nearby excited states.<sup>[287]</sup> In a rigorous calculation of the correspondent resonance fields and EPR line intensities one would start from a Hamiltonian where the spin-orbit coupling and the coupling between the spin and rotational angular momenta are included.<sup>[287,290]</sup> But those interactions were not implemented in conventional simulation programs like EasySpin<sup>[294]</sup> or XSophe<sup>[295]</sup> by the time this topic was treated. On the other hand, the only interest could be shown toward the homogeneous linewidth of this signal, since it is the parameter which can be related to the gas pressure. For this purpose it would be sufficient to simulate the EPR signal of NO gas with a convenient spin Hamiltonian, which gives in good approximation the correct resonance frequencies and EPR intensities of each of the nine transitions.

The X-band EPR signal of gaseous NO can be fitted in good approximation by a

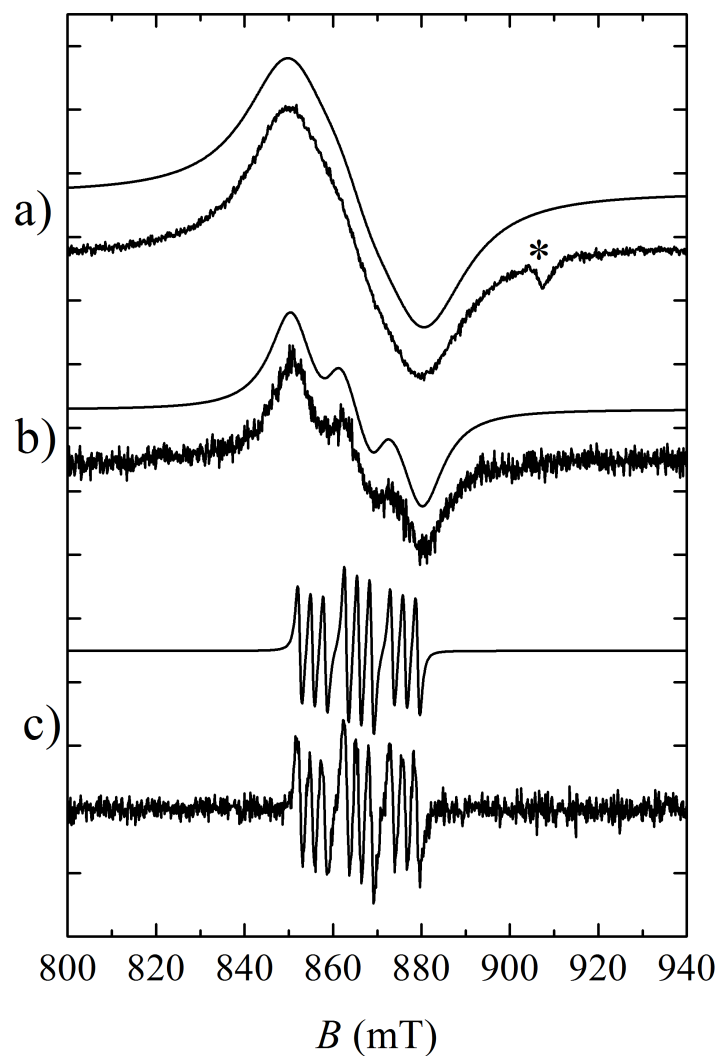


Figure 16: Room temperature X-band CW EPR spectra of samples of pure NO gas with room temperature gas pressures of 60 mbar (a), 30 mbar (b) and 1 mbar (c). Above each spectrum its simulation is shown (see section 3.1). The *asterisk* marks an artifact. This picture was first published by Mendt and Pöpl.<sup>[222]</sup>



phenomenological Hamiltonian:<sup>[296]</sup>

$$\hat{H} = \hat{H}_Z + \hat{H}_{\text{HF}} + \hat{H}_{\text{FS}}, \quad (52)$$

defining  $B_0||z$ . Here,  $\hat{H}_Z$  describes the Zeeman interaction between the total angular momentum  $J$  and the external magnetic field, and  $\hat{H}_{\text{HF}}$  describes the hfi between  $J$  and the  $^{14}\text{N}$  nuclear spin  $I^{14\text{N}}$  as they have been introduced in the equations (42) and (43). The third term in equation (52) has the form of an fs interaction:

$$\hat{H}_{\text{FS}} = D \left[ \hat{J}_z^2 - \frac{1}{3} J(J+1) \right]. \quad (53)$$

But it is not the usual fs interaction, namely the zfi, where the parameter  $D$  is constant (compare with equation (4)). In the present case  $\hat{H}_{\text{FS}}$  is introduced in a phenomenological way as the parameter  $D$  depends on the magnetic field where the signal occurs, and therefore it differs with the mw frequency of the EPR experiment. A rigorous calculation<sup>[290]</sup> proves the absence of any splitting of the  $m_J$  energy levels at zero magnetic field. Thus, the term zero-field splitting (zfi) is avoided here for the description of the Hamiltonian's part defined by equation (53).

Nevertheless, in Mendt and Pöppl<sup>[222]</sup> it has been justified that in an X-band experiment this fs term fits the line positions of the nine EPR transitions and their intensities in very good approximation to the experimental ones. For example, at a mw frequency of  $\nu_{\text{mw}} = 9.411$  GHz a simulation with an fs parameter  $D = 57 \pm 1.5$  MHz would match the experimental NO gas spectrum.<sup>[222]</sup> Only an isotropic convolutional Lorentzian peak-to-peak linewidth parameter  $\delta B_{\text{pp}}$ <sup>[222,294]</sup> has to be added phenomenologically, a parameter, which is of interest for this thesis. It turns out that in all cases which were investigated here, the proposed spin Hamiltonian and line broadening model are appropriate for an accurate simulation of the NO gas EPR signals at different temperatures or NO gas pressures (Figure 16).

### 3.2 The relation between the NO gas EPR linewidth and the NO gas pressure

Room temperature X-band CW spectra of the NO gas samples  $\text{NO}_p$  ( $1 \leq p \leq 60$ ) with room temperature gas pressures  $1 \text{ mbar} \leq p \leq 60 \text{ mbar}$  are shown in Figure 17a (see appendix A.2 for the preparation procedure). The linewidths of the spectra increase with growing pressure. Whereas at  $p = 1$  mbar all nine transitions are resolved, for  $p > 10$  mbar each hfi triplet has collapsed into a single line and at  $p = 60$  mbar all transitions have collapsed into one broad line. It was possible to simulate each EPR signal keeping the values  $g$ ,  $a_{\text{iso}}$  and  $D$  constant (see subsection 2.3.3 and section 3.1). Only the linewidth parameter  $\delta B_{\text{pp}}$  was changed. Three exemplary simulations are shown in Figure 16.

In Figure 17b the room temperature NO gas pressures  $p$  of the samples  $\text{NO}_p$  are plotted against their room temperature linewidth parameters  $\delta B_{\text{pp}}$  as they were determined by simulation. A linear relation

$$p = a \cdot \delta B_{\text{pp}} + b \quad (54)$$

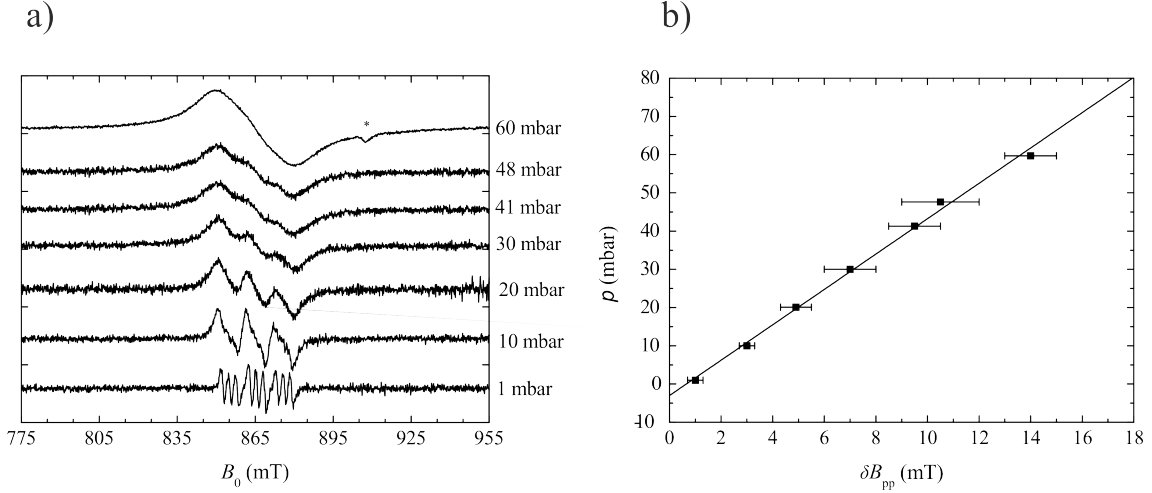


Figure 17: a) Room temperature X-band CW spectra of samples  $\text{NO}_p$  (see appendix A for the notation) measured with a modulation amplitude of 0.5 mT and a mw power of 10 mW. The room temperature NO gas pressures of the samples are denoted at the right. The *asterisk* marks an artifact. b) The room temperature gas pressures of different samples  $\text{NO}_p$  plotted against the corresponding linewidth  $\delta B_{pp}$ , which has been determined for the room temperature X-band CW spectrum of each sample  $\text{NO}_p$  by simulation. The linear fit of the data points (equation (54)) is also shown. This picture was first published by Mendt and Pöpl. [222]

between both parameters is found, where  $a = 4.62 \pm 0.35 \frac{\text{mbar}}{\text{mT}}$  and  $b = -3.01 \pm 2.73 \text{ mbar}$ . Such a linear dependence between the gas pressure and the EPR linewidth has been observed for paramagnetic  $\text{O}_2$  molecules in the presence of perturbing  $\text{O}_2$ , Ar or He species [319,320] and for paramagnetic F atoms in the presence of perturbing F, He or  $\text{F}_2$  species, [321] and has been explained by kinetic theory. [319,321] Consequently, the EPR linewidth theory and kinetic theory have been applied for the rationalization of relation (54), as it has been published by Mendt and Pöpl as outlined in the following. [222]

Simulations (Figure 16) indicated that the linewidth of the NO gas EPR signal is almost purely Lorentzian and mainly determined by the lifetime of the lowest rotational  $^2\Pi_{3/2}$  state. Hence, it can be assumed that it is related to a decay rate of: [222]

$$\tau^{-1} = \tau_c^{-1} + \tau_{dd}^{-1} + \tau_w^{-1} + \tau_i^{-1}. \quad (55)$$

Here, the rates  $\tau_c^{-1}$ ,  $\tau_{dd}^{-1}$  and  $\tau_w^{-1}$  are produced by collisions between two NO molecules, by magnetic dipole-dipole interactions between different NO molecules and by collisions with the inner tube wall, respectively. Collisions involving more than two molecules inside the tube or more than one molecule involved in collisions with the wall were neglected. The rate  $\tau_i^{-1}$  corresponds to the intrinsic lifetime of the lowest rotational  $^2\Pi_{3/2}$  state in the absence of any perturbing molecules or walls.

Each rate  $\tau_k^{-1}$  with  $k \in \{c, dd, w, i\}$  produces a Lorentzian peak-to-peak linewidth contribution  $\delta B_{pp}^k$  to the total linewidth  $\delta B_{pp}$  according to the following formula: [319,321]

$$\tau_k^{-1} = \frac{\mu_B g \sqrt{3} \pi}{h} \delta B_{pp}^k. \quad (56)$$

The total linewidth is

$$\delta B_{\text{pp}} = \delta B_{\text{pp}}^{\text{c}} + \delta B_{\text{pp}}^{\text{dd}} + \delta B_{\text{pp}}^{\text{w}} + \delta B_{\text{pp}}^{\text{0}}, \quad (57)$$

where the linewidth

$$\delta B_{\text{pp}}^{\text{0}} = \delta B_{\text{pp}}^{\text{i}} + \delta B_{\text{pp}}^{\text{inh}} \quad (58)$$

at zero gas pressure has been introduced with  $\delta B_{\text{pp}}^{\text{inh}}$  comprising all inhomogeneous contributions in an approximate fashion.

As verified by acoustic measurements,<sup>[322]</sup>  $\tau_{\text{c}}^{-1}$  must be almost equal to or larger than the rate of all “hard-sphere collisions”.<sup>[323]</sup> It can be expressed by kinetic theory<sup>[319,321,324]</sup> starting from the formula

$$\tau_{\text{c}}^{-1} = n\bar{v}\sigma, \quad (59)$$

where  $n$  is the number density of the gas,  $\sigma$  is an effective collisional cross section and  $\bar{v}$  is the average relative velocity of two NO molecules. Taking into account equation (56) one ends up with the following linear relation:<sup>[222]</sup>

$$p = \frac{\sqrt{3}\pi^{\frac{3}{2}}g\mu_{\text{B}}\sqrt{k_{\text{B}}T\mu}}{\sqrt{8}h\sigma}\delta B_{\text{pp}}^{\text{c}}, \quad (60)$$

where  $k_{\text{B}}$  is the Boltzmann constant and  $\mu = \frac{m}{2}$  is the reduced mass of two NO molecules each of them having the mass  $m$ .

It was further argued<sup>[222]</sup> that the linewidth contribution  $\delta B_{\text{pp}}^{\text{dd}}$  can be safely neglected, transferring the results of an estimation of the dipole-dipole relaxation rate  $\tau_{\text{dd}}^{-1}$  published for  $^{19}\text{F}$  or  $^{129}\text{Xe}$  nuclear spins interacting with the  $\text{O}_2$  electron spins to the present case.<sup>[325–327]</sup>

It was also estimated that collisions with the inner tube wall contribute with less than three percent to the total EPR linewidth of NO gas<sup>[222,328]</sup> and therefore  $\delta B_{\text{pp}}^{\text{w}}$  can be also neglected in equation (57).

Following approximated relation is the result:

$$\delta B_{\text{pp}} = \delta B_{\text{pp}}^{\text{c}} + \delta B_{\text{pp}}^{\text{0}}, \quad (61)$$

which rationalizes together with equation (60) the linear dependence between the pressure  $p$  and the linewidth  $\delta B_{\text{pp}}$  of the EPR signal of NO gas. According to the experimentally determined linear relation (54)  $\delta B_{\text{pp}}^{\text{0}} = 0.65 \pm 0.55$  mT and an effective collisional cross section  $\sigma = \sigma_{\text{EPR}} = 80.75 \pm 5.76 \text{ \AA}^2$  which corresponds to a kinetic diameter  $d_{\text{EPR}} = 5.07 \pm 0.18 \text{ \AA}$  with  $\sigma_{\text{EPR}} = \pi d_{\text{EPR}}^2$  is obtained. As observed for  $\text{O}_2$  gas<sup>[319]</sup>, this cross section is larger than the collisional cross section  $\sigma_{\text{VIS}} \approx 38 \text{ \AA}^2$  that can be obtained from viscosity measurements<sup>[323]</sup>, since both methods measure different kinds of definitions for a molecular collision.<sup>[222]</sup>

The previous derivation has shown that one can easily determine the amount of NO gas from the experimental NO gas EPR linewidth if a cryostat, which keeps the whole sample volume at the same temperature, is used and if the temperature dependence of the effective collisional cross section  $\sigma_{\text{EPR}}$  is known.

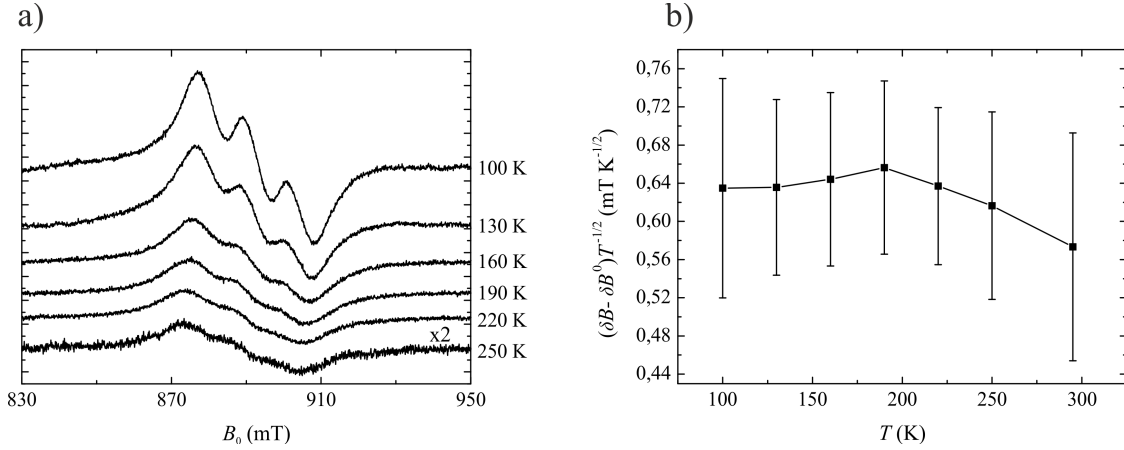


Figure 18: a) Temperature-dependent X-band EPR spectra of sample  $\text{NO}_{48}$  measured on the ELEXYS E580 spectrometer, equipped with a cryostat which cools the whole sample tube. In all experiments the modulation amplitude was 1 mT and the mw power 2 mW. The temperatures are denoted on the right. The spectrum which was measured at  $T = 250$  K is enlarged by a factor of 2. b)  $\frac{\delta B_{\text{pp}} - \delta B_{\text{pp}}^0}{\sqrt{T}}$  vs.  $T$  as determined by the simulations of the X-band EPR spectra of sample  $\text{NO}_{48}$ , which are shown in a) and Figure 17a and which were measured at temperatures  $100 \text{ K} \leq T \leq 295 \text{ K}$ . This picture was first published by Mendt and Pöpl.<sup>[222]</sup>

To investigate the temperature dependence of  $\sigma_{\text{EPR}}$ , temperature-dependent CW experiments of the sample  $\text{NO}_{48}$  have been conducted with an ELEXYS E580 spectrometer equipped with an Oxford Instruments He cryostat CF 935 (see appendix B.1). The latter cools the whole tube minimizing the temperature gradient along its length.

The corresponding spectra are shown in Figure 18a. The linewidth parameters  $\delta B_{\text{pp}}$  of those experimental NO gas signals were determined by simulation. The temperature dependence of the quantity  $\frac{\delta B_{\text{pp}} - \delta B_{\text{pp}}^0}{\sqrt{T}}$  is shown in Figure 18b. According to the relations (60), (61) and the ideal gas equation it should be constant if  $\sigma_{\text{EPR}}$  is temperature independent and if any temperature gradient in the EPR tube is absent.<sup>[222]</sup> This parameter stays always constant at  $\frac{\delta B_{\text{pp}} - \delta B_{\text{pp}}^0}{\sqrt{T}} \approx 0.62 \text{ mT/K}$  within the experimental error. From the given equations it follows that the effective collisional cross section as determined by EPR stays roughly constant at  $\sigma_{\text{EPR}} = 84 \pm 17 \text{ \AA}^2$  between  $T = 100 \text{ K}$  and  $T = 295 \text{ K}$ .<sup>[222]</sup>

According to the previous discussion the determination of the amount of desorbed NO gas from its EPR linewidth at low temperatures can be easily realized when the whole EPR tube is kept at the same temperature. Unfortunately, conventional top-loading continuous He-flow cryostats for CW EPR experiments cool only the small volume of an EPR tube which contains the sample. The other end of the EPR tube is in most cases outside the cryostat. Consequently, there is a temperature gradient over the length of the EPR tube. Since this gradient is not precisely known, the gas density distribution over the whole tube length is also not known. This prevents at low temperatures the direct EPR linewidth based determination of the total amount of desorbed NO as it has been outlined.

To obtain quantitative results from the NO gas EPR linewidth for low temperature measurements, which have been conducted with a Bruker ER 4119HS cylindrical cavity equipped with an Oxford Instruments He flow cryostat ESR 900, experiments of pure

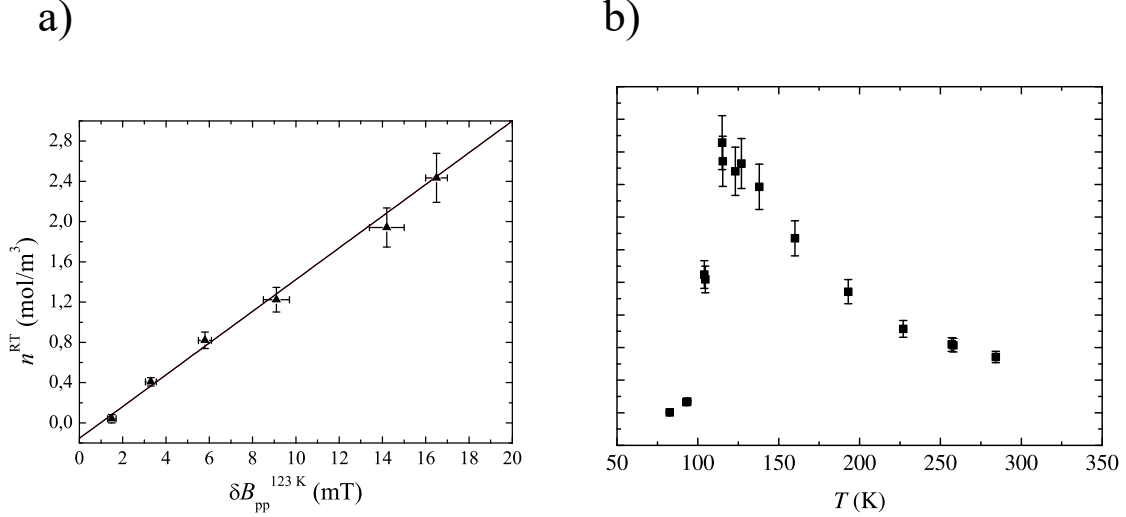


Figure 19: a) Room temperature density  $n^{\text{RT}}$  of desorbed NO gas in certain EPR reference samples with pure NO gas and almost same geometries vs. the homogeneous Lorentzian peak-to-peak linewidth  $\delta B_{\text{pp}}^{123 \text{ K}}$  as determined by simulation of the NO gas EPR spectra measured for the corresponding signals at  $T = 123 \text{ K}$  in a Bruker ER 4119HS cylindrical cavity that was equipped with an Oxford Instruments He flow cryostat ESR 900. b) The temperature-dependent intensity  $I_{\text{NOgas}}$  of the EPR signal of gaseous NO in the X-band EPR sample NO<sub>48</sub>.

NO gas reference samples have been performed with this setup at  $T = 123 \text{ K}$  and the corresponding NO gas EPR linewidths  $\delta B_{\text{pp}}^{123 \text{ K}}$  have been sustained by simulations.<sup>[224]</sup> The room temperature gas density  $n^{\text{RT}}$  of those samples is plotted over  $\delta B_{\text{pp}}^{123 \text{ K}}$  in Figure 19a.  $n^{\text{RT}}$  depends almost linearly on this linewidth. The corresponding linear fit

$$n^{\text{RT}} = a \cdot \delta B_{\text{pp}}^{123 \text{ K}} + b \quad (62)$$

with  $a = 0.158 \pm 0.009 \frac{\text{mol}}{\text{m}^3 \text{mT}}$  and  $b = -0.15 \pm 0.04 \frac{\text{mol}}{\text{m}^3}$  is also shown in Figure 19a and will be used in the following section 3.3 to determine approximately the amount of desorbed NO in certain EPR MOF samples at  $T \approx 123 \text{ K}$ . It has its root at  $\delta B_{\text{pp},0}^{123 \text{ K}} = 0.96 \pm 0.3 \text{ mT}$  which is consistently at a proximity equal to the NO gas linewidth  $\delta B_{\text{pp}}^0 = 0.65 \pm 0.55 \text{ mT}$  in the limit of zero gas pressure at room temperature, as was determined in relation (54).

The EPR signal of NO gas cannot be measured at too low temperatures when it becomes liquid or immediately solid at pressures below  $p \approx 219 \text{ mbar}$  at the triple point.<sup>[329]</sup> To determine the temperature, where gaseous NO freezes out, temperature-dependent X-band EPR measurements have been performed for sample NO<sub>48</sub>.<sup>[224]</sup> For each spectrum the EPR NO gas signal intensity  $I_{\text{NOgas}}$  was determined by the double integration of its simulation. Its temperature dependence is shown in Figure 19b. It has a maximum at  $T \approx 130 \text{ K}$ . Above this temperature it decreases with growing temperature, which can be explained

by the Curie law in combination with a depopulation of the lowest rotational  $^2\Pi_{3/2}$  state in favor for the population of higher rotational states.<sup>[198]</sup> Going to lower temperatures,  $I_{\text{NOgas}}$  decreases drastically until it approaches almost zero in a temperature range  $82 \text{ K} < T < 115 \text{ K}$ . This range matches the range that includes the boiling point of NO gas at  $T = 120 \text{ K}$  and  $p = 867 \text{ mbar}$ , and the point of sublimation at  $T = 100.15 \text{ K}$  at  $p = 40 \text{ mbar}$  and  $T \approx 80 \text{ K}$  at almost zero gas pressure.<sup>[329]</sup> Therefore, the decrease of  $I_{\text{NOgas}}$  at temperatures  $T < 130 \text{ K}$  can be assigned to the condensation or desublimation of gaseous NO into the liquid or solid phase, respectively.

### 3.3 EPR of desorbed NO in the MOF samples

As pointed out in the previous section, the determination of the amount of desorbed NO from its EPR linewidth is feasible. In the present section the developed methodology will be applied to four exemplary model systems, comprising the NO adsorption on the MOF materials MIL-53(Al/Cr), MIL-100(Al) and on the flexible and rigid derivatives of DUT-8(Ni), as it has been already partially published.<sup>[223,224]</sup> This choice includes MOFs with and without CUS and with and without structural flexibility. Particularly, the flexible MOF MIL-53 shows permanent porosity whereas the flexible DUT-8(Ni) stays in a non-porous phase at zero gas pressure (see section 2.1). For both DUT-8(Ni) derivatives, two samples with different amounts of loaded NO have been investigated (see appendix A.3, Table A.1). Thus, the chosen samples should represent a sound selection of the most prominent properties of MOFs that relate to gas adsorption.

In this section a first subsection will collect the results of the EPR experiments and the introduced NO gas line with analysis. A second subsection will discuss the results.

#### 3.3.1 Results

Six MOF and NO loaded EPR samples are considered. The samples Al/Cr-MIL-53 and Al-MIL-100 contain the MOFs MIL-53(Al/Cr) and MIL-100(Al). The two samples F\_DUT-8a and F\_DUT-8b contain the flexible derivative of DUT-8(Ni) whereas the samples R\_DUT-8a and R\_DUT-8b contain its rigid derivative. Samples Al/Cr-MIL-53, Al-MIL-100, F\_DUT-8a and R\_DUT-8a contain similar small amounts of NO whereas the other two DUT-8(Ni) samples were prepared with about 13 times higher NO amounts (see appendix A.3, Table A.1).

For all samples, X-band EPR spectra have been measured in full temperature cycles including the cooling and subsequent heating in the temperature range  $6 \text{ K} < T < 295 \text{ K}$  by using an ESR 900 cryostat. In some temperature regions between  $T \approx 90 \text{ K}$  and room temperature the EPR signal of desorbed NO was detected. An exemplary temperature-dependent series of such spectra is shown for sample Al-MIL-100 in Figure 20a.<sup>[223]</sup> The NO gas EPR linewidth increases with growing temperature indicating the desorption related pressure broadening. The same was observed for all other samples.<sup>[223,224]</sup>

Interestingly, for the flexible DUT-8(Ni) samples, NO gas EPR signals with different linewidths were measured in the cooling and heating period at same temperatures. This is illustrated in Figure 21, where both flexible DUT-8(Ni) samples show a larger NO gas

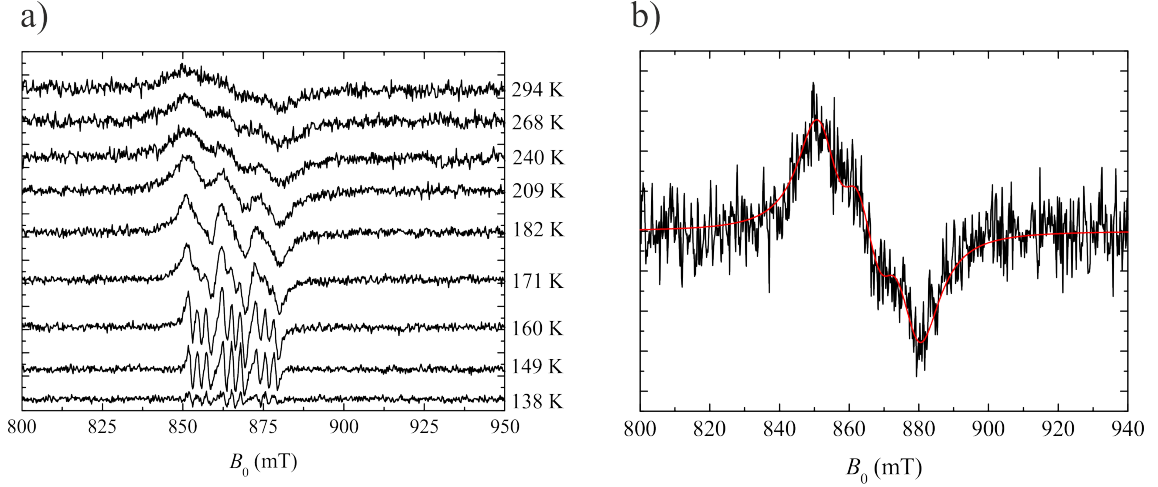


Figure 20: a) EPR spectra of sample Al-MIL-100 as measured during heating at different temperatures. They show the signal of desorbed NO and are identical to corresponding signals measured during cooling. This picture was first published by Barth, Mendt et al.<sup>[223]</sup> b) EPR spectrum (black) of sample Al-MIL-100 measured at room temperature. For the simulation (red) of the EPR signal of desorbed NO gas the linewidth parameter was  $\delta B_{pp}^{RT} = 8.5$  mT.

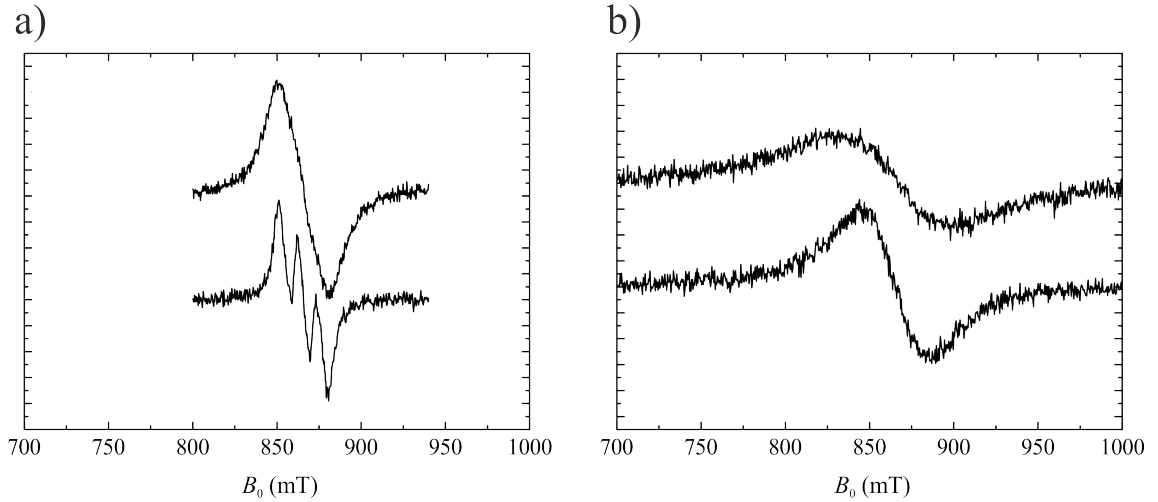


Figure 21: EPR spectra of desorbed NO gas in sample F\_DUT-8a measured at  $T = 115$  K (a) during cooling (above) and heating (below) and in sample F\_DUT-8b measured at  $T = 127$  K (b) during cooling (above) and heating (below). Both pictures were first published by Mendt et al.<sup>[224]</sup>

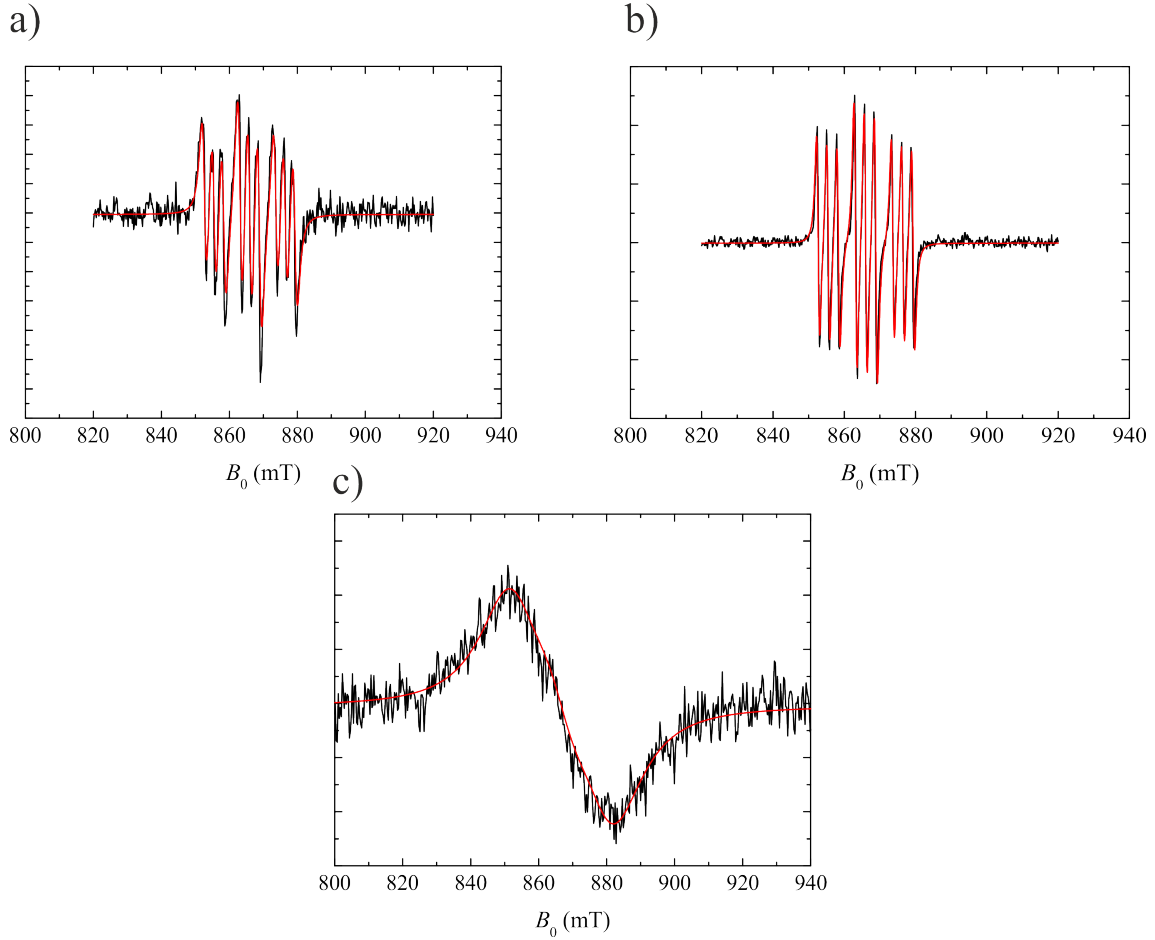


Figure 22: EPR spectra (black) of sample Al/Cr-MIL-53 measured at  $T = 127$  K during cooling (a) and heating (b) and at room temperature (c) after warming up the sample. Corresponding simulations are shown in red. For those, line with parameters  $\delta B_{pp}^{127\text{K}} = 1.5$  mT (a),  $\delta B_{pp}^{127\text{K}} = 0.7$  mT (b) and  $\delta B_{pp}^{\text{RT}} = 13$  mT (c) were used.

EPR linewidth during the cooling than heating period at  $T = 115$  K and  $T = 127$  K, respectively. Sample F\_DUT-8a with a low NO loading shows during heating an NO gas EPR signal, where all three  $\Delta m_J = \pm 1$  transitions but not the  $^{14}\text{N}$  hfi splitting are resolved whereas in the preceding cooling period those three line are almost broadened to a single one. The corresponding signals of sample F\_DUT-8b have much broader linewidths where all transitions have collapsed to one line, reflecting the higher NO loading in that sample. The observed linewidth hysteresis indicates that at those temperatures more NO is desorbed during cooling than heating in both samples.

A less pronounced but similar effect was observed for the MIL-53(Al/Cr) sample at the temperature  $T = 127$  K. Again, the NO gas EPR linewidth was slightly larger in the cooling than heating period as it is shown in Figure 22a,b (Table 1). In this case, the linewidth difference is quite small, but can be clearly resolved by simulations (Table 1).

All NO gas EPR linewidths determined for the different samples at  $T = 125.5 \pm 1.5$  K are summarized in Table 1. The corresponding simulations for the NO gas signals of the MIL-53 and DUT-8 samples are depicted in Figures 22 and 23. For the rigid DUT-8(Ni) samples as well as for the MIL-100(Al) sample the NO gas EPR signals measured during the



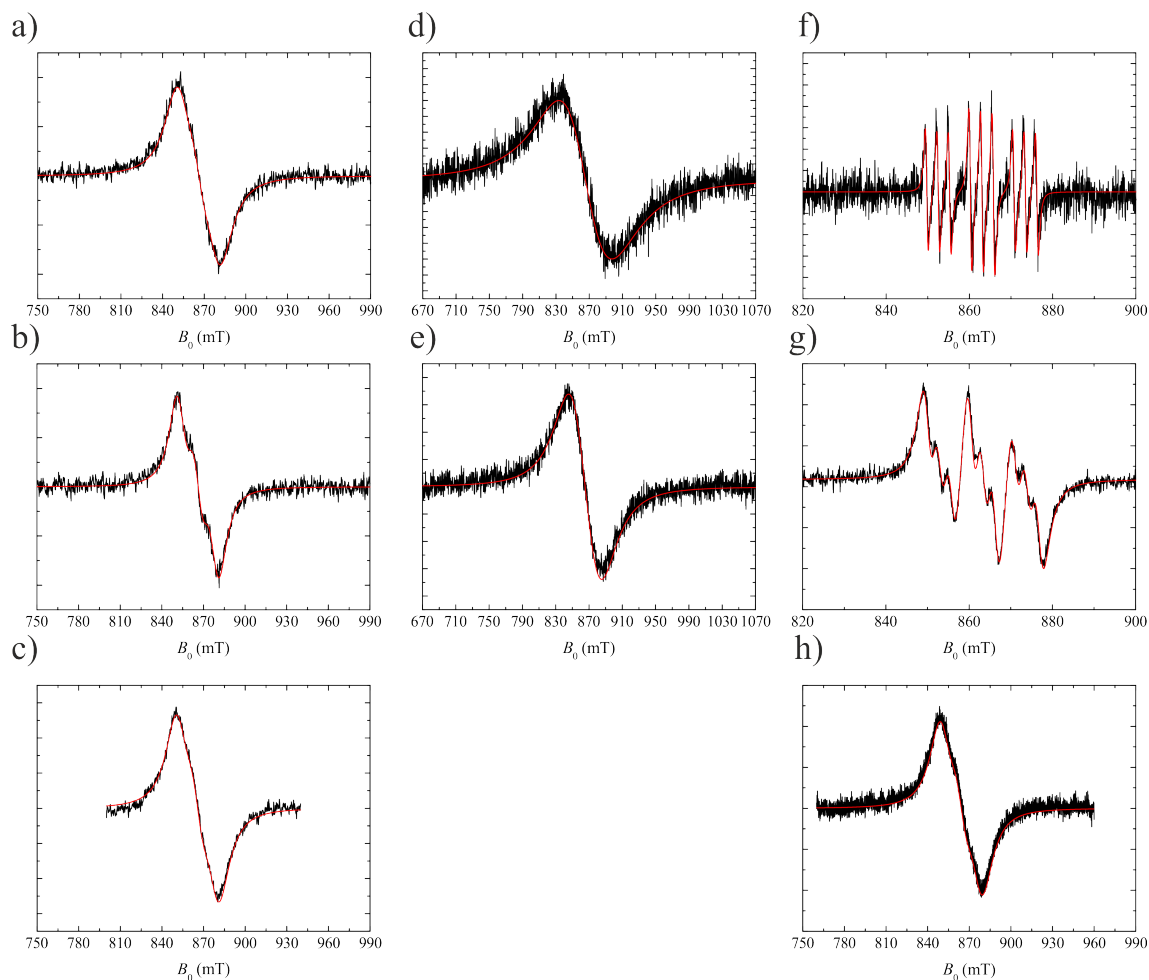


Figure 23: EPR spectra showing the signals of desorbed NO gas (black) and their simulations (red). Samples and experimental temperatures are (a) F\_DUT-8a at  $T = 127$  K during cooling, (b) F\_DUT-8a at  $T = 127$  K during heating, (c) F\_DUT-8a at  $T = 294$  K, (d) F\_DUT-8b at  $T = 127$  K during cooling, (e) F\_DUT-8b at  $T = 127$  K during heating, (f) R\_DUT-8a at  $T = 124$  K, (g) R\_DUT-8b at  $T = 126$  K and (h) R\_DUT-8a at  $T = 297$  K. The corresponding linewidth parameters of each simulation are given in Tables 1 and 2.

Table 1: Characteristic temperature  $T_{\text{ads/des}}$  where the adsorption or desorption of NO gas starts, the temperature  $T_{\text{max}}$  where the NO gas EPR signal intensity approaches its maximum, the Lorentzian peak-to-peak linewidth of the NO gas signals as determined by simulation of spectra measured at  $T = 125.5 \pm 1.5$  K, the amount  $N_{\text{ads}}^{125\text{ K}}$  of NO adsorbed on the solid surface at  $T \approx 125$  K given in units of  $\mu\text{mol}$  per mg MOF and as the fraction of all NO in percent (Table A.1). All parameters except  $T_{\text{ads/des}}$  and  $T_{\text{max}}$  were determined by the NO gas linewidth analysis. The errors in the last three columns cover only the uncertainty of the linewidth determination.

| EPR sample   | $T_{\text{ads/des}}$ (K) | $T_{\text{max}}$ (K)            | $\delta B_{\text{pp}}^{125\text{ K}}$ (mT) | $N_{\text{ads}}^{125\text{ K}}$ ( $\mu\text{mol}/\text{mg}$ ) | $N_{\text{ads}}^{125\text{ K}}$ (%) |
|--------------|--------------------------|---------------------------------|--|---|-------------------------------------|
| Al/Cr-MIL-53 | $120 \pm 5$              | $182 \pm 10$                    | $1.5 \pm 0.1/$ a<br>$0.7 \pm 0.1$          | $0.465 \pm 0.003/$ a<br>$0.480 \pm 0.002$                     | $96.5 \pm 0.6/$ a<br>$99.6 \pm 0.4$ |
| Al-MIL-100   | $149 \pm 11$             | $210 \pm 20$                    | - <sup>b</sup>                             | $> 0.31$ <sup>c</sup>   | $> 99.4$ <sup>c</sup>               |
| F_DUT-8a     | $< 93$ <sup>d</sup>      | $132 \pm 17/$ a<br>$149 \pm 22$ | $13.5 \pm 0.8/$ a<br>$8.7 \pm 0.4$         | $0.06 \pm 0.01/$ a<br>$0.144 \pm 0.004$                       | $22 \pm 5/$ a<br>$52 \pm 2$         |
| F_DUT-8b     | $104 \pm 11$             | $\geq 127/$ a,b<br>$\geq 138$   | $59 \pm 3/$ a<br>$31 \pm 3$                | $5.2 \pm 0.1/$ a<br>$6.1 \pm 0.1$                             | $74 \pm 2/$ a<br>$86 \pm 1$         |
| R_DUT-8a     | $124 \pm 9$              | $185 \pm 25$                    | $0.7 \pm 0.2$                              | $0.506 \pm 0.003$   | $99.3 \pm 0.7$                      |
| R_DUT-8b     | $121 \pm 5$              | $\geq 136$ <sup>b</sup>         | $2.8 \pm 0.2$                              | $9.90 \pm 0.01$   | $99.0 \pm 0.1$                      |

<sup>a</sup>during cooling/heating, <sup>b</sup>no NO gas signal was resolved at corresponding temperatures, <sup>c</sup>Considering the detection limit of NO gas (see appendix D.1), <sup>d</sup>Since NO seems to freeze out before the adsorption has finished, only an upper bound for  $T_{\text{ads/des}}$  could be given.

cooling and heating period were identical at same temperatures over the full temperature range. Thus, it seems that the occurrence of such linewidth differences correlates with the presence and absence of the structural flexibility of the MOF.

The temperature dependences of the NO gas EPR signals of the different samples can be further characterized by their intensities  $I_{\text{NOgas}}$ , as they are shown in Figure 24. With increasing temperatures all of them start to increase significantly from zero at characteristic temperatures  $93\text{ K} < T_{\text{ads/des}} < 160\text{ K}$ , which are collected in Table 1. At distinct temperatures  $T_{\text{max}} > 130\text{ K}$  (Table 1), the temperature dependences of  $I_{\text{NOgas}}$  approach their maxima. Their decrease at higher temperatures is related to the depopulation of the lowest rotational  ${}^2\Pi_{3/2}$  state in favor for the population of higher rotational states in combination with the Curie law.<sup>[198]</sup> For both DUT-8(Ni) samples with a larger amount of NO, the EPR signal of desorbed NO gas could not be resolved anymore at temperatures of  $T > 140\text{ K}$ . This observation indicates the desorption of such a high amount of NO gas that its detection was prevented by the large pressure broadening. Furthermore, only for both flexible DUT-8(Ni) samples the intensities determined during the cooling and heating period show a clear hysteresis in certain temperature ranges (Figure 24c,d), which reflects the just mentioned linewidth differences in both branches at low temperatures. Surprisingly, the subtle linewidth difference for the MIL-53(Al/Cr) sample observed at  $T = 127\text{ K}$  during cooling and heating is not complemented by any adsorption/desorption related hysteresis of the NO gas EPR signal intensity, which might be an issue of worse resolution (Figure 24a).

Using relation (62) from the previous section and considering the total NO and MOF amounts in the samples (see appendix A.3, Table A.1), from the NO gas EPR linewidth

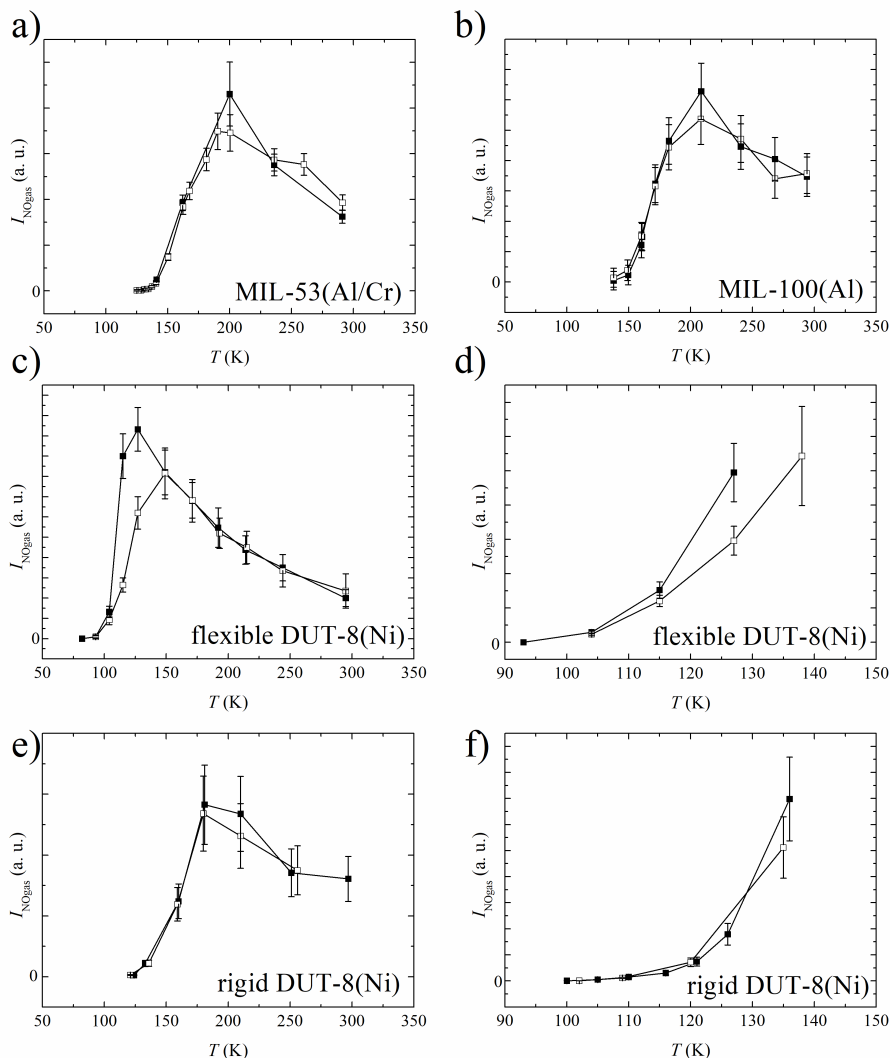


Figure 24: a) The intensity  $I_{\text{NOgas}}$  of the EPR signal of desorbed NO in the sample Al/Cr-MIL-53, as determined by the double integration of the corresponding baseline corrected signals at different temperatures.<sup>[223]</sup> b) The temperature-dependent intensity  $I_{\text{NOgas}}$  of the EPR signal of desorbed NO gas in the sample Al-MIL-100.  $I_{\text{NOgas}}$  was determined by the double integration of the corresponding baseline corrected experimental spectra. Intensities  $I_{\text{NOgas}}$  of the EPR signal of NO gas in the samples F\_DUT-8a (c), F\_DUT-8b (d), R\_DUT-8a (e) and R\_DUT-8b (f) as determined by the integration of the simulated signal. For all six samples the cooling (adsorption branch, filled squares) as well as the heating (desorption, empty squares) branches are shown. Similar figures are published in Barth, Mendt et al.<sup>[223]</sup> (a,b) and Mendt et al.<sup>[224]</sup> (d-f).

Table 2: Lorentzian peak-to-peak linewidth  $\delta B_{pp}^{\text{RT}}$  of the room temperature NO gas EPR signal, room temperature pressure  $p_{\text{RT}}$  of desorbed NO and the amount  $N_{\text{ads}}^{\text{RT}}$  of NO which is adsorbed on the solid surface at room temperature. The latter is given in units  $\mu\text{mol}/\text{mg}$  and percent as in Table 1. The pressure  $p_{\text{RT}}$  was determined from  $\delta B_{pp}^{\text{RT}}$  using the experimentally determined relation (54). From that pressure,  $N_{\text{ads}}^{\text{RT}}$  was estimated using the mass of the MOF and the mole number of all NO of each sample as given in the appendix A.3 (Table A.1). The errors cover only the uncertainty introduced by the linewidth determination.

| EPR sample   | $\delta B_{pp}^{\text{RT}}$ (mT) | $p_{\text{RT}}$ (mbar) | $N_{\text{ads}}^{\text{RT}}$ ( $\mu\text{mol}/\text{mg}$ ) | $N_{\text{ads}}^{\text{RT}}$ (%) |
|--------------|----------------------------------|------------------------|--|----------------------------------|
| Al/Cr-MIL-53 | $13 \pm 1.8$                     | $57 \pm 8$             | $0.05 \pm 0.05$  | $10 \pm 10$                      |
| Al-MIL-100   | $8.5 \pm 0.8$                    | $36 \pm 4$             | $0.03 \pm 0.03$  | $10 \pm 10$                      |
| F_DUT-8a     | $11.6 \pm 0.8$                   | $50 \pm 4$             | $0.03 \pm 0.03$  | $11 \pm 11$                      |
| F_DUT-8b     | - <sup>a</sup>                   | $> 224^{\text{b}}$     | $< 5.4^{\text{b}}$   | $< 74^{\text{b}}$                |
| R_DUT-8a     | $11.2 \pm 0.7$                   | $49 \pm 3$             | $0.10 \pm 0.03$  | $20 \pm 6$                       |
| R_DUT-8b     | - <sup>a</sup>                   | - <sup>a</sup>         | - <sup>a</sup>   | - <sup>a</sup>                   |

<sup>a</sup>not resolved due to the large pressure broadening of the NO gas signal, <sup>b</sup>The given limits are the corresponding values determined at  $T \approx 125$  K (see Table 1) since at room temperature the EPR signal of desorbed NO was not resolved due to its pressure broadening.

$\delta B_{pp}^{125\text{ K}}$  the amount  $N_{\text{ads}}^{125\text{ K}}$  of NO can be determined, which is adsorbed during the cooling or heating period at  $T \approx 125$  K. This determination considers that at present NO pressures the temperature  $T = 125$  K is above the boiling point (see section 3.2). The corresponding results are collected in Table 1. The same kind of analysis was performed for room temperature signals of NO gas. The room temperature NO gas EPR linewidths  $\delta B_{pp}^{\text{RT}}$  were determined by the simulations of the corresponding spectra (Figures 20, 22 and 23). Using the relation (54), the actual room temperature NO gas pressures  $p_{\text{RT}}$  were calculated, enabling the determination of the amount  $N_{\text{ads}}^{\text{RT}}$  of adsorbed NO at room temperature. The corresponding values are collected in Table 2. All errors in Tables 1 and 2 cover only the linewidth uncertainty to illustrate the sensitivity of that parameter. Errors, originating from the experimentally determined relations (54) and (62) are systematic and it should be possible to reduce them distinctly by more accurate and comprehensive measurements. The uncertainties of the MOF and NO amounts in the different samples (see appendix A.3, Table A.1) can be systematically reduced by a more precise preparation. The uncertainty of the NO gas EPR linewidth can be lowered by the reduction of the signal to noise ratio of the experimental spectra.

### 3.3.2 Discussion

Previous results illustrate that the determination of the amount of desorbed NO from its EPR signal linewidth is very sensitive in case of small gas pressures. For the MIL-53(Al/Cr) sample this approach was capable to resolve a small adsorption/desorption related hysteresis, whereas the measurement of the NO gas EPR signal intensity offered a too bad resolution for the detection of a hysteresis effect. It also seems that the corresponding errors of the amount of desorbed NO as determined from its EPR linewidth can compete with the

uncertainties which have been stated by Rudolf et al.<sup>[196,198]</sup> for the NO quantification by the measurement of the NO gas EPR signal intensity. But a more detailed comparison of the performance of both approaches is not an objective of this thesis.

The experiments that can be realized with the smallest effort are room temperature measurements. Regarding the determination of the amount of desorbed NO, they are useless for the two DUT-8(Ni) samples with high NO loading, since the large pressure broadening of the NO gas EPR signals prevents their detection. On a first glance, this is not the case for the four MOF samples with low NO loading, since they show reasonable NO gas EPR signals at room temperature. The presented analysis of their linewidths proves that about 80-100 percent of the total amount of NO are desorbed at that temperature (Table 2). But unfortunately, the errors in the simulation derived linewidths are too large to enable a clear resolution of the differences between the amounts of desorbed NO among these four samples. Consequently, the low temperature investigations are necessary to obtain deeper insights into the characteristics of the different materials with respect to the NO adsorption.

From the temperature-dependent measurements of the NO gas EPR signal intensity the characteristic temperature  $T_{\text{ads/des}}$  can be obtained, at which the desorption of the NO gas from the MOF surface starts. Among the considered samples it increases in the order  $F\_DUT-8a \lesssim F\_DUT-8b < R\_DUT-8a \approx R\_DUT-8b \approx Al/Cr-MIL-53 < Al-MIL-100$  (Table 1). The sample with the MOF MIL-100(Al) has the largest desorption temperature. This is reasonable since MIL-100(Al) is the only considered material which has CUS, acting presumably as preferred adsorption sites for NO. The other MOFs, namely MIL-53(Al/Cr) and DUT-8(Ni) have no CUS and show therefore a weaker adsorption affinity for NO. This result indicates an interaction between the adsorbed NO and the uncoordinated  $Al^{3+}$  sites in the MIL-100(Al) which matters at temperatures  $T < 149$  K. A more detailed analysis of the NO adsorption species in the MOF MIL-100(Al) will be the subject of chapter 5. Here, one has to note that an analogous analysis published by the author has shown that the MIL-100(Fe) MOF with  $Fe^{3+}$  CUS or the CPO-27(M) MOFs ( $M = Ni, Co$ ; CPO = Coordination Polymer of Oslo) with  $Ni^{2+}$  or  $Co^{2+}$  CUS result in even higher NO desorption temperatures  $T_{\text{ads/des}}$  than MIL-100(Al), indicating that the closed shell  $Al^{3+}$  CUS in the latter MOF have only a weak binding affinity for NO compared to metal ions with open shell electron configurations.<sup>[223]</sup>

It is further conclusive that the samples with the flexible derivative of DUT-8(Ni) have the smallest desorption temperatures. This is the only considered MOF which stays in a non-porous phase at high temperatures, preventing the adsorption of NO above a certain threshold temperature. Only below this temperature, the transformation to the porous phase and the adsorption of NO becomes favorable. This difference in porosity between the flexible and rigid DUT-8(Ni) derivatives was also proven by powder X-ray diffraction (PXRD).<sup>[224]</sup>

The rigid derivative of DUT-8(Ni) and MIL-53(Al/Cr) have similar desorption temperatures lying between that of the flexible DUT-8(Ni) and the MIL-100(Al) samples. This is in line with their properties that both show permanent porosity at all temperatures and

have no CUS as strong binding sites for NO. However, it is not evident that the desorption temperature of the rigid derivative of DUT-8(Ni) is similar to that of the MIL-53 material, since both structural phases of the MIL-53 material have significant smaller pore diameters than the open pore phase of DUT-8(Ni) (see section 2.1). This indicates that for the present low NO loading the mentioned differences of the pore sizes have a small influence on the interactions between the NO molecule and the MOF surface and among the adsorbed NO molecules themselves, which does not lead to significant different desorption temperatures. Since no CUS are present in both materials, the energetic landscape of adsorption sites might be comparable for those MOFs.

The temperature  $T_{\max}$ , where the NO gas intensity reaches its maximum, varies among the different samples in the order  $F\_DUT-8a < R\_DUT-8a \approx Al/Cr-MIL-53 < Al-MIL-100$  (Table 1). Thus,  $T_{\max}$  also reflects the non-porosity of the flexible DUT-8(Ni) material at high temperatures, the permanent porosity of the rigid DUT-8(Ni) and the MIL-53 and in the case of the MIL-100 MOF the presence of CUS, allowing for a stronger binding of NO than it occurs for the former three materials which have no CUS.

Further insights into the NO adsorption characteristics can be obtained from the NO gas EPR linewidth based quantification at  $T \approx 125$  K as it is summarized in Table 1. For the MIL-100, MIL-53 and the rigid DUT-8(Ni) materials the adsorption of NO has almost finished above the point where NO freezes out (Table 1 and section 3.2). Therefore, it can be concluded from the NO gas EPR linewidth analysis that almost all NO was absorbed at  $T \approx 125$  K. In particular for both rigid DUT-(Ni) samples the relative fraction of adsorbed NO at  $T \approx 125$  K is almost the same. This indicates that the saturation limit of the NO adsorption has not been reached, even at the respective high NO loading.

The case is different for both flexible DUT-8(Ni) samples. The sample F\_DUT-8b with high NO loading has absorbed a larger relative fraction  $N_{\text{ads}}^{125\text{ K}}$  of NO at  $T \approx 125$  K than the sample F\_DUT-8a with low NO loading (Table 1). Therefore, for sample F\_DUT-8b most NO should be absorbed inside the pores. Adsorption sites on the outer MOF surface should be equally accessible for NO in both samples and one would expect that the relative fraction  $N_{\text{ads}}^{125\text{ K}}$  of adsorbed NO should be equal or even larger for the flexible DUT-8(Ni) sample with low NO loading than for the sample with high NO loading, if adsorption sites at the outer MOF surface dominate.

The different relative fractions  $N_{\text{ads}}^{125\text{ K}}$  of both flexible DUT-8(Ni) samples might indicate that higher gas pressures are capable to trigger the cp to lp transformation for a larger amount of the MOF material allowing a larger fraction of NO to adsorb. But what has happened with the remaining gas?

The different availability of the lp phase for the NO adsorption might lead to the condensation or desublimation of a larger fraction of NO for the low loaded than high loaded flexible DUT-8(Ni) sample, since in the former case the larger amount of the non-porous cp phase partially prevents the NO adsorption at temperatures above the sublimation point. The experimental determined desorption temperatures of both flexible DUT-8(Ni) samples lie in the range of the NO sublimation point. It should be noted that for sample F\_DUT-8a the drop of the NO gas EPR signal intensity might originate from the NO gas

desublimation and the real desorption temperatures might be even smaller than is stated in Table 1.

During a slow cooling procedure of the flexible DUT-8(Ni) sample F\_DUT-8b with high NO loading, a partial change of the color yellow to the color green was observed.<sup>[224]</sup> This observation indicates that the NO adsorption has triggered the transformation from the cp to the lp phase.<sup>[240]</sup> The presence of such a transformation is also indicated by the significant hysteresis effects observed for the intensity and the linewidth of the NO gas EPR signals of both flexible DUT-8(Ni) samples. Especially the linewidth analysis at  $T \approx 125$  K proves that in the heating period significantly more NO has been adsorbed than during the cooling period (Table 1). This might be explained by the predominant presence of the non-porous cp phase during cooling, partially preventing the NO adsorption at  $T \approx 125$  K. The linewidth derived amounts of adsorbed NO at room temperature and at  $T \approx 125$  K in the cooling period are of the same order of magnitude for the sample F\_DUT-8a and indicate that a significant adsorption of NO occurred at lower temperatures. Some of the NO might open parts of the MOF to the porous phase at temperatures  $T < 125$  K, to allow for the adsorption. Consequently, during heating at  $T \approx 125$  K a larger fraction of the lp phase and of adsorbed NO is present than observed during cooling.

The previous results reflect the framework responsiveness of the flexible derivative of DUT-8(Ni), whereas for the rigid materials MIL-100(Al) and the rigid variant of DUT-8(Ni) no indication for any flexibility were observed. For the material MIL-53(Al/Cr), which is also known for its ability to transform from a lp to a np phase during gas adsorption (see subsection 2.1.2), such a hysteresis was not resolved by the EPR intensity  $I_{\text{NOgas}}$ . Only small adsorption/desorption related differences of the linewidth of the EPR signal of desorbed NO at  $T = 127$  K and the corresponding derived amounts of adsorbed NO (Table 1) might indicate the presence of framework responsiveness. But, to understand the reason why the EPR data of desorbed NO do barely show any presence of the prominent flexibility of MIL-53, it is necessary to know more about the phase composition of MIL-53(Al/Cr) during the performed experiments. Therefore, the signals of the paramagnetic  $\text{Cr}^{3+}$  probe ions with electron spin  $S = 3/2$ , replacing some  $\text{Al}^{3+}$  ions at the framework metal sites, were measured simultaneously with the EPR signals of NO. The former are known to act as fingerprints for the lp and np phase of MIL-53.<sup>[110,111]</sup> The appendix D.2 presents and discusses the corresponding results to highlight the important possibility offered by EPR, which allows to combine the detection of different magnetic species in one experiment. This experiments strongly indicate that during the NO adsorption the complete fraction of the lp phase is transformed to the np phase. Furthermore, when heating up the sample, NO is indicated to desorb solely from the np phase. Since for the np phase of MIL-53 and the rigid DUT-8(Ni) samples the desorption temperatures are almost identical (see Table A.1), the observation of hardly any NO adsorption/desorption related hysteresis for the MIL-53 material seems reasonable: If the smaller pore size of the np phase of MIL-53 does not significantly change the desorption temperature of NO compared to the large pores of the rigid DUT-8(Ni), the lp phase of MIL-53 is expected to have almost the same NO desorption temperature as the np phase since its pore size is in between.

Thus, one get strong evidence for the present porous MOF materials without CUS that significant differences in pore diameters and shapes have only a small, for NO gas EPR hardly resolvable, influence on the NO adsorption or desorption characteristics at low NO loading. This indicates that the energetic landscape of adsorption sites is similar in all present MOFs without CUS and even for the np phase of MIL-53 spatial hindrance seems to play no significant role for the small NO molecule regarding its adsorption characteristics for NO gas EPR at low gas loading.

### 3.4 Summary of chapter three

Desorbed NO gas shows a characteristic EPR signal which can be detected at low gas pressures. Both, its intensity as well as its linewidth can be used to quantify the amount of desorbed NO. In the first section of this chapter a simulation procedure was introduced, which allows for the easy derivation of the isotropic convolutional Lorentzian linewidth of an arbitrary EPR signal of desorbed NO gas. In the next section it was shown by EPR spectroscopy for certain NO gas samples that this linewidth depends linearly on the NO gas pressure at room temperature. This was rationalized by kinetic gas theory and a corresponding effective collisional cross section was derived from the experimental data. By appropriate temperature-dependent CW EPR measurements it was verified that this cross section stays almost constant between  $T = 100$  K and  $T = 295$  K. The temperature gradient along the EPR tube in standard top-loading continuous He-flow cryostats prevents the application of this established linear relation between the NO gas pressure and its EPR signal linewidth at low temperatures. To enable the derivation of the amount of desorbed NO gas from its EPR linewidth at low temperatures in such a setup, the experimental determined EPR linewidth of desorbed NO gas at  $T = 123$  K has been related to the room temperature density of this gas for certain NO gas samples. Again, a linear relation between both quantities was found. In the third section, both linear relations between the room temperature amount of desorbed NO and its EPR line width at  $T = 295$  K or  $T = 123$  K were used to derive the amount of desorbed NO at these temperatures for six NO loaded MOF samples including the materials MIL-53(Al), MIL-100(Al) as well as the flexible and the rigid derivative of DUT-8(Ni). In addition, the temperature dependences of the intensities of the corresponding EPR signals of desorbed NO were determined experimentally. The analysis of those data revealed that the flexible DUT-8(Ni) has the lowest NO adsorption/desorption temperatures which can be explained by its non-porosity at high temperatures and the absence of CUS in its structure. The rigid MIL-100(Al) MOF has the highest adsorption temperature among the samples, which are in the focus of this thesis, which relates to the presence of CUS in its structure. The porous phases of the rigid DUT-(Ni) and MIL-53 MOFs have adsorption/desorption temperatures in between those of the former. Their adsorption/desorption temperatures are almost the same although the rigid DUT-(Ni) has a much larger pore size than the np or even lp phase of MIL-53. This indicates that at low NO gas pressures the interaction of NO with the MOF surfaces is comparable among those samples, which is in line with their lack of any CUS and indicates similar adsorption sites provided by their organic parts, whereas the pore size has no



significant influence on the adsorption characteristics at those pressures for these samples. Furthermore, only for the flexible MOFs, adsorption/desorption related hysteresis effects of the amount of desorbed NO were observed by the linewidth analysis of the EPR signal of desorbed NO gas, indicating structural transformations during the NO adsorption. For the flexible DUT-8(Ni) samples such hysteresis effects were also observed by the NO gas EPR signal intensities. For the MIL-53, the EPR intensities did not resolve the hysteresis effect in contrast to the linewidth of the EPR signal of desorbed NO gas, reflecting again the small influence of the pore size on the adsorption characteristics of NO for porous MOF samples without CUS at low gas pressures. This demonstrates that at low NO gas pressure the linewidth based quantification of NO is more sensitive than the signal intensity based approach.

In general EPR offers the opportunity to estimate easily the amount of desorbed NO in temperature- or pressure dependent CW experiments at temperatures  $T > 80$  K, not only from the intensity but in addition from the linewidth of the EPR signal of NO gas. This method is particularly feasible in *in situ* experiments where the adsorption of NO on porous materials like MOFs, zeolites or on solid surfaces is explored. In particular the NO adsorption characteristics of selected MOF samples were explored by that approach, giving valuable insights. Now, the question arises, what is the nature of the interaction between the MOF surface and NO molecules, trapped within the pores of those MOFs, which will be addressed in the next three chapters.

## 4 NO adsorption species in MIL-53(Al), a MOF material without CUS

According to the previous section 3.3, NO adsorbs on the np phase of MIL-53 at low temperatures. In a next step, the NO interaction with the surface of the MIL-53 material will be investigated at low temperatures by EPR.

In this chapter, a distinct NO adsorption species of the MOF MIL-53(Al) is characterized in section 4.1 by the analysis of the corresponding CW-EPR signals measured at X-band and Q-band frequencies. Two-pulse ESE field sweep experiments prove the presence of a second NO adsorption species as discussed in section 4.2. In the same section, the interaction of both immobilized NO species with protons and  $^{27}\text{Al}$  nuclei will be further investigated by the analysis of corresponding HYSCORE spectra, characterizing the nature of the corresponding NO adsorption sites in more detail. A third summary section concludes the chapter.

### 4.1 CW-EPR

Figure 25 shows the X-band and Q-band CW EPR spectra of sample Al-MIL-53 measured at a temperature  $T = 10$  K. The same low temperature X-band CW signal was observed for sample Al/Cr-MIL-53.<sup>[223]</sup> The observed X-band signal can be simulated by an electron spin  $S = 1/2$  interacting with a nuclear spin  $I = 1$ , explaining the splitting of the low field powder edge singularity into three equally spaced lines. The simulation is also shown in Figure 25a. The g-tensor principal values as well as the hfi constant  $A_y^{14\text{N}}$  in  $y$ -direction, used for this simulation, are summarized in Table 3. It was assumed that the g-tensor and the hfi tensor are coaligned. The g-tensor principal values are close but slightly smaller than  $g_e = 2.0023$  and are ordered  $g_x \gtrsim g_y \gg g_z$ . They are typical for NO adsorbed at some diamagnetic surface site as it is discussed in subsection 2.3.4. In addition, the hfi splitting in  $y$ -direction is typical for the hfi with the  $^{14}\text{N}$  nucleus of such an NO species (see subsection 2.3.4). Hence, this species is attributed to an NO adsorption species called NO1a. The corresponding Q-band signal at  $T = 10$  K can be simulated with the same

Table 3: Simulation derived principal values of the g-tensor of the NO adsorbed in sample Al-MIL-53 at 10 K and of NO adsorbed in H-ZSM-5 zeolite.<sup>[198]</sup> The energy splitting  $\Delta$  between the  $^2\Pi_x$  and  $^2\Pi_y$  molecular states as calculated from the equations (44) as well as the simulation derived  $^{14}\text{N}$  hfi splitting  $A_y^{14\text{N}}$  in the g-tensors  $y$ -direction are also given (see subsection 2.3.4).

| Species                     | $g_x$              | $g_y$                        | $g_z$               | $\Delta(\text{kJ/mol})$    | $A_y^{14\text{N}}$ (MHz) |
|-----------------------------|--------------------|------------------------------|---------------------|----------------------------|--------------------------|
| NO1a                        | $1.9838 \pm 0.002$ | $1.9783 \pm 0.0014$          | $1.7637 \pm 0.0071$ | $10.5 \pm 0.6$             | $98.7 \pm 4$             |
| NO1b                        | - <sup>b</sup>     | $1.96 \pm 0.03$ <sup>c</sup> | $1.64 \pm 0.03$     | $7.7 \pm 1.0$ <sup>d</sup> | - <sup>e</sup>           |
| NOz1 (H-ZSM-5) <sup>a</sup> | $1.999 \pm 0.003$  | $1.999 \pm 0.003$            | $1.927 \pm 0.003$   | 25.5                       | $84.1 \pm 6.2$           |

<sup>a</sup>Rudolf et al.<sup>[198]</sup>, <sup>b</sup>not resolved within the theoretical reasonable range  $g_e > g_x > g_y$ , <sup>c</sup>derived from the two-pulse ESE field sweep spectrum (see section 4.2), <sup>d</sup>assuming  $l = 1$  (equations (44)), <sup>e</sup>not resolved

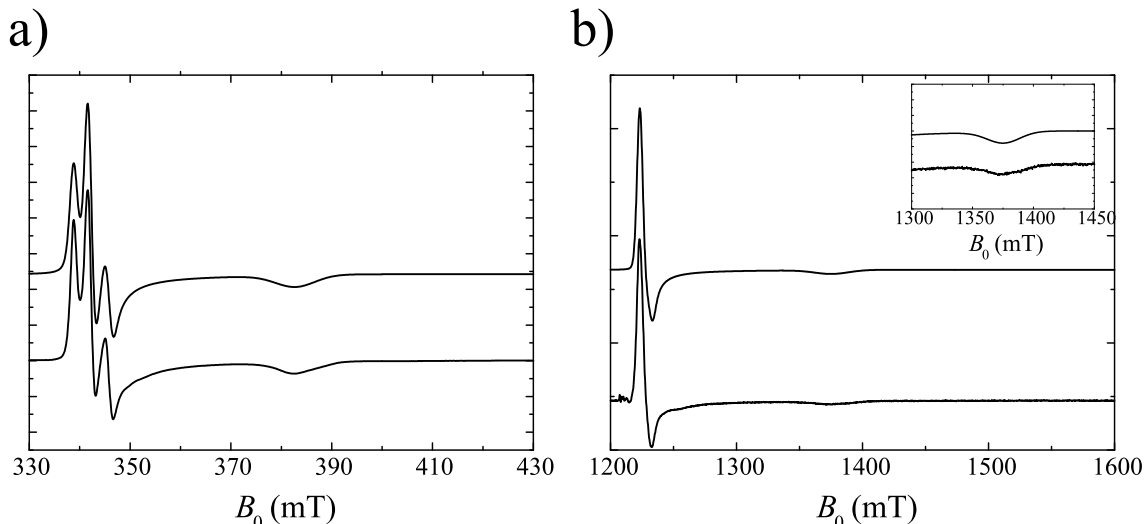


Figure 25: Experimental X-band (a, bottom) and Q-band (b, bottom) signals of NO, adsorbed in sample Al-MIL-53 at a temperature of 10 K. Above, simulations using parameters from Table 3 are shown. The  $^{14}\text{N}$  hfi principal values in the  $g$ -tensors  $x$ - and  $z$ -directions were set to zero. The same linewidth model was assumed for both simulations in (a) and (b), where the  $g$ -tensors principal values were independently Gaussian distributed with FWHM widths of  $\Delta g_x = \Delta g_y = 0.008$  and  $\Delta g_z = 0.04$ . The inset shows an enlargement of (b).

set of spin-Hamiltonian parameters as it is shown in Figure 25b and is also attributed to species NO1a. Here, the  $^{14}\text{N}$  hfi splitting in  $y$ -direction is not resolved anymore, which indicates that the broadening mechanism scales with the magnetic field and is mainly determined by  $g$ -strains. Consequently, the same  $g$ -strain line-broadening model was used for both simulations shown in Figure 25 (see caption of Figure 25).

The first question one might ask is whether NO1a adsorbs on the inner or outer surface of the porous material. There might be also the possibility of the adsorption on some impurity phase. An analysis of the corresponding temperature-dependent EPR signal intensities might give some insight. For sample Al/Cr-MIL-53 the temperature dependences of the intensities of the EPR signals of desorbed NO gas as well as of species NO1a are shown in Figure 26.<sup>[223]</sup> Whereas, almost all NO has been adsorbed below  $T_d = 120$  K (see section 3.3) the amount of the adsorption species NO1a starts to increase significantly below  $T = 80$  K.

A comparison of the EPR intensity  $I_{\text{ads}}$  of species NO1a with a reference signal of an ultramarine sample with known number of spins shows that at  $T = 25$  K about  $N = 0.21(9)$   $\mu\text{mol}$  spins contribute to the signal of species NO1a.<sup>[223]</sup> This is distinctly more than the number  $N_{\text{NOgas}} \approx 1.8$  nmol of desorbed NO molecules, which can be detected at the minimum<sup>[223]</sup> (see appendix D.1). The EPR signal of species NO1a increases significantly at temperatures  $T < 80$  K, where desorbed NO has been completely frozen out or absorbed. Therefore, it is most likely that species NO1a condenses from an NO phase inside the pores of the MOF material. So, the temperature dependences of the signal intensities of NO1a and desorbed NO gas indicate that NO1a adsorbs on the inner surface of the MOF.

It is remarkable that one observes for the MIL-53 samples at low temperatures a well

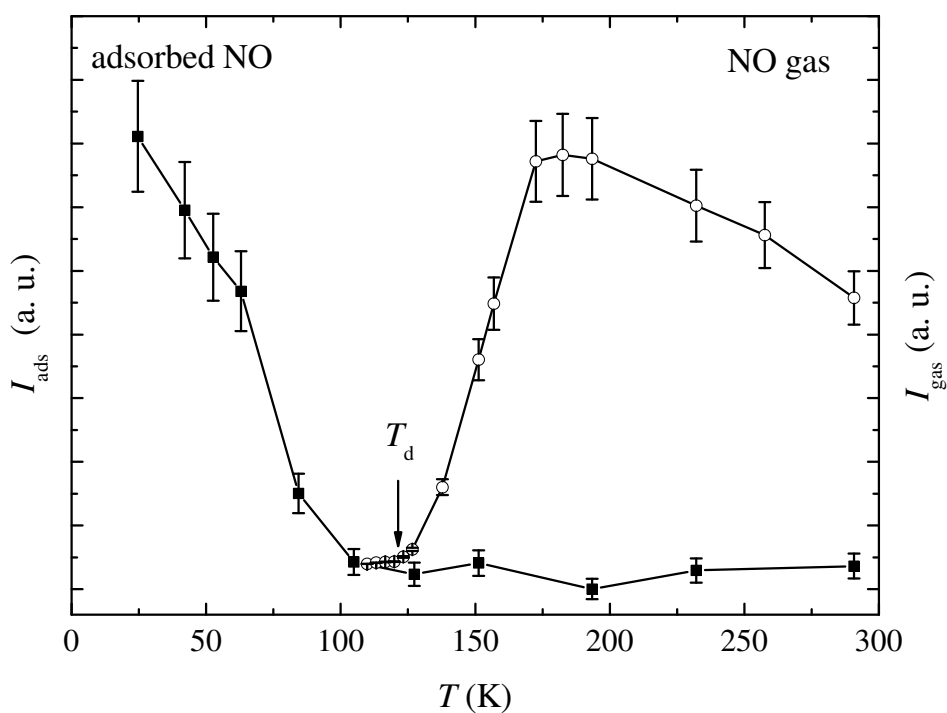


Figure 26: Intensities of the X-band EPR signal of NO1a (filled squares) and of the gas phase signal of desorbed NO (open circles) as determined for sample Al/Cr-MIL-53 at different temperatures. The figure contains data from both the cooling and heating branch. This figure was first published by Barth, Mendt et al.<sup>[223]</sup>

defined signal of adsorbed NO, although this MOF lacks any well defined CUS in its framework structure due to the octahedral coordination of the  $\text{Al}^{3+}$  cations. Nevertheless, species NO1a might adsorb at some defective CUS or some CUS of an impurity phase. Such an NO species NOz1 (z for zeolite), adsorbed either at  $\text{Al}^{3+}$  or  $\text{AlO}^+$  defect centers in H-ZSM-5 zeolite, has been characterized by EPR previously.<sup>[198]</sup> Thus, a comparison of the characteristic spectroscopic properties of species NO1a and NOz1 might give a first evidence, whether NO1a binds to some Al site.

Most importantly, the EPR signal of species NOz1 in the H-ZSM-5 zeolite shows a significant  $^{27}\text{Al}$  hfi splitting with a coupling constant  $A_y^{27\text{Al}} \approx 31.2 \text{ MHz}$ <sup>[198]</sup> whereas the signal of species NO1a in the MIL-53(Al) MOF lacks any resolved  $^{27}\text{Al}$  hfi. Simulations show, that a  $^{27}\text{Al}$  hfi of  $A_y^{27\text{Al}} < 10 \text{ MHz}$  can contribute to the line width of the EPR signal of NO1a. This is a first indication for the absence of any  $^{27}\text{Al}$  nuclei in the first coordination sphere of this NO adsorption species.

The NO1a species might be further characterized by the analysis of its g-tensor principal values. It is known that the energy splitting  $\Delta$  between the  $^2\Pi_x$  and  $^2\Pi_y$  molecular states of the adsorbed NO increases with growing electric surface field gradient (see subsection 2.3.4).<sup>[301]</sup> The g-tensor derived energy splitting  $\Delta$  (equations (44)) is more than twice as large for species NOz1 in the H-ZSM-5 zeolite than for species NO1a in the MIL-53(Al) MOF (Table 3). This additionally indicates that NO1a is not formed at an Al site where the electric surface field might be comparable to that at the adsorption site of species NOz1.

As shown in Table 3, the  $^{14}\text{N}$  hfi in  $y$ -direction is somewhat larger for species NO1a than for species NOz1. This indicates that more unpaired spin density is in the nitrogen's  $2p_y$  AO of species NO1a compared to NOz1. This in turn can be interpreted within the picture illustrated by relation (33), where the electronic structure of the NO molecule is understood as a superposition of two resonance structures with the unpaired electron staying either in the  $2p_y$  AO of the nitrogen or oxygen atoms. Consequently, a smaller value  $A_y^{14\text{N}}$  indicates a stronger electron pair acceptor strength of the adsorption site. Thus, the adsorption site of species NO1a seems to be a weaker Lewis acid than the Al site where species NOz1 adsorbs. This also indicates a non-metallic nature of the NO1a adsorption site.

The adsorption strength of the NO1a species can be characterized by the temperature dependence of its linewidth.<sup>[196,198]</sup> As illustrated in Figure 27a and b, the EPR signal of NO1a becomes broader with rising temperature until it almost vanished at  $T \approx 80 \text{ K}$ . The isotropic convolutional Lorentzian peak-to-peak linewidth parameters  $\delta B_{\text{pp}}$  were determined by the simulations of the X-band and Q-band signals of the NO1a species in sample Al-MIL-53 at different temperatures. They were fitted by the Arrhenius equation:

$$\delta B_{\text{pp}} = a \cdot e^{-\frac{E_A}{k_B T}} + b \quad (63)$$

as shown in Figure 27c and d, with the free parameters  $a$ ,  $b$  and  $E_A$ . This way an activation energy of  $E_A = 2.4 \pm 1.0 \text{ kJ/mol}$ , characterizing the energetic barrier for the desorption process of the NO1a in sample Al-MIL-53, was determined. Consistently, for the species NO1a in sample Al/Cr-MIL-53 an equivalent activation energy of  $E_A = 2.9 \pm 1.4 \text{ kJ/mol}$

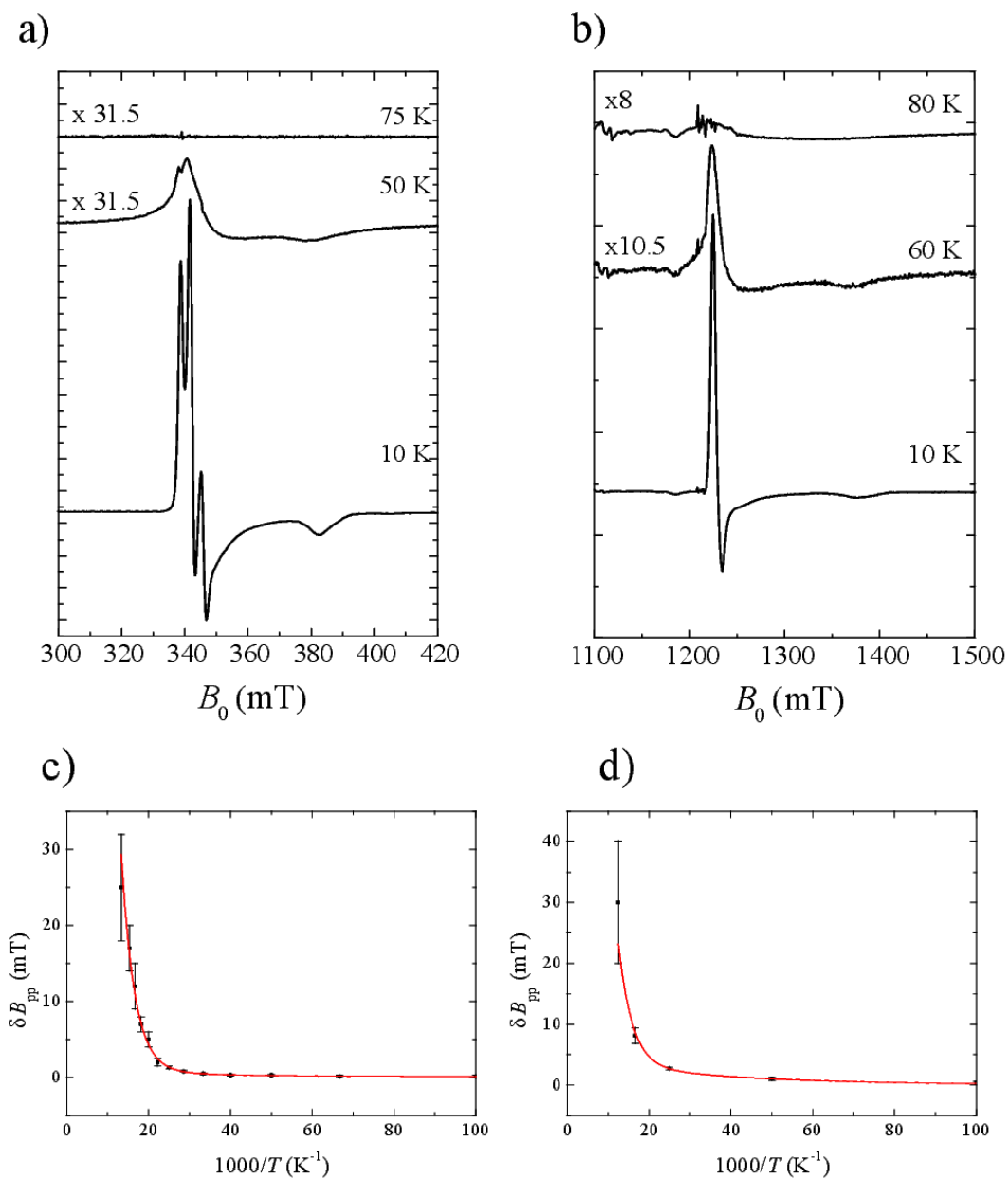


Figure 27: X-band (a) and Q-band (b) EPR spectra of the sample Al-MIL-53 showing the EPR signal of species NO1a at different temperatures as well as the temperature dependences of the isotropic convolutional Lorentzian peak-to-peak linewidth parameter  $\delta B_{pp}$ , as determined by simulations of the X-band (c) and Q-band (d) EPR signals of the NO adsorption species NO1a in the sample Al-MIL-53. The red lines are the fits with an Arrhenius law (equation (63)) where in both cases the same activation energy  $E_A = 2.4 \pm 1.0$  kJ/mol was used.

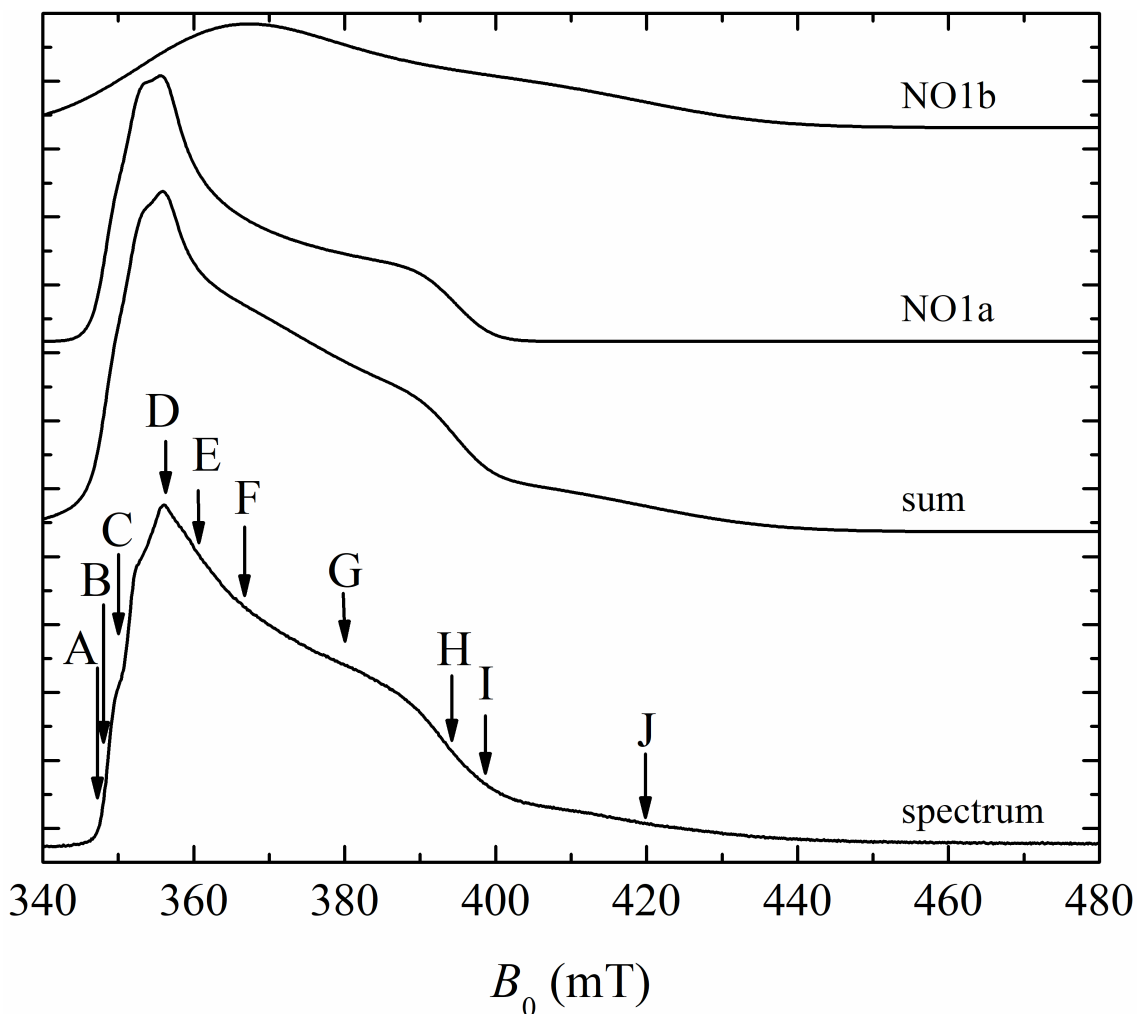


Figure 28: Two-pulse ESE field sweep spectrum of sample Al-MIL-53 measured at 10 K (bottom). The simulations of species NO1a (second from top), NO1b (top) and their sum are also shown. Field positions where HYSCORE experiments have been conducted are indicated by arrows.

was determined similarly. This value is distinctly smaller than  $E_A = 20.2 \pm 7.3$  kJ/mol as determined for species NOz1 and even smaller than  $E_A = 4.1 \pm 1.4$  kJ/mol and  $E_A = 7.2 \pm 2.1$  kJ/mol as determined for  $\text{Na}^+$ -NO adsorption species NOz2 and NOz3 in the zeolites Na-ZSM-5 and Na-A.<sup>[198]</sup> This offers additional evidence that NO1a is not adsorbed at a defective CUS in MIL-53.

In total, a comparison of distinct parameters derived from the CW EPR signals of species NO1a and NO adsorbed on certain zeolites indicates that the former does not bind to a defective or impurity related CUS in the MIL-53 samples. A further characterization of those species becomes necessary which has motivated a comprehensive study by two-pulse ESE field sweep and HYSCORE experiments presented in section 4.2.

## 4.2 Two-pulse ESE field sweep and HYSCORE spectroscopy

A two-pulse ESE field sweep experiment of sample Al-MIL-53 was conducted at X-band frequency and  $T = 10$  K. It shows the signal of the NO adsorption species NO1a as it is

indicated by the plot of its simulation in the same Figure 28. But obviously a broad tail of signal intensity contributes to the spectrum at higher magnetic fields  $400 \text{ mT} < B_0 < 430 \text{ mT}$ , where the signal of species NO1a does not occur anymore. This signal will be attributed to one or several immobilized NO species subsumed under the label NO1b. Due to its shallow spectral shape, species NO1b was not resolved by the first derivative like CW EPR spectrum (Figure 25).

From the two-pulse ESE field sweep spectrum one can estimate the NO1b g-tensor principal value  $g_z = 1.64 \pm 0.03$  (Table 3). Consequently, the energy splitting  $\Delta$  should be distinctly smaller for species NO1b compared to species NO1a (equations (44)), indicating weaker electric surface fields at the adsorption sites of species NO1b than at the site of species NO1a.<sup>[301]</sup>

In the previous section the NO adsorption species NO1a was characterized by CW EPR, indicating that this species does not bind to any Al atom in its first coordination sphere. Further evidence for this hypothesis, more detailed knowledge about the near environment of species NO1a as well as of the two-pulse ESE field sweep detected species NO1b might be obtained by more advanced pulsed EPR methods. For this purpose the HYSCORE technique was chosen (see subsection 2.2.3). Its spreading of the nuclear frequency spectrum into two frequency dimensions implicates a high resolution, especially in cases of small hfi,<sup>[268]</sup> and is favorable for the unraveling of spectral contributions from different nuclear species.

HYSCORE spectra of sample Al-MIL-53 have been measured at  $T = 6 \text{ K}$  at field positions A ( $B_0 = 346.8 \text{ mT}$ ) to J ( $B_0 = 420.0 \text{ mT}$ ) as they are indicated by arrows in Figure 28. All spectra are collected in the appendix E. Exemplary spectra are shown in Figure 29. All spectra show signals in the first quadrant distributed around the  $^{27}\text{Al}$  and the  $^1\text{H}$  proton Larmor frequencies  $\nu_{\text{Al}} \approx 4.0 \text{ MHz}$  and  $\nu_{\text{H}} \approx 15 \text{ MHz}$  indicative for weakly coupled  $^{27}\text{Al}$ , and proton nuclei with  $\text{hfi} \frac{A}{2} < \nu_I$  (see equation (21)). Signals of strongly coupled  $^{27}\text{Al}$  nuclei or protons ( $\frac{A}{2} > \nu_I$ ) in the fourth quadrant are absent in all spectra, indicating particularly the absence of  $\text{Al}^{3+}$  ions in the first coordination sphere of the NO species NO1a and NO1b.<sup>[242,279]</sup>

Both, protons and  $^{27}\text{Al}$  nuclei occur in the MIL-53 framework structure. For the  $^{27}\text{Al}$  nuclei at the framework metal sites of MIL-53(Al), NMR data of their nqi<sup>[238]</sup> allow for their comparison with the present  $^{27}\text{Al}$  HYSCORE signals. Therefore, first the  $^{27}\text{Al}$  data will be discussed.

All HYSCORE spectra of sample Al-MIL53a in Figure 29 show signals in the first quadrant that were distributed almost near the diagonal  $\nu_2 = \nu_1$  around the  $^{27}\text{Al}$  Larmor frequency  $\nu_{\text{Al}} \approx 4.0 \text{ MHz}$ . Therefore, this signals are attributed to weakly coupled  $^{27}\text{Al}$  nuclei, here called species Al1, interacting with the NO adsorption species NO1a and NO1b. As it will become evident in the following, the analysis of the measured HYSCORE signals does not allow for a significant spectral differentiation between  $^{27}\text{Al}$  nuclei, interacting either with NO1a or NO1b. From the extension of the Al1 peaks, perpendicular to the frequency diagonal, one can estimate by simulations that the dipolar hfi constant of this nuclei is small, namely  $T < 0.8 \text{ MHz}$ . Here, it was assumed that the isotropic hfi constant



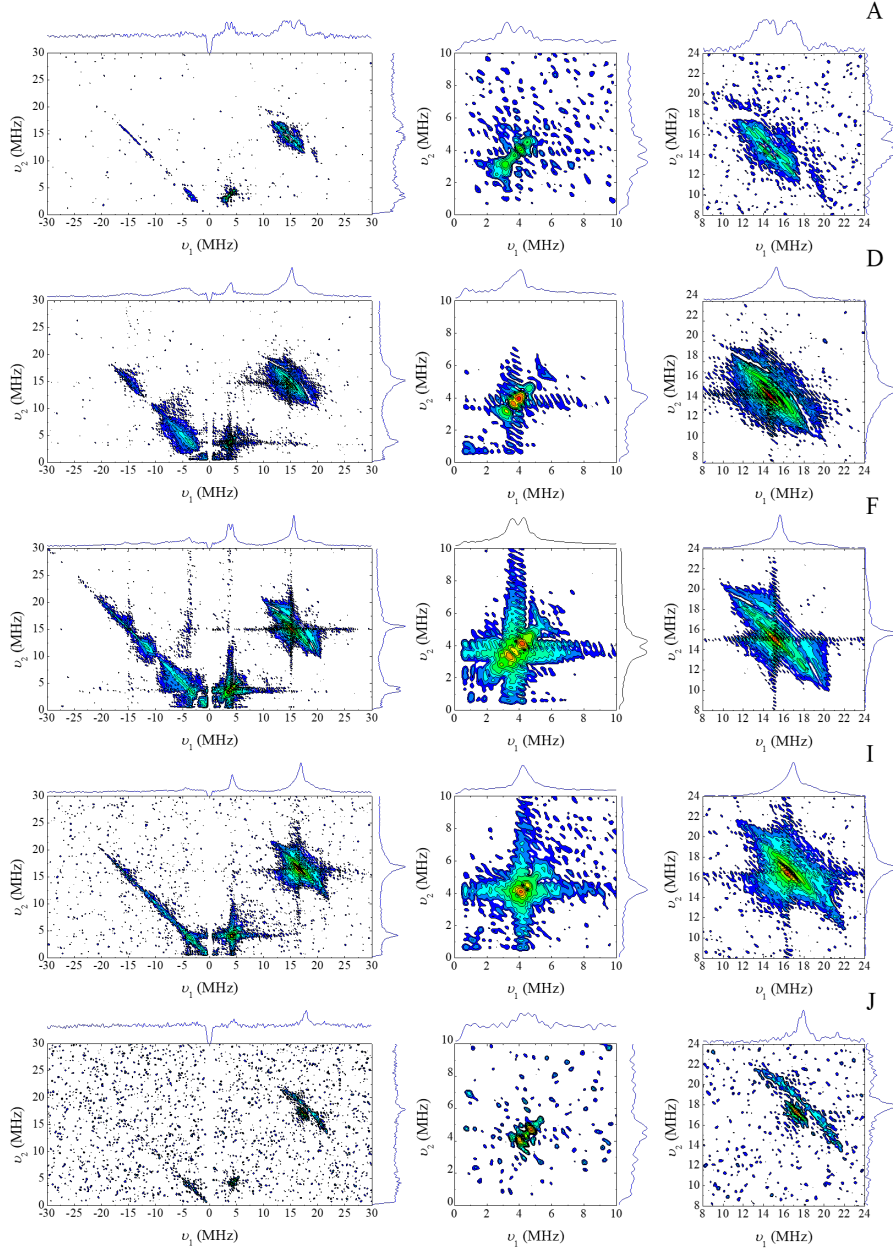


Figure 29: Exemplary HYSCORE spectra of sample Al-MIL-53 measured at the temperature  $T = 6$  K at field positions  $B_0 = 346.8$  mT (A),  $B_0 = 356.0$  mT (D),  $B_0 = 367.0$  mT (F),  $B_0 = 398.8$  mT (I) and  $B_0 = 420.0$  mT (J). The field position labels on the top right of each row are the corresponding labels shown in Figure 28. Each of the rows show on the left the whole HYSCORE spectrum, and in the middle and on the right corresponding enlargements of the HYSCORE signals of weakly coupled  $^{27}\text{Al}$  nuclei and protons, respectively. For each spectrum the sum projections are shown on its top and right. Each spectrum is the sum of two, measured with two different time delays  $\tau$  between the first and second pulse, optimizing the absence of blind spots for weakly and more strongly coupled protons according to Höfer.<sup>[280]</sup> These time delays were set to  $\tau = 102$  ns and  $\tau = 136$  ns (A),  $\tau = 98$  ns and  $\tau = 132$  ns (D),  $\tau = 96$  ns and  $\tau = 128$  ns (F),  $\tau = 88$  ns and  $\tau = 118$  ns (I), and  $\tau = 84$  ns and  $\tau = 112$  ns (J).

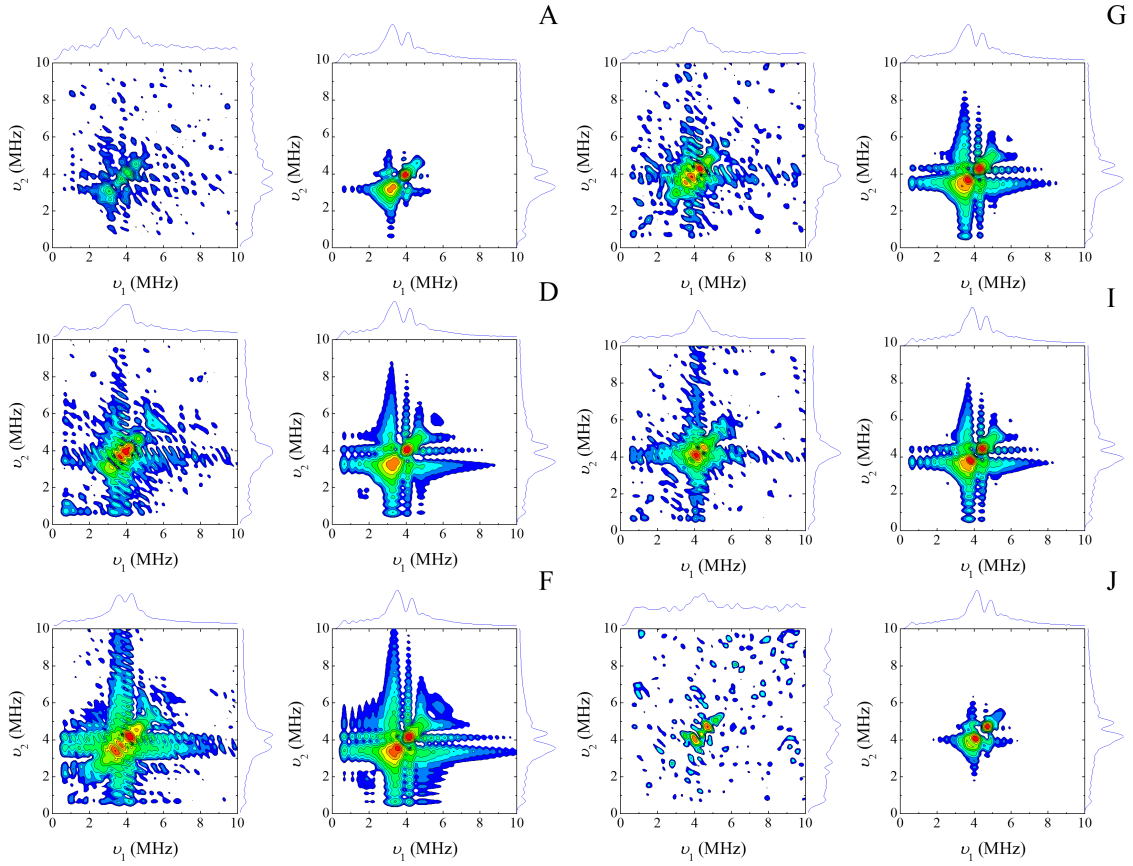


Figure 30: HYSORE signals of sample Al-MIL-53 (left) and the corresponding simulated signals of distant  $^{27}\text{Al}$  nuclei (species A11, right). The spectra were measured at  $T = 6$  K at different field positions A ( $B_0 = 346.8$  mT,  $\tau = 102$  ns), D ( $B_0 = 356.0$  mT,  $\tau = 98$  ns), F ( $B_0 = 367.0$  mT,  $\tau = 96$  ns), G ( $B_0 = 378.8$  mT,  $\tau = 94$  ns), I ( $B_0 = 398.8$  mT,  $\tau = 88$  ns) and J ( $B_0 = 420.0$  mT,  $\tau = 84$  ns) (see Figure 28) and showed signals of distant  $^{27}\text{Al}$  nuclei. The simulations are explained in detail in the text and were conducted with parameters collected in Table 4. Sum projections are shown on the top and right.

Table 4:  $^{27}\text{Al}$  nqi parameters as determined by HYSORE spectroscopy in this work for species A11 at  $T = 6$  K and as determined by Loiseau et al.<sup>[238]</sup> with NMR at room temperature for the calcined MIL-53(Al) in the lp phase, and for the fully hydrated MIL-53(Al) in the np phase.

| Species  | $C_Q$ (MHz) | $\eta$        |
|--|-------------|---------------|
| A11  | $11 \pm 2$  | $0.2 \pm 0.2$ |
| $^{27}\text{Al}$ in MIL-53(Al) (lp) <sup>a</sup> | 8.36        | 0             |
| $^{27}\text{Al}$ in MIL-53(Al) (np) <sup>a</sup> | 10.67       | 0.15          |

<sup>a</sup>data are from Loiseau et al.<sup>[238]</sup>

$a_{\text{iso}}$  is almost zero, which is a reasonable assumption for such weakly coupled nuclei. So, one can estimate with a point dipole approximation (equation (12)) that the distance between Al1 and the NO adsorption species NO1a and NO1b is larger than  $r_{\text{min}} \approx 3.0 \text{ \AA}$ . Therefore, the attribution of species Al1 to a variety of distant Al nuclei including matrix Al nuclei seems probable. Nevertheless, such information does not allow for an unambiguous attribution of species Al1 to the framework metal sites in MIL-53(Al). The adsorption of NO on an impurity phase or near defective Al sites is not excluded by the analysis of the hfi alone.

Interestingly, all measured HYSCORE signals of species Al1 show different local maxima lying on the diagonal. They might be partially attributed to different cross peaks, each correlating a single  $\Delta m_{\text{Al}} = \pm 1$  transitions where the degeneracy is lifted by the nqi, and partially to different powder edge singularities of the central  $m_I = -1/2 \leftrightarrow +1/2$  transition. The interpretation of those signals has been addressed by a simulation protocol applying the spherical-averaging approximation.<sup>[330]</sup> In detail, it was assumed that a variety of distant  $^{27}\text{Al}$  nuclei contribute to the measured signals, having all the same nqi parameters  $C_Q$  and  $\eta$  and small hfi modeled here by constant but small values  $T = 0.1$  MHz and  $a_{\text{iso}} = 0$ . To account for the contribution of many such distant  $^{27}\text{Al}$  nuclei, which number is expected to increase with their distances to the NO adsorption species, sums of powder spectra of this  $^{27}\text{Al}$  species interacting with the NO molecule were calculated. Here, the orientation selection was switched off and the three Euler angles, defining the relative orientation between the hfi and nqi tensors, were treated as uniformly distributed random numbers defined on non-redundant intervals. Six exemplary simulations are shown in Figure 30. They fit the experimental signals at all field positions. The simulation derived nqi parameters are always the same within the errors with  $C_Q = 11 \pm 2$  and  $\eta = 0.2 \pm 0.2$ . This shows that an interpretation of those HYSCORE signals, origination from a single species of distant matrix nuclei and all having the same nqi, is consistent to the data.

Since the same model explains the  $^{27}\text{Al}$  nuclei signals measured at field positions A and J (Figure 28), both species NO1a and NO1b seem to interact with the same kind of matrix  $^{27}\text{Al}$  nuclei species Al1. Finally, the EPR derived nqi parameters fit to the NMR derived nqi parameters as determined for the np phase of MIL-53(Al) at room temperature<sup>[238]</sup> (Table 4), indicating that species Al1 is the  $^{27}\text{Al}$  nucleus at the framework metal site of the np phase of MIL-53(Al). Therefore, both species NO1a and NO1b can be attributed to NO species, adsorbed on the np phase of MIL-53(Al). This observation is consistent to the EPR study of the NO loaded sample Al/Cr-MIL-53, using  $\text{Cr}^{3+}$  as a paramagnetic probe (appendix D.2). It also indicates that all NO is adsorbed on the np phase at  $T = 6$  K.

From the HYSCORE experiments one can conclude that neither species NO1a nor NO1b interacts with  $^{27}\text{Al}$  in its first coordination sphere. Nevertheless, all HYSCORE spectra show long ridges distributed around the proton Larmor frequency  $\nu_{\text{H}} \approx 15$  MHz in the first quadrant (Figures 29 and 31). Three kind of ridges can be identified according to their shifts to higher frequencies along the diagonal: A less extended ridge crosses the diagonal at the proton Larmor frequency  $\nu_{\text{H}} \approx 15$  MHz and is attributed to a proton

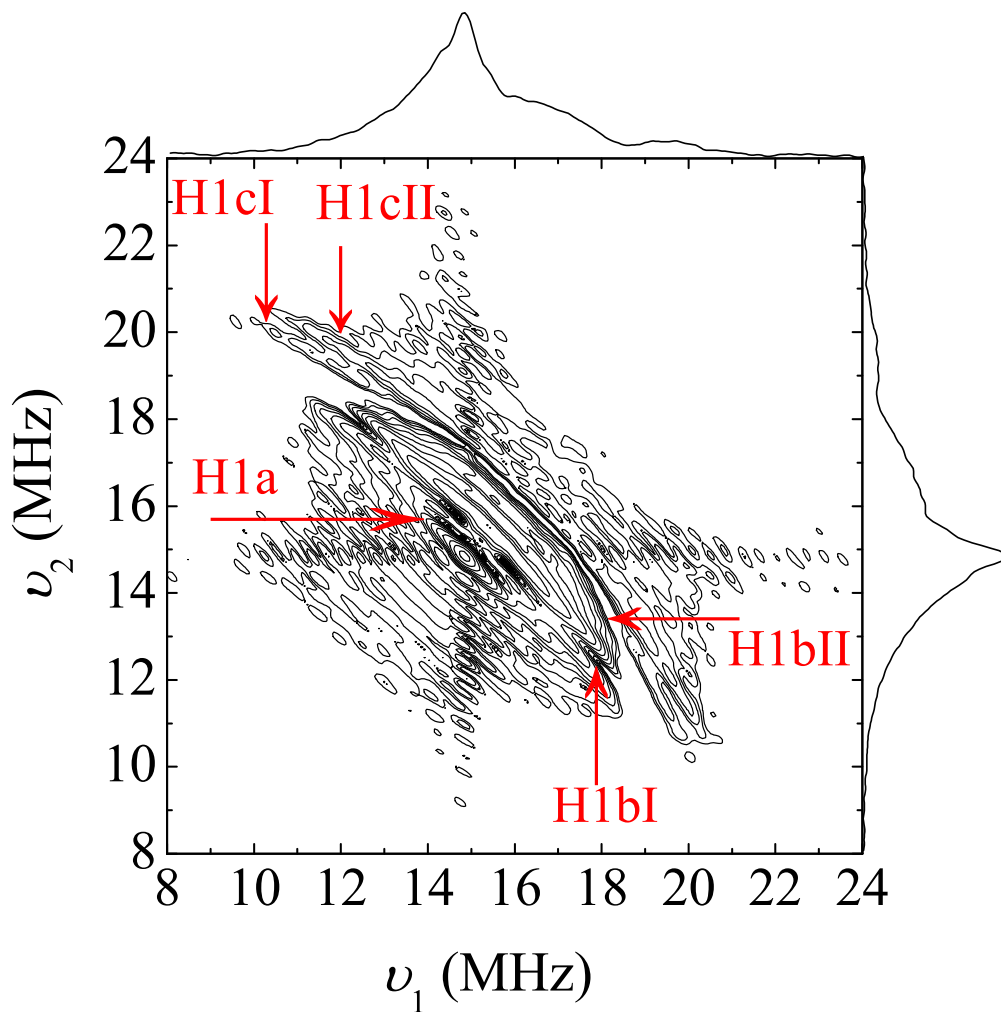


Figure 31: HYSCORE spectrum of sample Al-MIL53a showing the signals of the five different proton species H1a , H1bI, H1bII, H1cI and H1cII. The spectrum was measured at  $T = 6$  K at a magnetic field  $B_0 = 348.6.0$  mT. It is the sum of two spectra measured with different time durations  $\tau = 102$  ns and  $\tau = 134$  ns. Sum projections are shown on the top and right.

Table 5: Simulation derived hfi parameters (equation (10)) of various proton species observed in HYSCORE spectra of sample Al-MIL-53 measured at  $T = 6$  K. The parameter  $T_{\min}$  is an experimental derived lower bound for the corresponding hfi parameter  $T$ .

| Proton species     | $a_{\text{iso}}$ (MHz) | $T$ (MHz)        | $\rho$           |
|--------------------|------------------------|------------------|------------------|
| H1a                | $< 3^{\text{a}}$       | $< 1.4$          | $-^{\text{b}}$   |
| H1bI               | $-4.6 \pm 0.4$         | $4.4 \pm 0.4$    | $0.49 \pm 0.15$  |
| H1bII              | $-1.6 \pm 0.6$         | $5.1 \pm 0.4$    | $0.34 \pm 0.1$   |
| Proton species     | $A_x$ (MHz)            | $A_z$ (MHz)      | $T_{\min}$ (MHz) |
| H1cI <sup>c</sup>  | $-10.9 \pm 0.35$       | $16.6 \pm 3.8$   | $9.2 \pm 1.4$    |
| H1cII <sup>c</sup> | $-13.05 \pm 0.25$      | $13.95 \pm 0.65$ | $9.0 \pm 0.3$    |

<sup>a</sup>in magnitude, <sup>b</sup>not resolved, <sup>c</sup>only the relative sign between  $A_x$  and  $A_z$  was determined experimentally, meaning that the given signs might be actually inverted. The third principal value  $A_y$  was not resolved.

species called H1a (Figure 31). Going to higher frequencies the next kind of ridges are attributed to a proton species called H1b whereas the kind of proton signals crossing the diagonal at highest frequencies are attributed to a proton species named H1c (Figure 31). It will turn out that species H1b comprises two protons H1bI and H1bII whereas at least two protons H1cI and H1cII contribute to species H1c, as it is indicated in Figure 31.

In the following, the HYSCORE signals of the three proton species H1a, H1b and H1c will be analyzed in more detail.

The signals of proton species H1a have the following properties: They almost cross the proton Larmor frequency on the diagonal, show the smallest extension perpendicular to the diagonal, are visible at all field positions A to J and show no significant orientation selection (Figures 29 and 31). From the maximal distance of the H1a ridge (Figure 31) to the anti-diagonal through the proton Larmor frequency one can estimate that species H1a comprises protons with dipolar hfi coupling constants smaller than  $T_{\max} = 1.4$  MHz (Table 5).<sup>[331]</sup> Thus, the protons contributing to species H1a are indicated to have distances to the NO molecule larger than  $r_{\min} = 3.8$  Å, as one can derive from the point-dipole approximation (equation (12)) Consequently, this species is attributed to distant matrix protons of the MIL-53(Al) material interacting with both NO adsorption species NO1a and NO1b.

The signals of the proton species H1b are present in HYSCORE spectra measured at the field positions A to I but not at position J (Figure 28). Thus, they are attributed to protons, interacting only with the NO adsorption species NO1a. These signals are rather complex. They show a quite broad distribution parallel to the diagonal  $\nu_2 = \nu_1$  and fan out into at least two well separated ridges at their high hfi ends (Figure 31). This indicates either a significant orthorhombicity of the hfi tensor of a single proton species or contributions of more than one proton species to the signal of H1b. This observation is illustrated at the best by the HYSCORE signal measured at the field position A (Figure 29a), where mainly crystal orientations with a magnetic field almost parallel to the  $y$ -direction of the NO1a g-tensor contribute. This strong orientation selection results from the large  $^{14}\text{N}$  hfi in the g-tensors  $y$ -direction, which shifts the corresponding resonance of the  $m_{\text{N}} = 1$  EPR

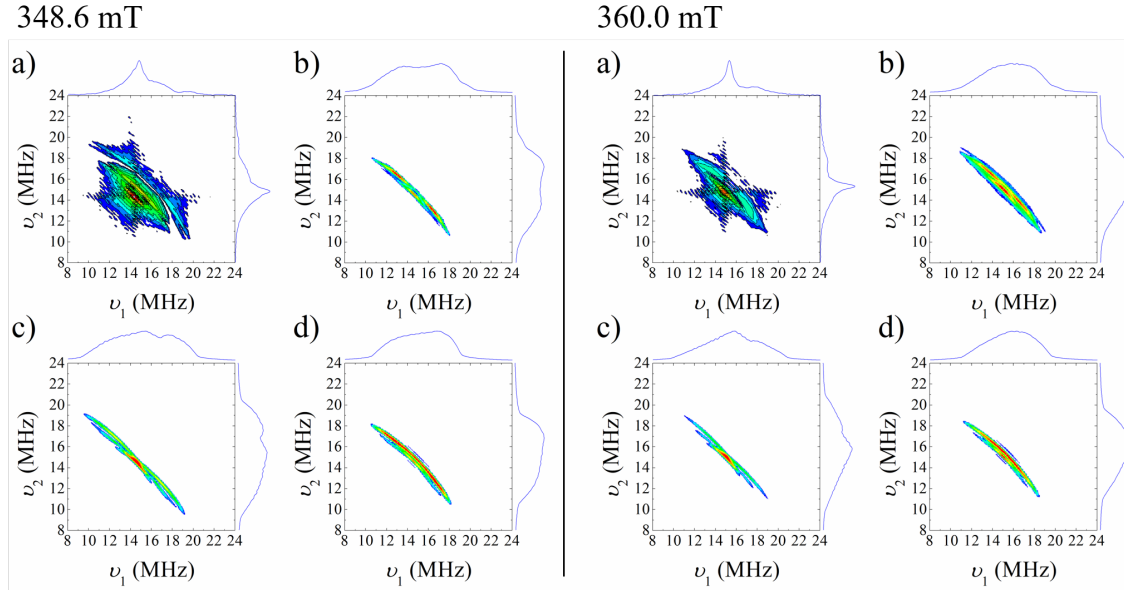


Figure 32: HYSORE spectra of sample Al-MIL-53 (a), measured at  $T = 6$  K,  $B_0 = 348.6$  mT (left) and  $B_0 = 360.0$  mT (right). They are the sum of two and three different spectra, respectively measured with different inter-pulse delays  $\tau$  for blind spot compensation. The simulations (b) are the sums of the simulated signals of the proton species H1bI (c) and H1bII (d) switching of any orientation selection. Sum projections are shown on the top and right.

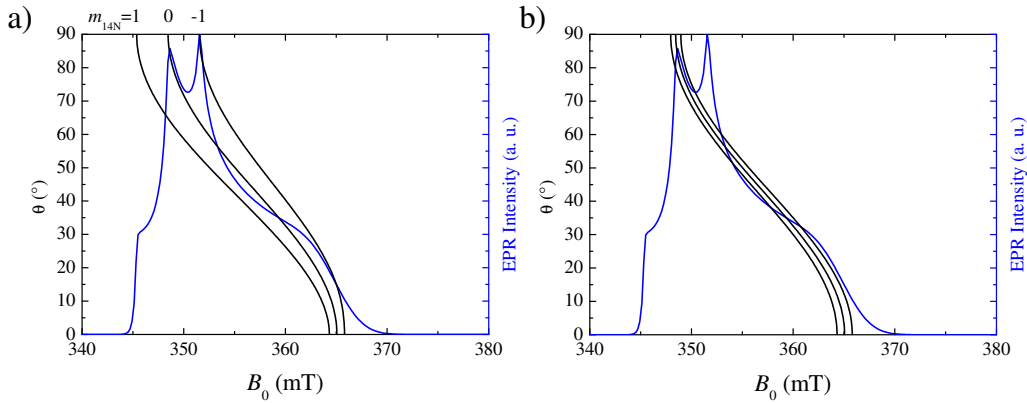


Figure 33: Exemplary simulated absorption powder spectrum of nitric oxide at X-band frequency (blue) together with the  $\theta$  vs. resonance field dependency of all three  $m_{14N} = 1, 0, -1$  transitions (black) in the  $y, z$ -plane (a) and  $x, z$ -plane (b). Here,  $\theta$  is the angle between the magnetic field and the  $g$ -tensors principal  $z$ -direction. The black lines relate a specific magnetic field  $B_{\text{res}}$  to the angle  $\theta$  of spin packets which transitions match the mw frequency at the magnetic field  $B_{\text{res}}$ .

transition to the low field edge of the NO1a powder spectrum, as illustrated in Figure 33. At that field position two well separated ridges, attributed to species H1b, are resolved (Figure 29a). This proves that no more than two proton species contribute to the signal of species H1b. The HYSCORE signals of species H1b show a large orientation selection with varying magnetic field, indicating that not a large variety but rather less proton species like one or two, with well defined orientations relative to the NO molecule, contribute (Figure 29).

Unfortunately, extensive orientation selective simulations of all measured signals of species H1b, varying the hfi principal values and Euler angles of one or two proton species, did not lead to unique and satisfying agreements between the experimental and simulated signals at magnetic field positions A to I. The reason for this failure might be a corresponding large number of hfi tensor parameters in case that two protons contribute and a significant distribution of the hfi parameters. Also, in case of the presence of only one proton species contributing to H1b, its possible orthorhombicity of the hfi tensor combined with some inhomogeneous distribution of the hfi parameters, might have prevented the determination of the full hfi tensor.

For the mentioned reasons a determination of the orientation of the hfi tensors of one or maybe two proton species, contributing to H1b, was not successful. To derive at least the corresponding hfi principal values to some precision, the following protocol was used:

For almost all experimental HYSCORE signals of species H1b, two distinct ridges are resolved at their outer endings but overlap in regions near the diagonal (Figure 31). Each of those resolved ending parts of a ridge have been fitted by a straight line in the square frequency spectrum according to equation (30) (see also subsection 2.2.3). In this way, the magnitudes of two hfi principal values and their relative signs have been attributed to each of the two resolved ridge parts of each HYSCORE signal of species H1b. The corresponding errors of those principal values have been estimated by the variation of the applied straight line fit. It was assumed that each of such pair of hfi principal values belongs to the hfi tensor of one proton species. At least four different hfi principal values have been determined and even more values might be present but not resolved due to a distinct uncertainty in the hfi parameters. Thus, it can be concluded that more than one proton contribute to species H1b. Taking into account the HYSCORE spectrum at the lowest field position A, as it was discussed above, this analysis of the HYSCORE signal of species H1b shows that two protons contribute most significantly to H1b, which are called H1bI and H1bII.

In a next step a little script was written, which derives all possible combinations of the hfi principal values that belong to those two protons and which are consistent to the set of pairs of hfi principal values determined at each field position within certain errors. From the analysis of the dataset, the hfi parameters have been determined for both species H1bI and H1bII as summarized in Table 5. The negative isotropic hfi constants  $a_{\text{iso}}$  (Table 5) indicate spin polarization of the hydrogen's s-orbitals by the electron spin density at the NO. Corresponding simulations without orientation selection are shown exemplarily for the HYSCORE spectra measured at  $B_0 = 348.6$  mT and  $B_0 = 360$  mT in Figure 32.

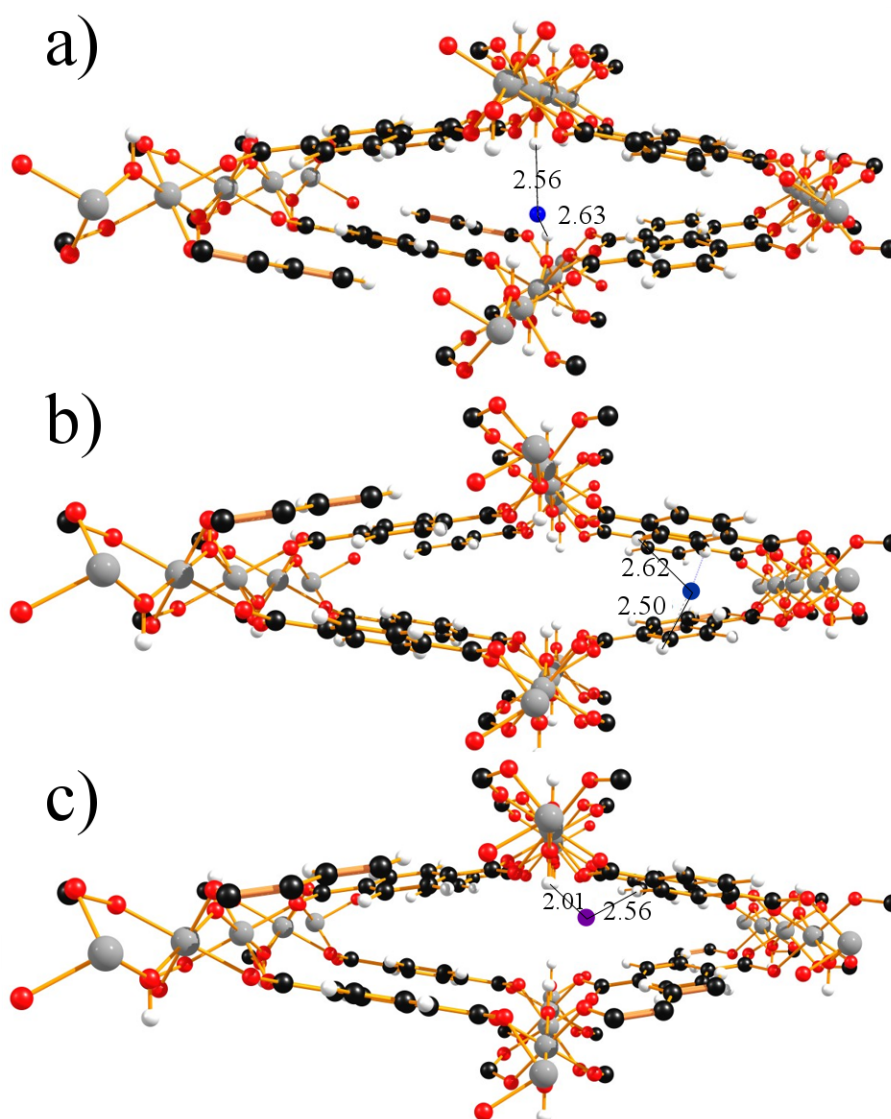


Figure 34: Schematic structures illustrating qualitatively a possible position of the NO1a NO molecule (blue in a and b, purple in c) in the np structure of MIL-53,<sup>[1]</sup> as it is indicated by the HYSORE data. For case a, where species H1c does not interact with NO1a, the NO molecule might sit in the middle of the channel between two metal-oxygen chains (a). If it is true that some protons of H1c interact with NO1a (case b), a structure might be possible, where the NO interacts with the aromatic ring of the bdc ligand as in (b). Figure (c) shows a position, where NO1b might interact with two different protons at the same time. The distances to neighbored protons, which might be H1bI and H1bII (a,b) or H1cI and H1cII (c), are shown. In (b) the distances to the nearest protons belonging possibly to H1cI or H1cII are not shown. Atoms are colored in white (H), black (C), red, purple (O) and gray (Al).



The HYSCORE spectra measured at the field positions A to J show distinctly the signal of the proton species H1c. Thus, H1c comprises protons interacting with the NO adsorption species NO1b. It cannot be ruled out that protons, interacting with the NO adsorption species NO1a, contribute likewise to the signal of species H1c. The HYSCORE signals of species H1c cover a horn shaped area as it is typical for species with orthorhombic hfi tensors (Figures 29, 31).<sup>[274]</sup> Nevertheless, a straight line fit of the borders of that horn shaped area in the square frequency plot using equation (30) still enables the determination of some hfi principal values.<sup>[274]</sup> Several spectra of species H1c resolve two distinct ridges edging the horn shaped area, as they are denoted in Figure 31 with H1cI and H1cII. Their analysis using equation (30) attribute to both ridges the hfi principal values  $A_x$  and  $A_z$  as they are summarized in Table 5. Since those two pairs have four well distinguished hfi principal values, the presence of at least two distinct proton species H1cI and H1cII, contributing to H1c, is indicated. For both proton species a third hfi principal values with even larger magnitude, than the two determined hfi values have, is indicated by the horn like shape of the H1c HYSCORE signals. But its determination is hindered by the bad signal resolution. Nevertheless, a lower bound for the dipolar hfi parameter  $T$  might be obtained by the formula  $T_{\min} = \frac{(A_z - A_x)}{3}$  which is for both protons H1cI and H1cII  $T_{\min} \approx 9$  MHz.

As discussed above, the nqi of the signal of the distant  $^{27}\text{Al}$  nuclear species A11 indicates that species NO1a and NO1b interact with the inner surface of the np phase of MIL-53. Unfortunately, it was not possible to derive unambiguously from the HYSCORE data distinct structural models for species NO1a and NO1b. But as a proof of principle the nitrogen or oxygen atom of the NO molecule was put virtually into the np framework of MIL-53<sup>[1]</sup> using the program Chemcraft 1.8. Then, its position was varied until its distances to the next neighbored protons were consistent to the approximated HYSCORE derived proton distances. The further discussion of the observed HYSCORE signals might distinguish two cases. In *case a* one assumes that no proton contributing to species H1c interacts with the NO adsorption species NO1a. In *case b* some protons contributing to species H1c might interact with NO1a.

*Case a:* From the dipolar hfi constants  $T$  of the protons H1bI and H1bII (Table 5), distances to NO1a of about  $r_{\text{NO-H}} = 2.6 \pm 0.1 \text{ \AA}$  and  $r_{\text{NO-H}} = 2.5 \pm 0.1 \text{ \AA}$  can be estimated, respectively (equation (12)), within a point-dipole approximation. The magnitude of those estimated proton distances excludes the possibility that NO1a is adsorbed at an aromatic ring of the bdc ligand in the np phase. The reason for this are two opposing bdc ligands in the np phase that are quite close to each other. They have a distance of about  $r_{\text{bdc-bdc}} \approx 3.6 \text{ \AA}$ .<sup>[1]</sup> Thus, the spatial density of the bdc ligand protons is so high in the np region between the stacked bdc ligands that an NO molecule, adsorbed at an aromatic ring, would have more than two protons neighbored within a radius of  $r = 2.6 \text{ \AA}$ . Thus, additional protons should have been detected by HYSCORE spectroscopy. This is assumed in *case a*. Therefore, only a structure model, where the NO molecule is in the center of the np phase channel, sitting between both metal-oxygen planes as illustrated in Figure 34a, can hold for species NO1a. The two protons H1bI and H1bII are both from two  $\mu_2$ -(OH) groups of

two opposite metal-oxygen chains. Other protons have distances larger than  $r_{\min} = 3.8 \text{ \AA}$  and should contribute to proton species H1a, and also the next nearest  $^{27}\text{Al}$  nucleus is at a distance of  $r_{\text{Al-N}} \approx 3.0 \text{ \AA}$  and should therefore contribute to the signal of the distant Al species Al1. In this scenario the experimental observed proton species H1cI and H1cII interacting with the NO adsorption species NO1b might indicate a structural model as it is illustrated schematically in Figure 34c. The *case a* seems reasonable, since a similar scenario was observed for  $\text{CO}_2$  adsorbed in MIL-53(Cr),<sup>[260]</sup> where  $\text{CO}_2$  molecules are also located in the centre of the narrow pore, interacting with the  $\mu_2\text{-(OH)}$  groups. It was proposed that this interaction pulls both  $\mu_2\text{-(OH)}$  groups toward each other due to the formation of an electron donor-acceptor complex between the oxygen and the carbon and a weak quadrupolar interaction between the  $\text{CO}_2$  and the proton, triggering by that way the lp to np transition of the MOF during the  $\text{CO}_2$  adsorption.<sup>[260]</sup> Since we have observed by  $\text{Cr}^{3+}$  EPR also an lp to np transition during cooling of an NO loaded MIL-53 (see appendix section D.2), similar mechanisms, namely the interaction of species NO1a with the  $\mu_2\text{-(OH)}$  groups might explain the shift of the corresponding transition temperature to higher values compared to the non-loaded activated MOF. That dispersion forces can significantly affect structural transition kinetics was recently shown for the DUT-8(Ni) material.<sup>[332]</sup>

*Case b:* If some of the protons, which contribute to the HYSCORE signal of species H1c, interact with the NO adsorption species NO1a and not only with species NO1b, it might be possible that NO1a interacts with the aromatic ring of a bdc ligand as it is illustrated in Figure 34b. In the model in Figure 34b two protons of two opposed bdc ligands are at distances to the NO molecule of about  $r_{\text{NO-H}} = 2.6 \text{ \AA}$  and  $r_{\text{NO-H}} = 2.5 \text{ \AA}$ , respectively, and might be identified with the protons H1bI and H1bII. Two other protons are at distances  $r_{\text{NO-H}} = 1.6 \text{ \AA}$  and  $r_{\text{NO-H}} = 2.2 \text{ \AA}$  (not indicated in Figure 34b) which roughly translate, according to equation (12), to dipolar hfi coupling constants in the order of  $T = 19 \text{ MHz}$  and  $T = 7.5 \text{ MHz}$ . Hence, these protons might contribute to the species H1c. In the exemplary model shown in Figure 34b, all other protons are at distances  $r_{\text{NO-H}} > 3.8 \text{ \AA}$  and should contribute to the signal of the protons species H1a. The next neighbored  $^{27}\text{Al}$  nucleus has a distance of  $r_{\text{NO-Al}} = 4.5 \text{ \AA}$  and contributes therefore to species Al1a of distant Al nuclei.

As pointed out, in both cases some of the protons belonging to species H1c must interact with the weakly bound NO adsorption species NO1b, since the HYSCORE spectrum at position J (Figure 28) shows the signal of H1c. For this species it was estimated, based on the HYSCORE data, that the anisotropic hfi is of the order or even larger than  $T_{\min} \approx 9 \text{ MHz}$ . Since the small g-values of the NO adsorption species NO1b indicates a weak interaction with the surface, this interaction might be a hydrogen bonding between the oxygen of NO1b and protons of the MOF framework. A comparable large dipolar hfi parameter of  $T \approx 7.65 \text{ MHz}$  has been reported for a hydrogen of an NOHA substrate interacting with the NO of a Ferrous-NO heme center via a hydrogen bond.<sup>[333]</sup> The fact that at least two protons contribute to species H1, might reflect the presence of several non-equivalent proton sites in the MIL-53 material, comprising the proton of the  $\mu_2\text{-(OH)}$  group

bridging the  $\text{Al}^{3+}\text{O}_6$  octahedra and those of the bdc ligands. Hydrogen bonds between the NO1b and both kind of protons might be possible, even at the same time for a single NO molecule. This is illustrated in Figure 34c. Here, an NO position is suggested, where the NO1b molecule can interact via two hydrogen bonds with a proton of a  $\mu_2$ -(OH) group and a proton of the bdc ligand at the same time. It might be also possible that more than one NO adsorption species contribute to NO1b, interacting with different single protons via hydrogen bonds.

### 4.3 Summary of chapter four

Temperature-dependent CW EPR and low temperature two-pulse ESE field sweep as well as HYSCORE experiments were performed with NO loaded samples of MIL-53(Al) and its  $\text{Cr}^{3+}$  doped variant, strongly indicating the adsorption of NO on the np phase of this MOF at low temperatures. Both, the signal of desorbed NO gas at temperatures above  $T \approx 120$  K and that of adsorbed NO at temperatures below  $T \approx 85$  K were detected. The analysis of the temperature dependences of the EPR intensities of adsorbed and desorbed NO proved that the EPR detected adsorbed NO does not condense directly from the gas phase of desorbed NO and thus the adsorption of NO inside the pores of MIL-53 is strongly indicated. Various spectroscopic parameters of the EPR signal of the adsorbed NO species NO1a as its g-tensor principal values, its temperature-dependent linewidth, its  $^{14}\text{N}$  hfi as well as the absence of any resolved  $^{27}\text{Al}$  hfi in the CW EPR spectrum indicate the adsorption of that EPR detected species at non-metallic sites. By two-pulse ESE field sweep EPR, an additional NO adsorption species NO1b was detected at  $T = 10$  K. Low temperature HYSCORE experiments at various field positions resolved signals of distant  $^{27}\text{Al}$  nuclei and protons, interacting with the EPR detected NO adsorption species. The nqi principal values of the distant  $^{27}\text{Al}$  species could be derived from the experimental data and equals those derived by NMR for the np phase. In particular, the HYSCORE results confirm that the EPR detected NO species NO1a and NO1b interact with non-metallic sites of the MIL-53(Al) framework. The HYSCORE spectra further resolve at least four different non-equivalent non-distant protons. The hfi principal values of two protons, interacting with NO1a, could be derived from the analysis of their HYSCORE signals, and are consistent to a position of the NO molecule in the middle of the np phase, interacting with protons of two  $\mu_2$ -(OH) groups belonging to opposite metal-oxygen chains. For each of the two proton species, interacting with NO1b, only two hfi principal values could be derived from their HYSCORE signals. Their unusually large magnitudes indicate hydrogen bonds between those protons and the NO molecule. In total, the presented EPR results indicate a weak physisorption of NO at non-metallic sites of the np phase of MIL-53(Al), strongly interacting with the protons of the framework, presumably altering the structural transition kinetics.

## 5 NO adsorption species in MIL-100(Al), a MOF material with CUS

The previous chapter presented detailed CW and pulsed EPR experiments that revealed the weak physisorption of NO in the np phase of MIL-53 at low temperatures, with protons but no aluminum atoms in its first coordination sphere. The next case study investigates the aluminum based MOF MIL-100(Al), which possess  $\text{Al}^{3+}$  CUS. Such  $\text{Al}^{3+}$  sites are known to be strong Lewis acid sites<sup>[119,198,201–203]</sup> which makes trivalent aluminum based MOFs particularly interesting for heterogeneous catalysis applications. Among MOFs they are favored for industrial applications<sup>[334]</sup> since their strong metal-oxygen bonds<sup>[201,335]</sup> makes them extraordinarily thermally and chemically stable and they are low in price.<sup>[201]</sup> Consequently, there is a special need for the spectroscopic characterization of Lewis acid sites in such MOFs.

Common methods for the characterization of Lewis acid sites in MOFs are IR spectroscopy, temperature-programmed desorption, or the determination of the isosteric heats of adsorption of certain probe molecules.<sup>[204]</sup> Particularly, the Lewis acidity of the CUS in some MIL-100(M) (M = trivalent metal) MOFs was investigated, using CO, pyridine and acetonitrile as IR active probe molecules.<sup>[202,205–207]</sup> But unfortunately, those methods alone do not allow for the unambiguous determination of the characterized Lewis acid sites nature. Attributions to other sites rather than the framework CUS, like to defects or extra-framework species, cannot be excluded in certain cases. The usage of NO as an EPR active probe for the characterization of the Lewis acidity of  $\text{Al}^{3+}$  CUS might overcome this disadvantage of the aforementioned methods. EPR of adsorbed NO was used successfully for the characterization of Lewis acid sites in various zeolites.<sup>[92,198,200]</sup> The EPR detected  $^{14}\text{N}$  hfi of an NO molecule adsorbed at a CUS characterizes its Lewis acidity as explained in subsection 2.3.1. In case of aluminum based MOFs, one might resolve in addition by EPR the hfi of the  $^{27}\text{Al}$  nucleus of the corresponding site, interacting with the unpaired electron spin of the NO molecule, since this nucleus has a nuclear spin  $I = 5/2$  and 100 percent natural abundance. A detailed spectroscopic determination of this hfi combined with ab initio quantum chemical calculations might enable the reliable attribution of the EPR characterized  $\text{Al}^{3+}$  site to a defined open metal site species.

The present chapter presents a case study for this approach. The present investigation combines CW-EPR and high resolution pulsed EPR methods with DFT calculations, applied to the model system MIL-100(Al)<sup>[239]</sup> that is loaded with NO.

A thermal treatment of the material MIL-100(Al) removes water molecules coordinating to the  $\text{Al}^{3+}$  ions producing the CUS.<sup>[201]</sup> The two giant cavities of MIL-100(Al) with free diameters of about 2.5 nm and 2.9 nm<sup>[336]</sup> might be used as a host for encapsulated metal complexes for further catalytic applications.<sup>[337]</sup> Apart from its potential applications in catalysis this MOF might be also suitable as drug carrier since it induces no significant *in vitro* cell toxicity.<sup>[338]</sup> In this context, it is worth to mention that its iron based variant MIL-100(Fe) adsorbs large amounts of the medically relevant (see chapter 1) molecule NO at room temperature due to the chemisorption of NO at the  $\text{Fe}^{3+}$  CUS.<sup>[178,223]</sup> The NO

Table 6: Experimentally derived  $g$ -tensor and  $^{14}\text{N}$  hfi principal values for various NO adsorption species in the MIL-100(Al) MOF

| NO adsorption species | $g_x$                      | $g_y$                      | $g_z$                        | $ A_x^{14\text{N}} (\text{MHz})$ | $ A_y^{14\text{N}} (\text{MHz})$ | $ A_z^{14\text{N}} (\text{MHz})$ |
|-----------------------|----------------------------|----------------------------|------------------------------|----------------------------------|----------------------------------|----------------------------------|
| NO2a                  | $1.997 \pm 0.003$          | $1.997 \pm 0.003$          | $1.909 \pm 0.003^{\text{a}}$ | $14 \pm 8^{\text{b}}$            | $86 \pm 3$                       | $20 \pm 6^{\text{b}}$            |
| NO2b <sup>c</sup>     | $1.993 \pm 0.005$          | $1.993 \pm 0.005$          | $1.945 \pm 0.005$            | - <sup>d</sup>                   | $84 \pm 12$                      | - <sup>d</sup>                   |
| NO2c                  | $1.995 \pm 0.006$          | $1.995 \pm 0.006$          | $1.88 \pm 0.01^{\text{e}}$   | - <sup>d</sup>                   | $86 \pm 24$                      | - <sup>d</sup>                   |
| NO2d                  | $1.97 \pm 0.03^{\text{f}}$ | $1.97 \pm 0.03^{\text{f}}$ | $1.4...1.88^{\text{f,g}}$    | - <sup>d</sup>                   | $100 \pm 80^{\text{f}}$          | - <sup>d</sup>                   |

<sup>a</sup>as determined by selective two-pulse ESE field sweep EPR,<sup>[242]</sup> <sup>b</sup>as determined by Davies ENDOR spectroscopy, <sup>c</sup>as determined at  $T = 45$  K, <sup>d</sup>not resolved. <sup>e</sup>This value is derived from an analysis of the HYSORE spectra measured at various fields, <sup>f</sup>as roughly estimated from two-pulse ESE field sweep spectra. <sup>g</sup>The species NO2d might comprise a variety of weakly bound NO with  $g_z$  principal values inhomogeneously distributed in the given range.

release can be triggered in humid conditions by adsorption of water.<sup>[178]</sup> In a combined IR and CW EPR study it was shown by Barth and Mendt et al. that the MIL-100(Al) MOF binds NO much weaker than the MIL-100(Fe).<sup>[223]</sup> In that study EPR detects for NO loaded samples of MIL-100(Fe) only the signal of desorbed NO whereas no EPR signal of any NO adsorption species was observed. This was reasoned by a high local density of paramagnetic species or a total integer spin of possible  $\text{Fe}^{3+}$ -NO complexes. An understanding of the different adsorption strengths of both MIL-100 materials on an atomic scale is also addressed by the work presented in this chapter, which gives a comprehensive insight into the microscopic and electronic structure of the NO- $\text{Al}^{3+}$  complex in the MIL-100(Al) at low temperatures.

The content of this chapter is published in two papers.<sup>[223,242]</sup> The first four sections will summarize the results obtained by different EPR methods, namely CW EPR, two-pulse ESE field sweep EPR, HYSORE spectroscopy and Davies ENDOR spectroscopy. The fifth section covers the results obtained by the DFT calculations. The sixth section discusses those results in more detail. The last section summarizes this chapter. Experimental and computational details can be found in the appendix F.

## 5.1 CW-EPR

An X-band CW EPR spectrum of sample Al-MIL-100, measured at 8 K, is shown in Figure 35. It shows a signal which has been attributed to a superposition of three NO adsorption species called NO2a, NO2c and NO2d according to a comprehensive analysis of CW and pulsed EPR data (see also the following sections in this chapter).<sup>[223,242]</sup> Interestingly, the  $g_{x,y}$  powder edge singularity of this signal features a super hyperfine (shf) splitting with more than 13 resolved lines (Figure 35), which cannot be explained by the  $^{14}\text{N}$  hfi alone. That large number of shf lines have been attributed to an additional hfi with a neighbored  $^{27}\text{Al}$  nucleus, here called  $^{27}\text{Al}$  species Al2a.<sup>[223,242]</sup> This attribution is confirmed

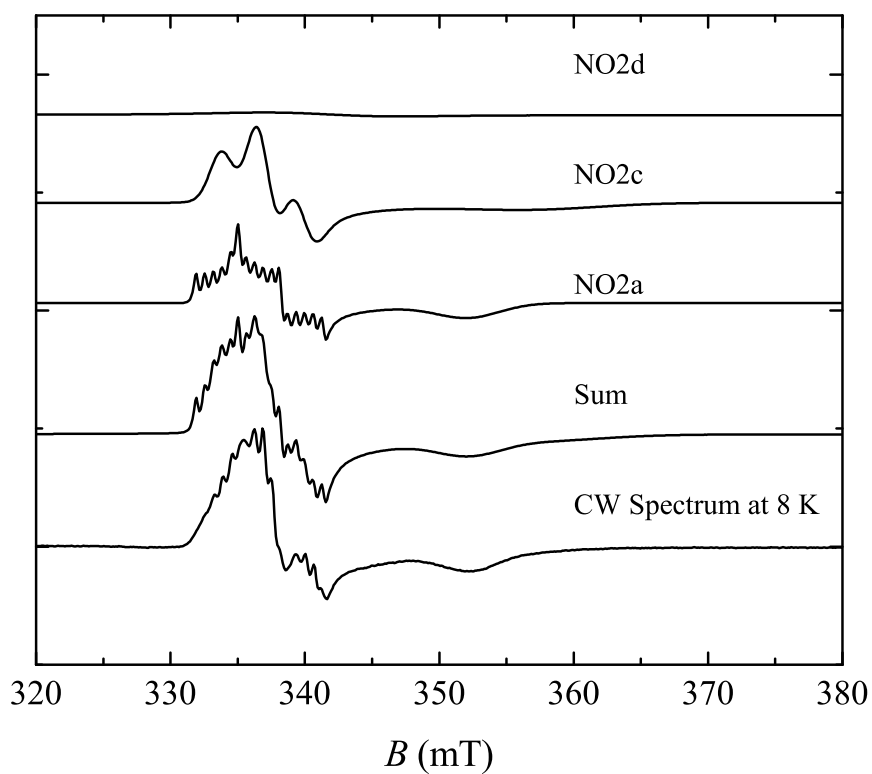


Figure 35: X-band EPR spectrum of sample Al-MIL-100 measured at  $T = 8$  K (bottom). The simulated signals (above) are the sum of the signals of species NO2a, NO2c and NO2d with parameters given in Tables 6 and 7. The signal of species NO2d is not resolved by CW EPR, but shown here with the same relative amount as determined by two-pulse ESE field sweep spectroscopy with non-selective pulses (see section 5.2).

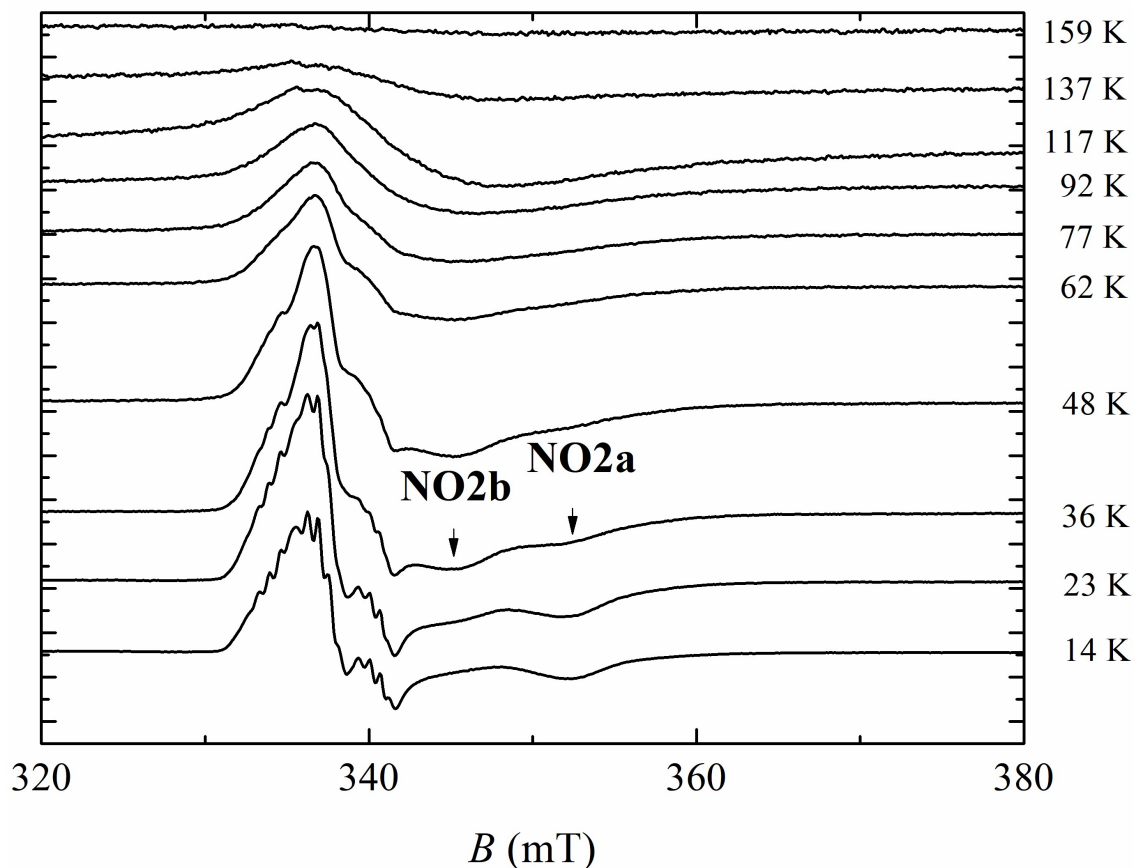


Figure 36: CW EPR spectra of sample Al-MIL-100 measured at different temperatures during heating (shown on the right). The EPR spectra have been normalized with respect to experimental parameters and multiplied with the temperature to correct for the Curie's law.

by a simulation of this signal (Figure 35), assuming a hfi of species NO2a with the  $^{27}\text{Al}$  nuclear species Al2a with full  $^{14}\text{N}$  and  $^{27}\text{Al}$  hfi tensors derived by the pulsed EPR experiments (see following sections and Table 7). The restricted resolution of the CW spectrum forbids the determination of the full Al2a and  $^{14}\text{N}$  hfi tensors,<sup>[223]</sup> but the ENDOR and HYSCORE studies presented below achieved this target with certain precision.<sup>[242]</sup> Nevertheless, temperature-dependent CW EPR measurements of sample Al-MIL-100 gave first and interesting insights into the binding of the NO adsorption species in MIL-100(Al).<sup>[223]</sup>

In Figure 36 EPR spectra of sample Al-MIL-100 are shown, which were measured at different temperatures during heating. Interestingly, above  $T = 14$  K another signal occurs at  $B_0 \approx 345$  mT, which is most likely the  $g_z$  powder edge singularity of a second NO adsorption species NO2b (Table 6).<sup>[223]</sup> Its origin will be discussed in more detail in section 5.6.

The temperature-dependent intensity  $I_{\text{NO2a-d}}$  of the sum EPR signal of the species NO2a to NO2d (Figure 37a) was determined by the integration of the corresponding baseline corrected spectra and corrected for the Curie law by the multiplication with the temperature. It starts growing with decreasing temperature below  $T = 160$  K indicating the formation of adsorbed NO species. It reaches a maximum at  $T \approx 115$  K. Interestingly,

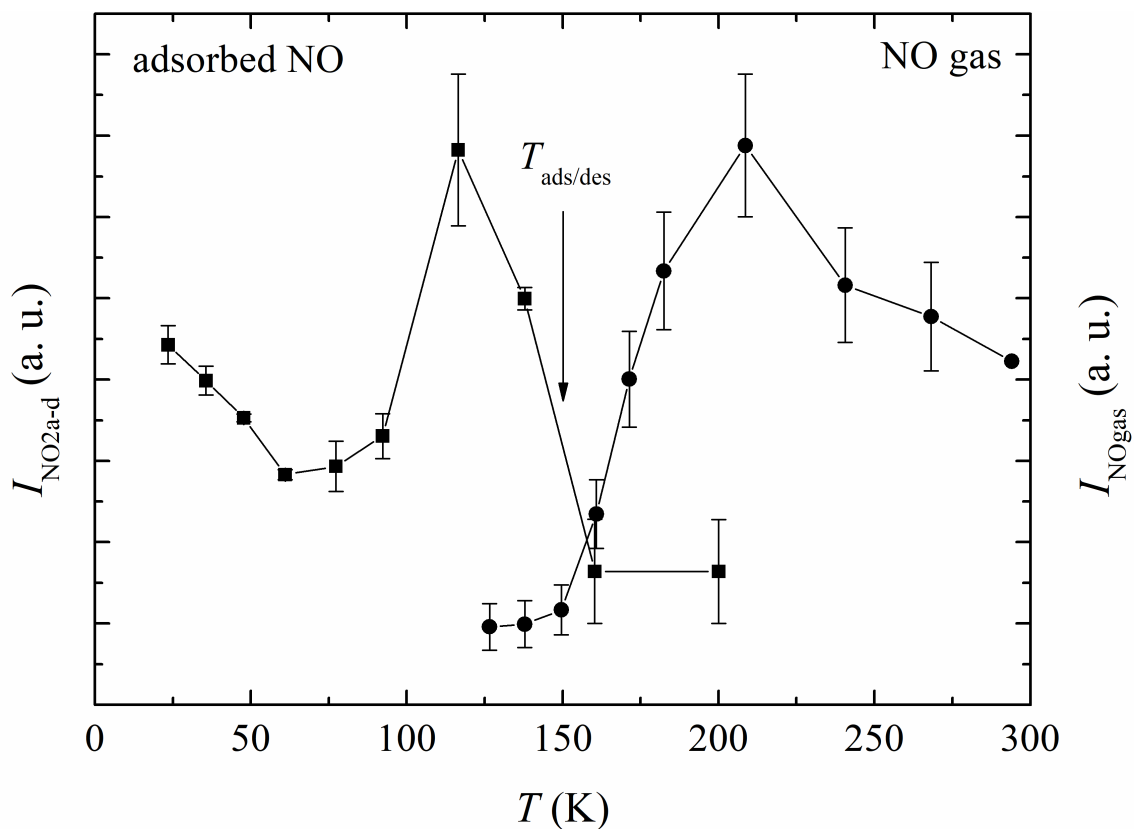


Figure 37: The temperature-dependent intensity  $I_{\text{NO}_{2\text{a-d}}}$  (left) of the sum CW EPR signal of the NO adsorption species in sample Al-MIL-100, determined by the double integration of the baseline corrected experimental spectra and multiplied with the temperature to correct for the Curie law. The temperature-dependent intensity  $I_{\text{NO}_{\text{gas}}}$  of the EPR signal of desorbed NO in this sample is also shown (right - same as in Figure 24). This figure was first published by Barth, Mendt et al.<sup>[223]</sup>



below this temperature  $I_{\text{NO}_{2\text{a-d}}}$  decreases with decreasing temperature, which is not the expected behavior. It reaches a minimum at  $T \approx 70$  K. This range corresponds to the range  $65 \text{ K} < T < 90 \text{ K}$  where the formation of diamagnetic  $(\text{NO})_2$  in nanometre-sized pores of the mesoporous silica MCM-41 was observed by other authors.<sup>[339]</sup> Thus, this unexpected decrease of the EPR intensity  $I_{\text{NO}_{2\text{a-d}}}$  might be explained by the inseting formation of diamagnetic  $(\text{NO})_2$  which shifts the equilibrium of the reaction  $2 \text{NO}_{2\text{a-d}} \leftrightarrow (\text{NO})_2$  toward the product. The presence of a large fraction of such EPR silent phase is also indicated by the rough EPR derived amount of species NO2a to NO2d at  $T = 27$  K which is  $N_{\text{NO}} = 0.07 \pm 0.03 \mu\text{mol}$ .<sup>[223]</sup> This is only a fraction of the total amount of NO in this sample (see appendix A.3, Table A.1) The subsequent growing of  $I_{\text{NO}_{2\text{a-d}}}$  with decreasing temperature below  $T = 70$  K (Figure 37a) might indicate the formation of a third weakly bound NO adsorption species like species NO2d. The latter interpretation seems reasonable since for sample Al-MIL-53 the weakly adsorbed NO species NO1b formed at temperatures  $T < 100$  K. And as for the MIL-53(Al), one should expect for the MIL-100(Al) the formation of similar NO adsorption species weakly interacting with the organic part. As shown for the MIL-53(Al) MOF in the previous chapter, the presence of such a species NO2d is indicated for sample Al-MIL-100 by the two-pulse ESE field sweep experiments that are presented in the next section.

Below  $T = 23$  K, the experimental signal intensity  $I_{\text{NO}_{2\text{a-d}}}$  decreased again as it is indicated by the EPR spectrum at  $T = 14$  K in Figure 36. Detailed mw power dependent measurements showed no indication that this an effect of saturation. Here we can only speculate if this decrease in intensity is a real effect or the result of an inaccurate temperature measurement at such low temperatures, were small absolute errors in the temperature determination have a large relative impact on the normalized EPR intensity. We therefore omit a discussion of  $I_{\text{NO}_{2\text{a-d}}}$  at such low temperatures.

## 5.2 Two-pulse ESE field sweep EPR

Figure 38 shows two two-pulse ESE field sweep spectra of sample Al-MIL-100 which were measured at  $T = 6$  K. One was conducted with non-selective pulses (16 ns long  $\frac{\pi}{2}$ -pulses) and an inter-pulse time delay of  $\tau = 140$  ns (Figure 38a) which resembles the experimental conditions of the HYSORE experiments covered in the next section. The second was performed with selective pulses (100 ns long  $\frac{\pi}{2}$ -pulses) and an inter-pulse time delay  $\tau = 1200$  ns (Figure 38b) which reflects the experimental conditions of the Davies ENDOR experiments discussed later. These spectra show signals which can be attributed to three different NO adsorption species NO2a, NO2c and NO2d.<sup>[242]</sup> The field sweep spectrum with the larger inter-pulse delay  $\tau = 1200$  ns (Figure 38b) shows most significantly a signal which can be attributed to the NO adsorption species NO2a that was already resolved by CW EPR (see previous section 5.1). The spectral shape of the field sweep spectrum with the small inter-pulse delay  $\tau = 140$  ns (Figure 38a) deviates distinctly from the former, indicating the contribution of additional NO adsorption species which signals might have been suppressed in the former spectrum by the long time  $\tau = 1200$  ns due to their short phase memory times.

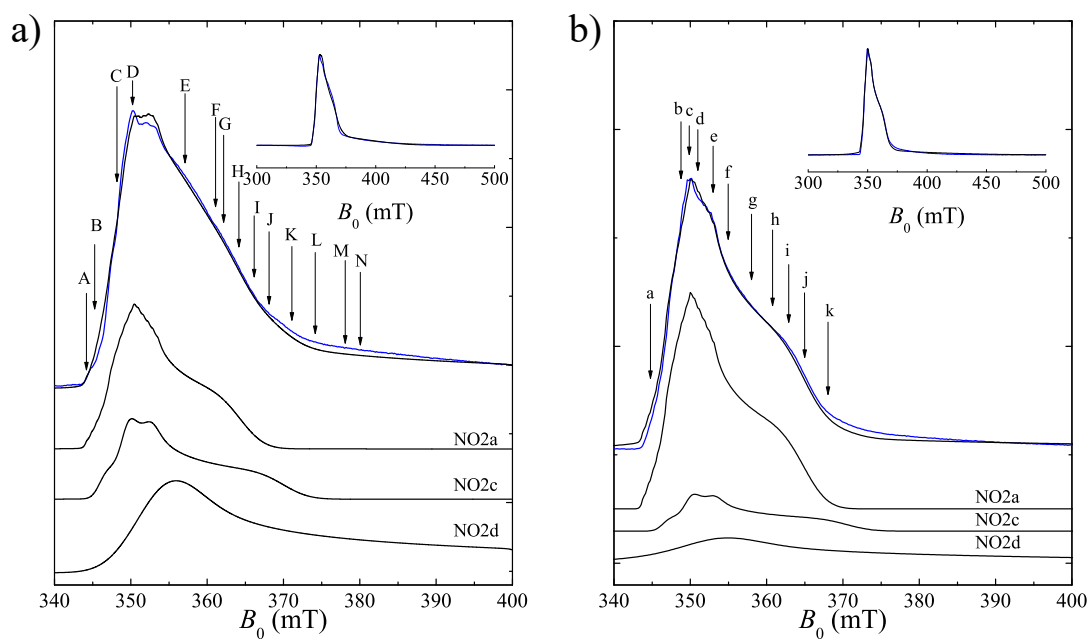


Figure 38: Two-pulse ESE field sweep spectra (blue) of sample Al-MIL-100 measured with non-selective pulses and an inter-pulse time delay  $\tau = 140$  ns (a) and selective pulses and an inter-pulse time delay  $\tau = 1200$  ns (b) at a temperature  $T = 6$  K. The insets show the corresponding spectra in a larger field range. Below the spectra the simulated signals of the NO adsorption species NO2a, NO2c and NO2d (black) are shown in descending order (see Table 6 and Table 7 for simulation parameters). Their sum (black) is shown, overlapping with the corresponding experimental spectra. The positions A to N label magnetic fields, where HYSORE experiments were conducted whereas the positions a to k indicated magnetic fields, where Davies ENDOR experiments were performed. This figure was first published in Mendt et al.<sup>[242]</sup>

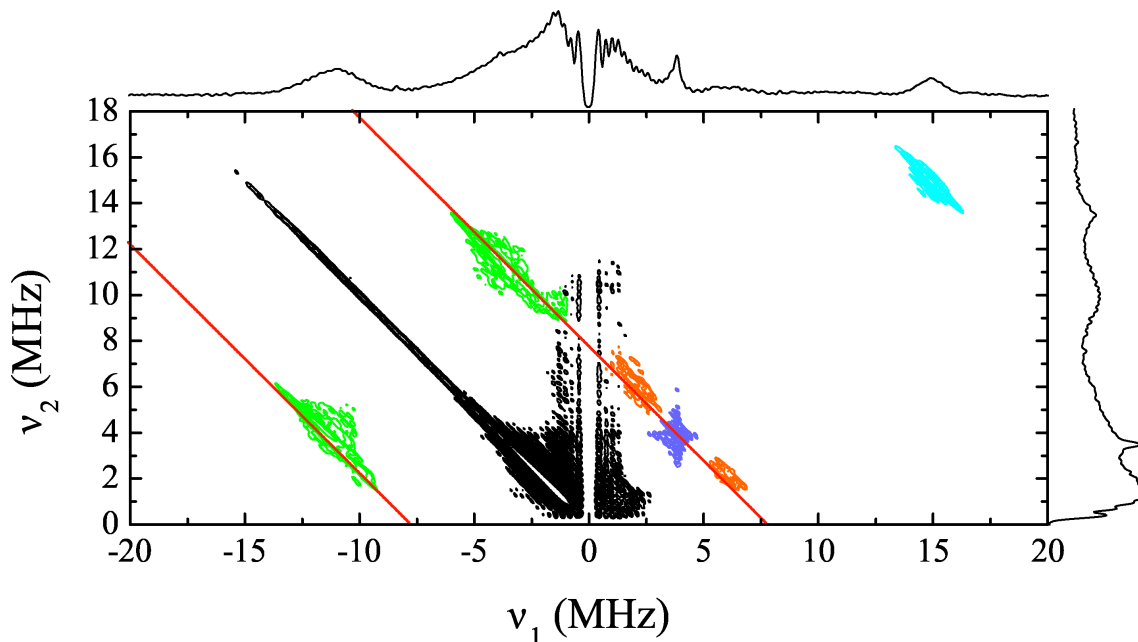


Figure 39: Representative HYSCORE spectrum of sample Al-MIL-100, measured at  $B_0 = 350.0$  mT (position D in Figure 38a) and  $T = 6$  K. It is the sum of two spectra, measured with time delays  $\tau = 92$  ns and  $\tau = 128$  ns between the first two pulses to address different blind spots of the  $^{27}\text{Al}$  and  $^1\text{H}$  signals. The spectrum shows signals of three different  $^{27}\text{Al}$  species, here called Al2a (green), Al2b (orange) and Al2c (purple) as well as weak couplings to protons (cyan). The black signals on the diagonal in the IV<sup>th</sup> quadrant might be caused by an incomplete inversion of the  $\pi$ -mixing pulse.<sup>[268]</sup> The red lines are the anti-diagonals  $\nu_2 = \nu_1 \pm 2\nu_{\text{Al}}$ . Sum projections are shown on the top and right. This figure was first published in Mendt et al.<sup>[242]</sup>

The spectrum with short  $\tau$  shows a pronounced spectral feature in the magnetic field range  $366 \text{ mT} < B_0 < 374 \text{ mT}$  which was attributed to the  $g_z$  powder edge singularity of an NO adsorption species NO2c.<sup>[242]</sup> Its  $g_{x,y}$  values could not be determined directly from the ESE field sweep spectrum since in the corresponding spectral region the signal of species NO2a dominates. Nevertheless, those values could be estimated by CW EPR (see section 5.1). The two-pulse ESE field sweep spectrum shows further a broad descending tail of signal intensity at higher magnetic fields (Figure 38a), which was attributed to a third NO adsorption species NO2d<sup>[242]</sup> and that was not resolved by CW EPR. The corresponding small and inhomogeneously distributed  $g_z$  values are indicative for a large variety of weakly physisorbed NO contributing to species NO2d,<sup>[301]</sup> indicating its interaction with the organic part of the MOF. The corresponding range of g-tensor principal values have been roughly estimated by simulations (Figure 38a). The experimental derived g-tensor principal values of the various NO adsorption species are collected in Table 6.

### 5.3 HYSCORE spectroscopy

HYSCORE spectra of sample Al-MIL-100 have been measured at  $T = 6$  K at the magnetic field positions A to N as they are indicated by arrows in Figure 38a. All spectra are shown in the appendix F.1<sup>[242]</sup> and a representative spectrum is displayed in Figure 39. It

Table 7: Experimentally derived hfi and nqi parameters describing the interaction of various  $^{27}\text{Al}$  nuclear species with different NO adsorption species. The first three parameters describe the principal values of the hfi tensor as defined in equation (10). The Euler angles  $\alpha$  and  $\beta$  are defined as used by the MatLab toolbox EasySpin.<sup>[294]</sup> They describe the rotation which transforms the g-tensor frame to the hfi tensor frame. The last two parameters describe the nqi tensor as defined in equation (15).

| $^{27}\text{Al}$ species                | $a_{\text{iso}}$ (MHz) | $T$ (MHz)          | $ \rho $           | $\alpha$ ( $^\circ$ ) | $\beta$ ( $^\circ$ ) | $C_Q$ (MHz)              | $\eta$                     |
|---|------------------------|--------------------|--------------------|-----------------------|----------------------|--------------------------|----------------------------|
| Al2a                                    | $14.7 \pm 1.7$         | $3.4 \pm 0.5$      | $< 0.5^{\text{a}}$ | $90 \pm 30$           | $50 \pm 10$          | $_{\text{b}}$            | $_{\text{b}}$              |
| Al2b                                    | $-4.2 \pm 0.6$         | $1.4 \pm 0.6$      | $_{\text{b}}$      | $_{\text{b}}$         | $55 \pm 35$          | $2.8 \pm 2.0$            | $_{\text{b}}$              |
| Al2c                                    | $_{\text{c}}$          | $< 0.3^{\text{c}}$ | $_{\text{d}}$      | $_{\text{d}}$         | $_{\text{d}}$        | $5.2 \pm 0.8^{\text{c}}$ | $0.26 \pm 0.26^{\text{c}}$ |
| $^{27}\text{Al@MIL-100(Al)}^{\text{e}}$ | -                      | -                  | -                  | -                     | -                    | 1.3 ... 5.5              | 0.04 ... 0.30              |

<sup>a</sup>within the resolution of Davies ENDOR spectroscopy, <sup>b</sup>not resolved, <sup>c</sup>as a mean value of a large number of different and distant nuclei, <sup>d</sup>not resolved, since this species probably comprises a large number of different and distant nuclei, <sup>e</sup>NMR derived values from Haouas et al.<sup>[201]</sup>

demonstrates the high resolution of this method which unravels signals of different nuclear species into two frequency dimensions (see subsection 2.2.3). A ridge crossing the point  $(\nu_{\text{H}}, \nu_{\text{H}})$  with  $\nu_{\text{H}} = 14.90$  MHz being the proton Larmor frequency (Figure 39 cyan ridge) was attributed to distant proton species. Signals of this species are visible in HYSORE spectra measured at all observer positions. These signals resolve no significant orientation selection, indicating that a variety of proton species contribute to them. This prevents an unambiguous determination of their hfi parameter. Nevertheless, the maximum extension of the proton signals ridges at the observer positions A to N (Figure 38) allows for the estimation of the maximal proton hfi value being  $A_{\text{max}} = 3.7$  MHz.

In addition, the HYSORE spectra show signals extending along the anti-diagonals:

$$\nu_2 = -\nu_1 \pm 2\nu_{\text{Al}} \quad (64)$$

which have consequently been attributed (see equation (29)) to  $^{27}\text{Al}$  nuclei with the Larmor frequency  $\nu_{\text{Al}}$ , interacting with the different NO adsorption species (Figure 39).

One  $^{27}\text{Al}$  nuclear species show its signal in the fourth quadrant (Figure 39), indicating a large hfi parameter  $|A| > 2|\nu_{\text{Al}}|$ .<sup>[279]</sup> This  $^{27}\text{Al}$  nuclear species is called Al2a. Its signal was only resolved by HYSORE spectroscopy at the observer positions A to I but not J to N (Figure 38a, and figures in the appendix F.1) Even oversampling the HYSORE spectrum at the position J by setting the time steps  $\Delta t_1 = \Delta t_2 = 12$  ns and increasing the signal to noise ratio in this way (see appendix F.1 Figure F.17) does not resolve any signal of this species. This verifies the attribution of this species to an  $^{27}\text{Al}$  nucleus interacting with the NO adsorption species NO2a.<sup>[242]</sup> Detailed spectral simulations of the orientation selectively measured HYSORE signals and ENDOR spectra presented in the next section allowed for the determination of the species Al2a full  $^{27}\text{Al}$  hfi tensor as it is given in Table 7.<sup>[242]</sup> Particularly, the signals measured at the positions A and I show a pronounced orientation selection allowing for the determination of the Al2a hfi Euler angles  $\alpha$  and  $\beta$

(Figures F.1 and F.16). The third Euler angle  $\gamma$  was not resolved due to the almost axial symmetric  $^{27}\text{Al}$  hfi tensor. At the position A only the  $^{14}\text{N}$  hfi  $m_I = +1$  EPR transition in the y-direction of the g-tensors principal axis frame of species NO2a contributes to the HYSCORE signal of this species, leading to a strong orientation selection at that observer position (see Figure 33). In Figure 40, two HYSCORE spectra, measured at position C with different  $\tau$  values, are shown exemplarily together with the simulated signals of species Al2a. The  $\tau$ -dependent modulations of the protons and Al2a signals reflect  $\tau$ -dependent blindspots inherent to the HYSCORE pulse sequence, as they are described for protons by Höfer<sup>[280]</sup> and illustrated for  $^{27}\text{Al}$  with strong hfi in Figure 12.

The Al2a HYSCORE signals show a significant distribution along the anti-diagonals described by equation (64). The Al2a ENDOR signals described in the next section have broad linewidths. These broadenings indicate significant distributions of the hfi parameters, particularly of the Al2a isotropic hfi parameter  $a_{\text{iso}}^{\text{Al2a}}$ . This has been considered by using for the spectral simulations, of both the HYSCORE and ENDOR signals, the same linewidth model assuming Gaussian distributions for  $a_{\text{iso}}^{\text{Al2a}}$  and the  $^{14}\text{N}$  hfi principal values  $A_x^{14\text{N}}$  and  $A_z^{14\text{N}}$  with standard deviations  $\Delta a_{\text{iso}}^{\text{Al2a}} = 2$  MHz and  $\Delta A_x^{14\text{N}} = \Delta A_z^{14\text{N}} = 1.25$  MHz, respectively. That  $^{14}\text{N}$  hfi broadening considers the linewidths of the Al2a ENDOR signals but has only minor influence on the Al2a HYSCORE signals. The  $^{14}\text{N}$  nqi was not resolved in the Al2a HYSCORE and ENDOR signals and was therefore set to zero for spectral simulations. To account for further experimental inhomogeneous broadenings the excitation band width was set to a large value of  $\Delta\nu = 62.5$  MHz in all spectral simulations of the Al2a HYSCORE signal.

For the Al2a signal only its central transition ridge, correlating the  $^{27}\text{Al}$   $\left(\nu_{-\frac{1}{2},\frac{1}{2}}^\alpha, \nu_{-\frac{1}{2},\frac{1}{2}}^\beta\right)$  frequencies, was observed by HYSCORE spectroscopy (Figures 39 and 40).<sup>[242]</sup> But the  $^{27}\text{Al}$  nucleus has a spin  $I = \frac{5}{2}$ . Thus, one would expect additional ridges correlating single quantum (SQ) transition frequencies  $\nu_{m_I, m_I+1}^\alpha$  and  $\nu_{m_I, m_I+1}^\beta$  or even multi quantum (MQ) transitions as they are also resolved by Al2a simulated HYSCORE signals at certain field positions (see for example Figure F.2 in the appendix F.1). But only one additional and less intense ridge was observed in some experimental spectra as indicated by an arrow in Figure 40b, which is indicative for cross peaks correlating a SQ and a double quantum (DQ) transition of this species. The absence of other ridges correlating different nuclear transitions can be understood by their large first order nqi broadening, which does not effect the nuclear central transition (equation (16)).<sup>[242,268,279]</sup> This has been justified by exemplary simulations<sup>[242]</sup> with an  $^{27}\text{Al}$  nqi determined for MIL-100(Al) by NMR spectroscopy,<sup>[201]</sup> as shown exemplarily in the appendix F.1 in Figures F.6 and F.8.

In certain spectra the Al2a  $\left(\nu_{-\frac{1}{2},\frac{1}{2}}^\alpha, \nu_{-\frac{1}{2},\frac{1}{2}}^\beta\right)$  ridge splits at its low frequency end into two ridges as one would expect for an orthorhombic hfi (Figure 40b). But, extensive simulations, assuming for the species Al2a an orthorhombic hfi tensor and no additional distribution model for the Al2a hfi parameters, did not lead to a satisfying agreement between the experimental and simulated HYSCORE spectra at all magnetic field positions simultaneously. On the other hand, all experimental HYSCORE signals of species Al2a could be simulated, assuming an axial symmetric Al2a hfi (Table 7) and in addi-

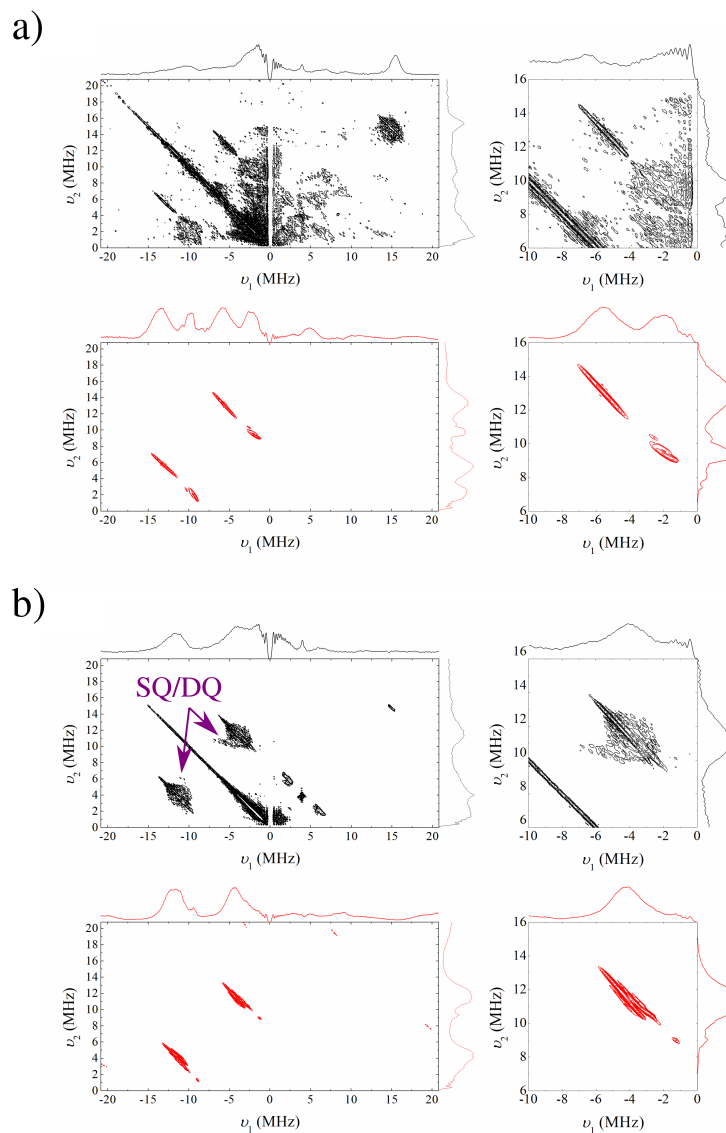


Figure 40: Experimental HYSORE spectra of sample Al-MIL-100 (black) measured at  $B_0 = 348.0$  mT and  $T = 6$  K with inter-pulse delays  $\tau = 92$  ns (a) and  $\tau = 130$  ns (b). Simulated HYSORE signals of species Al2a are shown in red below. Enlargements of the signals are shown on the right. Sum projections are on the top and right. The SQ/DQ label indicates ridges, correlation  $^{27}\text{Al}$  single- and double quantum transitions. This figure was first published in Mendt et al.<sup>[242]</sup>

tion the linewidth model mentioned above, where a Gaussian distribution of the isotropic hfi parameter  $a_{\text{iso}}^{\text{Al2a}}$  was assumed. This model reproduces the observed splitting of the  $\left(\nu_{-\frac{1}{2},\frac{1}{2}}^{\alpha}, \nu_{-\frac{1}{2},\frac{1}{2}}^{\beta}\right)$  ridge of the powder spectrum (40b), as one can understand in the following way: Without any distribution model of the hfi parameters and assuming an axial symmetric hfi tensor, the  $\left(\nu_{-\frac{1}{2},\frac{1}{2}}^{\alpha}, \nu_{-\frac{1}{2},\frac{1}{2}}^{\beta}\right)$  ridge is expected to have two local intensity maxima. One occurs in a region where orientations with angles  $\theta \approx 45^\circ$  between the hfi-tensors  $z$ -principal direction and the external magnetic field contribute. For such orientations the pseudo-secular constant  $B$  is large (equations (21)) and maximizes the modulation depth factor<sup>[268]</sup>  $k = \left(\frac{B\nu_I}{\nu_{\alpha}\nu_{\beta}}\right)^2$ , and therefore the HYSCORE signal intensity in that part of the ridge. A second local intensity maximum of the this ridge might occur at its low frequency end, since here a large number of orientations with angles  $\theta \approx 90^\circ$ , namely all crystals where the magnetic field lies in or near the hfi-tensors  $x, y$ -plane, contribute. The assumed distribution of the isotropic hfi parameter  $a_{\text{iso}}^{\text{Al2a}}$  shifts both intensity maxima parallel to the anti-diagonal described by equation (29). This might explain the splitting of the  $\left(\nu_{-\frac{1}{2},\frac{1}{2}}^{\alpha}, \nu_{-\frac{1}{2},\frac{1}{2}}^{\beta}\right)$  ridge at its low frequency end, since both maxima have different distances to this anti-diagonal.

HYSCORE spectroscopy proves additionally the presence of two other  $^{27}\text{Al}$  species. One is responsible for a signal in the first quadrant indicating weak hfi  $|A| < 2|\nu_{\text{Al}}|$ .<sup>[268]</sup> It is colored in orange in Figure 39. It was attributed to the three  $\left(\nu_{-\frac{3}{2},-\frac{1}{2}}^{\alpha}, \nu_{-\frac{3}{2},-\frac{1}{2}}^{\beta}\right)$ ,  $\left(\nu_{-\frac{1}{2},\frac{1}{2}}^{\alpha}, \nu_{-\frac{1}{2},\frac{1}{2}}^{\beta}\right)$  and  $\left(\nu_{\frac{1}{2},\frac{3}{2}}^{\alpha}, \nu_{\frac{1}{2},\frac{3}{2}}^{\beta}\right)$  ridges of the  $^{27}\text{Al}$  species Al2b.<sup>[242]</sup> The corresponding  $m_I = \pm\frac{5}{2} \leftrightarrow \pm\frac{3}{2}$  transitions might be not resolved due to their larger first order nqi broadening (see equation (16)). The signal of species Al2b was measured at the magnetic field positions B to J but not A and K to N (see Figure 38a).<sup>[242]</sup> Even increasing the signal to noise ratio of the HYSCORE signal at the field position M (see Figure F.22) and oversampling<sup>[268]</sup> the signal by setting  $\Delta t_1 = \Delta t_2 = 12$  ns, does not resolve the signal of species Al2b. Consequently, it can be neither attributed to the NO adsorption species NO2a nor NO2d. Thus, species Al2b must interact with the NO adsorption species NO2c (see subsection 5.2).<sup>[242]</sup>

The hfi and nqi spin Hamiltonian parameters of species Al2b in Table 7 were determined by simulation within certain error ranges.<sup>[242]</sup> Exemplarily, simulations of two experimental Al2b HYSCORE signals, measured at  $B_0 = 348.0$  mT with different inter pulse delays  $\tau$ , are shown in Figure 41. To account for the experimental inhomogeneous broadening an excitation band width of  $\Delta\nu = 37$  MHz was used for the simulations of the Al2b HYSCORE signals.

The nqi parameter  $C_Q$  of species Al2b (Table 7) could be estimated by simulations from the Al2b signals spread perpendicular to the anti-diagonal (equation (64)).<sup>[242]</sup>

Some cross peaks, correlating SQ transitions with MQ transitions of species Al2b, are present in the simulation derived but not in the experimental spectra (Figure 41). The reason for this is most likely a significant first order nqi broadening, which matters for the corresponding measured but not the simulated ridges. Nevertheless, some additional cross

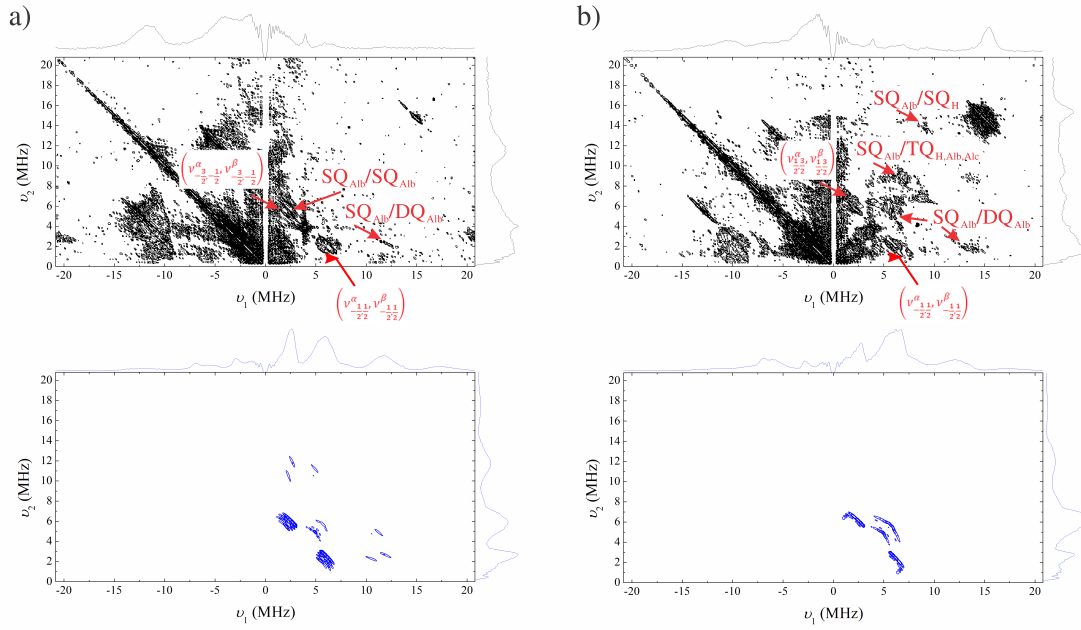


Figure 41: Experimental HYSORE spectra of sample Al-MIL-100 (black) were measured at  $B_0 = 348.0$  mT and  $T = 6$  K with inter-pulse delays  $\tau = 130$  ns (a) and  $\tau = 92$  ns (b) between the first two pulses. In blue, the simulated signal of the  $^{27}\text{Al}$  species Al2b is shown. For the simulations, g-tensor and hfi principal values were used as given in Table 6 and Table 7. Those hfi and nqi Euler angles, which were not determined by simulations, have been arbitrarily set to zero. The labels indicate HYSORE signals correlating SQ, DQ or TQ transitions with the involvement of nuclear frequencies of species Al2b, Al2c and protons (H).



peaks, correlation SQ transitions with DQ transitions, have been measured as indicated by arrows in Figure 41.

The two spectra in Figure 41 show an interesting  $\tau$  dependent behavior. Some spectral features only appear in the spectrum with  $\tau = 92$  ns, where the signal of weakly coupled protons is not suppressed by the  $\tau$  dependent blind spot factor.<sup>[280]</sup> These are namely the ridges at the positions  $(\nu_{1,2}, \nu_{2,1}) \approx (9.1 \text{ MHz}, 13.8 \text{ MHz})$  and  $(\nu_{1,2}, \nu_{2,1}) \approx (6.9 \text{ MHz}, 8.9 \text{ MHz})$  (Figure 41). For the spectrum measured with  $\tau = 130$  ns, the proton signal is suppressed by a blind spot as the just mentioned ridges are (Figure 41). This observation indicates that the first ridge can be attributed to cross peaks, correlating SQ transitions of the Al2b species with SQ transitions of a weakly coupled proton species. This gives direct evidence that some protons are in the vicinity of the species NO2c in addition to the  $^{27}\text{Al}$  species Al2b. But the resolution of this ridge is not good enough in quality for a determination of that proton species hfi, which distinguishes it from the variety of protons contributing to the already discussed HYSCORE signals.

The attribution of the mentioned second ridge is less obvious. Only correlations between nuclear frequencies of different electron spin manifolds are allowed.<sup>[268]</sup> With respect to this, no combinations of nuclear frequencies, belonging to a proton or to the observed  $^{27}\text{Al}$  species, enable an interpretation of that ridge involving only correlations of SQ or DQ transitions.<sup>[242]</sup> Thus, it is most likely that this ridge correlates an Al2b SQ transition with a triple quantum (TQ) transition which frequency is a combination of the Al2b and protons nuclear frequencies as well as the frequency of distant matrix  $^{27}\text{Al}$  nuclei.

The NO adsorption species NO2c interacts with the  $^{27}\text{Al}$  species Al2b, with at least one proton species and with distant matrix  $^{27}\text{Al}$  nuclei, also indicated by the observation of characteristic combination frequencies in the experimental spectra. At all magnetic field positions, signals, hardly extending beyond the spectral region of the  $^{27}\text{Al}$  Larmor frequency  $\nu_{\text{Al}} \approx 4 \text{ MHz}$ , have been observed in the first quadrant.<sup>[242]</sup> Thus, they can be most likely attributed to distant  $^{27}\text{Al}$  matrix nuclei, as it is also justified by spectral simulations (see below). This is the third  $^{27}\text{Al}$  species shown in the exemplary spectrum in Figure 39, which is called Al2c.

As mentioned, the signal of species Al2c was observed at all magnetic field positions A to N (Figure 38a). It follows that Al2c interacts at least with species NO2d. Since at the observer position A the HYSCORE signal of Al2c is quite intense, although the signal of species NO2d is expected to be absent or weak (Figure 38a) and the signal of species NO2c is known to be absent here, the interaction of species Al2c with species NO2a is strongly indicated. As just discussed, an interaction of species NO2c with distant matrix  $^{27}\text{Al}$  nuclei is also suggested by the HYSCORE data.

All HYSCORE spectra of species Al2c are presented in the appendix F.1 in Figure F.25. Interestingly, they show almost no orientation selectivity. This indicates that a variety of  $^{27}\text{Al}$  nuclei contribute to them. Almost all experimental HYSCORE signals of species Al2c show two maxima along the diagonal  $\nu_2 = \nu_1$ , one above the  $^{27}\text{Al}$  Larmor frequency  $\nu_{\text{Al}}$  and one below  $\nu_{\text{Al}}$ , as illustrated for an exemplary spectrum in Figure 42. These signals were simulated with a variant of the well known spherical-averaging approximation,<sup>[330]</sup>

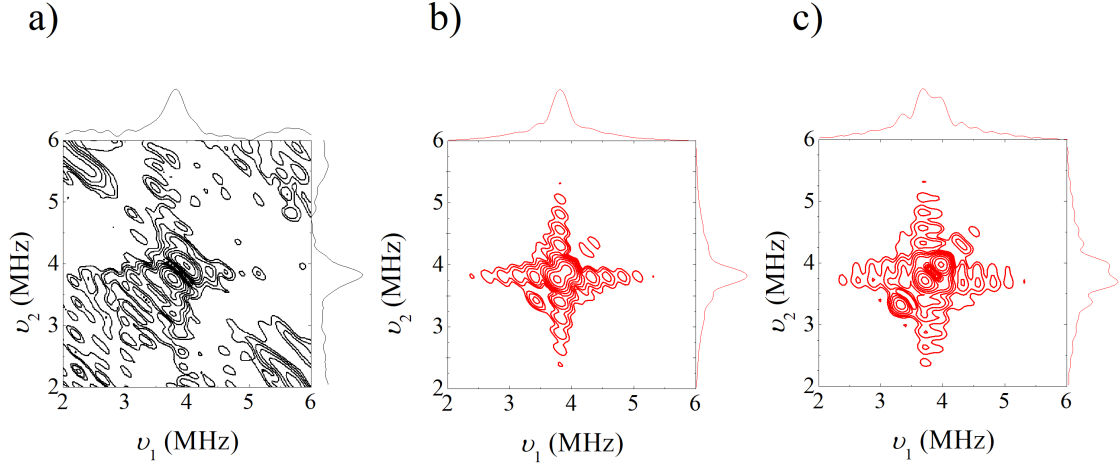


Figure 42: Exemplary HYSORE spectrum (a) of sample Al-MIL-100 measured at  $B_0 = 348.0$  mT and  $T = 6$  K with an inter-pulse delay  $\tau = 92$  ns between the first two pulses. Simulations of species Al2c are shown with nqi parameters  $C_Q = 4.5$  MHz and  $\eta = 0.26$  (b) as well as  $C_Q = 6.0$  MHz and  $\eta = 0.26$  (c). Sum projections are shown on the top and right. This figure was first published by Mendt et al.<sup>[242]</sup>

switching of any orientation selection. It was assumed that the experimental signal can be approximated by a uniform sum of powder spectra running over all relative orientations between the hfi and nqi tensors of a single  $^{27}\text{Al}$  species with defined nqi parameters  $C_Q$  and  $\eta$  and hfi values  $a_{\text{iso}} \approx 0$  MHz and  $T \ll 1$  MHz.<sup>[242]</sup> Hence, those four parameters have been derived by simulations within certain error ranges as given in Table 7. The corresponding upper bound of  $T$  translates into a minimal distance between the NO molecule and the matrix  $^{27}\text{Al}$  nuclei of  $r = 4.1$  Å (equation (12)). The simulation derived nqi parameters of species Al2c are similar to those determined by NMR for  $^{27}\text{Al}$  species in MIL-100(Al) (Tab.7).<sup>[201]</sup> This strongly suggests that Al2c are distant  $^{27}\text{Al}$  nuclei at the framework metal sites in the MOF. The simulation based analysis of the HYSORE signal shows that the maximum of the Al2c HYSORE signal below  $\nu_{\text{Al}}$  is the  $\theta_{\text{nqi}} = 40.4^\circ$  powder edge singularity of the  $\left(\nu_{-\frac{1}{2},\frac{1}{2}}^\alpha, \nu_{-\frac{1}{2},\frac{1}{2}}^\beta\right)$  powder signal, whereas the maximum above  $\nu_{\text{Al}}$  is the corresponding  $\theta_{\text{nqi}} = 90^\circ$  powder edge singularity. Here,  $\theta_{\text{nqi}}$  defines the angle between the external magnetic field and the  $z$ -principal axis of the nqi tensor. As illustrated in Figure 42, the proposed analysis of the experimental Al2c spectra indicate a significant distribution of the parameter  $C_Q$  among all  $^{27}\text{Al}$  nuclei contributing to the species Al2c. To fit the low frequency maximum of the Al2a HYSORE signal a value  $C_Q = 4.5$  MHz had to be adjusted. To fit the corresponding high frequency maximum one has to set  $C_Q = 6.0$  MHz within the proposed simulation model. This distribution of the Al2c nqi parameters might reflect the structural disorder in the MIL-100(Al) material, indicated already by NMR spectroscopy.<sup>[201,239]</sup>

#### 5.4 Davies ENDOR spectroscopy

Orientation selective Davies ENDOR spectra of sample Al-MIL-100, measured at  $T = 6$  K at the field positions a to k (see Figure 38b), are shown in Figures 43 and 44. In all

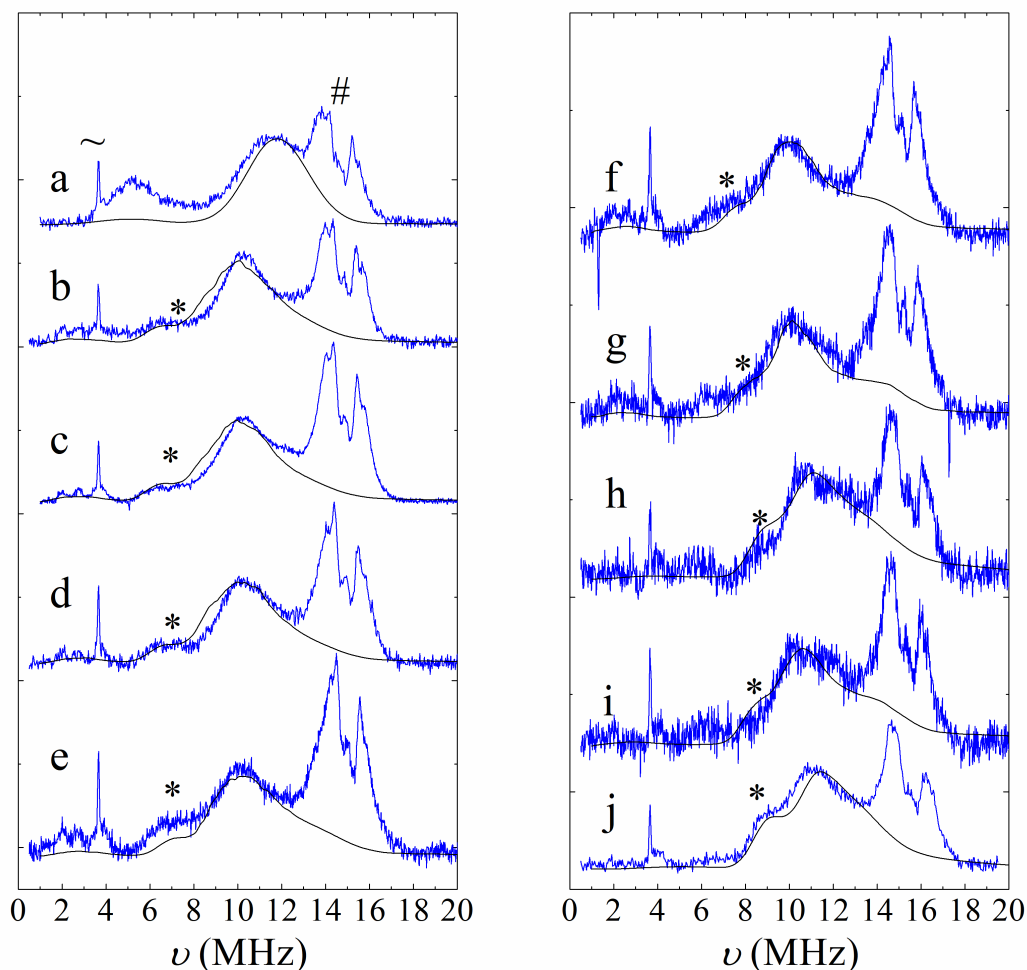


Figure 43: Davies ENDOR spectra of sample Al-MIL-100 (blue) are shown, which have been measured at  $T = 6$  K at magnetic field positions a to j like they are defined in Figure 38b. The corresponding magnetic fields are  $B_0 = 345.0$  mT (a), 348.7 mT (b), 349.8 mT (c), 350.7 mT (d), 352.8 mT (e), 355.3 mT (f), 358.0 mT (g), 360.7 mT (h), 362.9 mT (i) and 365.0 mT (j). The black signals are the simulated ENDOR spectra of the NO adsorption species NO2a interacting with the  $^{27}\text{Al}$  species Al2a. An experimental artifact signal, signals of weakly coupled protons and signals of the NO  $^{14}\text{N}$  are labeled by the symbols  $\sim$ , # and \*. To account for the broad linewidth, each simulated ENDOR spectrum was calculated as sum of 1040 simulated frequency domain signals, for which distinct hfi parameters were assumed to be independently Gaussian distributed random numbers. Namely, the Al2a hfi parameter  $a_{\text{iso}}^{\text{Al}2\text{a}}$  was assumed to be randomly distributed with a standard deviation of  $\Delta a_{\text{iso}}^{\text{Al}2\text{a}} = 2$  MHz. In addition, the  $^{14}\text{N}$  hfi parameters  $A_x^{14\text{N}}$  and  $A_z^{14\text{N}}$  were assumed to be distributed with standard deviations  $\Delta A_x^{14\text{N}} = \Delta A_z^{14\text{N}} = 1.25$  MHz. To account further the inhomogeneous broadened line shape, an mw excitation with of  $\Delta\nu_{\text{mw}} = 60$  MHz as well as an isotropic convolutional Voigtian broadening with a full width at half maximum (FWHM)  $\Delta\nu = 0.16$  MHz were assumed for all simulation.<sup>[242]</sup> This figure was first published by Mendt et al.<sup>[242]</sup>

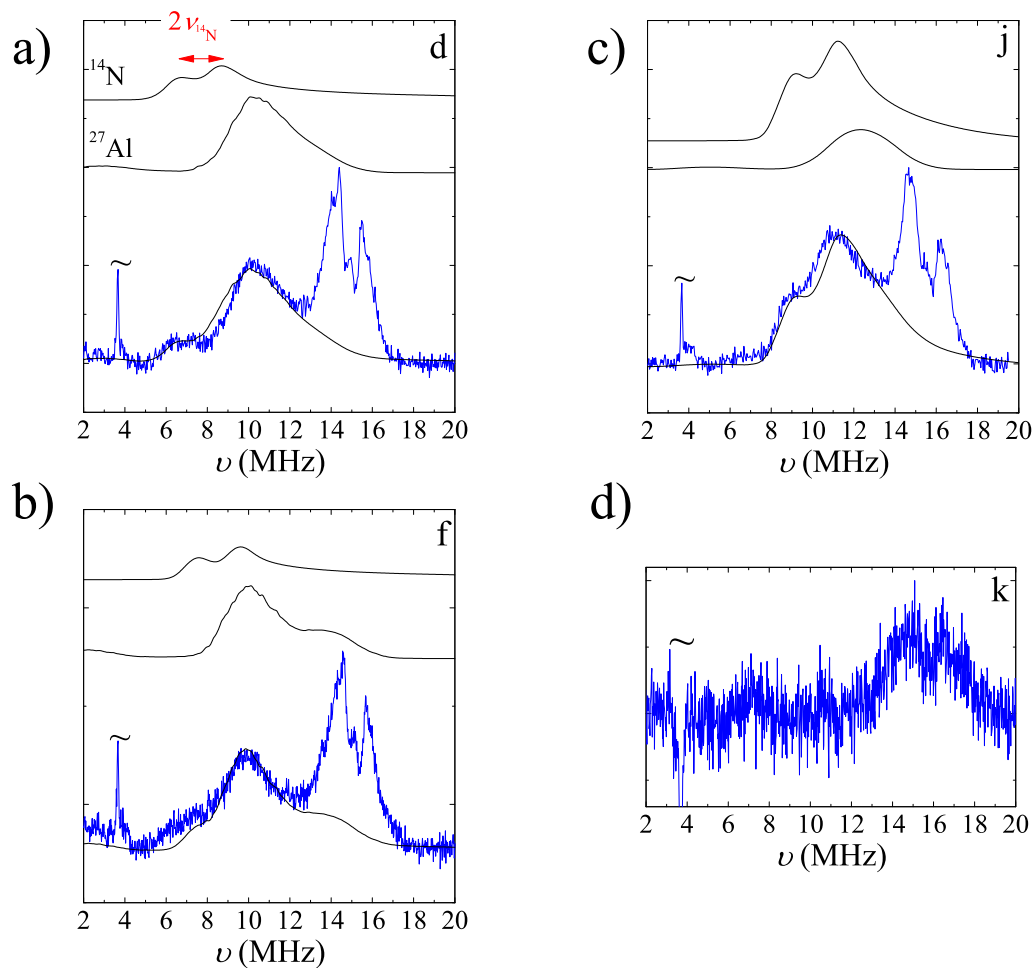


Figure 44: Selected ENDOR spectra of sample Al-MIL-100 (blue) are shown, which have been measured at  $T = 6$  K and at magnetic field positions  $B_0 = 350.7$  mT (a), 355.3 mT (b), 365.0 mT (c) and 368.0 mT (d). On the top right of each subfigure Latin letters are shown, which are the labels defined in Figure 38b. Above, simulated ENDOR signals of the NO  $^{14}\text{N}$  and the Al2a  $^{27}\text{Al}$  nuclei are shown (black). Their sum (black) overlays with the experimental spectra. The symbol  $\sim$  denotes an experimental artifact. This figure was first published by Mendt et al.<sup>[242]</sup>

spectra signals are present, which are symmetrically distributed around the proton Larmor frequency  $\nu_{\text{H}} \approx 15$  MHz. Consequently, they have been attributed to the  $\nu_{\alpha,\beta}^{\text{H}} = \nu_{\text{H}} \pm \frac{A}{2}$  spectral components of weakly coupled protons.<sup>[242]</sup> Those proton signals show almost no orientation selectivity, which indicates that a variety of protons contribute to these signals. This prevents an unambiguous determination of their hfi parameters. Nevertheless, using equations (20) with  $B \rightarrow 0$ , one can estimate for the proton signals in the spectra a to j (Figure 43) a maximal hfi of  $A_{\text{max}} \approx 3.5$  MHz. Thus, this signal is attributed to the same variety of protons observed already by HYSORE spectroscopy. Interestingly,  $A_{\text{max}}$  is larger for the signal measured at the highest field position k (Figure 44) with  $A_{\text{max}} \approx 5.0$  MHz. This might have been not resolved by HYSORE spectroscopy due to a low signal intensity. According to the two-pulse ESE field sweep spectra in Figure 38, the signals of the NO adsorption species NO2c and NO2d are expected to have a larger spectral contribution at that magnetic field k than species NO2a, indicating differences in the arrangement of neighbored protons for the different NO moieties.

All ENDOR spectra measured at the field positions  $B_0 < 368$  mT show a broad signal at frequencies  $\nu \approx 7.7...17.3$  MHz overlapping partially with the proton signals (Figure 43). This signal was not observed at the field position k ( $B_0 = 368$  mT) (Figure 44d) and was therefore attributed to a nuclear species interacting with the NO adsorption species NO2a.<sup>[242]</sup> A second broad signal in the range  $\nu \approx 3.0...7.4$  MHz was detected only at the field position a ( $B_0 = 345$  mT, Figure 43a). The difference between the maxima of those two signals,  $\nu_{\text{max}} \approx 5.2$  MHz and  $\nu_{\text{max}} \approx 11.7$  MHz, is almost twice the  $^{27}\text{Al}$  nuclear Larmor frequency  $\nu_{\text{Al}} \approx 3.8$  MHz. Consequently, those signals were attributed to the central transition ( $m_I = -\frac{1}{2} \leftrightarrow +\frac{1}{2}$ ) spectral components  $\nu_{\alpha,\beta}^{\text{Al}} = \frac{A}{2} \pm \nu_{\text{Al}}$  of a strongly coupled  $^{27}\text{Al}$  nuclear species with spin  $I = \frac{5}{2}$ , interacting with the NO adsorption species NO2a. Since its ENDOR signals can be simulated within the spectral resolution by the same spin Hamilton parameters and linewidth model as applied for the simulation of the HYSORE signals of species Al2a, this species is identified as Al2a.<sup>[242]</sup> Its  $m_I = \pm\frac{5}{2} \leftrightarrow \pm\frac{3}{2}$  and  $m_I = \pm\frac{3}{2} \leftrightarrow \pm\frac{1}{2}$  nuclear transitions might either be not resolved due to their first order nqi broadening which does not affect the central transition,<sup>[268]</sup> or due to the small size of the nqi. Spectral simulations indicate that an  $^{27}\text{Al}$  nqi, as determined by NMR for the framework Al species in MIL-100(Al)<sup>[201]</sup>, is not resolved by an ENDOR signal with such large linewidth. Accordingly, the  $^{27}\text{Al}$  nqi was set to zero in all ENDOR simulations of species Al2a.<sup>[242]</sup>

At almost all field positions b to j (38b) only the spectral component  $\nu_{\alpha}^{\text{Al}}$  of the Al2a was observed whereas the  $\nu_{\beta}^{\text{Al}}$  spectral component is absent in the corresponding spectra (Figure 43). As verified by spectral simulations this observation is most likely caused by the hyperfine enhancement effect.<sup>[268,340,341]</sup> In a classical picture this effect originates from an rf field modulation of the electrons induced magnetic field at the nucleus, leading to an altered transition probability between the nuclear states in the electronic  $\beta$  and  $\alpha$  submanifolds.<sup>[268]</sup> Quantum-mechanically this effect arises from the higher order contributions to the eigenstates wave functions which lead to distinct non-vanishing components  $\langle \alpha \setminus \beta, m_I | \hat{S}_x | \alpha \setminus \beta, m_{I\pm 1} \rangle$  contributing to the total transition probabilities of the ENDOR

transitions.<sup>[341]</sup> Only at the lowest magnetic field position a ( $B_0 = 345.0$  mT) the Al2a  $\nu_\beta^{\text{Al}} = \frac{A}{2} - \nu_{\text{Al}}$  spectral component shows a significant intensity in the experimental ENDOR spectrum which was not reproduced by spectral simulations, including the hyperfine enhancement (Figure 43).

Not all spectral features of the ENDOR spectra in Figure 43 could be explained by protons or species Al2a. Most spectra show a less intense shoulder at the low frequency end of the Al2a  $\nu_\alpha \approx \frac{A}{2} + \nu_{\text{Al}}$  spectral component as it is indicated by the symbol \* in Figure 43. This shoulder was tentatively attributed to the  $\nu_\alpha^{14\text{N}} \approx \left| \frac{A_{x,z}}{2} + \nu_{14\text{N}} \right|$  spectral component of the ENDOR signals of the NO2a  $^{14}\text{N}$  nucleus with  $A_{x,z} < 0$  according to the DFT results presented later.<sup>[242]</sup> The  $\nu_\alpha^{14\text{N}} \approx \left| \frac{A_{x,z}}{2} - \nu_{14\text{N}} \right|$  component is expected to overlap with the Al2a signal.<sup>[242]</sup> Taking advantage of the orientation selectivity at the field positions d ( $B_0 = 350.7$  mT) and j ( $B_0 = 365.0$  mT) one can derive by the simulation of the observed  $^{14}\text{N}$  ENDOR signals two hfi principal values of the  $^{14}\text{N}$  nucleus. At the former magnetic field position, orientations, lying in the g-tensors  $x, y$ -plane, contribute mainly to the signal allowing for the determination of the magnitude of the  $^{14}\text{N}$  hfi value  $A_x^{14\text{N}}$ . At the latter magnetic field position the g-tensors  $z$ -direction contributes mainly to the signal. So, from its simulation one can derive the magnitude of the  $^{14}\text{N}$  hfi value  $A_z^{14\text{N}}$ . In both cases one assumes, as it is typical for NO adsorption complexes,<sup>[196]</sup> that the  $^{14}\text{N}$  hfi tensor is almost coaligned with the g-tensor. This assumption is verified by the DFT derived results presented below. The magnitude of the third  $^{14}\text{N}$  hfi principal value  $A_y^{14\text{N}}$  was determined by CW EPR as explained in subsection 5.1. All three values are summarized in Table 6. Neither the absolute nor the relative signs of the  $^{14}\text{N}$  hfi parameters could be derived experimentally by the simulations of the ENDOR spectra. Here, it is claimed that this is a result of the large pseudo-secular  $^{14}\text{N}$  hfi parameters, dominating the orientation dependence of the ENDOR frequencies like it is expressed analogously in the equations (20). The simulated different contribution of the Al2a nucleus and the  $^{14}\text{N}$  to the ENDOR signals are shown for exemplary spectra in Figure 44. For the spectral simulations the  $^{14}\text{N}$  nqi was set to zero. Values of the nqi as derived by DFT below are considered by the experimental errors of the  $^{14}\text{N}$  hfi parameters (Table 6).

## 5.5 DFT calculations

The CW and pulsed EPR measurements of sample Al-MIL-100 identified four NO adsorption species at low temperatures. Spin Hamiltonian parameters were determined by spectral simulations, which characterizes those species and their interactions with certain paramagnetic nuclei. The natural question arises, if one of these NO species binds to a framework CUS of the MIL-100(Al) material. But without any computational support, the determined EPR parameters enable only a rude analysis of the electronic and geometric structure of the corresponding NO adsorption complexes, as it was for instance done by Pöppl et. al.<sup>[200]</sup> One might expect a more precise insight into the nature of the spectroscopically characterized NO adsorption species, if one reproduces the experimental determined EPR parameters by reasonable ab initio calculations for an appropriate model system. If the computed and experimentally determined spin Hamiltonian parameters are

in good agreement, the assumption seems to be justified that the electronic ground state of the computationally derived model system describes the real structure of the EPR detected NO adsorption species accurately. In that case, one can derive a variety of properties of that NO adsorption species, like the complex geometry, the spin density distribution, the binding energy and the nature of the bond between NO and the surface.

Following these considerations, DFT calculations for specific cluster models of an NO molecule, binding to an  $\text{Al}^{3+}$  CUS of the trimeric metal-oxygen building unit of the MOF MIL-100(Al), were performed as it is published in detail elsewhere (see also appendix F.2).<sup>[242]</sup> In the present section the corresponding DFT derived results will be summarized. In the following discussion section, outcomes will be related to the experimental results which were presented in the previous sections.

To obtain a suitable model, which accurately describes the NO adsorption complex at the  $\text{Al}^{3+}$  CUS, a cluster was cut out from the MIL-100(Al) structure which was experimentally derived by single-crystal X-ray microdiffraction.<sup>[239,242]</sup> This starting cluster consists of the  $[\text{Al}_3(\mu_3-\text{O})]^{7+}$  core (Figures 3a and 45) saturated with six 1,3,5 -btc ligand ions with the formula  $[\text{C}_9\text{O}_6\text{H}_3]^{3-}$  (Figures 3b and 45). Such a btc ion has four outer oxygen atoms, one at each of the two carboxylate groups, which do not coordinate to the trimetallic core. One of both oxygen atoms of each non-coordinating carboxylate groups, namely the outermost, was saturated with a hydrogen atom, setting the net charge of the total cluster to +1 (see Figure 45a-c). For charge compensation one hydroxyl group binding at one  $\text{Al}^{3+}$  site was added.<sup>[201,239]</sup> A solid state NMR study<sup>[201]</sup> has indicated that after activation one water molecule remains at one  $\text{Al}^{3+}$  site of the metal core and only one  $\text{Al}^{3+}$  site becomes a CUS. Thus, one water molecule, binding to the second  $\text{Al}^{3+}$  site, was added. According to a recent solid state NMR study of Khan et al.<sup>[135]</sup> some metal cores of the MIL-100(Al) are indicated to have two CUS after activation, a possibility, which is not considered in the present DFT study, which was published earlier.<sup>[242]</sup> The cluster obtained in this way has been geometry optimized by DFT before further procession, as described in Mendt et al.<sup>[242]</sup> (see also appendix F.2). Here, and in all further mentioned DFT calculations, where the geometry of a cluster including the btc ligands was optimized, the positions of the 24 oxygen atoms of the non-coordinating carboxylate groups were constrained to the experimental derived values of the starting cluster.<sup>[239]</sup> The final cluster model **ML** was obtained attaching an NO molecule at the remaining free  $\text{Al}^{3+}$  site. A cluster called **M** was derived from the cluster **ML**, removing all btc ligands (Figure 45d-g). It includes the  $[\text{Al}_3(\mu_3-\text{O})(\text{OOC})_6]^{+}$  core plus the hydroxyl, water and NO ligands. The open bonds at the carbon atoms of **M** were saturated by six hydrogen atoms (see Figure 45d-g). In the following, the  $\text{Al}^{3+}$  ions, where NO, water and the  $\text{OH}^-$  group bind, will be called Al1, Al2 and Al3.

The detailed settings of the DFT calculations, which were carried out with the ORCA 3.0.0 program package,<sup>[317]</sup> are described and motivated in Mendt et al.<sup>[242]</sup> and are summarized in the appendix F.2. Here, only the overall approach and important characteristics will be presented.

The first problem was to find the geometric structures of the models **ML** and **M**, where

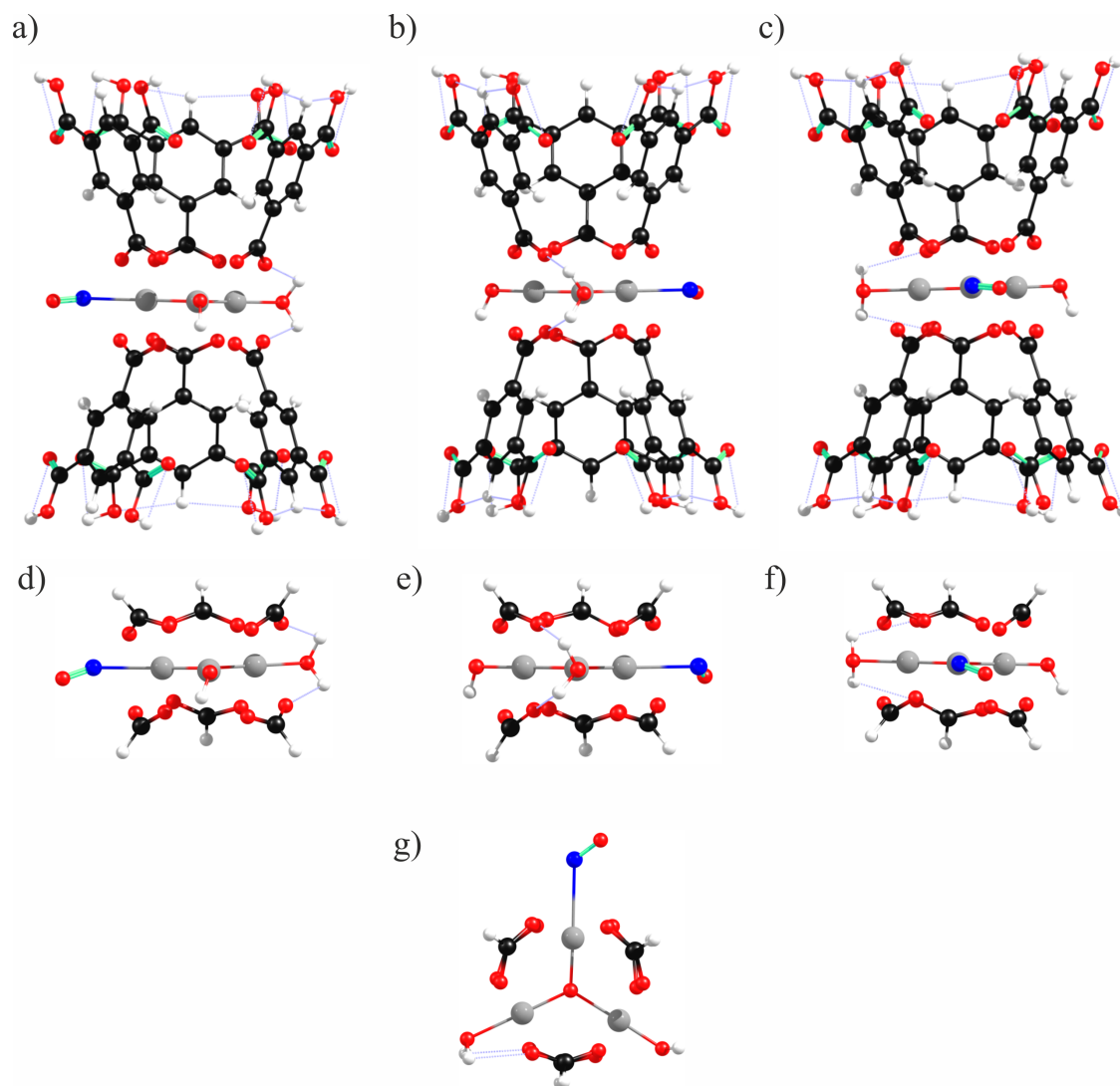


Figure 45: The finally B3LYP/def-2TZVP-optimized cluster models **ML** (a)-(c) and **M** (d)-(g) from different perspectives. Atoms are colored in gray (Al), red (O), blue (N), black (C) and white (H). This figure was first published by Mendt et al.<sup>[242]</sup>



Table 8: Structural parameters of the finally optimized clusters **ML** and **M**. Here,  $r_{\text{Al1-NO}}$  is the distance between the N and Al1 atoms,  $\theta_{\text{Al1-N-O}}$  is the Al1-N-O bond angle and  $\varphi_{\text{A-Al1NO}}$  is the angle between the plane A, containing all three Al atoms, and the plane containing the NO molecule and the atom Al1.

| Cluster model derived<br>with the stated<br>functional | $r_{\text{Al1-NO}}$ (Å) | $\theta_{\text{Al1-N-O}}$ (°) | $\varphi_{\text{A-Al1NO}}$ (°) |
|--|-------------------------|-------------------------------|--------------------------------|
| <b>ML</b> /B3LYP                                       | 2.460                   | 127.71                        | 7.14                           |
| <b>ML</b> /PBE0  | 2.374                   | 128.37                        | 5.81                           |
| <b>M</b> /B3LYP  | 2.654                   | 126.11                        | 20.65                          |
| <b>M</b> /PBE0   | 2.550                   | 126.95                        | 22.22                          |

the total wave functions approach their global energetic minima, namely their ground states at  $T = 0$  K. Just starting the geometry optimization with an arbitrary structure might converge at a local energetic minimum that is not the global one. To address this problem, relaxed surface scans have been performed for both clusters **ML** and **M**, first. Here, the potential energy surface (PES) was scanned by an appropriate structural parameter.<sup>[242]</sup> This parameter was chosen for both cluster models to be the dihedral angle  $\varphi$  between the plane containing the Al1-N-O adsorption complex and the plane containing the atoms N, Al1 and Al2. It was varied in steps of  $\Delta\varphi = 10^\circ$  over a full circle. At each step a geometry optimization was performed where  $\varphi$  was constrained but all other degrees of freedom were let to fully relax. These calculations were done with the famous B3LYP<sup>[342,343]</sup> functional choosing the def2-TZVP basis set for the  $[\text{Al}_3(\mu_3\text{-O})(\text{OOC})_6]^+$  core and the  $\text{OH}^-$ ,  $\text{H}_2\text{O}$  and NO ligands. All other atoms were treated with the cheaper def2-SV(P)<sup>[344]</sup> basis set. In that way, for both models **ML** and **M** parts of the PES were obtained as they are shown in Figure 46. According to these calculations, those parts of the PES attained their global minima at the dihedral angles  $\varphi = 170 \pm 10^\circ$  and  $\varphi = 162 \pm 10^\circ$  for the models **ML** and **M**, respectively. Those structures were the starting points for the final geometry optimizations on the B3LYP/def2-TZVP and PBE0/def2-TZVP<sup>[236,345-347]</sup> levels of theory. Now, the angle  $\varphi$  was let to fully relax. The finally optimized cluster models **ML** and **M** are shown in Figure 45. Some structural parameters of the Al1-NO adsorption complexes of both geometries are summarized in Table 8. More structural parameters of those optimized models are given in the appendix F.2, Table F.1. Full xyz-coordinates have been published in Mendt et al.<sup>[242]</sup> including the optimized structures without the NO ligand.

Unfortunately, the vibrational frequencies could not be calculated for the finally optimized structure **ML**, due to the constrained oxygen positions. But since the geometry optimization of the cluster **M** was performed without any constrains on the coordinates, the vibrational frequencies could be calculated. They were all positive, proving that the attained structure is a local energetic minimum. Since the Al1-N-O adsorption complexes of the optimized **ML** and **M** models have similar structures (Table 8, Figure 45), the former is also indicated to have attained an energetic minimum.

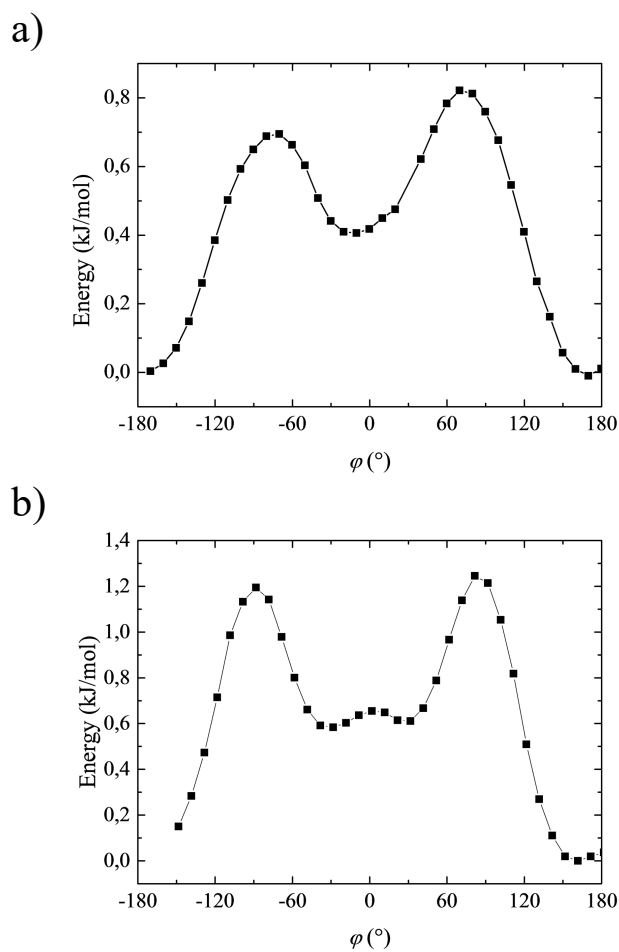


Figure 46: Single point energies, relative to the global energetic minimum, as calculated by relaxed surface scans for the cluster models **ML** (a) and **M** (b) varying the dihedral angle  $\varphi$  between the plane, containing the NO molecule and the Al1 atom, and the plane containing the N, Al1 and Al2 atoms. This figure was first published by Mendt et al.<sup>[242]</sup>

Table 9: Spin Hamilton parameters as derived by DFT for the B3LYP/def2-TZVP optimized cluster model **ML**, using the B3LYP or PBE0 functional as indicated in the header row. The header row also indicates the basis set used for all Al atoms. All oxygen atoms next to the Al atoms as well as the NO molecule and the oxygen atoms of the OH<sup>-</sup> and water ligands have been described by the IGLO-III<sup>[348]</sup> basis set. All other atoms were treated with the EPR-II<sup>[349]</sup> basis set. The Euler angles  $\alpha^g, \dots, \gamma^g$  of the g-tensor refer to a molecular frame, which z-axis is parallel to the internuclear axis of the NO molecule whereas its x-axis is perpendicular to the plane spanned by the Al1 atom and the NO molecule. Euler angles of other hfi and nqi tensors refer to the g-tensors principal axis frame. The hfi and nqi parameters are labeled with the atoms name as well as the interaction, to which they belong. Experimental parameters for the NO adsorption species NO2a and the <sup>27</sup>Al nuclear species Al2 are given in the last column.

| Parameter                              | B3LYP/<br>aug-cc-<br>pVTZ <sup>[350]</sup> | PBE0/<br>aug-cc-pVTZ | B3LYP/<br>IGLO-III | Exp.<br>NO2a<br>Al2a        |
|--|--|----------------------|--------------------|-----------------------------|
| $g_x$                                  | 2.0062                                     | 2.0062               | 2.0063             | $1.997 \pm 0.003$           |
| $g_y$                                  | 2.0023                                     | 2.0023               | 2.0023             | $1.997 \pm 0.003$           |
| $g_z$                                  | 1.9519                                     | 1.9479               | 1.9517             | $1.909 \pm 0.003$           |
| $\alpha^g$ (°)                         | 90.24                                      | 90.26                | 90.00              | 0 <sup>a</sup>              |
| $\beta^g$ (°)                          | 2.24                                       | 2.29                 | 2.20               | 0 <sup>a</sup>              |
| $\gamma^g$ (°)                         | -90.72                                     | -90.76               | -90.42             | 0 <sup>a</sup>              |
| $a_{\text{iso}}^{\text{Al1}}$ (MHz)    | 21.67                                      | 22.82                | 23.71              | $14.7 \pm 1.7$              |
| $T^{\text{Al1}}$ (MHz)                 | 3.59                                       | 3.55                 | 3.62               | $3.4 \pm 0.5$               |
| $\rho^{\text{Al1}}$                    | 0.029                                      | 0.026                | 0.030              | < 0.5                       |
| $\alpha_{\text{hfi}}^{\text{Al1}}$ (°) | 90.78                                      | 90.80                | 90.72              | $90 \pm 30$                 |
| $\beta_{\text{hfi}}^{\text{Al1}}$ (°)  | 47.95                                      | 47.71                | 47.97              | $50 \pm 10$                 |
| $\gamma_{\text{hfi}}^{\text{Al1}}$ (°) | 90.29                                      | 90.27                | 90.57              | _b                          |
| $C_Q^{\text{Al1}}$ (MHz)               | 4.28                                       | 4.04                 | 2.96               | _b                          |
| $\eta^{\text{Al1}}$                    | 0.326                                      | 0.329                | 0.20               | _b                          |
| $\alpha_{\text{nqi}}^{\text{Al1}}$ (°) | 94.40                                      | 94.39                | 86.04              | _b                          |
| $\beta_{\text{nqi}}^{\text{Al1}}$ (°)  | 73.05                                      | 73.62                | 29.40              | _b                          |
| $\gamma_{\text{nqi}}^{\text{Al1}}$ (°) | 94.22                                      | 93.95                | 95.37              | _b                          |
| $A_x^{\text{N}}$ (MHz)                 | -17.92                                     | -19.95               | -17.80             | $ \cdot  = 14 \pm 8$        |
| $A_y^{\text{N}}$ (MHz)                 | 86.38                                      | 82.47                | 86.52              | $ \cdot  = 86 \pm 3$        |
| $A_z^{\text{N}}$ (MHz)                 | -18.27                                     | -20.80               | -18.17             | $ \cdot  = 20 \pm 6$        |
| $a_{\text{iso}}^{\text{N}}$ (MHz)      | 16.73                                      | 13.91                | 16.85              | $17.3 \pm 3.0^{\text{c}}$   |
| $T^{\text{N}}$ (MHz)                   | 34.83                                      | 34.28                | 34.84              | $34.3 \pm 2.0^{\text{c}}$   |
| $\rho^{\text{N}}$                      | -0.01                                      | -0.01                | -0.01              | $-0.09 \pm 0.09^{\text{c}}$ |
| $\alpha_{\text{hfi}}^{\text{N}}$ (°)   | 110.02                                     | 98.32                | 107.01             | 0 <sup>a</sup>              |
| $\beta_{\text{hfi}}^{\text{N}}$ (°)    | 0.78                                       | 0.90                 | 0.80               | 0 <sup>a</sup>              |
| $\gamma_{\text{hfi}}^{\text{N}}$ (°)   | -109.77                                    | -98.10               | -106.84            | 0 <sup>a</sup>              |
| $C_Q^{\text{N}}$ (MHz)                 | 6.84                                       | 6.67                 | 6.84               | _b                          |

|   |        |         |         |    |
|---|--------|---------|---------|----|
| $\eta^{\text{N}}$                           | 0.398  | 0.375   | 0.398   | _b |
| $\alpha_{\text{nqi}}^{\text{N}} (^{\circ})$ | 0.23   | -179.79 | -179.85 | _b |
| $\beta_{\text{nqi}}^{\text{N}} (^{\circ})$  | 90.03  | 89.97   | 89.98   | _b |
| $\gamma_{\text{nqi}}^{\text{N}} (^{\circ})$ | -90.10 | -89.07  | -89.90  | _b |

<sup>a</sup> values have been not derived experimentally, but they are typical for NO adsorption species,<sup>[196]</sup> <sup>b</sup>not resolved, <sup>c</sup>assuming DFT derived signs for the <sup>14</sup>N hfi principal values

DFT derived spin Hamiltonian parameters are summarized in Table 9.<sup>[242]</sup> Spin Hamiltonian parameters, calculated with other functionals, can be found elsewhere.<sup>[242]</sup> As explained in detail in the appendix F.2 and in Mendt et al.,<sup>[242]</sup> the g-tensor, the hfi tensors of the <sup>14</sup>N nucleus and the various <sup>27</sup>Al nuclei and protons as well as the electric field gradients at the <sup>27</sup>Al, and <sup>14</sup>N sites have been calculated with DFT for the B3LYP/def2-TZVP as well as the PBE0/def2-TZVP optimized structure of the cluster model **ML**. Those calculations have been performed using various functionals as motivated in Mendt et al.<sup>[242]</sup>

In dependence on the cluster (B3LYP or PBE0 optimized), various hybrid functionals (B3LYP, PBE0, PBE<sup>[351,352]</sup>), GGA functionals (BP86,<sup>[353,354]</sup> O3LYP,<sup>[355]</sup> OLYP,<sup>[356]</sup> PW91<sup>[357]</sup>, PWP<sup>[354,358,359]</sup>) and the *meta*-GGA functional TPSS<sup>[360]</sup> and its hybrid version TPSSh,<sup>[360]</sup> as well as in dependence on the Al basis sets (Table 9), the DFT derived <sup>14</sup>N hfi principal values of the **ML** cluster span ranges  $-26.7 \text{ MHz} \leq A_x^{\text{N}} \leq -13.6 \text{ MHz}$ ,  $72.50 \text{ MHz} \leq A_y^{\text{N}} \leq 87.1 \text{ MHz}$  and  $-27.0 \text{ MHz} \leq A_z^{\text{N}} \leq -14.9 \text{ MHz}$  and therefore  $6.3 \text{ MHz} \leq a_{\text{iso}}^{\text{N}} \leq 19.5 \text{ MHz}$  and  $32.26 \text{ MHz} \leq T^{\text{N}} \leq 34.84 \text{ MHz}$ . The corresponding values of the DFT derived, almost axially symmetric hfi tensor of the Al1 nucleus span ranges  $21.7 \text{ MHz} \leq a_{\text{iso}}^{\text{Al1}} \leq 45.8 \text{ MHz}$  and  $3.55 \text{ MHz} \leq T^{\text{Al1}} \leq 4.79 \text{ MHz}$ .<sup>[242]</sup> For both the nitrogen as well as the Al1 atom the calculated isotropic hfi constants depend highly on the chosen functional whereas the corresponding dipolar hfi constants show a less pronounced functional dependence. This difficulties of DFT, to predict exactly the isotropic hfi parameter, is well known and related to difficulties of calculating accurate spin polarizations.<sup>[233,361,362]</sup> The smallest values for  $a_{\text{iso}}^{\text{Al1}}$  and  $T^{\text{Al1}}$  and large values for  $a_{\text{iso}}^{\text{N}}$  are obtained systematically with the B3LYP, PBE0 and TPSSh functionals, indicating that including exact exchange locates less spin density at the Al1 nucleus and more at the nitrogen nucleus. A larger isotropic Al1 hfi was calculated for the PBE0 optimized than B3LYP optimized **ML** model, which most likely reflects the 0.1 Å shorter distance between the Al1 and nitrogen atoms of the former structure. The dependence of those hfi parameters on the chosen basis set for the Al atoms is less pronounced.<sup>[242]</sup> It turns out that the smallest isotropic Al1 hfi parameter was calculated with the B3LYP functional using an aug-cc-pVTZ basis set for the Al atoms (Table 9).

The calculated Euler angles describing the orientations of the Al1 and <sup>14</sup>N hfi tensors as well as of the calculated nqi tensors are also summarized in Table 9. The calculated <sup>14</sup>N hfi tensor is co-aligned with the g-tensor as it is typical for adsorbed NO (see Figure 47c).<sup>[125,196,301]</sup> The DFT derived hfi and nqi parameters of the other <sup>27</sup>Al nuclei of the model cluster **ML** are summarized in Table F.2 in the appendix F.2. More magnetic

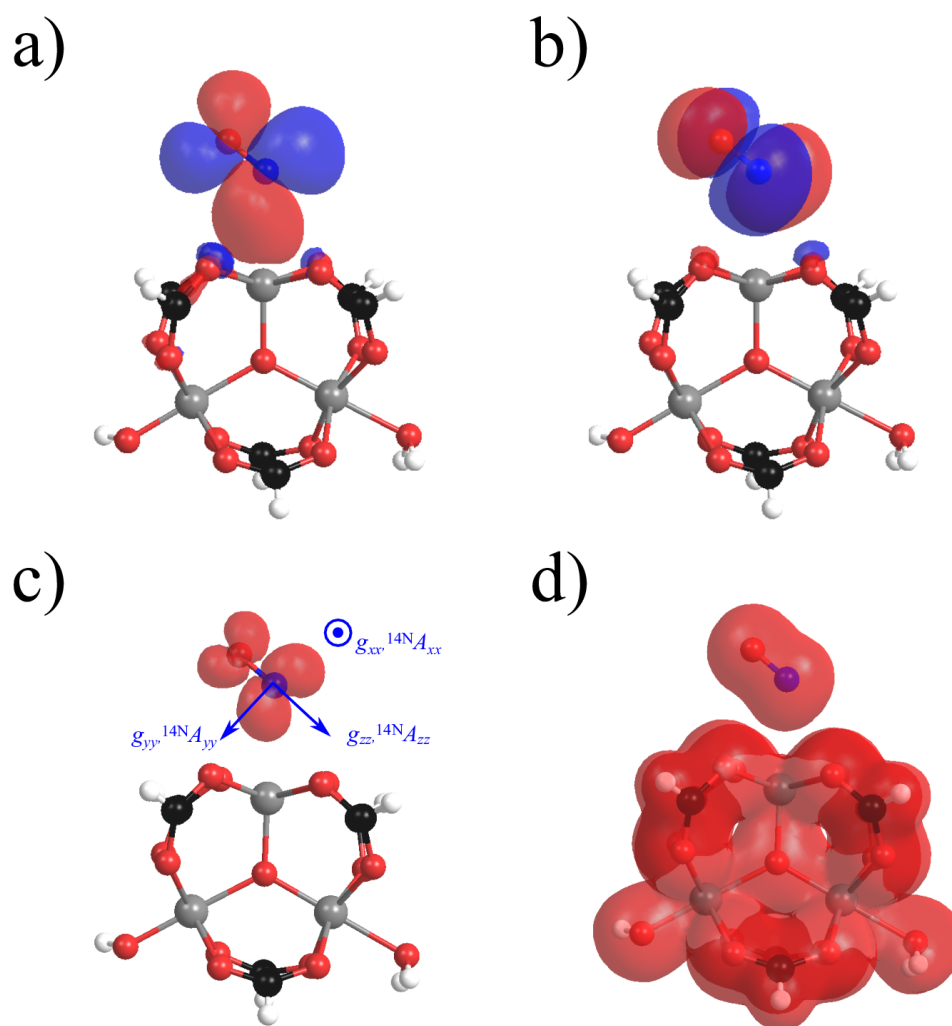


Figure 47: The antibonding  $\pi_y^*$  HOMO containing the unpaired electron (a), the antibonding  $\pi_x^*$  LUMO (b), the spin density (c) and the electronic density (d) as derived by DFT for the finally optimized model cluster **M** on the B3LYP/def2-TZVP level. Atoms are colored in gray (Al), red (O), blue (N), black (C) and white (H). In (c) the principal axes directions of the  $g$ - and  $^{14}\text{N}$  hfi tensors are displayed. This figure was first published by Mendt et al.<sup>[242]</sup>

parameters, including those of the btc ligand protons, as well as calculated nqi tensors for the  $^{27}\text{Al}$  nuclei of model clusters without an adsorbed NO molecule have been also calculated and published in Mendt et al.<sup>[242]</sup>

For the B3LYP optimized cluster **ML** the binding energy<sup>[236]</sup> of the NO molecule was calculated to be  $\Delta E_{\text{NO}} = -22.4$  kJ/mol, using the counterpoise correction of the basis set superposition error.<sup>[363]</sup>

## 5.6 Insights into the low temperature adsorption of NO

Three NO adsorption species NO2a, NO2c and NO2d were observed by CW and pulsed EPR experiments for sample Al-MIL-100 at the temperature  $T = 6$  K, whereas a fourth NO adsorption species NO2b was observed by CW EPR at temperatures  $T > 14$  K. In addition, the ground state of NO adsorbed at an  $\text{Al}^{3+}$  CUS of the MIL-100(Al) at  $T = 0$  K was investigated by detailed DFT calculations. In the present section, the results of the previous ones will be discussed and related to each other.

Three  $^{27}\text{Al}$  species Al2a, Al2b and Al2c have been detected by pulsed EPR experiments at  $T = 6$  K. It has been verified that the first species Al2a interacts with the species NO2a, the second Al2b with the species NO2c and all three species NO2a, NO2c and NO2d are strongly indicated to interact with distant Al atoms, here called species Al2c. As one expects for NO adsorbed in the hydrogen containing MIL-100(Al), signals of weakly coupled protons have been measured by ENDOR and HSCORE spectroscopy at all observer field positions.

All calculated hfi parameters of the  $^{27}\text{Al}$  Al1 and the  $^{14}\text{N}$  nucleus in the optimized model cluster **ML** are in good agreement with those, determined experimentally for the  $^{27}\text{Al}$  species Al2a and NO2a as shown in Table 9. The best agreement between the DFT and the experimentally derived parameters was achieved with the B3LYP functional. The largest discrepancy concerns the DFT derived  $^{27}\text{Al}$  hfi constant  $a_{\text{iso}}^{\text{Al1}}$ , which exceeds with  $\Delta a_{\text{iso}} = 7$  MHz the experimentally derived one of species Al2a (Table 9). This corresponds to a spin density difference in the Al 3s valence orbital of about 0.2 percent.<sup>[364]</sup> But, such a difference between the DFT derived and real isotropic hfi seems to lie within the restricted accuracy of DFT for calculating small spin densities or spin polarizations.<sup>[233,361]</sup> This is also reflected by the strong functional dependency of the calculated  $a_{\text{iso}}^{\text{Al1}}$  parameter.<sup>[242]</sup> Nevertheless, the calculated anisotropic hfi part of the Al1 nuclei, including its parameters  $T^{\text{Al1}}$  and  $\rho^{\text{Al1}}$  as well as the orientation of the hfi tensor, equals the experimentally determined values for species Al2a with good accuracy (Table 9). Since this part of the hfi is expected to reflect the geometry of the NO adsorption complex to a much higher degree than the isotropic hfi, it is supposed that the optimized cluster **ML** is a quite accurate model for the electronic and geometric structure of the experimentally observed NO adsorption species NO2a, as assumed in the further discussion. Particularly, the cluster **ML** is a reasonable and experimentally justified model for the species NO2a.

From the experimentally derived value  $T = 3.4$  MHz, describing the anisotropic hfi of species Al2a, one can calculate within a point dipole approximation (equation (12)) an Al1-NO distance  $r_{\text{Al1-NO}} = 1.8$  Å. This distance is distinctly smaller than the DFT derived

Table 10: Reduced spin populations in percent according to Mulliken and Löwdin for the Al1 and NO’s N atoms, as derived on the B3LYP/def2-TZVP level for the cluster models **ML** and **M**. They are given for the whole atom as well as for different reduced shells as labeled in brackets.

| Atom       | <b>ML</b> |        | <b>M</b> |        |
|------------|-----------|--------|----------|--------|
|            | Mulliken  | Löwdin | Mulliken | Löwdin |
| Al (total) | 1.99      | 3.35   | 1.26     | 2.57   |
| Al (s)     | -0.08     | 0.21   | 0.17     | 0.10   |
| Al (p)     | 1.52      | 1.14   | 0.25     | 0.66   |
| Al (d)     | 0.12      | 1.20   | 0.55     | 1.08   |
| Al (f)     | 0.42      | 0.80   | 0.30     | 0.73   |
| N (total)  | 62.36     | 59.71  | 64.45    | 61.44  |
| N (s)      | -0.02     | 1.06   | -0.18    | 0.92   |
| N (p)      | 62.03     | 53.39  | 64.35    | 55.52  |
| N (d)      | 0.37      | 4.50   | 0.32     | 4.24   |
| N (f)      | -0.03     | 0.77   | -0.04    | 0.76   |
| O (total)  | 34.45     | 35.52  | 33.2     | 34.66  |
| O (s)      | 1.33      | 0.42   | 1.17     | 0.38   |
| O (p)      | 32.82     | 30.64  | 31.71    | 29.77  |
| O (d)      | 0.30      | 3.88   | 0.33     | 4.02   |
| O (f)      | 0.00      | 0.48   | 0.01     | 0.49   |

distance  $r_{\text{Al1-N}} = 2.4 \pm 1 \text{ \AA}$  between the Al1 and N atoms. This is an indication for significant spin density in the Al1 3p or 3d orbitals, as the Mulliken and Löwdin population analysis of the DFT derived wave function of model **ML** (Table 10) suggests. The NO adsorption complex in **ML** has an Al-N-O bond angle  $\theta_{\text{Al-N-O}} = 128^\circ$  (Table 8) and thus a bent end-on structure. Similar parameters, namely  $r_{\text{Na-NO}} = 2.1 \text{ \AA}$  and  $\theta_{\text{Na-N-O}} = 142^\circ$ , have been derived by a comprehensive analysis of ENDOR experiments characterizing an  $\text{Na}^+$ -NO adsorption complex in the Na-A zeolite.<sup>[200]</sup> Since the  $\text{Na}^+$  ion has a similar size and the same electron configuration as the  $\text{Al}^{3+}$  ion, the physical validity of the calculated **ML** ground state seems to be justified. The somewhat larger distance  $r_{\text{Al1-NO}}$  might indicate a partial shielding of the  $\text{Al}^{3+}$  caused electric surface field by the adjacent planar oxygen atoms.<sup>[205]</sup> This bent Al-NO structure is a first indication, that the binding between NO and the  $\text{Al}^{3+}$  ion is mainly ionic, since for a covalent Al-nitrosyl bond a linear Al-NO complex is expected.<sup>[365]</sup>

From the DFT derived wave functions of the optimized models **ML** and **M**, the Mulliken and Löwdin atomic charges<sup>[242]</sup> and spin populations (Table 10) of the Al1 atom and NO molecule have been calculated.<sup>[242]</sup> They are similar for both models as also their geometric structures are (Table 8, Figure 45). Thus, the electronic structure of the NO adsorption complex seems to depend mainly on the trimeric metal-oxygen unit and is quite independent from the presence of the btc ligands. This is an important information for further ab initio investigations of this NO adsorption complex with more accurate but also computational more demanding multi-determinant methods.<sup>[314]</sup>

Figure 47 shows the  $\pi_y^*$  highest occupied canonical molecular orbital (HOMO) of the

optimized model **M**, which is involved in the NO binding and which contains the unpaired electron. It further shows the  $\pi_x^*$  lowest unoccupied canonical molecular orbital (LUMO) as well as the spin and electronic densities of the optimized model **M**. Corresponding orbitals and densities for the optimized model **ML** are qualitatively the same. The HOMO, which is usually responsible for the main characteristics of the bonding,<sup>[365]</sup> contains almost all spin density. This observation is supported and quantified by the Mulliken and Löwdin spin population analysis (Table 10), which predicts that about 95-97 percent spin density is located on the NO molecule, two to four percent at the Al1 atom and less than 0.5 percent at each of the four next neighbored planar oxygen atoms.<sup>[242]</sup> According to that population analysis 53-62 percent spin density is in the  $2p_y$  AO of the nitrogen, whereas 34-36 percent remains in the  $2p_y$  AO of the NO molecules oxygen.<sup>[242]</sup> These values can be compared to the measured  $^{14}\text{N}$  dipolar hfi constant  $T^{\text{N}} = 33$  MHz (Table 7 and assuming DFT derived signs for the  $^{14}\text{N}$  hfi principal values), which translates to about 59 percent spin density in the nitrogen's  $2p_y$  AO.<sup>[364]</sup> This confirms the prediction of the population analysis. Accordingly, the measured nitrogen's isotropic hfi constant  $a_{\text{iso}}^{\text{N}} = 20$  MHz translates to about 1.1 percent spin density in the  $2s$  AO of the nitrogen<sup>[364]</sup> which reproduces the Löwdin predicted value (Table 10). Here, the Mulliken population analysis derives a value of -0.02, which indicates the better performance of the Löwdin than Mulliken method.<sup>[314]</sup> Similarly, one can derive from the experimental Al2a isotropic hfi constant  $a_{\text{iso}}^{\text{Al2a}} = 14.7$  MHz that about 0.38 percent spin density occupies the Al2a  $s$  orbital.<sup>[364]</sup> Again, this value is reproduced by the Löwdin analysis which predicts 0.21 percent spin density in the Al1  $s$ -like AOs whereas the Mulliken analysis fails, predicting small negative spin density in the  $s$ -like AOs of the Al1 atom (Table 10).

According to the previous spin-density analysis, the NO molecules  $\pi_y^*$  MO is in first approximation a linear combination of the nitrogen and oxygen atoms  $2p_y$  AOs with some small  $s$ -like contributions. The composition of the calculated  $\pi_y^*$  MO in terms of contributing AOs was also analyzed according to Mulliken, which reflects the spin density analysis almost one-to-one.<sup>[242]</sup> Mostly, AOs from the NO contribute to this HOMO whereas Al1 AOs contribute with less than two percent.<sup>[242]</sup> This is also reflected by the electronic density shown in Figure 47 which adopts only small values in between the NO molecule and Al1 atom. All in all, the EPR and DFT based wave function analysis of the NO2a adsorption species strongly indicates its almost purely ionic binding at the framework MIL-100(Al) CUS without any significant covalent contributions. Since the  $\text{Al}^{3+}$  is a closed shell cation, this result seems to be reasonable.<sup>[198]</sup>

A weak ionic binding is also indicated by the NO binding energy  $\Delta E_{\text{NO}} = -22.4$  kJ/mol at  $T = 0$  K as calculated for the optimized model **ML**. Such a low binding energy is rather typical for a physisorption than chemisorption.<sup>[198]</sup> It is almost equal to the binding energy  $\Delta E_{\text{CO}} = -28.1$  kJ/mol, which was calculated by other authors<sup>[236]</sup> for a CO molecule bound to an  $\text{Al}^{3+}$  CUS of the same  $\mu_3$ -oxo-bridged cluster. This calculated binding energy  $\Delta E_{\text{NO}}$  is significantly larger than the energy barrier  $\Delta E_{\text{PES}} \approx 0.8$  kJ/mol of the part of the PES scanned by the dihedral angle  $\varphi$  between the Al1-N-O and N-Al-Al2 planes (Figure 46). This strongly indicates that at intermediate temperatures the NO molecule is



able to rotate almost freely around the Al-N bond axis, while still binding to the CUS. Such kind of thermally activated motion is experimentally indicated by the occurrence of the NO adsorption species NO2b in CW EPR spectra measured at temperatures  $T > 14$  K.<sup>[223]</sup> Its g-value  $g_z = 1.947 \pm 0.003$  is significantly larger than that for species NO2a (Table 9) which might be explained by a partial motional averaging of the g-tensor principal values. This has been suggested already by other authors to explain the occurrence of an additional  $\text{Na}^+$ -NO adsorption species in the Na-A zeolite by a thermally activated two-site jump process of the adsorbed NO species.<sup>[196]</sup>

The NO stretching vibration for the cluster **M** was calculated by DFT to be  $\bar{\nu} = 2002 \text{ cm}^{-1}$  at  $T = 0$  K. The corresponding value for gaseous NO is with  $\bar{\nu} = 1876 \text{ cm}^{-1}$ <sup>[366]</sup> significantly smaller. One might explain this difference by a small transfer of spin density from the antibonding  $\pi_y^*$  HOMO to the Al1 atom, stiffening the N-O bond. Interestingly, no distinct IR signal of the NO adsorbed at the MIL-100(Al) CUS was resolved in a combined IR and EPR study of this system at temperatures down to  $T = 173$  K.<sup>[223]</sup> Admittedly, EPR has detected the signal of NO adsorbed at the CUS at lower temperatures  $T < 160$  K and therefore additional IR experiments performed at low temperatures are strongly recommended. Nevertheless, IR resolves signals on a faster time scale and is therefore expected to detect signals of adsorbed NO species at higher temperatures than EPR. This is the case for NO species, weakly interacting with the organic part of the MOF MIL-100. A variety of such species has been observed by IR even at room temperature,<sup>[223]</sup> whereas EPR has detected the signal of the weakly coupled NO species NO2d only at low temperatures and even the EPR signal of the strongly coupled species NO2a was not observed anymore at temperatures  $T > 160$  K (section 5.1).<sup>[223]</sup> But the presented ab initio investigation of the model **ML** indicates a weak interaction between the NO and the  $\text{Al}^{3+}$  cation, which is more characteristic for a physisorption. This suggests that the NO- $\text{Al}^{3+}$  species contributes to the IR signals of the variety of weakly bound NO species interacting with the MOFs organic part. One might expect that at  $T = 173$  K more spin density has returned from the Al1 atom to the NO molecules antibonding  $\pi_y^*$  HOMO, shifting the NO stretching vibration into the range  $1820 \text{ cm}^{-1} < \bar{\nu} < 1920 \text{ cm}^{-1}$ , where IR signals of a variety of physisorbed NO were observed.<sup>[223]</sup> As indicated by two-pulse ESE field sweep EPR the amount of NO2a is of the same order of magnitude than that of NO2d. (Figure 38a). This small amount of species NO2a might explain why the IR signal of NO2a does not stand out from the background signal of weakly physisorbed NO.<sup>[223]</sup> In addition, the IR signal of the NO- $\text{Al}^{3+}$  might be significantly inhomogeneously broadened, hindering its resolution from the IR signal background of other weakly bound NO species. The flat PES, established by DFT, supports an inhomogeneous variation of the NO- $\text{Al}^{3+}$  structure among all such adsorption species. Note further that for the MIL-100(Fe) material an intensive and well resolved IR signal was observed,<sup>[223]</sup> which was attributed to NO- $\text{Fe}^{3+}$ , indicating the stronger interaction between the NO and the  $\text{Fe}^{3+}$  cation than with the  $\text{Al}^{3+}$ .

The ground state, where the unpaired electron resides in the  $\pi_y^*$  MO of the NO molecule is the  $^2\Pi_y$  molecular state, whereas the excited state, where the unpaired electron occupies

Table 11: Energy splitting  $\Delta$  describing the HOMO-LUMO gap as derived from the experimental NO g-tensor principal values (equations (44)) or derived directly from the DFT derived energy levels in the last row. In addition, the experimental  $^{14}\text{N}$  hfi parameter  $A_y^{14\text{N}}$  is listed for various NO adsorption species.

| Species                        | $T$ (K) | $\Delta$ (kJ/mol)         | $A_y^{14\text{N}}$ (MHz) |
|--------------------------------|---------|---------------------------|--------------------------|
| NO2a (MIL-100(Al))             | 6       | $23.3 \pm 7.3$            | $86 \pm 3$               |
| NO2b (MIL-100(Al))             | 45      | $17.2 \pm 5.1$            | $84 \pm 12$              |
| NO2c (MIL-100(Al))             | 6       | $22.2 \pm 1.9^{\text{a}}$ | $-^{\text{b}}$           |
| NO2d (MIL-100(Al))             | 6       | $14.5 \pm 9.0^{\text{a}}$ | $-^{\text{b}}$           |
| NOz1 (H-ZSM-5 <sup>c,d</sup> ) | 10      | $25.5 \pm 2.8$            | 84.1                     |
| NOz2(Na-ZSM-5 <sup>c,e</sup> ) | 10      | $15.9 \pm 2.8$            | 102.0                    |
| NOz3 (Na-A <sup>c,e</sup> )    | 10      | $26.2 \pm 3.8$            | 91.6                     |
| B3LYP/def2-TZVP ( <b>ML</b> )  | 0       | 317.5                     | 86.4                     |

<sup>a</sup>assuming  $l = 1$ , <sup>b</sup>note resolved, <sup>c</sup>NO adsorbed on zeolite matrix, <sup>d</sup>g-tensor values from Rudolf et al.<sup>[198]</sup>, the values  $\Delta$  and  $l$ , calculated in the present work, differ from those stated there, <sup>e</sup>Rudolf et al.<sup>[197]</sup>

the  $\pi_x^*$  MO is the  $^2\Pi_x$  molecular state, as introduced in the subsection 2.3.4. Thus, the energy difference  $\Delta$  between the  $^2\Pi_x$  and  $^2\Pi_y$  states should be almost equal to the HOMO-LUMO gap.<sup>[196,302]</sup> It reflects the electric surface field strength at the adsorption site<sup>[301]</sup> and is therefore an important parameter to characterize the NO adsorption site. It can be derived from the NO g-tensor principal values in a second order approximation as stated in the equations (44) and as it is summarized in Table 11 for various NO adsorption species. According to the similarity of the g-tensor derived energies  $\Delta$  (Table 11), the electric surface field at the site of species NO2a should be comparable to those of the NO adsorption species at an Al site in the H-ZSM-5 zeolite<sup>[198]</sup> and of NO-Na<sup>+</sup> complexes in the Na-ZSM-5 and Na-A zeolites.<sup>[197]</sup> However, the DFT derived HOMO-LUMO gap exceeds the experimental value  $\Delta$  for species NO2a dramatically by one order of magnitude (Table 11). This seems to be related to the overestimation of the g-tensor principal values of the model **ML** by DFT. They obey the relation  $g_x \gtrsim g_y \approx g_e > g_z$  (Table 9) which does not fit to the expected relation  $g_e > g_x \gtrsim g_y > g_z$ , which holds typically for adsorbed NO.<sup>[301]</sup> Since the calculated value  $g_x = 2.0062$  value is larger than  $g_e = 2.0023$  (Table 9), it is non-physical and cannot be reproduced by the equations (44). But assuming  $g_x = 2.0023$  one derives with the equations (44) with the remaining DFT derived g-tensor principal values an energy splitting  $\Delta \approx 330$  kJ/mol which almost matches the calculated HOMO-LUMO gap (Table 11). This indicates that the second order approach for the derivation of  $\Delta$  from the g-tensor principal values with the equations (44) is accurate and the overestimation of the calculated g-tensor principal values by DFT is related to an overestimated HOMO-LUMO gap. This seems reasonable since the calculation of excited state energies by DFT is known to be problematic, if those states have the same spatial and spin symmetry as the ground state has.<sup>[314]</sup> For such states DFT has problems to ensure the orthogonality between the ground and excited states.<sup>[314]</sup> This situation applies for the  $^2\Pi_y$  ground and  $^2\Pi_x$  excited state of the **ML** system. Accordingly, the DFT derived g-tensor principal

values and the DFT derived HOMO-LUMO gap are expected to have no validity and one should only rely on the experimental results. Particularly, the EPR derived g-tensor values indicate a real HOMO-LUMO gap for species NO2a of  $\Delta_{\text{HOMO-LUMO}} = 23.7 \pm 7.3$  kJ/mol. Nevertheless, the DFT derived g-tensor principal directions are oriented as expected (Table 9).<sup>[125,301]</sup> The  $z$ -axis points along the N-O bonding axis and the  $y$ -axis is aligned parallel to the  $\pi_y^*$  orbital containing the unpaired electron as shown in Figure 47c.

According to the aforementioned discussion, it can be concluded that the combined EPR and DFT based results allow for a reliable attribution of species NO2a to NO adsorbed at the framework CUS of the MOF MIL-100(Al). Such a result is enabled by the experimental determination of the Al2a  $^{27}\text{Al}$  hfi. Simultaneously, the experimentally determined value  $A_y^{14\text{N}}$  enables a quantitative characterization of the Lewis acidity of the  $\text{Al}^{3+}$  CUS by EPR. This value is sensitive to the fraction of unpaired spin density in the nitrogen's  $2p_y$  orbital<sup>[364]</sup> and measures in that way the contribution of both resonant structures in the relation (33) to the total wave function. Thus, this value can be used to characterize the electron pair acceptor strength of a Lewis acid site probed by an NO molecule.<sup>[198]</sup> The hfi parameter  $A_y^{14\text{N}}$  is summarized for different NO adsorption species in Table 11. According to Table 11, species NO2a has a similar Lewis acidity than NO adsorbed in H-ZSM-5 zeolite.<sup>[198]</sup> With IR spectroscopy of the C-N stretching vibration  $\nu(\text{CN})$  of acetonitrile ( $\text{CD}_3\text{CN}$ ), identical values for  $\nu(\text{CN})$  of  $\text{CD}_3\text{CN}$  adsorbed at the Lewis acid sites in MIL-100(Al) and H-ZSM-5 zeolite have been measured within the spectral resolution.<sup>[205,242,367]</sup> It has been claimed that  $\text{CD}_3\text{CN}$  is a reliable IR spectroscopic probe for the characterization of the Lewis acidity of such sites.<sup>[205]</sup> Thus, the accordance of those comparative IR and EPR studies indicates that the EPR detected  $^{14}\text{N}$  hfi probes reliably the Lewis acidity of  $\text{Al}^{3+}$  sites, where the corresponding NO molecule adsorbs. In particular, the  $A_y^{14\text{N}}$  parameters of the different NO adsorption species indicate that both of the Al sites, the MIL-100(Al) CUS and the defect site in H-ZSM-5 zeolite, have a larger electron pair acceptor strength than the corresponding sodium cations in the Na-A and Na-ZSM-5 zeolites (Table 11).<sup>[197]</sup>

What about the magnetic couplings of species NO2a to other  $^{27}\text{Al}$  and proton nuclei which are present in the MIL-100 framework? According to the optimized model **ML** the Al2 and Al3 atoms have distances to the NO nitrogen of about  $r_{\text{Al-N}} \approx 5.4$  Å. This large distance explain (equation (12)) their almost zero isotropic hfi and their small dipolar hfi parameters  $T \approx 0.13$  MHz as derived by DFT<sup>[242]</sup> (see Table F.2 in the appendix F.2). This means that both nuclei contribute to the variety of distant matrix nuclei Al2c observed by HYSCORE spectroscopy and one can exclude that one of them is the experimental observed species Al2b. In the model **ML** the four nearest neighbored protons of the NO molecule have distances to the NO nitrogen of about  $r_{\text{H-N}} \approx 4.0$  Å and their DFT derived hfi parameters are  $a_{\text{iso}} \approx 0$  MHz and  $T \approx 1.1$  MHz. Since for the ENDOR and HYSCORE detected proton species a maximum hfi value  $A_{\text{max}} \approx 3.5$  MHz was estimated from the corresponding signals, the next nearest btc protons should contribute to the variety of weakly coupled protons observed by those spectroscopic methods.

As verified by HYSCORE experiments, the  $^{27}\text{Al}$  nuclear species Al2b is interacting

with the NO adsorption species NO2c. The corresponding isotropic hfi constant is negative (Table 7), indicating significant spin polarization effects. The small dipolar hfi constant of species Al2b (Table 7) indicates a weaker interaction between the NO adsorption species NO2c and the Al nucleus Al2b than between the NO adsorption species NO2a and the Al2a Al nucleus. In addition, the  $g$ -values of species NO2c are smaller than those of species NO2a (Table 6), indicating in total the weaker physisorption of the former compared to the latter.<sup>[301]</sup> The size of the Al2b's quadrupole coupling parameter  $C_Q = 2.8 \pm 2$  MHz (Table 7) indicates that species Al2b might belong to the framework trimetallic-oxygen unit of the MIL-100(Al) MOF, since this magnitude is comparable to the NMR<sup>[201]</sup> derived range  $C_Q = 1.3...5.5$  MHz for sixfold coordinated Al species in the activate MIL-100(Al) material at room temperature as well as to the DFT derived basis set dependent range  $C_Q = 2.8...4.3$  MHz for the Al species Al2a (Table 9).<sup>[242]</sup> It can be verified that the first order nqi broadening of species Al2b is quite small, since the cross peak ridges correlating the  $m_I = \pm\frac{1}{2} \leftrightarrow \pm\frac{3}{2}$  transitions are resolved. So, the Al species Al2b is at a well-defined framework or defective site of the MIL-100(Al)'s structure and not some ill-defined site of a certain impurity phase or an extraframework Al species. Alternatively, it may adsorb at some extraframework Al(OH)<sub>3</sub> impurity phase, which existence in the pores was indicated by a recent NMR study.<sup>[135]</sup>

HYSCORE spectroscopy has also verified the coupling of at least one proton species to the NO adsorption species NO2c, supporting the hypothesis that NO2c is interacting with the proton containing MIL-100(Al) MOF framework. Corresponding HYSCORE combination peaks, indicative for protons which might be located even at distant positions, were not observed for species NO2a. This might be explained by the deep Al2a modulations which causes cross-suppression of possible protons signals<sup>[368]</sup> as it has been verified by exemplary simulations.<sup>[242]</sup>

In total, an NO2c adsorption site at the MIL-100(Al) framework with an <sup>27</sup>Al nucleus in its first or second coordination sphere and protons at minimal distances  $r_{\min} \approx 3.0$  Å is indicated by the experimental data. Since all attempts to derive by DFT a structural model explaining the EPR characteristics of species NO2c failed, it is proceeded without any further suggestions for the detailed structure of this NO adsorption complex.

As verified by HYSCORE spectroscopy, only the distant matrix <sup>27</sup>Al species Al2c and weakly coupled protons interact with the weakly bound fourth NO adsorption species NO2d. The nqi constant of species Al2c was determined experimentally to  $C_Q = 5.2 \pm 0.8$  MHz (Table 7) and fits to the range  $C_Q = 1.3...5.5$  MHz as measured by NMR<sup>[201]</sup> for five and six fold coordinated <sup>27</sup>Al in the activated MIL-100(Al). The DFT derived values  $C_Q = 1.3...6.5$  MHz for the atoms Al1 and Al2 of the model **ML** and a corresponding model without an NO molecule<sup>[242]</sup> also fit to the experimental ones. Only the nqi constant  $C_Q \approx -20$  MHz for the atom Al3, calculated by DFT<sup>[242]</sup> (see Table F.2 in the appendix F.2), was neither resolved by EPR nor NMR.<sup>[201]</sup> This large nqi magnitude reflects the binding of the charged OH<sup>-</sup> anion to the Al3 atom. The indicated invisibility of the Al3 nuclei for EPR and NMR might be most likely related to the broad line shape of the nuclear frequency spectrum due to the large  $C_Q$  value, which in addition contributes with its second

power to the second order nqi.<sup>[272]</sup> The absence of any other  $^{27}\text{Al}$  species, interacting with NO2d, indicates its weak adsorption at the organic part of the MOF. Such a physisorption is also indicated by its small  $g_z$  value (Table 6), which suggests a weak electric surface field at the adsorption site.<sup>[301]</sup> The presence of such weakly bound NO adsorption species was also observed for the MIL-100(Al) by IR spectroscopy.<sup>[223]</sup>

## 5.7 Summary of chapter five

Four different NO adsorption species NO2a to NO2d could be resolved by X-band CW EPR and two-pulse ESE field sweep experiments on NO loaded samples of the MIL-100(Al) material at low temperatures. Temperature-dependent CW EPR experiments between  $8\text{ K} < T < 295\text{ K}$  detected the EPR signals of desorbed NO at  $T > 150\text{ K}$  and adsorbed NO at  $T < 160\text{ K}$ , indicating the low temperature adsorption and thus physisorption of NO on the MOF material at temperatures  $T < 160\text{ K}$ . The temperature-dependent intensity of the EPR signal of adsorbed NO suggests further the formation of diamagnetic  $(\text{NO})_2$  below  $T \approx 115\text{ K}$ . The strong  $^{27}\text{Al}$  hfi of species NO2a, resolved by CW EPR, HYSORE and Davies ENDOR spectroscopy at  $T < 50\text{ K}$ , undoubtedly proves the interaction of this NO adsorption species with a  $^{27}\text{Al}$  nuclear species Al2a. The mentioned EPR methods enable the experimental determination of the magnitudes of all g-tensor and  $^{14}\text{N}$  hfi principal values of species NO2a, as well as the determination of the complete Al2a  $^{27}\text{Al}$  hfi tensor, including its orientation relative to the g-tensors' principal axes frame. The determined  $^{14}\text{N}$  hfi enabled a characterization of the Lewis acidity of the corresponding  $\text{Al}^{3+}$  CUS. At the same time a structural model for NO adsorbed at the framework CUS of the MIL-100(Al) framework could be derived by DFT. The  $^{14}\text{N}$  and  $^{27}\text{Al}$  hfi tensors, calculated for this structural model, are in good agreement with those measured by the mentioned methods for species NO2a interacting with the  $^{27}\text{Al}$  species Al2a. Thus, species NO2a is assigned to NO, adsorbed at the framework CUS of MIL-100(Al). The analysis of the DFT derived results reveal a weak ionic binding of that NO molecule at the CUS in a bent end-on fashion, without any significant covalent contributions. Such weak physisorption of this species is reflected by the already mentioned temperature dependence of its CW EPR signal and might further explain the absence of a distinctly resolved IR signal of this NO adsorption species at  $T = 173\text{ K}$ .<sup>[223]</sup> Furthermore, the DFT calculations indicate the ability of the NO adsorbed at the CUS, performing some rotational motion while still binding to the metal ion. This might explain the occurrence of the NO adsorption species NO2b, which was observed by CW EPR at temperatures  $T > 20\text{ K}$  and might show the inset of some thermally activated motion of species NO2a partially averaging its g-tensor principal values.

HYSORE spectroscopy further proves unambiguously that the third resolved NO adsorption species NO2c interacts with a second  $^{27}\text{Al}$  nuclear species Al2b. Its EPR derived  $^{27}\text{Al}$  hfi as well as its g-tensor indicate a weaker adsorption of NO2c than found for species NO2a. In addition, the rough size of the  $^{27}\text{Al}$  nqi of species Al2b as well as a coupling of species NO2c with protons could be resolved. Unfortunately, no distinct structural model could be derived for species NO2c, but its EPR characteristics indicate that species

NO<sub>2</sub>c adsorbs at some site of the MOF surface with an <sup>27</sup>Al nucleus in its first or second coordination sphere.

Based on its EPR characteristics the fourth NO adsorption species NO<sub>2</sub>d was attributed to NO, weakly physisorbed at the organic part of the MOF. Signals of distant <sup>27</sup>Al matrix nuclei were observed by HYSCORE spectroscopy at all magnetic field positions, indicating their interaction with all NO adsorption species. The rough EPR derived <sup>27</sup>Al nqi for this species fits to the NMR derived <sup>27</sup>Al nqi for Al nuclei in the MIL-100(Al) material,<sup>[201]</sup> giving additional evidence for the successful adsorption of all observed NO species on the surface of the MOF framework.

---

## 6 EPR investigation of defect centers in rigid and flexible derivatives of DUT-8(Ni) using NO as a probe molecule

As mentioned in section 2.1, some MOFs possess framework flexibility. This property, combined with the microporosity of MOFs, can offer great opportunities for potential applications in storage, separation, sensing, drug release or catalysis.<sup>[218,219]</sup> In this context it might be useful to finetune the flexibility of a MOF material by the kind of metal ion<sup>[244]</sup> or linker molecule<sup>[369]</sup> as well as the crystal size,<sup>[241]</sup> in principle. Nevertheless, most MOFs are rigid and only a few of them show this interesting property.<sup>[219]</sup> Thus, the ability to predict, whether a MOF structure is flexible or not, would extremely simplify the search for flexible MOFs that are tailored for a specific application. Unfortunately, up to now no such profound understanding of the origins of flexibility of MOFs exist so that the latter has become predictive. A joint effort of computational modeling and experimental studies is still necessary to reach this goal. The MOF DUT-8(Ni) has been chosen as an ideal model system for this research, since it can show flexibility and rigidity in departure on the synthesis conditions.<sup>[241,254]</sup> This has been verified by PXRD, nitrogen physisorption<sup>[224,241,246]</sup> and recently by IR and Raman as well as solid state <sup>13</sup>C NMR.<sup>[241]</sup>

In addition, EPR of desorbed NO in samples of two DUT-8(Ni) derivatives has also reflected their difference in flexibility (see subsection 2.1.4 and section 3.3).<sup>[224]</sup> One of them shows the prominent “gate pressure” flexibility of the DUT-8(Ni)<sup>[244]</sup> whereas the other variant stays rigid at any gas pressure and temperature. The difference between those flexible and rigid derivatives of DUT-8(Ni) is a result of a slightly modification of their synthesis procedures, where for the latter an excess of the dabco ligand was applied among other minor changes.<sup>[224,241,246,254]</sup> Such variations of the synthetic protocol should lead to characteristic microscopic properties which differ among both derivatives of the DUT-8(Ni) and are responsible for their different flexibility. The PXRD pattern of the rigid DUT-8(Ni) equals that of the open pore phase of the flexible DUT-8(Ni)<sup>[224]</sup> and gives no indication for any differences in the crystal structure. But PXRD is a non-local method which is not capable to resolve defects in the crystal structure, except some contributions to the line broadening of the PXRD pattern. By scanning electron microscopy (SEM) it has been verified that the rigid DUT-8(Ni) has systematically smaller crystallites than the flexible derivative.<sup>[241]</sup> Crystallites smaller than 500 nm in diameter retain in the porous lp phase, whereas crystallites larger than 1  $\mu$ m transform into the non-porous cp phase upon solvent removal.<sup>[241]</sup> But also SEM gives no insight into potential microscopic reasons for this difference in flexibility. This has motivated an EPR study as a part of this thesis,<sup>[224]</sup> where the adsorption of NO on both DUT-8(Ni) derivatives was investigated by X-band CW EPR. The framework Ni<sup>2+</sup> ions in the DUT-8(Ni) have no CUS for the adsorption of the NO molecule. But defective Ni<sup>2+</sup> paddle wheel units, where bonds to the dabco or ndc ligands are broken, might offer CUS as potential NO adsorption sites. Corresponding NO-Ni<sup>2+</sup> adsorption complexes are expected to be paramagnetic showing characteristic EPR signals (see subsection 2.3.5).<sup>[309]</sup> This kind of an NO probed characterization of defective sites in both DUT-8(Ni) derivatives complements the EPR study of desorbed NO discussed

in section 3.3 and will be elucidated in the present chapter.<sup>[224]</sup> This study deals with the same samples F\_DUT-8a and F\_DUT-8b, containing the flexible derivative of DUT-8(Ni), and the samples R\_DUT-8a and R\_DUT-8b, containing its rigid derivative, as they have been used for the EPR study of desorbed NO gas (see section 3.3 and subsection A.2 as well as Table A.1 in subsection A.3). The different observed paramagnetic NO adsorption species were identified and characterized by a detailed analysis of the CW EPR spectra of all four samples, as summarized in the first section. The second section presents and discusses first and recent pulsed EPR experiments of an NO loaded flexible DUT-8(Ni) sample, which has not been published yet, demonstrating the potential of such an approach for coming studies. A final section summarizes the results of this chapter.

## 6.1 Identification and characterization of NO adsorption species by CW EPR

EPR spectra of the samples F\_DUT-8a, F\_DUT-8b, R\_DUT-8a and R\_DUT-8b, measured at temperatures  $7\text{ K} < T < 298\text{ K}$ , are collected in Figure 48. One exemplary low temperature spectrum of each sample as well as their simulations are shown in Figure 49. The  $\text{Ni}^{2+}$  ions of the Ni-DUT-8 material have a  $3d^8$  electron configuration and can either be in a diamagnetic state with electron spin  $S = 0$  or a paramagnetic state with electron spin  $S = 1$ . Thus, the framework  $\text{Ni}^{2+}$  paddle wheels of the DUT-8(Ni) can have an electron spin  $S = 0$  or  $S = 2$  ground state. Interestingly, for all samples and at all temperatures no EPR signals attributable to the framework  $\text{Ni}^{2+}$  paddle wheels have been detected by EPR.<sup>[224]</sup> This might indicate either that the paddle wheels are in their  $S = 0$  ground state<sup>[370]</sup> or that the zero field splitting is larger than 80 GHz, in case those paddle wheels have integer spin larger than zero, as it is verified by spectral simulations.<sup>[224]</sup> The NO loaded samples show in addition at temperatures  $T < 60\text{ K}$  and g-values  $g_e > g > 1.3$  weak signals which are attributed to a variety of NO weakly physisorbed at diamagnetic surface sites,<sup>[301]</sup> here called species NO3 (Figures 48 and 49). This species might include NO moieties physisorbed at the organic part of the DUT-8(Ni) material. Its signal was better resolved by two-pulse ESE field sweep EPR at low temperatures, as it is discussed in section 6.2.

Interestingly, all spectra in Figure 48 show signals at magnetic field positions  $260\text{ mT} < B_0 < 330\text{ mT}$  corresponding to a range of g-values  $2.58 > g_x, g_y, g_z > g_e = 2.0023$  as they are typical for paramagnetic species with electron spin  $S = 1/2$ . Admittedly, they are typical for  $\text{Ni}^+$  which has a  $3d^9$  electron configuration or low spin  $\text{Ni}^{3+}$  species with a  $3d^7$  electron configuration.<sup>[371-373]</sup> But an attribution of those signals to monovalent or trivalent nickel seems unlikely, since such signals were neither observed for the activated flexible DUT-8(Ni), which stays in the non-porous phase, nor for the activated rigid DUT-8(Ni), staying in the porous phase.<sup>[224]</sup> Thus, a change of the nickels valency by an NO induced structural phase transformation seems unlikely. Since both of those activated samples were prepared without any loaded NO, the EPR signals observed for the NO loaded samples were attributed to NO adsorption species.<sup>[224]</sup> But all respective g-tensor values are larger than the free electron g-value  $g_e$ . This excludes the assignment to NO



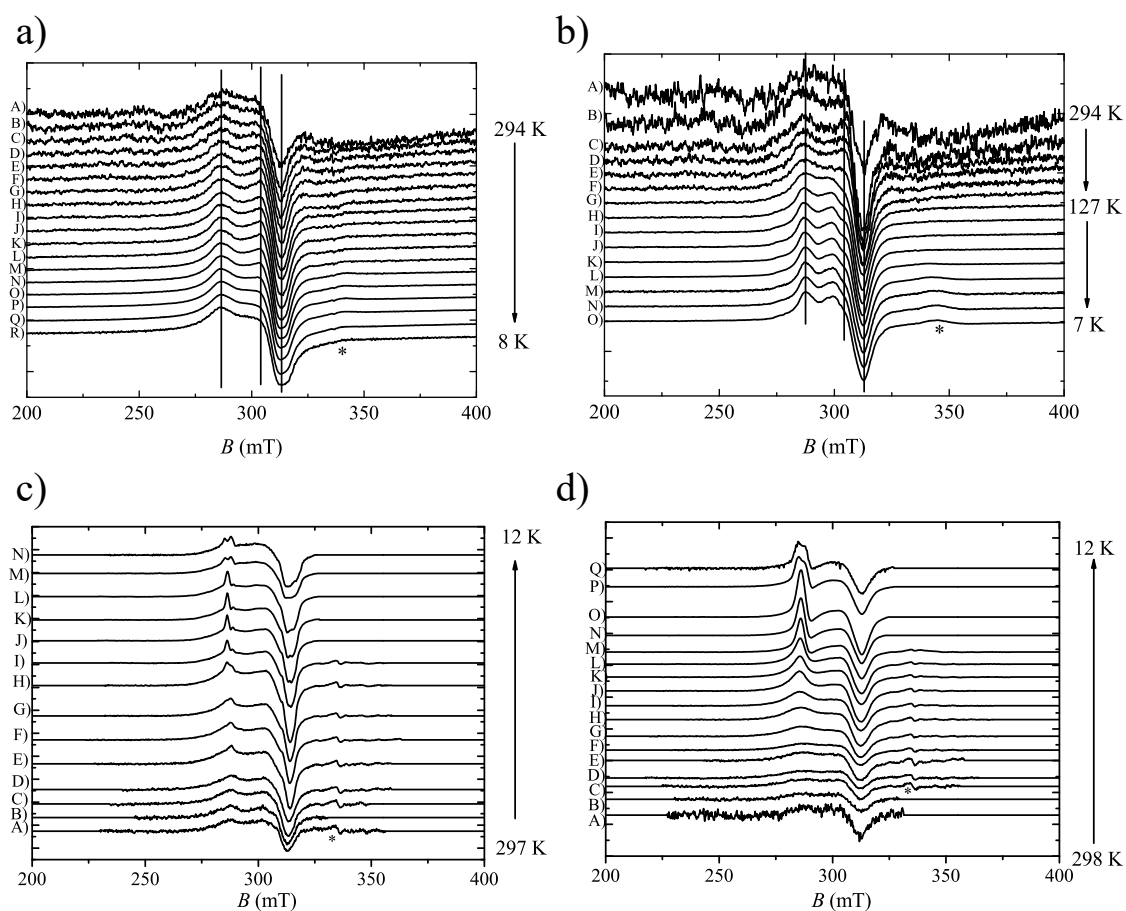


Figure 48: (a) X-band EPR spectra of sample F\_DUT-8a measured during cooling at temperatures 294 K (A), 258 K (B), 229 K (C), 204 K (D), 180 K (E), 161 K (F), 141 K (G), 118 K (H), 102 K (I), 94 K (J), 83 K (K), 66 K (L), 39 K (M), 31 K (N) 23 K (O), 17 K (P), 12 K (Q) and 8 K (R). The signal of weakly physisorbed NO (species NO<sub>3</sub>) is labeled by an asterisk symbol. The vertical lines are guides for the eyes. (b) X-band EPR spectra of sample F\_DUT-8b measured during cooling at temperatures 294 K (A), 236 K (B), 195 K (C), 171 K (D), 151 K (E), 138 K (F), 127 K (G), 115 K (H), 104 K (I), 94 K (J), 62 K (K), 43 K (L), 27 K (M), 14 K (N) and 7 K (O). The signal of weakly physisorbed NO (species NO<sub>3</sub>) is labeled by an asterisk symbol. the vertical lines are guides for the eyes. (c) X-band EPR spectrum of sample R\_DUT-8a measured during cooling at temperatures 297 K (A), 251 K (B), 210 K (C), 181 K (D), 133 K (E), 124 K (F), 116 K (G), 104 K (H), 90 K (I), 79 K (J), 62 K (K), 44 K (L), 21 K (M) and 12 K (N). (d) X-band EPR spectra of sample R\_DUT-8b measured at the temperatures 298 K (A), 249 K (B), 211 K (C), 181 K (D), 161 K (E), 138 K (F), 126 K (G), 121 K (H), 116 K (I), 110 K (J), 105 K (K), 100 K (L), 82 K (M), 64 K (N), 47 K (O), 21 K (P) and 12 K (Q). All spectra of samples R\_DUT-8a (c) and R\_DUT-8b (d) have been baseline corrected to subtract unwanted but present signals of NiO impurities and weakly physisorbed NO.<sup>[224]</sup> The signal of a free radical is marked by an asterisk in (c) and (d).

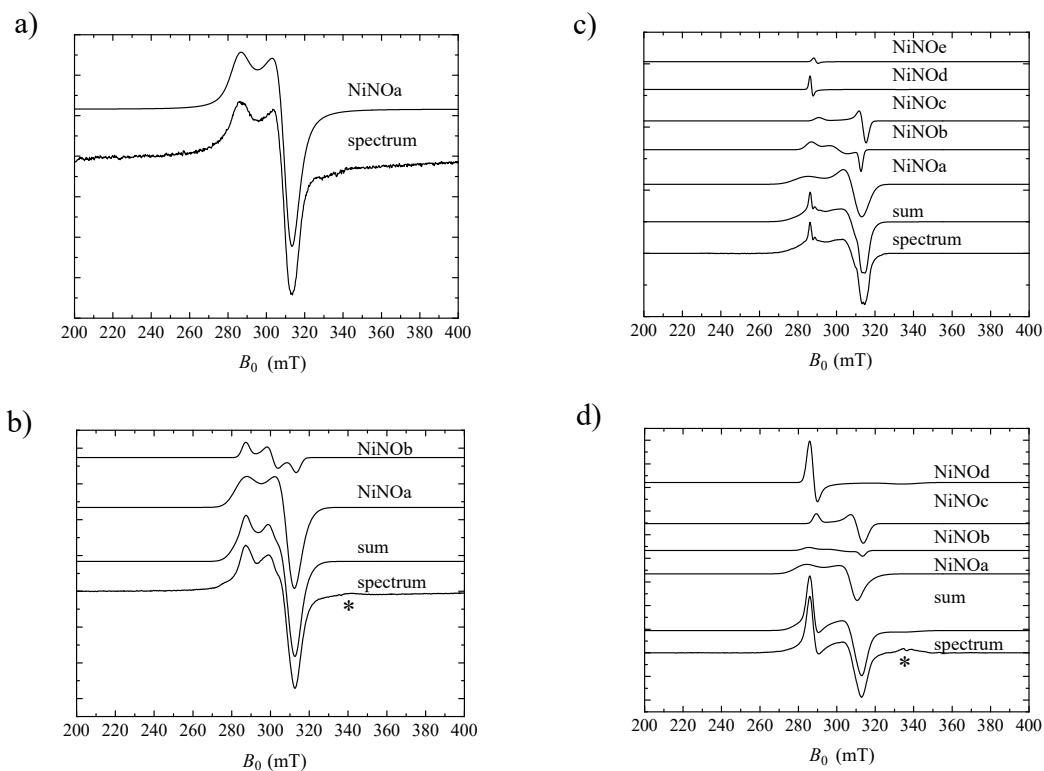


Figure 49: Low Temperature EPR spectra (lowest) and simulations (above) of DUT-8 samples F\_DUT-8a at  $T = 82$  K (a), of sample F\_DUT-8b at  $T = 62$  K (b), of sample R\_DUT-8a at  $T = 79$  K (c) and of sample R\_DUT-8b at  $T = 82$  K (d). Simulations of the EPR signals of single  $\text{Ni}^{2+}$ -NO species are designated in the figures, respectively, as well as their sum. The signal of the weakly physisorbed NO species NO3 is marked by an asterisk. This figure was first published by Mendt et al.<sup>[224]</sup>

Table 12: Samples where the corresponding Ni<sup>2+</sup>-NO adsorption species is present and the experimental derived g-tensor principal values of those species observed for the DUT-8 samples and for samples from literature.

| Species  | Samples   | $g_x$                    | $g_y$                    | $g_z$             |
|--|---|--------------------------|--------------------------|-------------------|
| NiNOa  | F_DUT-8a,<br>F_DUT-8b,<br>R_DUT-8a,<br>R_DUT-8b | $2.169 \pm 0.009$        | $2.169 \pm 0.009$        | $2.355 \pm 0.014$ |
| NiNOb  | F_DUT-8b,<br>R_DUT-8a,<br>R_DUT-8b <sup>c</sup> | $2.145 \pm 0.012$        | $2.199 \pm 0.038$        | $2.332 \pm 0.038$ |
| NiNOc  | R_DUT-8a,<br>R_DUT-8b                           | $2.137 \pm 0.018$        | $2.137 \pm 0.018$        | $2.294 \pm 0.043$ |
| NiNOd  | R_DUT-8a,<br>R_DUT-8b                           | $2.336 \pm$<br>$0.005^e$ | $2.336 \pm$<br>$0.005^e$ | $< 2.23$          |
| NiNOe  | R_DUT-8a <sup>d</sup>                           | $2.325 \pm 0.003$        | $2.325 \pm 0.003$        | $< 2.23$          |
| NO@Ni(65%)-<br>Y<br>Zeolite <sup>a</sup>               | -   | $2.171 \pm 0.002$        | $2.171 \pm 0.002$        | $2.346 \pm 0.005$ |
| Ni <sup>2+</sup> -<br>NO@SiO <sub>2</sub> <sup>b</sup> | -   | 2.156                    | 2.184                    | 2.369             |

<sup>a</sup>Data from Kasai and Bishop<sup>[374]</sup>, <sup>b</sup>Data from Sojka et al.<sup>[310]</sup>, <sup>c</sup>The absence of species NiNOb in sample R\_DUT-8b cannot be fully excluded.<sup>[224]</sup> <sup>d</sup>Perhaps, species NiNOe is also present in sample R\_DUT-8b, even it was not resolved by EPR, <sup>e</sup> $T > 21$  K, <sup>f</sup> $T \leq 21$  K.

adsorbed at diamagnetic or closed shell surface sites as it was observed for the MIL-53(Al) and MIL-100(Al) materials (see subsection 2.3.4). However, the NO can bind to Ni<sup>2+</sup> ions, which are open shell due to their  $3d^8$  electron configuration. As mentioned in subsection 2.3.4, this range of g-values is also typical for Ni<sup>2+</sup>-NO adsorption species<sup>[92,309]</sup> where the unpaired electron of the NO occupies with a second electron from the nickel the Ni<sup>2+</sup>-NO bonding orbital, leaving one unpaired electron at the Ni<sup>2+</sup> ion. Thus, the latter has now an effective electron configuration as Ni<sup>+</sup>, explaining the characteristic g-tensor principal values. Consequently, all those EPR signals, observed for the four NO loaded samples, have been attributed to Ni<sup>2+</sup>-NO complexes.<sup>[224]</sup>

Contributions of up to five Ni<sup>2+</sup>-NO species to the CW EPR signals of the four NO loaded DUT-8(Ni) sample, here called NiNOa, NiNOb, NiNOc, NiNOd and NiNOe, have been suggested by a detailed simulation based analysis (see Figure 49).<sup>[224]</sup> Their presence among the four samples as well as their simulation derived g-tensor principal values are documented in Table 12. The simulations were aided by automatic least square fits. But their signals superposition prevents an undoubtedly determination of all their spectral characteristics. More details are reported in Mendt et al.<sup>[224]</sup> For the flexible DUT-8(Ni) sample F\_DUT-8a the EPR signal of only one Ni<sup>2+</sup>-NO species NiNOa was observed at

all temperatures (Figure 49a), having an almost axially symmetric g-tensor with principal values  $g_x \approx g_y < g_z$  (Table 12). All spectra of the other three NO loaded DUT-8(Ni) samples are also indicated to show the signal of species NiNOa, although undoubtedly other species contribute.<sup>[224]</sup> For the flexible DUT-8(Ni) sample F\_DUT-8b a new bump was observed for spectra, measured at temperatures  $T \leq 127$  K. It was attributed to a second Ni<sup>2+</sup>-NO species NiNOb (Figure 49b). Least square fits of all temperature-dependent spectra of sample F\_DUT-8b suggest an orthorhombic g-tensor for species NiNOb (Table 12).<sup>[224]</sup>

Five Ni<sup>2+</sup>-NO species are indicated to contribute to the EPR signals measured for the rigid DUT-8(Ni) sample R\_DUT-8a (Figure 49c). An unique unraveling determination of all single component signals from the experimental spectra was not possible without any additional assumptions. Thus, it was supposed that both species NiNOa and NiNOb contribute to the EPR spectra of sample R\_DUT-8a. As in all cases, it was assumed that among different samples the g-tensor principal values of one Ni<sup>2+</sup>-NO species do not change, but linewidth parameters can, reflecting potential differences in the inhomogeneity or local concentration of the species among the different samples. The high field powder edge singularity of the R\_DUT-8a spectrum measured at  $T = 79$  K (Figure 49c) shows a slight splitting as well as a shoulder at its low field edge. This detailed structure was not reproduced by extensive simulations assuming contributions of species NiNOa and NiNOb alone.<sup>[224]</sup> But by assuming the contribution of an additional Ni<sup>2+</sup>-NO species NiNOc, having an axially symmetric g-tensor with principal values  $g_x \approx g_y < g_z$  (Table 12), a satisfying agreement between the simulated and measured high field signal components was obtained at all temperatures (see for example 49c).<sup>[224]</sup>

The g-tensor principal values of all species NiNOa, NiNOb and NiNOc hold the relation  $g_x, g_y < g_z$  (Table 12). Interestingly, for the rigid DUT-8(Ni) sample R\_DUT-8a, signals of two additional species NiNOd and NiNOe have been observed as shown in Figure 49c. Both species have an almost axially symmetric g-tensor but with an reversed order of its g-tensor principal values, namely  $g_x, g_y > g_z$ .<sup>[224]</sup> Whereas the signal intensities of those two species are small in the spectra of sample R\_DUT-8a with less NO (Figure 48c), for sample R\_DUT-8b with an larger amount of NO (Table A.1) the signal of species NiNOd becomes quite intense at low temperatures. As a result, no signal of species NiNOe was observed anymore (Figure 49d). Again, the distinct linewidths of the total EPR signals, measured for sample R\_DUT-8b at various temperatures (Figure 48d), prevent an unique unraveling determination of each signal component belonging to a single Ni<sup>2+</sup>-NO species. But with the hypothesis that only the species NiNOa, NiNOb and NiNOc contribute in addition to species NiNOd to the EPR spectra of sample R\_DUT-8b, a satisfying agreement between all temperature-dependent experimental and simulated spectra could be obtained (see for example Figure 49d and Table 12).<sup>[224]</sup>

The most valuable information, obtained by EPR and characterizing distinctly the Ni<sup>2+</sup>-NO complexes NiNOa to NiNOe, are their g-tensor principal values. As already discussed in the subsection 2.3.5, the order  $g_x, g_y < g_z$  indicates a structural model where the antibonding  $\pi_y^*$  MO of the NO, containing the unpaired electron, adds with the  $d_{z^2}$  orbital

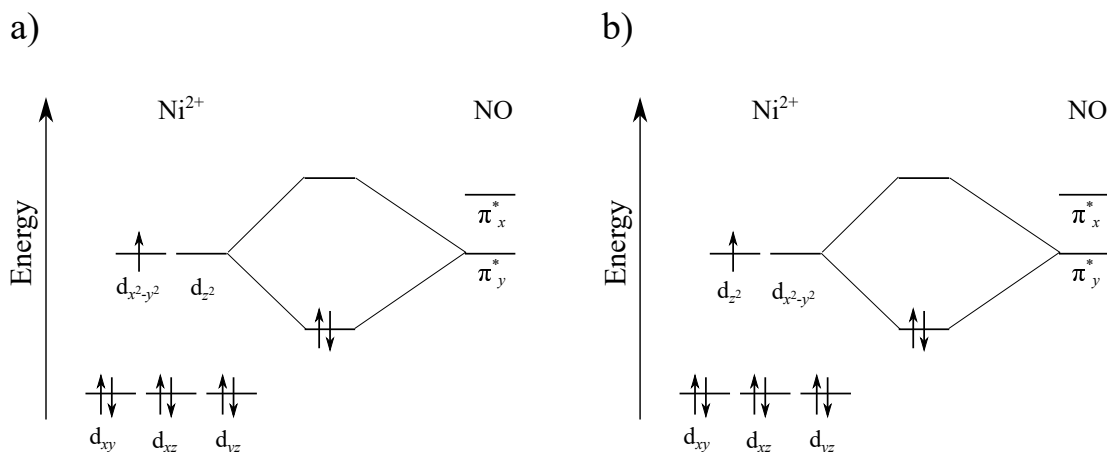


Figure 50: MO diagrams describing qualitatively the bonding of the  $\text{Ni}^{2+}$ -NO species NiNOa, NiNOb and NiNOc (a) as well as NiNOd and NiNOe (b), as it is indicated by the order of their g-tensor principal values (Table 12).<sup>[309]</sup>

of  $\text{Ni}^{2+}$  to a double occupied bonding ( $d_{z^2} + \pi_y^*$ ) MO, forming a covalent bond between the NO and the  $\text{Ni}^{2+}$ .<sup>[309]</sup> Now, an unpaired electron remains in the nickel  $d_{x^2-y^2}$  orbital, which explains the characteristic g-tensor principal values in second order.<sup>[312,375,376]</sup> The resulting ground state configuration is  $(d_{z^2} + \pi_y^*)^2 (d_{x^2-y^2})^1 (d_{z^2} - \pi_y^*)^0$  as illustrated in Figure 50a. Accordingly, for all three species NiNOa, NiNOb and NiNOc the Ni  $d_{z^2}$  AO is involved in the bonding and consequently the NO molecule is indicated to bind to the  $\text{Ni}^{2+}$  along the  $z$ -axis, which obeys the highest rotational symmetry of the  $\text{Ni}^{2+}$  environment.<sup>[224]</sup> Particularly, for those three species structural models seem reasonable, where the NO binds axially to a  $\text{Ni}^{2+}$  in a defective paddle wheel, replacing either a dabco ligand or the second  $\text{Ni}^{2+}$ . Thus, two possible structural models are proposed, which might explain species NiNOa, NiNOb and NiNOc and which are illustrated in Figure 51a,b:

**Ni-ax-1Ni.** The NO molecule binds along the fourfold symmetry axis to a  $\text{Ni}^{2+}$  ion of a defective paddle wheel, which contains only one  $\text{Ni}^{2+}$  ion. Such kind of a defective paddle wheel was already identified in a MOF with  $\text{Cu}^{2+}$  paddle wheels.<sup>[377]</sup>

**Ni-ax-2Ni.** In this model both  $\text{Ni}^{2+}$  ions are present in the paddle wheel. Now, at least one dabco ligand does not coordinate along the fourfold symmetry axis to a  $\text{Ni}^{2+}$  ion, but NO does instead. Here, the second neighbored  $\text{Ni}^{2+}$  ion should stay in its low spin state with  $S = 0$ , since otherwise its  $S = 1$  spin would prevent the detection of such well defined  $S = 1/2$  powder signals as they were observed by EPR.<sup>[224]</sup>

Species NiNOb might belong to one of these two structural models. But due to the observed orthorhombicity of its g-tensor, an additional distortion of the four equatorial oxygen binding sites should be present, which modifies the local  $C_4$  symmetry of the  $\text{Ni}^{2+}$  site, maybe indicating a broken bond to at least one of the 2,6-ndc ligand molecules.

For the species NiNOd and NiNOe the order of their g-tensor principal values  $g_x, g_y > g_z$  is reversed compared to those of the species NiNOa to NiNOc. Such g-tensor principal values are typical for a  $\text{Ni}^+$  ion or a low spin  $\text{Ni}^{3+}$  ion where the unpaired electron resides in the  $d_{z^2}$  orbital.<sup>[312,313,378,379]</sup> As for the species NiNOa to NiNOc one can argue that no  $\text{Ni}^+$  and  $\text{Ni}^{3+}$  ions are present in the DUT-8 samples.<sup>[224]</sup> Again, their occurrence must

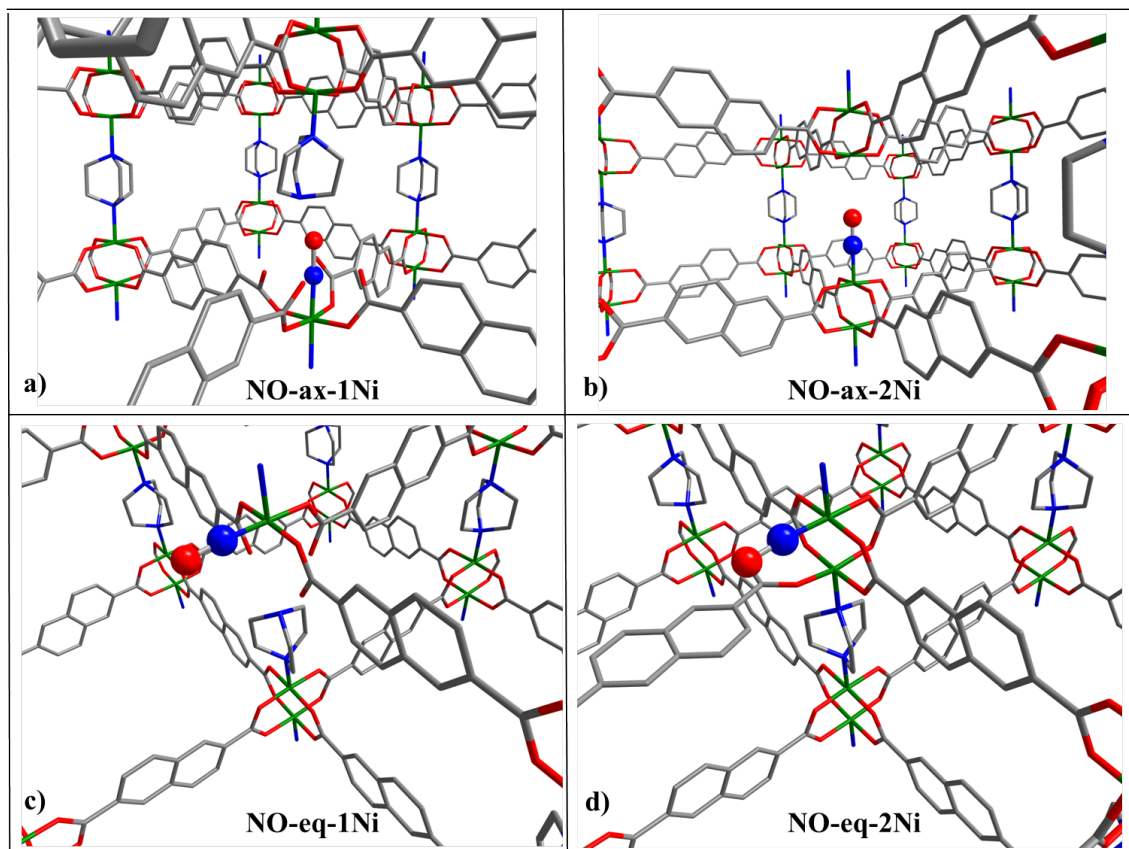


Figure 51: Different qualitative structural models proposed for the coordination of an NO molecule to a defective paddle wheel unit of the DUT-8(Ni) MOF. The abbreviations of the models are written at the bottom of the respective subfigures (a) - (d). The corresponding models are explained in more detail in the text. This figure was first published by Mendt et al. <sup>[224]</sup> and shows oxygen (red), nitrogen (blue), nickel, carbon (grey) and nickel (green) atoms.

be related to the presence of NO. Thus, those signals are similarly explained as for the species NiNOa to NiNOc. They are attributed to  $\text{Ni}^{2+}$ -NO adsorption species, where the unpaired electron is now in the  $\text{Ni}^{2+}$   $d_{z^2}$  orbital, according to the order of their g-tensor values;<sup>[224,312,375,376]</sup> a quite interesting conclusion. According to the MO configuration illustrated in Figure 50b, this interpretation indicates that the double occupied bonding orbital of the  $\text{Ni}^{2+}$ -NO species NiNOd and NiNOe is the bonding MO formed by the  $\text{Ni}^{2+}$   $d_{x^2-y^2}$  AO and the NO  $\pi_y^*$  MO containing the NO's unpaired electron, leaving a single unpaired electron in the  $d_{z^2}$  orbital at the Ni ion. The effective ground state configuration of those complexes is then  $(d_{x^2-y^2} + \pi_y^*)^2 (d_{z^2})^1 (d_{x^2-y^2} - \pi_y^*)^0$ , explaining the EPR derived g-tensor values of the species NiNOd and NiNOe.

Since the  $d_{x^2-y^2}$  AO of the  $\text{Ni}^{2+}$  is involved in the bond to the NO molecule, the following two structural models might be proposed for the species NiNOd and NiNOe as they are also shown schematically in Figure 51c,d:

**NO-eq-1Ni.** The NO molecule binds equatorially to the  $\text{Ni}^{2+}$  ion, replacing a 2,6-ndc ligand of a broken paddle wheel with one missing  $\text{Ni}^{2+}$  ion.

**NO-eq-2Ni.** The NO molecule binds again equatorially to a  $\text{Ni}^{2+}$  ion, which belongs now to a paddle wheel having both  $\text{Ni}^{2+}$  ions. Again, there must be at least one broken bond to a 2,6-ndc ligand providing the adsorption site for the NO molecule. As in case for the scenario NO-ax-2Ni, the second  $\text{Ni}^{2+}$  which is not involved in the NO bond, must be in its  $S = 0$  low spin state.

For the binding scenarios NO-eq-1Ni and NO-eq-2Ni the  $C_4$  pseudo symmetry of the  $\text{Ni}^{2+}$  coordination environment should be destroyed by the equatorial binding of the NO to the  $\text{Ni}^{2+}$ . Thus, one might expect a g-tensor with lower than axial symmetry for the species NiNOd and NiNOe. Indeed, an orthorhombic g-tensor has been resolved for species NiNOd at temperatures  $T < 32$  K for both rigid DUT-8 samples R\_DUT-8a and R\_DUT-8b, as it is shown in Figure 52.<sup>[224]</sup> The corresponding g-tensor principal values are listed in Table 12.

In total, the species NiNOa to NiNOe are most probably NO moieties adsorbed at defective  $\text{Ni}^{2+}$  paddle wheel units of the DUT-8 material. A rough quantification of the observed EPR signals of those species supports this interpretation. The number density of framework  $\text{Ni}^{2+}$  ions in the DUT-8 MOF should be  $N_{\text{Ni}} = 3.04 \mu\text{mol}/\text{mg}$ . Sample R\_DUT-8b, which show the largest number of EPR active  $\text{Ni}^{2+}$ -NO species (see Figure 53),<sup>[224]</sup> contains about  $N_{\text{NO}} \approx 10 \mu\text{mol}/\text{mg}$  NO. But from a rough estimation of the number of spins, contributing to the observed EPR signals of  $\text{Ni}^{2+}$ -NO species in sample R\_DUT-8b at low temperatures (Figure 53d), one obtains that about  $N_{\text{Ni-NO}} \approx 10 \text{nmol}/\text{mg}$  EPR active  $\text{Ni}^{2+}$ -NO species are present in this sample.<sup>[224]</sup> This number is 2 orders of magnitude smaller than  $N_{\text{Ni}}$  and  $N_{\text{NO}}$  indicating the defective nature of the involved  $\text{Ni}^{2+}$  species.

It is worth to mention that no lifetime broadening due to the NO desorption process has been observed for the signals of the species NiNOa to NiNOd up to room temperature for any sample. This is consistent to the proposed covalent bonding model for those species, which would imply a chemisorption of the NO at the  $\text{Ni}^{2+}$  rather than a physisorption, leading to lifetimes of those complexes larger than nanoseconds, even at room temperature.

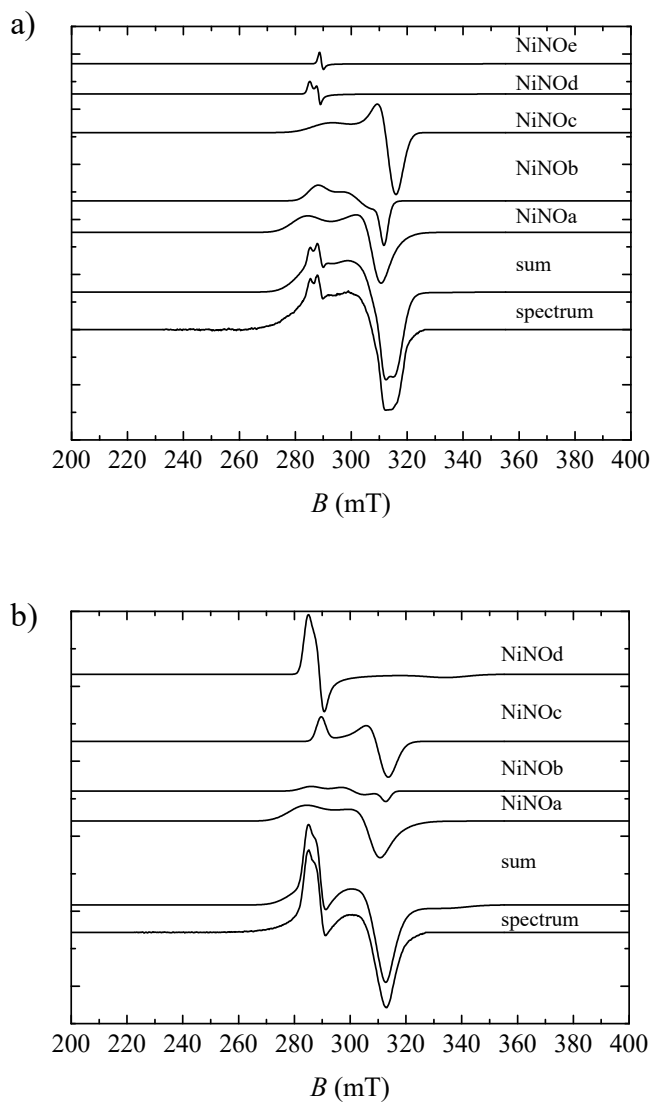


Figure 52: X-band EPR spectra (lowest) and simulations (upper) of sample R\_DUT-8a measured at  $T = 21$  K (a) and sample R\_DUT-8b measured at  $T = 21$  K (b). This figure was first published by Mendt et al.<sup>[224]</sup>



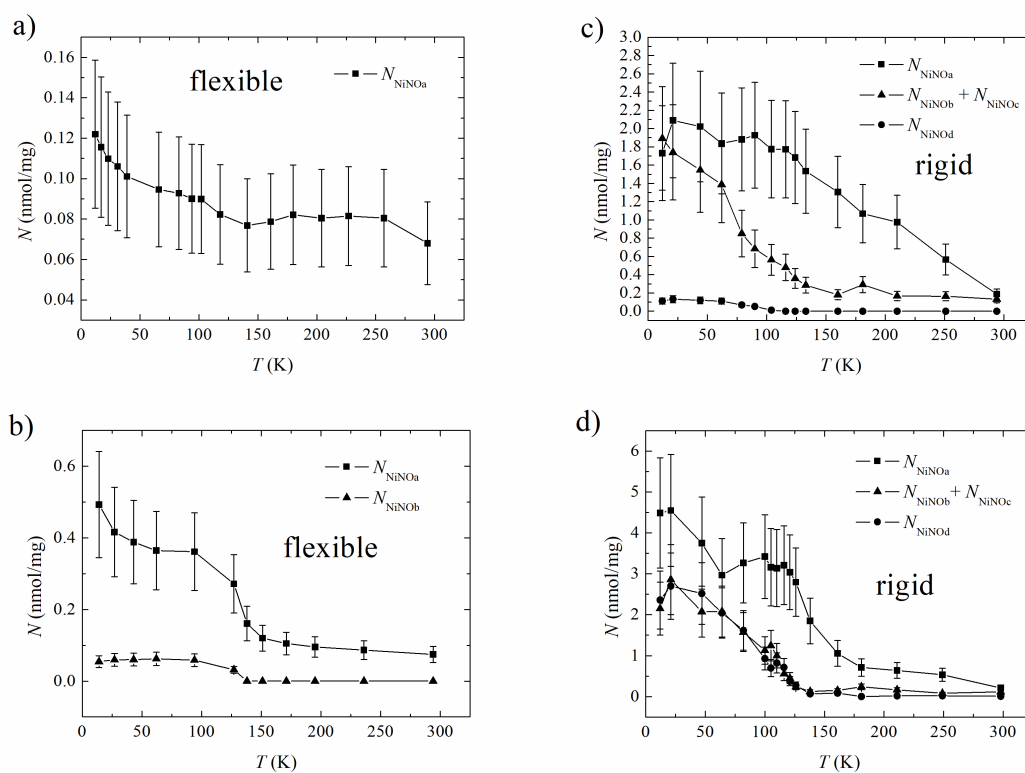


Figure 53: Temperature-dependent simulation derived numbers  $N_{\text{NiNOa}}$  to  $N_{\text{NiNOd}}$  of spins per mass DUT-8(Ni), contributing to the EPR signals of species NiNOa to NiNOd in the samples F\_DUT-8a (a), F\_DUT-8b (b), R\_DUT-8a (c) and R\_DUT-8b (d). This figure was first published by Mendt et al.<sup>[224]</sup>

Nevertheless, an increase of the amount of the EPR active species NiNOa to NiNOd with decreasing temperature was observed experimentally for all four samples as it is illustrated in Figure 53. But this is no contradiction to lifetimes of the  $\text{Ni}^{2+}$ -NO complexes which are long on an EPR time scale. Still, in case of long lifetimes the dynamic equilibrium of the back- and forward reaction:



might be shifted by low temperatures and increasing concentration  $c_{\text{NO}}$  of non-bound NO, with spatial access to the defective  $\text{Ni}^{2+}$  sites, towards the product.

The attribution of the observed  $\text{Ni}^{2+}$ -NO species to defect sites on the surface of the DUT-8 MOF remains somewhat unclear. The absence of any hysteresis effect in the EPR spectra of  $\text{Ni}^{2+}$ -NO as well as their intensities (Figure 53), as observed for the flexible DUT-8(Ni) samples,<sup>[224]</sup> might be an indication for the thesis that at least species NiNOa belongs to a defect on the outer surface of the microcrystals. The presence of some NiNOa signal at room temperature might be also seen as such an indication. On the other hand, the temperature dependences of the EPR intensities of species NiNOa in the samples F\_DUT-8b and R\_DUT-8b show stepwise increases during cooling in temperature ranges where the adsorption of NO occurs or has been almost finished (Figure 53).<sup>[224]</sup> This is a strong indication that the species NiNOa also occurs in the pores of the MOF.<sup>[224]</sup> In addition, the change of the number of spins contributing to the EPR signals of species NiNOb and NiNOc for sample R\_DUT-8a, is  $\Delta(N_{\text{NiNOb}} + N_{\text{NiNOc}}) \approx 1.4$  nmol/mg going from  $T = 116$  K to  $T = 12$  K (Figure 53c). For species NiNOa in sample R\_DUT-8b the corresponding change is  $\Delta N_{\text{NiNOa}} \approx 1$  nmol/mg, going from  $T = 100$  K to  $T = 12$  K (Figure 53d). But in the first case, no signal of any desorbed NO was detected at temperatures  $T < 120$  K whereas in the second case no signal of any desorbed NO was detected at temperatures  $T < 100$  K (Figure 24).<sup>[224]</sup> However, both values  $\Delta(N_{\text{NiNOb}} + N_{\text{NiNOc}})$  and  $\Delta N_{\text{NiNOa}}$  are larger than the detection limit  $N_{\text{limit}} \approx 0.5$  nmol/mg for desorbed NO gas (see appendix D.1).<sup>[224]</sup> This proves that in both cases the formation of additional species NiNOa to NiNOc was not induced by an NO adsorption directly from the reservoir of desorbed NO, indicating that it was supplied from some EPR silent phase of mobilized NO, most probably within the pores of DUT-8. The presence of possible other EPR silent NO phases in the pores of the MOF, like NO weakly interacting with the MOF surface or diamagnetic  $(\text{NO})_2$ ,<sup>[223,339]</sup> is indicated for all MOFs discussed in this thesis and will be picked up in the conclusive chapter 7.

Clearly, species NiNOa occurs in both the flexible and rigid DUT-8(Ni), as proven by EPR (Figure 49). Species NiNOb might occur in both derivatives whereas species NiNOc to NiNOe have been only observed by EPR for the rigid DUT-8(Ni) material, which is an interesting observation. Only species NiNOd and NiNOe indicate an equatorial coordination of the NO molecule to the  $\text{Ni}^{2+}$  paddle wheel. Thus, EPR suggests that only in the rigid but not flexible DUT-8(Ni), defective paddle wheels with broken bonds to the 2,6-ndc ligands are present. This might indicate the absence of a fraction of the ndc ligands in the rigid material, weaken the attractive forces between the ndc ligand molecules, which might

be one reason for the rigidity of that DUT-8(Ni) derivative.<sup>[224]</sup> That London dispersion interactions between stacked ndc ligands are crucial for the stabilization of the non-porous phase of DUT-8(Ni) was recently indicated by comprehensive DFT calculations.<sup>[332]</sup> Also, the EPR derived result that the number density of EPR detected Ni<sup>2+</sup>-NO defect species with a missing dabco ligand is one order of magnitude larger in the rigid than in the flexible derivative of DUT-8(Ni), as observed for the samples F\_DUT-8b and R\_DUT-8b with similar amounts of NO per MOF material (see Figure 53 and Table A.1 in the appendix A) might be related to their difference in flexibility. Indeed, it has been verified recently by SEM<sup>[241]</sup> that the rigid DUT-8(Ni) variant has systematically smaller microcrystals than the flexible one which might correlate with a larger number density of defects in the rigid than flexible DUT-8(Ni). It might be also possible that corresponding defects with a missing dabco ligand might stabilize the open pore structure, preventing their transformation to the cp phase in the absence of any adsorbents.<sup>[224]</sup>

## 6.2 First pulsed EPR experiments

By CW EPR experiments on NO loaded samples with the flexible and rigid variants of DUT-8(Ni), several Ni<sup>2+</sup>-NO adsorption species have been detected. Based on their g-tensor principal values, defect models have been proposed and attributed to those species, as they are illustrated schematically in Figure 51. Nevertheless, some uncertainty remains, regarding these attributions, since the g-tensor principal values reflect only the overall symmetry of the coordination complex and the nature of the Ni<sup>2+</sup>-NO bonding orbital. But more information are obtainable by pulsed EPR methods, which might resolve hfi couplings to neighbored magnetic nuclei like the <sup>14</sup>N of the NO and the dabco ligand as well as protons of the ndc ligands, in principle. In this way, a detailed analysis of the local geometric structure as well as the spin density distribution might be possible. This section presents and discusses first pulsed EPR experiments on the flexible DUT-8(Ni) sample F\_DUT-8b, thought not as a complete and exhaustive study but rather as a proof of principle, motivating further studies for the future.

Figure 54 shows a two-pulse ESE field sweep spectrum of sample F\_DUT-8b, measured at  $T = 6$  K. Two different signals have been detected. One occurs at magnetic fields  $350 \text{ mT} < B_0 < 500 \text{ mT}$ . Similar signals have been observed for the NO loaded samples of the MIL-53(Al) (Figure 28) and MIL-100(Al) (Figure 38) MOF materials. Correspondingly, that signal, observed for sample F\_DUT-8b, is attributed to an NO adsorption species NO3. Its simulation derived g-tensor principal values (Figure 54) are summarized in Table 13. The g-tensor principal values of species NO3 are comparable or even smaller than those g-tensor principal values, which have been determined in the present thesis for NO adsorption species, interacting weakly with the organic parts of the MOFs MIL-53(Al) or MIL-53(100) (see Table 13). Consequently, species NO3 is also attributed to an NO adsorption species occupying surface sites at the organic parts of the DUT-8(Ni) material.<sup>[301]</sup> Pulsed EPR measurements, investigating this species in more detail, might be feasible but are not in the scope of this thesis.

The second signal in the two-pulse ESE field sweep spectrum in Figure 54 is typical for

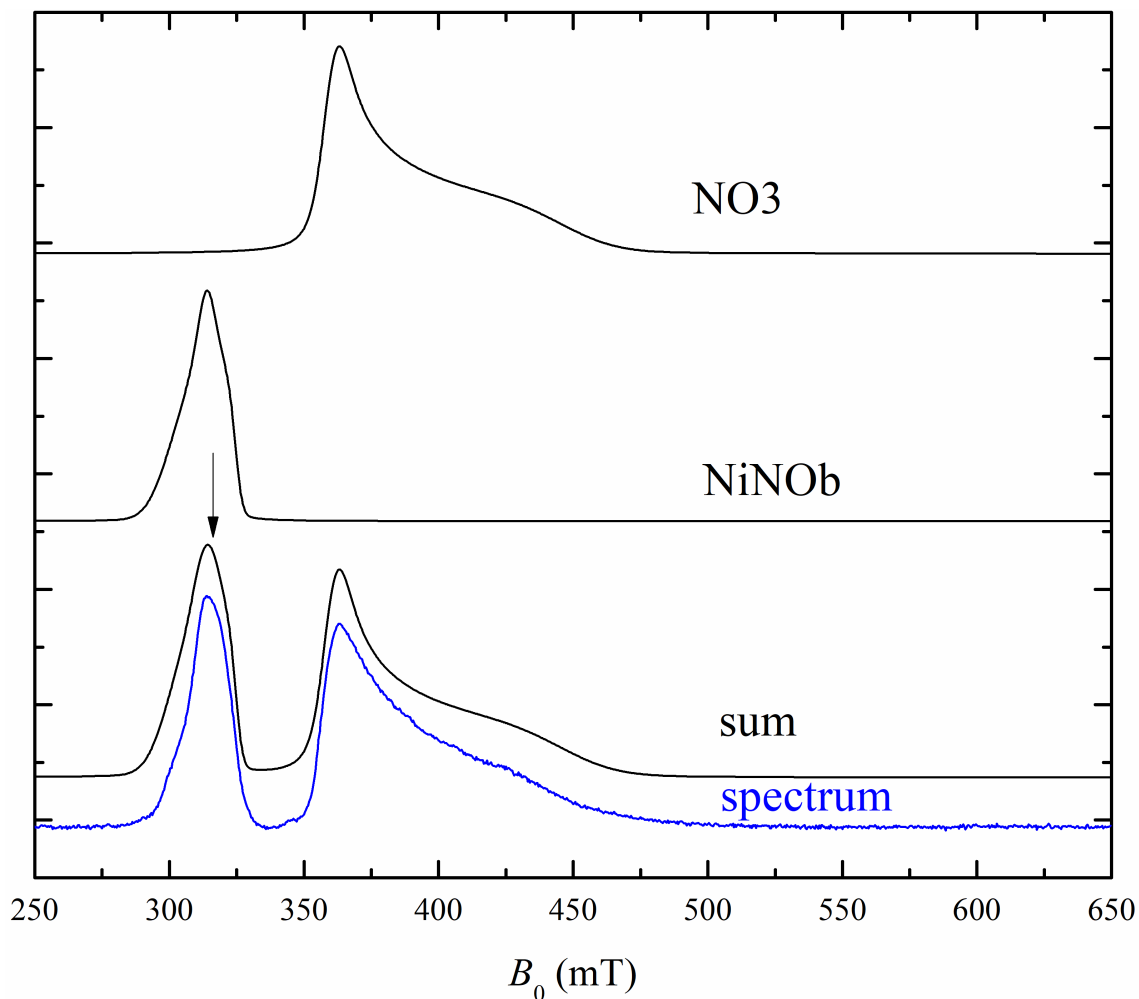


Figure 54: Two-pulse ESE field sweep spectrum (blue) of sample F\_DUT-8b, measured at  $T = 6$  K. The  $\pi/2$  and  $\pi$  pulse lengths were 16 ns and 32 ns, respectively, and the time delay between both pulses was  $\tau = 120$  ns. Simulations of the species NO3 of weakly physisorbed NO and of the  $\text{Ni}^{2+}$ -NO species NiNOb as well as their sum are shown in black. The arrow marks the field position, where the HYSORE and three-pulse ESEEM experiments have been conducted.

Table 13: g-tensor principal values of four different paramagnetic species which have been attributed in this thesis to NO, weakly physisorbed at the organic part of the corresponding MOF.

| Species           | MOF         | $g_x$              | $g_y$               | $g_z$               |
|-------------------|-------------|--------------------|---------------------|---------------------|
| NO1a <sup>a</sup> | MIL-53(Al)  | $1.9838 \pm 0.002$ | $1.9783 \pm 0.0014$ | $1.7637 \pm 0.0071$ |
| NO1b <sup>a</sup> | MIL-53(Al)  | - <sup>b</sup>     | $1.96 \pm 0.03$     | $1.64 \pm 0.03$     |
| NO2d <sup>c</sup> | MIL-100(Al) | $1.97 \pm 0.03$    | $1.97 \pm 0.03$     | 1.4 ... 1.88        |
| NO3               | DUT-8(Ni)   | $1.93 \pm 0.007$   | $1.93 \pm 0.007$    | $1.55 \pm 0.03$     |

<sup>a</sup>Table 3, <sup>b</sup>not resolved within the reasonable range  $g_e > g_x > g_y$ , <sup>c</sup>Table 6

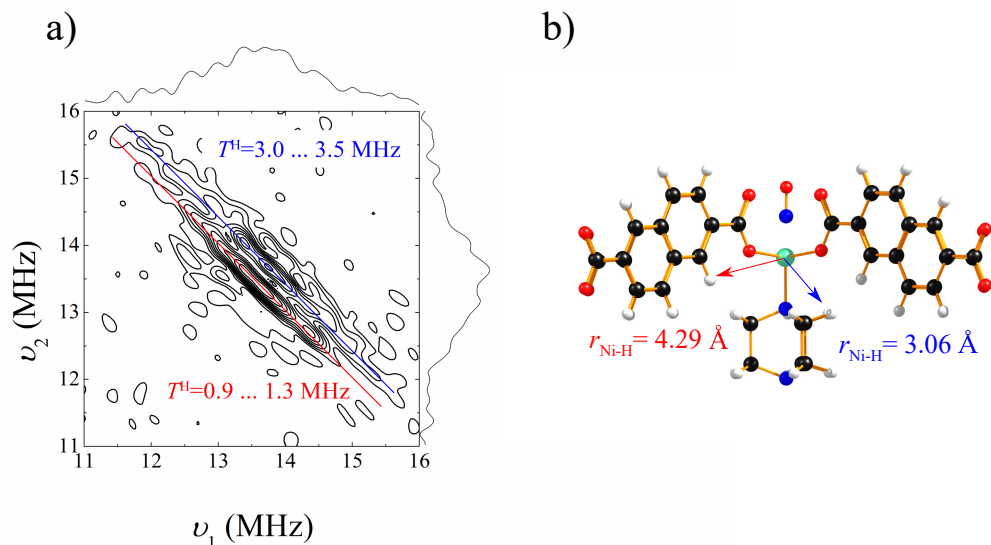


Figure 55: HYSCORE spectrum of sample F\_DUT-8b (a), measured at the temperature  $T = 6$  K and the magnetic field  $B_0 = 317.4$  mT with an inter pulse delay  $\tau = 112$  ns between the first two pulses. The spectrum shows two proton species H1 (red) and H2 (blue). From the maximum distance of their ridges to the anti-diagonal through the proton Larmor frequency, their dipolar hfi parameter  $T^{\text{H}}$  have been estimated as stated in the figure.<sup>[331]</sup> In (b) the schematic structural model NO-ax-1NO (see also Figure 51a) is given, which is consistent to the measured HYSCORE signal of the two proton species H1 and H2. In this model, species H1 are the protons of the ndc ligand, next neighbored to the  $\text{Ni}^{2+}$  ion. Their distance  $r_{\text{Ni-H}}$  to the  $\text{Ni}^{2+}$  ion is given in red. Species H2 are the protons of the dabco ligand, next neighbored to the  $\text{Ni}^{2+}$  ion. Their distance  $r_{\text{Ni-H}}$  to the  $\text{Ni}^{2+}$  ion is given in blue.

an  $S = 1/2$  species with the same g-tensor principal values as species NiNOb has (Table 12). This species is therefore attributed to the  $\text{Ni}^{2+}$ -NO adsorption complex NiNOb. As derived by CW EPR, at that temperature the amount of species NiNOa should be almost one order of magnitude larger than that of species NiNOb (Figure 53). The fact that two-pulse ESE only resolves the signal of species NiNOb might be explained by a short phase memory time of species NiNOa, preventing the formation of a corresponding reasonable electron spin echo.

The species NiNOb was further investigated by recording a HYSCORE spectrum at the observer position  $B_0 = 317.4$  mT at a temperature  $T = 6$  K. Signals of two proton species have been observed as shown in Figure 55a. From the maximum shift of the  $^1\text{H}$  cross peak ridges from the anti-diagonal through the proton Larmor frequency along the diagonal, their dipolar hfi parameters  $T^{\text{H}}$  have been estimated as summarized in Table 14.<sup>[331]</sup> From these values the distances of the corresponding protons to the  $\text{Ni}^{2+}$  ion with the unpaired spin have been estimated (Table 14), using equation (12). Comparing the structural models NO-ax-1Ni and NO-ax-2Ni (Figure 51) the determined proton distances strongly indicate that the former seems to correspond to species NiNOb (Figure 55b, Table

Table 14: Distances  $r_{\text{Ni-H}}$  of different proton species from the 2,6-ndc and the dabco ligands in the defect models NO-ax-1Ni and NO-ax-2Ni, next nearest to the  $\text{Ni}^{2+}$  ion with the unpaired electron,<sup>[240]</sup> dipolar hfi constant  $T^{\text{H}}$  as estimated by HYSCORE spectroscopy for proton species H1 and H2 or from the distance of the  $\text{Ni}^{2+}$  to species H3 as well as the distance  $r_{\text{Ni-H}}(T^{\text{H}})$  between the corresponding protons and the  $\text{Ni}^{2+}$  ion with the unpaired electron, as derived from  $T^{\text{H}}$  using equation (12)

| Proton species                      | $r_{\text{Ni-H}}$ (Å) <sup>b</sup> | $T^{\text{H}}$ (MHz)       | $r_{\text{Ni-H}}(T^{\text{H}})$ (Å) |
|-------------------------------------|------------------------------------|----------------------------|-------------------------------------|
| ndc (H1)                            | 4.29                               | $1.1 \pm 0.2^{\text{c}}$   | $4.2 \pm 0.3$                       |
| dabco (NO-ax-1Ni) (H2)              | 3.06                               | $3.25 \pm 0.25^{\text{c}}$ | $2.9 \pm 0.1$                       |
| dabco (NO-ax-2Ni) (H3) <sup>a</sup> | 5.3                                | $0.53^{\text{d}}$          | -                                   |

<sup>a</sup>This is the next nearest proton of the dabco ligand in model NO-ax-2Ni, which coordinates to the second  $\text{Ni}^{2+}$  ion. <sup>b</sup>as determined from the crystal structure of the lp phase of DUT-8(Ni),<sup>[240]</sup> <sup>c</sup>as determined by HYSCORE spectroscopy, <sup>d</sup>estimated from  $r_{\text{Ni-H}}$  using equation (12).

14). One proton signal (H1) is indicated by its  $T^{\text{H}}$  derived distances to belong to the ndc ligands, whereas the  $T^{\text{H}}$  derived distance of the second proton H2 indicates its affiliation to a dabco ligand coordination to the same  $\text{Ni}^{2+}$  ion, where the NO molecule binds (Figure 55b, Table 14).

At nearly the same observer position where the HYSCORE experiment was performed, a three-pulse ESEEM experiment was conducted for sample F\_DUT-8b at  $T = 6$  K with an inter-pulse delay  $\tau = 112$  ns. The corresponding Fourier-transformed signal is shown in Figure 56. In addition, to signals of distant proton species three frequencies are resolved, which can be attributed to the  $\nu_0 = 1.7 \pm 0.1$  MHz,  $\nu_- = 3.3 \pm 0.3$  MHz,  $\nu_+ = 4.4 \pm 0.2$  MHz and the double quantum transition  $\nu_{\text{dq}} = 7.7 \pm 0.5$  MHz of a  $^{14}\text{N}$  nuclear species.<sup>[380]</sup> Assuming the near cancellation regime  $\frac{A}{2} \approx \nu_{\text{N}}$ , where  $\nu_{\text{N}}$  is the  $^{14}\text{N}$  nucleus Larmor frequency, one derives for that  $^{14}\text{N}$  nuclear species nqi parameters  $C_Q = 1.28 \pm 0.09$  MHz and  $\eta = 0.66 \pm 0.09$  MHz.<sup>[380]</sup> But an assignment of that species to either the NO or dabco  $^{14}\text{N}$  is not feasible from these data alone. Furthermore, for a reliable determination of the  $^{14}\text{N}$  hfi and nqi parameters more orientation selective three-pulse ESEEM and HYSCORE experiments are necessary, which are not part of this thesis. Here, it was shown that sound  $^{14}\text{N}$  ESEEM EPR is possible. Future experiments with  $^{15}\text{NO}$  should enable a clear attribution of the observed nitrogen signals to either NO or the dabco ligand.

### 6.3 Summary of chapter six

X-band CW experiments were performed for NO loaded samples with a flexible and a rigid derivative of the DUT-8(Ni) MOF in a temperature range  $7 \text{ K} < T < 295 \text{ K}$ , searching for microscopic characteristics correlating with the different flexibility of both materials. In total, signals of five different species with electron spin  $S = 1/2$  have been observed and attributed to five different NO- $\text{Ni}^{2+}$  adsorption species NiNOa to NiNOe. They should be of impurity or defect related nature, since the DUT-8(Ni) framework provides no CUS for preferred NO adsorption. The EPR derived estimate of the number of such NO- $\text{Ni}^{2+}$

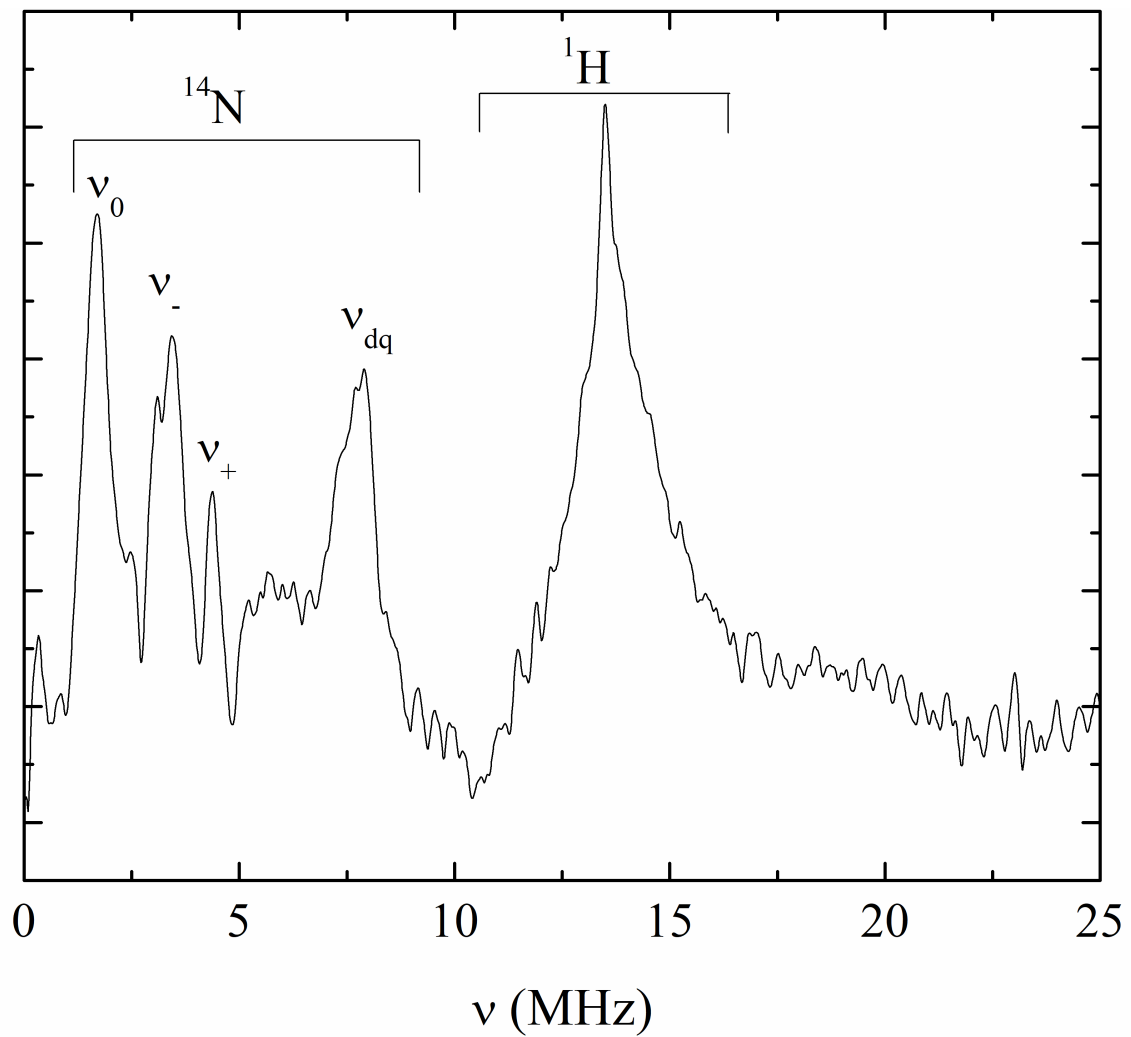


Figure 56: Three-pulse ESEEM spectrum measured at  $T = 6$  K and  $B_0 = 316.4$  mT for sample F\_DUT-8b with an inter-pulse delay between the first two pulses of  $\tau = 112$  ns. Signals that are attributed to a  $^{14}\text{N}$  species and protons are indicated.

species clearly supports their defective nature. A detailed analysis of the temperature-dependent amounts of those species indicates that they form mainly at low temperatures rather from an EPR silent NO phase in the microcrystals than from a phase of desorbed NO gas.

The order of the g-tensor principal values determined by EPR for the species NiNOa to NiNOe give strong indication about the nature of the NO-Ni<sup>2+</sup> bond. For the species NiNOa to NiNOc, which have been observed for both the flexible and rigid derivatives, the unpaired electron is indicated to occupy the  $d_{x^2-y^2}$  AO at the Ni<sup>2+</sup> ion indicating that the  $d_{z^2}$  AO of the Ni<sup>2+</sup> is involved in the bond formed with the NO molecule. Thus, structural models for those species are indicated, where NO binds along the axial direction to the Ni<sup>2+</sup> ion of a paddle wheel unit with either a broken bond to the dabco ligand or with a missing Ni<sup>2+</sup> ion. Indeed, the latter structural model is indicated for species NiNOb by a first pulsed EPR experiments. Signals of two proton species in the vicinity of species NiNOb are resolved by HYSORE experiments for an NO loaded sample with the flexible DUT-8(Ni) and might be attributed to next nearest protons of the adjacent dabco and ndc ligands. A three-pulse ESEEM experiment of the same sample resolves the interaction to a <sup>14</sup>N nitrogen nucleus which might belong either to the NO molecule or to the dabco ligand.

The order of the g-tensor principal values of species NiNOd and NiNOe is different to that of the former three species, indicating that for NiNOd and NiNOe the unpaired electron occupies the  $d_{z^2}$  AO at a Ni<sup>2+</sup> ion. As a consequence, for those both species the  $d_{x^2-y^2}$  AO of the Ni<sup>2+</sup> is indicated to be involved in the bond formed with the NO molecule. These results indicate structural models for species NiNOd and NiNOe, where NO binds equatorial to a Ni<sup>2+</sup> ion of a broken paddle wheel unit with either one or two Ni<sup>2+</sup> ions, namely along a former but now broken bond to an ndc ligand. The corresponding distortion of the pseudo  $C_4$  symmetry axis of this complex can be resolved by the EPR signal of species NiNOd at low temperatures.

Species NiNOd and NiNOe have been only observed for the NO loaded samples of the rigid DUT-8(Ni), indicating that this specific kind of defect might be related to the rigidity of this DUT-8(Ni) derivative. These results might indicate a scenario, where missing ndc ligands weaken the attractive London dispersion interaction of those ligands<sup>[332]</sup> possibly preventing the collapse of the framework to the non-porous phase. In addition, it is observed by EPR that one order of magnitude more defective NO-Ni<sup>2+</sup> species are present for the rigid than the flexible DUT-8(Ni) derivative, which might relate to published SEM results<sup>[241]</sup> where it was observed that the rigid DUT-(Ni) has significantly smaller microcrystals than its flexible variant. This indicates that either the small size of such crystals or the large number of defects or both factors might stabilize the porous phase of DUT-8(Ni), keeping it rigid.



---

## 7 Conclusive discussion

This thesis presents the first detailed characterization of NO adsorption in MOFs by EPR spectroscopy. The investigated model systems, MIL-53(Al), MIL-100(Al) and DUT-8(Ni), comprise MOFs with closed shell metal ions without and with CUS, and one MOF material with open shell metal ions but without CUS in its framework structure, respectively. Experiments on a fourth MOF MIL-100(Fe) with an open shell metal ion and with CUS showed no signals of adsorbed NO and are therefore not presented in this thesis.<sup>[223,381]</sup> Furthermore, the choice of MOFs include rigid MOFs as well as two MOFs showing two kind of different flexibility, namely breathing and gate pressure opening.

Detailed results of the studies are summarized in the sections 3.4, 4.3, 5.7 and 6.3 and are also listed in the next chapter 8. It was shown, how one can quantify the pressure and amount of desorbed NO in an EPR tube *in situ* from the line width of its EPR signal. Both, the intensity and line width of the EPR signal of desorbed NO provided information about the NO adsorption and desorption characteristics for all investigated MOF samples. This way it was found that the characteristic NO adsorption/desorption temperature increases for the MOF materials in the order flexible DUT-8(Ni) < rigid DUT-8(Ni)  $\approx$  MIL-53(Al/Cr) < MIL-100(Al), reflecting the kind of porosity and the absence or presence of CUS in those materials. Adsorption and desorption related hysteresis effects were resolved by the NO gas signals EPR line width for all flexible materials but not for the rigid ones. For the MIL-53(Al/Cr) material the EPR signal intensity of desorbed NO resolves no such hysteresis effect, demonstrating that at low gas pressures the line width based quantification of desorbed NO is more sensitive than the EPR intensity based approach. Furthermore, such a small hysteresis effect for the MIL-53(Al/Cr) material as well as the similarity of its NO adsorption/desorption temperature to that of the rigid DUT-8(Ni) material indicate that at low gas pressures the NO adsorption characteristics of the investigated porous MOF materials are almost independent of the pore size shape and are defined primarily by the inner surface sites characteristics.

Different kinds of NO adsorption species were detected and characterized by CW EPR and high resolution pulsed EPR spectroscopy at low temperatures, including NO species interacting with protons in the MIL-53(Al) material, NO weakly physisorbed at the framework Al<sup>3+</sup> CUS of the MIL-100(Al) MOF and NO chemisorbed at defective Ni<sup>2+</sup> CUS in flexible and rigid DUT-8(Ni) derivatives. It was shown by CW and pulsed EPR that NO adsorbs at low temperatures in the np phase of MIL-53, interacting with protons of the framework. In particular, hydrogen bonds to the NO are indicated and positions of the NO species in the pores were suggested based on the EPR results. A structure is consistent to the EPR results, where NO interacts with two opposite  $\mu_2$ -(OH) groups in the np phase. The absence of any aluminum species in the first coordination sphere of NO adsorbed in MIL-53 indicates that the amount of defective open metal sites in this MOF is either comparatively small or that such defective CUS are not spatially accessible for NO. But not only for the MIL-53(Al) material NO adsorption species, interacting with the organic part of the MOF framework, were observed. Also for the MIL-100(Al) and the DUT-8(Ni) MOFs NO adsorption species were observed and characterized by EPR, for which their

physisorption at the MOFs organic part is strongly indicated.

The study presented in chapter 5 succeeds in a complete determination of the electronic and geometric structure of the low temperature NO adsorption complex at the framework CUS of the MIL-100(Al) MOF material by a combined EPR and DFT approach. It has high significance for the field of heterogeneous catalysis that this study exemplarily shows successfully that one can probe with EPR by the NO  $^{14}\text{N}$  hfi reliably the Lewis acidity of an  $\text{Al}^{3+}$  CUS in an Al-based MOF, determining at the same time its real nature by the  $^{27}\text{Al}$  hfi, which modulates the EPR signal of the adsorbed NO. In particular the presented EPR results, concerning species NO<sub>2</sub>a adsorbed on MIL-100(Al), indicate that the  $\text{Al}^{3+}$  CUS in the MIL-100(Al) has a similar Lewis acidity as Lewis acid sites in the H-ZSM-5 zeolite have. This is in line with results obtained independently by IR spectroscopy using acetonitrile as an IR active probe molecule.<sup>[205,367]</sup> But IR might not allow in general for an unambiguous decision about the true nature of the probed Lewis acid site. Particularly, this method might not rule out the possibility that the probed metal site is rather a defect or impurity species than a framework CUS in a MOF. It is a result of the present study that EPR of adsorbed NO is in this sense better suited for the characterization of the Lewis acid sites in Al-based MOFs than IR of certain probe molecules, since it provides an additional spectroscopic feature, namely the  $^{27}\text{Al}$  hfi, which can be determined by EPR in principle. In combination with comprehensive DFT calculations, this additional information enables a reliable decision about the true nature of the  $\text{Al}^{3+}$  Lewis acid site, probing by the same time its Lewis acidity by the adsorbed NO  $^{14}\text{N}$  hfi. To the best of the authors knowledge, the combined EPR and DFT based approach for the characterization of  $\text{Al}^{3+}$  Lewis acid sites presented in this thesis, is the first of its kind that was reported in literature. Future studies might extend this method to other Al-based MOFs or solid surfaces and might be particularly helpful for studies of catalytically active materials with several  $\text{Al}^{3+}$  CUS species, where the origin of the catalytic activity and its relation to the different open metal sites needs to be understood.

Of similar significance might be the CW EPR characterization of defective NO- $\text{Ni}^{2+}$  species in the flexible and rigid DUT-8(Ni) derivatives, as reported in chapter 6. Hardly any other method can give as detailed insights into the nature of such defects as EPR can do as shown in the present study. A rough EPR based quantification of such defective species indicate that the rigid DUT-8(Ni) has one order of magnitude more defects than its flexible counterpart. Assuming that the EPR probed defects are broken paddle wheel units, EPR provides the information, which bound to which ligand is broken. In particular, the rigid derivative of DUT-8(Ni) appears to have a unique kind of defective  $\text{Ni}^{2+}$  ion species, which does not occur in the flexible DUT-8(Ni) derivative. The presented EPR results indicate that this specific kind of defect is a paddle wheel unit with at least one broken bond to an organic ndc ligand. This opens the door to further detailed studies investigating the relation between such different kinds of defects and different kinds of flexibility of the DUT-8(Ni) derivatives. These studies should include high-resolution pulsed EPR methods of NO adsorbed on the DUT-8(Ni) materials, possibly including  $^{15}\text{NO}$  to distinguish between spectroscopy signals of the dabco and NO nitrogen nuclei. That such studies are feasible,

---

is exemplarily shown by first pulsed EPR experiments of Ni<sup>2+</sup>-NO adsorption complexes in the DUT-8(Ni) material as presented in this thesis. Such experiments are able to provide additional information about the types and the arrangement of the ligand molecules that bind to the NO-Ni<sup>2+</sup> species.

Several results of this thesis concern the interaction of NO with the organic part of the MOF materials. For every MOF one expects low temperature EPR signals of NO species, weakly physisorbed at the organic part, since MOFs possess organic building units. This thesis shows that one observes EPR signals characteristic for NO, adsorbed at the organic part, for all three MOFs MIL-53(Al), MIL-100(Al) and DUT-8(Ni). For the former two, those weakly physisorbed NO adsorption species were further investigated by HYSORE spectroscopy. Interestingly, the corresponding NO species in MIL-53(Al) show unusually large hfi with protons, whereas NO adsorbed in the MIL-100(Al) show only weak hfi with protons. One can speculate that this is related to spatial restrictions in the narrow pores of the np phase of MIL-53(Al), forcing smaller distances between the NO and the hydrogen atoms in this MOF material, whereas the large pores of the MIL-100(Al) allow for larger distances between NO and hydrogen atoms. Nevertheless, the interaction energy should be small and similar: As it was already mentioned, EPR of desorbed NO shows that the NO adsorption characteristics depend on the MOF surface sites characteristics but not on the MOF pore size at low gas pressures.

Within a certain temperature range  $85 \text{ K} < T < 120 \text{ K}$  no significant EPR signal of any NO species was detected for the sample Al/Cr-MIL-53 (Figure 26) as it was also not observed for sample Al-MIL-53. This means that within this temperature range most of the NO must be present in some EPR silent phase. Since most of the desorbed NO was not detectable anymore above the temperature  $T = 115 \text{ K}$ , where NO gas is known to freeze out (see section 3.2), the EPR silent NO species are most likely completely absorbed within the pores of the MIL-53. The presence of such EPR silent NO species absorbed in the pores of the MOF material is also indicated for the DUT-8(Ni) and MIL-100(Al) samples. Both show only a small fraction of EPR active adsorbed NO moieties at low temperatures which is much lower than the NO amount in those samples, indicating that most NO is present in an EPR silent state. A large fraction of EPR silent NO does not seem to occur only for MOFs but was also observed for NO adsorbed in some zeolites.<sup>[198]</sup>

What is the nature of these EPR silent phases? This question is not accessible by EPR and should be addressed with other methods like IR spectroscopy.<sup>[223]</sup> Here, one can only speculate and some possible explanations are listed in the following:

- Collisions between NO molecules and between NO molecules and the MOF surface might shorten the lifetime of their magnetic states and, therefore, their EPR signal broadens and becomes undetectable.
- Another possibility might be that NO is weakly physisorbed at surface sites within the MOF where the electric field gradient is too weak to quench the orbital momentum significantly.<sup>[301]</sup> Therefore, the g-values of those species might be too high and perhaps too inhomogeneously distributed to enable a detection by EPR. Indeed, a broad landscape of NO weakly physisorbed on MOFs was observed by IR spec-

troscopy and partially attributed to NO interacting with the aromatic carboxylic acid linkers.<sup>[223]</sup>

- It is also possible that NO forms diamagnetic (NO)<sub>2</sub> inside the MOF as it was observed for the mesoporous silica MCM-41 which has pore diameters of about  $D = 3.0$  nm.<sup>[339]</sup> There, the NO dimers form at temperatures  $T < 90$  K almost independently of the filling ratio. Such a formation is indicated in the present study by a drop of the EPR intensity of NO adsorbed on the MIL-100(Al) material likewise at lower temperatures.<sup>[223]</sup> For MOFs, the formation of diamagnetic (NO)<sub>2</sub> might occur at higher temperatures. There is computational evidence that aromatic environments, as they are usually provided by the ligand molecules of MOFs, promote the occurrence of such NO-dimers. Ab initio quantum mechanical calculations have indicated that in the presence of a benzene molecule the NO monomer is still favored, but that the dimerization equilibrium is significantly shifted towards the product.<sup>[382]</sup>

Beyond such speculations, one has to rely on other methods. IR spectroscopy indicates the formation of a variety of adsorbed N<sub>x</sub>O<sub>y</sub> species in NO loaded MOF samples<sup>[223]</sup> and is therefore an indispensable method to get a full picture of the NO adsorption on MOFs, addressing also EPR silent species.

The present thesis shows that EPR is an irreplaceable method for the detailed investigation of selective NO adsorption species in MOFs. EPR has the ability to resolve the hfi between NO and paramagnetic nuclei like <sup>27</sup>Al or protons. The high sensitivity, offered by EPR, allows for the selective detection and detailed characterization of even less abundant NO adsorption species. Here, it is shown how EPR of adsorbed NO reveals results of high significance for research concerning heterogeneous catalytic applications using Al-based MOFs and concerning an understanding of the microscopic origins of framework flexibility in MOFs. As further shown in this thesis, the ability of EPR to resolve and quantify the signal of desorbed NO and NO, weakly interacting with the organic part of the MOF, gives additional insight into the adsorption characteristics of NO, completing the picture in this way. Thus, the present study hopefully inspires further studies, extending the proposed methodologies to a broader application in MOF research.

---

## 8 Summary

Metal-organic frameworks (MOFs) are a class of porous solids that have gained a lot of interest since the pioneering works in the early 1990.<sup>[4-9]</sup> They consist of metal-oxygen clusters which are connected by organic ligand molecules forming microporous crystalline networks.<sup>[2,3]</sup> Their ultrahigh porosity, large internal surface areas and the enormous number of possible MOF designs<sup>[3]</sup> promise applications<sup>[10,12]</sup> like in gas storage,<sup>[20]</sup> separation,<sup>[28]</sup> catalysis, sensors<sup>[47]</sup> and drug delivery.<sup>[70]</sup>

The small molecule nitric oxide (NO) plays important roles in many physiological processes.<sup>[140,144-150]</sup> Therefore, the usage of porous materials<sup>[163]</sup> acting as NO drug delivery agents has become an important task aiming at medical applications like wound-healing or cancer treatment.<sup>[155,156]</sup> In particular, MOFs can store and release NO in a controlled manner<sup>[173-183]</sup> but further research toward a MOF based drug delivery agent is still necessary. In this context, an understanding of the fundamentals of NO adsorption on MOFs has uttermost significance.

The sorption characteristics of NO are mainly determined by the interaction between the NO molecule and the MOF surface. Since NO has one unpaired electron, valuable information about the local microscopic characteristics of NO adsorption sites can be obtained by electron paramagnetic resonance (EPR) spectroscopy which measures the energy differences between the magnetic states of the NO's electron spin altered by its local microscopic environment. This has been demonstrated for NO adsorption on zeolites and metal-oxide surfaces<sup>[92]</sup> but not yet for NO adsorption on MOFs.

Information obtained by EPR spectroscopy are not only relevant for the fundamentals of NO sorption related applications of MOFs. They might also shed light on other fundamental questions related to the characterization of catalytic active<sup>[383]</sup> or defective sites in MOFs<sup>[384]</sup> for which NO can be used as an EPR active probe molecule. Motivated by the mentioned reasons, the present thesis thoroughly studies the NO adsorption on MOFs by EPR for the first time, namely on the MIL-53(Al)<sup>[238]</sup> material and its chromium doped variant,<sup>[110]</sup> on the MIL-100(Al)<sup>[239]</sup> and on flexible and rigid derivatives of the DUT-8(Ni).<sup>[240,241]</sup> This representative selection covers important properties of MOFs like the presence or absence of coordinative unsaturated metal sites (CUS), metal ions with closed or open shell electron configuration, and materials with and without intrinsic structural flexibility. The general scientific question of this thesis asks for characteristics of the interaction between NO and the MOF surfaces, which can be obtained by cw and high resolution pulsed EPR methods. This includes the exploration of the NO sorption properties by EPR as well as the study of the local geometric and electronic structure of NO adsorption species. The present thesis has found the following results:

- The only material with CUS, namely MIL-100(Al), has the highest, and the only non-porous MOF, namely the flexible DUT-8(Ni) in its closed-pore phase, has the lowest NO sorption temperature.<sup>[223,224]</sup>
- All porous MOF phases without CUS have almost identical sorption temperatures, although their pore sizes differ significantly.<sup>[223,224]</sup> This indicates that the interac-

tions between NO and the organic part of the MOF surface and not the geometric characteristics of the MOF frameworks dominate the sorption processes in porous MOFs without CUS at low NO loading. In fact, in all materials weakly physisorbed NO is observed by EPR spectroscopy at low temperatures,<sup>[223,224,242]</sup> and its interaction with the organic part of the MOF is indicated by pulsed EPR experiments.<sup>[242]</sup>

- Quantitative EPR of desorbed NO gas resolved ad- and desorption related hysteresis effects only for the flexible materials, indicating the occurrence of NO sorption triggered structural phase transitions for the MIL-53 and flexible DUT-8(Ni) materials.<sup>[224]</sup>
- The linewidth of the EPR signal of desorbed NO depends on the NO gas pressure linearly.<sup>[222]</sup> This relation allowed a rough quantification of the amount of desorbed NO in the MOF containing EPR samples. The quantification of desorbed NO by its EPR signal linewidth is at small gas pressures more precise than the quantification by its EPR signal intensity. In addition, from the linewidth-pressure dependence of desorbed NO gas an effective collisional cross-section was determined in terms of kinetic theory, and turned out to be almost temperature independent.
- For the MIL-53(Al) material, two NO adsorption species were found by EPR spectroscopy, which weakly physisorb at non-metallic sites in the narrow pore phase. Hyperfine couplings to protons are consistent to a scenario where one species is located in the middle of the pore interacting with the protons of two opposite  $\mu_2$ -OH group. The second species also interacts with protons of the framework. Here, unusual large proton hyperfine couplings indicate hydrogen bonds between the protons and the NO.
- By thorough EPR experiments and density functional theory (DFT) calculations, the low temperature NO adsorption at the  $\text{Al}^{3+}$  CUS of the MIL-100(Al) material was verified and its geometric and electronic structure was determined in detail.<sup>[223,242]</sup> This NO- $\text{Al}^{3+}$  complex has a bent end-on geometry where the binding is ionic with almost no covalent contributions. The DFT derived binding energy is characteristic for a physisorption which is also supported by temperature dependent EPR experiments.<sup>[223]</sup> This explains the absence of any distinct infrared spectroscopic (IR) signal of this species.<sup>[223]</sup> The DFT derived flat potential energy surface indicates the inset of rotations about the N-Al axis at temperatures, where the NO still binds to the metal site. Accordingly, EPR observed a distinct NO adsorption species which seems to show some thermally activated motion on the EPR time scale. In addition, EPR characterizes the Lewis acidity of the  $\text{Al}^{3+}$  CUS in MIL-100(Al), qualitatively confirming results obtained independently by IR spectroscopy by other authors using the probe molecule acetonitrile.<sup>[383]</sup>
- Several NO- $\text{Ni}^{2+}$  adsorption species were observed by EPR in all NO loaded samples of DUT-8(Ni).<sup>[224]</sup> They were attributed to NO species chemisorbed at open metal sites of defective paddle wheel units of the DUT-8(Ni). Two different kind of defects could

---

be identified: One where NO binds axially, and one where NO binds equatorially to the Ni<sup>2+</sup> ion. Thus, the former kind represents most likely defects with broken bonds to an 1,4-diazabicyclo[2.2.2]octane ligand, and the latter defects with broken bonds to a 2,6-naphthalenedicarboxylate ligand. Pulsed EPR indicates further, that defective paddle wheels with one missing Ni<sup>2+</sup> ion contribute to the former kind. The latter kind of defect could be only observed for the rigid DUT-8(Ni) material. Also the EPR derived number density of defects is one order of magnitude larger for the rigid than for the flexible DUT-8(Ni). This correlation of the kind and amount of defects with the framework responsiveness of the DUT-8(Ni) can be hardly studied by other methods and contributes to fundamental questions concerning the origin of flexibility in MOFs.<sup>[224]</sup>

- In all materials a large amount of EPR silent NO is present at low temperatures. Particularly, for MIL-100(Al) the low temperature formation of diamagnetic (NO)<sub>2</sub> is indicated.<sup>[223]</sup>

In summary, this thesis gives significant insights into the interaction of NO with the surface of a representative selection of MOFs. It demonstrates how CW and pulsed EPR investigations of NO adsorbed on MOFs can characterize framework as well as defective surface sites, complementing other experimental methods and addressing fundamental questions in current MOF research.

## A Samples

### A.1 Synthesis and Characterization

The MIL-53 materials were synthesized under mild hydrothermal conditions in the group of Prof. Dr. Martin Hartmann, Erlangen.<sup>[110,223,238]</sup> In case of MIL-53(Al/Cr) about two percent of the framework  $\text{Al}^{3+}$  ions were replaced by  $\text{Cr}^{3+}$ .<sup>[223]</sup> The MIL-100(Al) was also synthesized under hydrothermal conditions,<sup>[223,385,386]</sup> whereas the flexible<sup>[243]</sup> and rigid DUT-8(Ni)<sup>[246]</sup> materials were synthesized by solvothermal procedures.<sup>[224]</sup>

The MIL-53(Al/Cr) and MIL-100(Al) materials were characterized by PXRD and  $\text{N}_2$  sorption measurements at 77 K and thermogravimetric analysis (TGA) combined with mass spectroscopy (MS).<sup>[223]</sup> The DUT-8(Ni) materials were characterized by PXRD and  $\text{N}_2$  sorption experiments at 77 K.<sup>[224]</sup>

### A.2 Preparation of EPR experiments

For the preparation of the EPR samples with pure NO gas, conventional X-band EPR quartz glass tubes with an inner diameter  $d_{\text{tube}} = 2.8$  mm were connected to a stainless steel vacuum line.<sup>[222]</sup> After their evacuation to pressures  $p < 10^{-4}$  mbar the vacuum line and the sample tube were filled with NO gas with 99.5 percent purity. The pressure  $p_{\text{NO}}$  of the NO gas was measured with a Leybold CM 1000 capacitance gauge. Keeping this pressure the EPR tube was sealed at room temperature.

All EPR samples containing MOF powders were prepared in similar ways.<sup>[223,224]</sup> First a small amount (see Table A.1) of the material was filled into an X-band or Q-band quartz glass tube. Then, this tube was connected to a stainless steel vacuum line via a stainless steel valve. The sample was outgassed at pressures  $p < 10^{-4}$  mbar for about one hour and subsequently activated for more than 16 hours. The activation temperatures were 523 K, 393 K, 443 K and 393 K for the MIL-53(Al), MIL-53(Al/Cr), MIL-100(Al) and DUT-8(Ni) materials, respectively. Then, the EPR sample tube was sealed or loaded with NO. In the latter case a small and defined amount of NO gas with 99.5 percent purity was condensed in the EPR tube at the stainless steel vacuum line (Table A.1), using liquid nitrogen as a cold trap. Then, the valve with the EPR tube was disconnected from the vacuum line. The EPR tube was sealed immediately during the application of a cold trap at 77 K, which ensures that the whole amount of NO was condensed in the tube before and during the sealing. Only for sample Al-MIL-53 the sample volume was cooled just before but not during the sealing procedure, which is considered by the large error of the amount of loaded NO (Table A.1).

### A.3 Nomination of the EPR samples

An EPR sample with pure NO gas with a room temperature gas pressure  $p_{\text{NO}}$  is denoted as  $\text{NO}_p$  where the number  $p$  is  $p_{\text{NO}}$  in mbar. The MIL-53(M) (M = Al or Al/Cr) EPR samples with NO are called M-MIL-53. The MIL-100(Al) EPR samples with NO are called Al-MIL-100. The DUT-8(Ni) EPR samples containing NO are called X\_DUT-8y (X = F,R), (y = a,b). The first letters 'F' or 'R' denote samples with the flexible or rigid derivative of



Table A.1: The amount of NO in the different EPR samples. The mass  $m$  is the amount of the MOF material in the EPR tube before the activation.  $M^{n+}:NO$  is the estimated ratio between the number of metal cations of the MOF material and the number of loaded NO molecules,  $N_{NO}$  is the total amount of loaded NO and  $p_{NO}$  is the room temperature pressure of desorbed NO in the sample tube assuming the full desorption of the gas. Note that this table lists both, the X-band and Q-band sample of Al-MIL-53 as indicated.

| EPR sample         | $m$ (mg) | $M^{n+}:NO^a$          | $N_{NO}$ ( $\mu\text{mol}$ ) | $p_{NO}$ (mbar)  |
|--------------------|----------|------------------------|------------------------------|------------------|
| Al-MIL-53 (X-band) | 9.3      | 1:1...6:1 <sup>b</sup> | $32 \pm 21^b$                | $695 \pm 455^b$  |
| Al-MIL-53 (Q-band) | 1.1      | 1:1.7                  | $6.4 \pm 0.7$                | $2800 \pm 600^c$ |
| Al/Cr-MIL-53       | 5.4      | 9:1                    | $2.6 \pm 0.3$                | $61 \pm 9$       |
| Al-MIL-100         | 9.0      | 14:1                   | $2.8 \pm 0.3$                | $35 \pm 5$       |
| F_DUT-8a           | 10.4     | 11:1                   | $2.9 \pm 0.3$                | $62 \pm 7$       |
| F_DUT-8b           | 5.7      | 1:2.3                  | $40 \pm 5$                   | $860 \pm 90$     |
| R_DUT-8a           | 5.5      | 6:1                    | $2.8 \pm 0.3$                | $60 \pm 6$       |
| R_DUT-8b           | 4.0      | 1:3.3                  | $40 \pm 5$                   | $800 \pm 80$     |

<sup>a</sup>This ratio was determined assuming that the whole material in the sample tube belongs to the MOF. Therefore, the number of metal centers might be slightly overestimated due to the presence of certain impurity phases, water or solvent molecules. <sup>b</sup>Here, the EPR samples were first cooled in liquid nitrogen to condense all the NO in the EPR tube, then quickly removed from the nitrogen and immediately sealed. Nevertheless, one expects that some NO gas moved out of the tube during the short time between cooling and sealing. This is considered by the large error. <sup>c</sup>This large room temperature pressure originates from the small volume of the Q-band sample tube.

this MOF. Small letters 'a' or 'b' at the end of the sample names denote samples with a small or large amount of NO, respectively. The amount of the MOF material and NO gas for NO loaded EPR samples are summarized in Table A.1.

## B Spectroscopic details

### B.1 Experimental setup

Almost all X-band CW EPR measurements were performed on a Bruker EMX micro (9.4 GHz) spectrometer fitted with a Bruker ER 4119HS cylindrical cavity. For enabling low temperature measurements between  $T = 5$  K and room temperature an Oxford Instruments He cryostat ESR 900 was used. For sample  $NO_{48}$  low temperature CW measurements were also performed on an ELEXYS E580 (9.5 GHz) spectrometer with a Bruker EN 4118X-MD-5 cylindrical cavity and equipped with an Oxford Instruments He cryostat CF935 which cools the whole sample.

CW EPR experiments at Q-band frequency were performed on a Bruker EMX 10-40 (34 GHz) spectrometer equipped with an Oxford Instruments CF935 He cryostat enabling the cooling between  $T = 5$  K and room temperature.

To ensure for low temperature measurements the presence of thermal equilibrated states of the samples, before each measurement at least two minutes for the DUT-8(Ni) samples and at least five minutes for all other samples, had been waited at a given temperature

before measuring the first spectrum. Test measurements after waiting ten minutes to one hour show no significant spectral differences of the signals, indicating that thermal equilibrium had been reached within the spectral resolution.

For CW EPR spectra, measurements at different microwave powers ensured that no linewidth distortion due to saturation effects were present.

For the pulsed EPR experiments at X-band frequency a Bruker ELEXYS E580 (9.75 GHz) spectrometer was used, equipped with an ER411X-MD-5 dielectric pulse ENDOR resonator. Here, cooling was enabled again by an Oxford Instruments CF935 He cryostat.

All two-pulse ESE field sweep experiments were performed using the two-pulse ESE pulse sequence (Figure 9a) measuring the induced electron spin echo in dependence of the magnetic field. In almost all cases pulse-lengths  $\tau_{\pi/2} = 16$  ns and  $\tau_{\pi} = 32$  ns were applied for the non-selective  $\pi/2$ - and  $\pi$ -pulses, respectively, and the inter-pulse delay time was set to  $\tau = 120$  ns for the MIL-53(Al) and DUT-8(Ni) samples and to  $\tau = 140$  ns for the MIL-100(Al) samples. For the MIL-100(Al) samples additional two-pulse ESE field sweep experiments were performed with selective mw pulses, setting  $\tau_{\pi/2} = 100$  ns,  $\tau_{\pi} = 200$  ns and  $\tau = 1200$  ns, reproducing the conditions of the respective ENDOR experiments of Davies type.

For HYSORE experiments the HYSORE pulse sequence (Figure 9c) was used with initial values  $t_1 = t_2 = 80$  ns for the MIL-53(Al) and MIL-100(Al) samples and  $t_1 = t_2 = 40$  ns for the DUT-8(Ni) samples. In all cases the same values for  $\tau_{\pi/2}$  and  $\tau_{\pi}$  were used as applied for the two-pulse ESE field sweep experiments with non-selective pulses. The values  $t_1$  and  $t_2$  were increased independently in time steps  $\Delta t = 16$  ns for the MIL-53(Al) samples,  $\Delta t = 24$  ns for the MIL-100(Al) samples and  $\Delta t = 28$  ns for the DUT-8(Ni) samples, optimized for the detection of  $^{14}\text{N}$  nuclei in the last case. In that way,  $170 \times 170$  2D time domain spectra of the HYSORE echo intensity were recorded in each case. Those spectra were base line corrected by third-order polynomials, zero filled to  $1024 \times 1024$  data points and after 2D Fourier transformations the 2D frequency domain HYSORE spectra were obtained. The blind spots inherent for the HYSORE experiments have been considered, adjusting field dependently the  $\tau$  value for optimized proton signals<sup>[280]</sup> or signals of strongly coupled  $^{27}\text{Al}$  nuclei (see Figure 12).<sup>[242]</sup> If necessary, HYSORE spectra have been recorded twice with two different  $\tau$  values to detect the whole proton or  $^{27}\text{Al}$  signals.

For the Davies type ENDOR experiments of the MIL-100(Al) samples the pulse sequence shown in Figure 9d was applied. The  $\pi/2$ - and  $\pi$ -pulses had lengths of  $\tau_{\pi/2} = 100$  ns and  $\tau_{\pi} = 200$  ns, respectively. The time between the first mw  $\pi$ - and second mw  $\pi/2$ -pulse was set to  $t = 14 \mu\text{s}$ . Within this time an rf pulse with length  $t_{\text{rf}} = 10 \mu\text{s}$  was applied. The time delay for the primary echo sequence was set to  $t = 1200$  ns.

A three-pulse ESEEM experiment was conducted for a DUT-8(Ni) sample using the pulse sequence as shown in Figure 9b in the subsection 2.2.3, setting the pulse lengths of the  $\pi/2$ - and  $\pi$ -pulses to  $\tau_{\pi/2} = 16$  ns and  $\tau_{\pi} = 32$  ns and the time delay between the first two pulses to  $\tau = 112$  ns. The time delay  $t$  was incremented in steps of  $\Delta t = 16$  ns. This way, a time domain signal with 512 data points was measured. After polynomial base

line correction, zero filling to 2048 points and 1D Fourier transformation the 1D frequency domain spectrum was obtained.

Note that no apodizing was applied before the Fourier transformations of the HYSCORE and three-pulse ESEEM time domain signals to avoid significant losses of the spectral resolution.

## B.2 Spectral analysis

All CW EPR, two-pulse ESE field sweep and Davies ENDOR spectra as well as the time domain HYSCORE and three-pulse ESEEM signals were baseline corrected with polynomials up to fifth order. The baseline-corrected time domain HYSCORE and three-pulse ESEEM signals were further processed as described in subsection B.1. To enable least-square fittings of the NO-Ni<sup>2+</sup> signals, for all CW spectra of samples R\_DUT-8a and R\_DUT-8b present signals of NiO impurities and the weakly physisorbed NO species NO<sub>3</sub> have been removed by appropriate baseline corrections, where the simulated NiO signals was subtracted from the spectrum and spectral regions where weakly physisorbed NO shows a signal were simply set to zero. After baseline correction, all CW EPR spectra were normalized by dividing them by the receiver gain, number of scans and square root of the power. All EPR spectra of NO adsorption species were further multiplied by the temperature to account for the Curie's law, which expresses the temperature dependency of the magnetic susceptibility. For NO gas such a temperature correction is not feasible, since also the population of higher rotational states of the NO molecule determines the temperature dependence of its magnetic susceptibility.<sup>[223]</sup> All other experimental parameters of EPR spectra, like the the time constant, the conversion time or the modulation amplitude, were kept constant during same temperature cycles.

For the samples Al/Cr-MIL-53 and Al-MIL-100 the Intensity  $I_{\text{NO}_{\text{gas}}}$  of the EPR signal of desorbed NO was determined by the double integration of the base line corrected and normalized spectra. For the DUT-8(Ni) samples  $I_{\text{NO}_{\text{gas}}}$  was determined by the double integration of the simulated EPR signals of desorbed NO, considering the mentioned normalization of the EPR spectra. For samples Al/Cr-MIL-53 and Al-MIL-100 the intensities of the EPR signals of adsorbed NO were obtained by the double integration of the corresponding normalized experimental signals. Again, the intensity of the EPR signals NO-Ni<sup>2+</sup> observed for the NO loaded DUT-8(Ni) samples was determined by the double integration of the simulated signals, considering the mentioned normalization conditions.

The number of spins, contributing to EPR signals of adsorbed NO in the Al/Cr-MIL-53 and DUT-8(Ni) samples, were roughly estimated experimentally comparing their low temperature signal to the room temperature signal of an ultramarine standard sample with known number of spins, measured under same coupling conditions.<sup>[223,224]</sup> This was realized using a rectangular Bruker ER4105DR dual mode cavity in combination with an Oxford Instruments He ESR 900 cryostat.

All spectral simulations including CW EPR signals, two-pulse ESE field sweep signals as well as HYSCORE and Davies ENDOR signals were realized with the MatLab toolbox EasySpin,<sup>[294]</sup> which employs exact numerical diagonalization of the full spin Hamiltonian

matrix. In addition, the simulations of the CW EPR signals and the two-pulse ESE field sweep signals were supported by least square fit procedures, using the interior-point algorithm, a large-scale algorithm, together with the non-linear programming solver *fmincon* for constrained non-linear multivariable functions, as it is implemented in the MatLab optimization toolbox. Simulations of HYSORE signals were obtained by the reasoned analysis of the signals, partially using square frequency plots<sup>[274]</sup> for proton signals as it is explained in subsection 2.2.3. The linewidth model, proposed for species Al2a, was implemented for HYSORE and Davies ENDOR simulations, by summing up 9312 and 1040 simulated time domain or frequency domain signals, respectively, where distinct parameters enter in each single simulated signal as independently Gaussian distributed random numbers with certain standard deviations ( $\Delta a_{\text{iso}}^{\text{Al2a}}$ ,  $\Delta A_x^{14\text{N}}$  and  $\Delta A_z^{14\text{N}}$ , see subsection 5.3).<sup>[242]</sup> Similarly, the HYSORE signals of distant  $^{27}\text{Al}$  nuclei were simulated assuming a spherical-averaging approximation.<sup>[330]</sup> Here, again a certain set of simulated time domain HYSORE signals of powders were summed up, treating the Euler angles between the hfi and nqi tensors as uniformly distributed random numbers.<sup>[242]</sup> Simulations of the Al2a Davies ENDOR signals were calculated including the hyperfine enhancement effect,<sup>[268,340,341]</sup> by considering the full Zeeman interaction spin Hamiltonian of the electron and nuclei.<sup>[294]</sup> The errors of spin Hamiltonian parameters, given in this thesis, were estimated by varying a single value of interest, keeping all other parameters constant at their best fit values. All Euler angle of various tensors in this thesis are given relative to the g-tensor frame, as it is defined by EasySpin,<sup>[294]</sup> if nothing else is stated. Sum projections of the experimental and simulated HYSORE signals are given on the top and right of each HYSORE spectrum.

## C Supplementary material for chapter two - the primary echo

The archetype of a spin echo, called the primary echo, is created by the pulse sequence  $\pi/2-\tau-\pi-\tau$ -echo as it is shown in Figure C.1a.<sup>[268]</sup> It can be understood in the classical picture introduced in subsection 2.2.3. Imagining a completely homogeneous ensemble of electron spins which all precess exactly with the same Larmor frequency. In thermal equilibrium the macroscopic magnetization  $\mathbf{M}$  would be aligned parallel to the external magnetic field  $\mathbf{B}_0$ . After the application of an on-resonant  $\pi/2$  pulse in  $x$ -direction this magnetization would point along the  $-y$ -axis as shown in Figure C.1b starting to precess in the  $x, y$ -

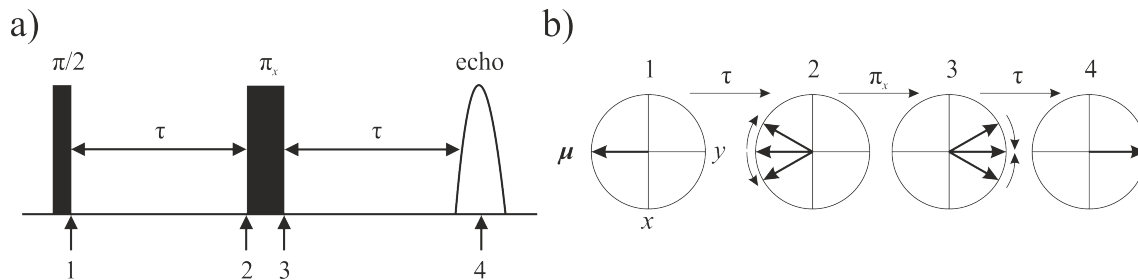


Figure C.1: Two-pulse sequence (a) and the corresponding motion of an inhomogeneous ensemble of microscopic magnetization vectors  $\mu$  in the rotating frame (b) at time points, which are denoted as numbers in (a).<sup>[268]</sup>

plane. Since all spins precess with exactly the same frequency, they would all stay in phase and the magnitude of the macroscopic magnetization would stay constant for all times if longitudinal and transverse relaxation processes are neglected.<sup>[268]</sup> Roughly speaking, this would induce a permanent voltage in the detection coils which can be measured. But in real-life systems one has always an inhomogeneous distribution of spin packets which see different local magnetic fields, and which precess therefore with slightly different Larmor frequencies. Immediately after a  $\pi/2$  pulse, all individual magnetic moment vectors  $\boldsymbol{\mu}$  of the electrons would point again along the  $-y$ -axis as shown in Figure C.1b. But now some of them precess slower and some of them faster than those precessing with the on-resonant Larmor frequency. Therefore, after the time  $\tau$  the ensemble of magnetization vectors has fanned out as shown in Figure C.1b, the total macroscopic magnetization would be zero if  $\tau$  was long enough and one would detect no signal any more, even each single electron spin still precesses in the  $x, y$ -plane. Fortunately, this spread of the magnetization vectors can be refocused by the application of a  $\pi$  pulse which rotates all magnetization vectors by  $180^\circ$  around the  $x$ -axis.<sup>[268]</sup> But the directions of the precession are not changed and therefore, after a second time duration  $\tau$  all magnetization vectors have been refocused and rotate for a distinct time interval with almost the same phase in the  $x, y$ -plane as illustrated in Figure C.1b. The corresponding net magnetization in  $y$ -direction, called the spin echo, produces a measurable signal.

## D Supplementary material for chapter three

### D.1 Estimation of the detection limit of the present X-band CW setup for the determination of the EPR signal of NO gas

An estimation of the minimal amount of desorbed NO, which can be resolved by X-band CW EPR with the used setup, gives an important argument for an answering of the question, whether NO adsorbs directly from an EPR silent phase inside the pore system of the host material to the MOF surface, or directly from the gas phase of desorbed NO outside the MOF microcrystals. If a larger amount of NO adsorbs than desorbed NO can be resolved, and this in a temperature range, where no EPR signal of NO gas was detected, than this is a strong indication that NO adsorbs from an EPR silent phase within the MOF microcrystals. Origins for such an EPR silent NO phase are discussed in chapter 7.

Since the detection limit for desorbed NO might depend on the temperature, this value is estimated for  $T = 95$  K and at room temperature.

As reported elsewhere,<sup>[224]</sup> for sample F\_DUT-8a a small EPR signal of desorbed NO was resolved at  $T = 95$  K with a simulation derived linewidth  $\delta B_{pp}^{95\text{ K}} \approx 0.8$  mT. If such linewidth  $\delta B_{pp}^{123\text{ K}} = 0.8$  mT would have been observed at  $T = 123$  K, from equation (62) (section 3.2) a mol density  $n_{\text{NO gas}}^{123\text{ K}} = 1$  mmol/m<sup>3</sup> of desorbed NO gas could be estimated. Assuming a typical length of the EPR tube of  $l = 19$  cm and an inner diameter of about  $d = 2.8$  mm, a total amount of desorbed NO in the whole EPR tube of  $N_{\text{NO gas}}^{123\text{ K}} \approx 1$  nmol is obtained. It follows from kinetic theory and EPR linewidth theory<sup>[222]</sup> that the linewidth

of the EPR signal of desorbed NO relates to its amount and temperature as:

$$\delta B_{\text{pp}}^T \propto N_{\text{NOgas}}^T \sqrt{T}. \quad (66)$$

Here, it is assumed that the whole EPR tube is kept at the same temperature and the collisional cross section does not vary significantly with the temperature which is a result of section 3.2. It follows from equation (66) that one would have resolved at  $T = 95 \text{ K}$  for sample F\_DUT-8a an amount of NO gas in the tube of at least  $N_{\text{NOgas}}^{95 \text{ K}} \approx N_{\text{NOgas}}^{123 \text{ K}} \sqrt{\frac{123}{95}} \approx 1.1 \text{ nmol}$ . This is an upper bound, since at  $T = 95 \text{ K}$  a temperature gradient along the EPR tube due to the EPR setup exists (subsection B.1). Thus, the mol density of NO gas is higher in the cooler part within the resonator than in the warmer part outside the resonator and  $N_{\text{NOgas}}^{95 \text{ K}} \approx 1.1 \text{ nmol}$  should overestimate the real amount of NO gas in the EPR tube.

At room temperature an EPR signal of desorbed NO could be resolved for sample NO<sub>1</sub> with a linewidth  $\delta B_{\text{pp}}^{\text{RT}} \approx 0.8 \text{ mT}$ . Since the room temperature NO gas pressure in this sample was  $p_{\text{NO}} = 1 \text{ mbar}$ , it follows from the ideal gas equation that the sample was loaded with  $N_{\text{NOgas}}^{\text{RT}} \approx 1.8 \text{ nmol}$  NO gas.

After a normalization of those values to the amount of MOF in the different samples (Table A.1), it can be concluded for all X-band samples that the amount of desorbed NO is  $N_{\text{NOgas}} < N_{\text{Limit}} \equiv 0.5 \text{ nmol/mg}$  if no EPR signal of desorbed NO was resolved at any temperature between  $95 \text{ K} < T < 295 \text{ K}$ .

## D.2 Insights into the phase composition of the NO loaded Al/Cr-MIL-53 sample by temperature-dependent Cr<sup>3+</sup>-EPR

The MOF MIL-53 can transform reversibly from a porous lp to a porous np phase triggered by external stimuli like the temperature<sup>[1,110,266]</sup> and gas adsorption.<sup>[111,255,260]</sup> The knowledge of its temperature-dependent phase composition is necessary to understand in detail the temperature driven adsorption and desorption of NO as it has been studied by NO gas EPR in section 3.3. In the present subsection, this discussion is complemented by an analysis of the temperature-dependent Cr<sup>3+</sup> EPR signals observed for sample Al/Cr-MIL-53.

In sample Al/Cr-MIL-53 some paramagnetic Cr<sup>3+</sup> ions, which have a 3d<sup>3</sup> electron configuration and therefore an electron spin  $S = 3/2$ , replace a small fraction of the diamagnetic Al<sup>3+</sup> framework ions. As verified by the author,<sup>[110,111]</sup> they can probe the presence of the lp and np phase by characteristic EPR signals, which clearly distinguish between both phases. The lp phase shows a distinct Cr<sup>3+</sup> EPR signal, which has an almost axially symmetric zfi tensor characterized by a zfi parameter  $|D| \approx 8300 \text{ MHz}$  whereas the np phase is responsible for an EPR signal determined by an orthorhombic zfi with the axial and orthorhombic zfi parameters  $|D| \approx 7000 \text{ MHz}$  and  $|E| \approx 1600 \text{ MHz}$  (see equation (4) and Table D.1).<sup>[110,111]</sup> According to the crystallographic data, this difference in the symmetry of the zfi reflects the symmetry of the metal-oxygen octahedra which slightly deviates from  $D_{4h}$  for the lp phase and is  $C_1$  for the np phase of the calcined

Table D.1: The simulation derived isotropic g-value  $g$  and the magnitudes of the zfi parameters  $D$  and  $E$  of the lp and np  $\text{Cr}^{3+}$  signals as determined for sample Al/Cr-MIL-53. The corresponding simulations are shown in in Figure D.2. The numbering with Latin letters after the temperature  $T$  is the same as in Figure D.2. For the simulations an inhomogeneous line broadening model was assumed, where both parameters  $D$  and  $E$  are independently and Gaussian distributed with full widths at half maximum  $\Delta D$  and  $\Delta E$ . An additional isotropic Lorentzian convolutional line broadening with a peak-to-peak linewidth  $\delta B$  was assumed for the simulations but was only significant for the lp signal in spectrum (c).

| $T$ (K) | 291 (a)           | 291 (b)           | 193 (c)           | 151 (d)          | 8 (e)            | 291 (f)           |                |
|---------|-------------------|-------------------|-------------------|------------------|------------------|-------------------|----------------|
| $g$     | $1.970 \pm 0.01$  | $1.972 \pm 0.008$ | $1.975 \pm 0.008$ | - <sup>a</sup>   | - <sup>a</sup>   | $1.970 \pm 0.01$  |                |
| lp      | $ D $ (MHz)       | $8300 \pm 150$    | $8300 \pm 200$    | $8450 \pm 150$   | - <sup>a</sup>   | - <sup>a</sup>    | $8300 \pm 150$ |
|         | $ E $ (MHz)       | $60 \pm 60$       | $40 \pm 40$       | $150 \pm 150$    | - <sup>a</sup>   | - <sup>a</sup>    | $60 \pm 60$    |
|         | $\Delta D$ (MHz)  | $700 \pm 300$     | $520 \pm 170$     | $700 \pm 400$    | - <sup>a</sup>   | - <sup>a</sup>    | $700 \pm 300$  |
|         | $\Delta E$ (MHz)  | $100 \pm 100$     | $208 \pm 100$     | $700 \pm 600$    | - <sup>a</sup>   | - <sup>a</sup>    | $100 \pm 100$  |
|         | $\delta B$ (mT)   | $1.5 \pm 1.5$     | $0.9 \pm 0.9$     | $7 \pm 3$        | - <sup>a</sup>   | - <sup>a</sup>    | $1.5 \pm 1.5$  |
| $g$     | $1.970 \pm 0.015$ | $1.965 \pm 0.02$  | $1.954 \pm 0.02$  | $1.954 \pm 0.02$ | $1.954 \pm 0.02$ | $1.970 \pm 0.015$ |                |
| np      | $ D $ (MHz)       | $7150 \pm 100$    | $7010 \pm 60$     | $7166 \pm 250$   | $7000 \pm 200$   | $7000 \pm 250$    | $7150 \pm 100$ |
|         | $ E $ (MHz)       | $1600 \pm 50$     | $1590 \pm 60$     | $1630 \pm 70$    | $1630 \pm 100$   | $1630 \pm 100$    | $1600 \pm 50$  |
|         | $\Delta D$ (MHz)  | $1000 \pm 400$    | $600 \pm 300$     | $1400 \pm 200$   | $1400 \pm 200$   | $1800 \pm 600$    | $1000 \pm 400$ |
|         | $\Delta E$ (MHz)  | $250 \pm 250$     | $450 \pm 250$     | $400 \pm 250$    | $400 \pm 250$    | $650 \pm 200$     | $250 \pm 250$  |
|         | $\delta B$ (mT)   | $1.5 \pm 1.5$     | $2 \pm 2$         | $2 \pm 2$        | $2 \pm 2$        | $3 \pm 3$         | $1.5 \pm 1.5$  |

<sup>a</sup>No signal of the lp phase was resolved.

dehydrated MIL-53(Al) material, respectively.<sup>[110]</sup> The g-tensors were determined to be almost isotropic within the resolution of Q-band experiments ( $\nu_{\text{mw}} \approx 34$  GHz) and the corresponding g-values were experimentally determined to  $g = 1.973 \pm 0.005$  and  $g = 1.976 \pm 0.002$  for the calcined and dehydrated lp and np phases, respectively.<sup>[110]</sup>

The  $\text{Cr}^{3+}$  EPR signals of the NO loaded sample Al/Cr-MIL-53 were measured temperature-dependently and simultaneously with the NO gas EPR signal and offer in this way additional information about the structural phase composition of this sample during those experiments. Some representative EPR spectra are shown in Figure D.1. They were measured in one series of consecutive X-band CW experiments within a full temperature cycle including a first heating in hot water ( $T \approx 370$  K), the subsequent cooling to low temperatures and an additional heating period to room temperature. After each temperature had been reached, and after a waiting time of at least five minutes the spectrum was measured. Test measurements at certain temperatures, which were performed after another ten minutes waiting period, show no spectral differences. This indicates that thermal equilibrium was approached already after five minutes within the spectral resolution. All EPR spectra, which were measured at temperatures  $T \gtrsim 120$  K, show the signal of desorbed NO gas as it has been discussed in section 3.3. Spectra measured at temperatures  $T < 80$  K show a signal, which was attributed to an NO adsorption species and is discussed in chapter 4 of this thesis. The isotropic narrow line at  $B_0 = 341$  mT might be attributed to  $\text{Cr}^{3+}$  or

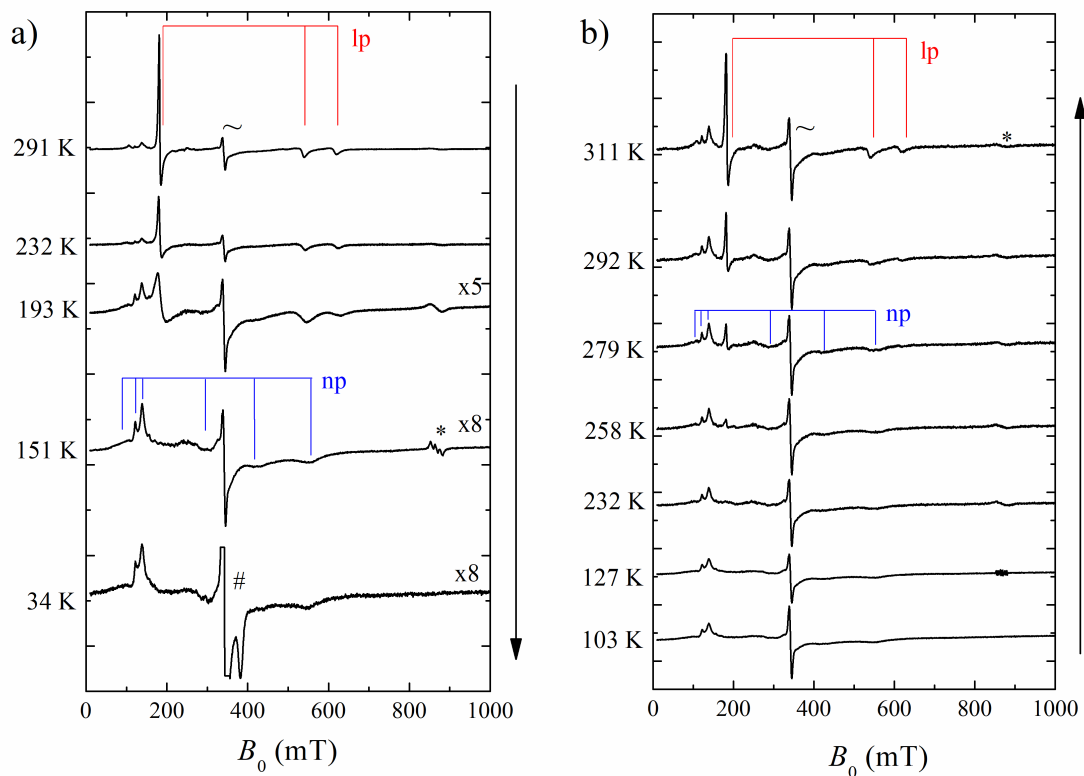


Figure D.1: X-band EPR spectra of sample Al/Cr-MIL-53 measured at different temperatures during cooling (a) and subsequent heating (b). All intensities were normalized with respect to experimental parameters and were multiplied with  $T$  to correct for the Curie law. The red and blue lines indicate spectral components belonging to the  $\text{Cr}^{3+}$  signals of the lp and np phase, respectively. Signals from  $\text{Cr}^{3+}$  or  $\text{Cr}^{5+}$  impurities are labeled with the symbol  $\sim$ . The signals of desorbed and adsorbed NO are labeled with the symbols \* and #, respectively. The latter was restricted to a certain intensity interval for a clear presentation of the  $\text{Cr}^{3+}$  signals.



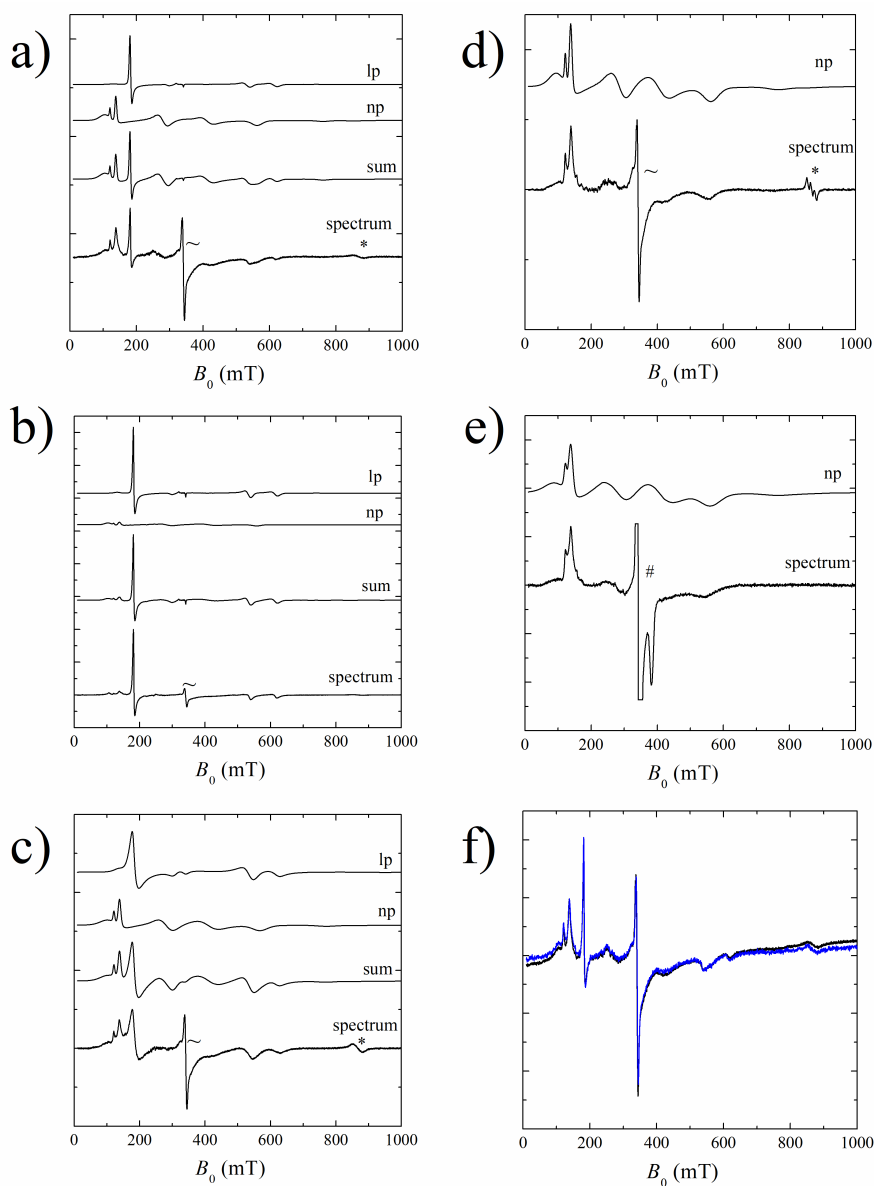


Figure D.2: Selective X-band EPR spectra of sample Al/Cr-MIL-53 and the corresponding simulations of the np and lp  $\text{Cr}^{3+}$ -signals as well as their sums. The spectra were measured at  $T = 291$  K before (a) and after (b) warming up the sample in hot water ( $T \approx 370$  K). Signals measured during cooling at  $T = 193$  K,  $T = 151$  K and  $T = 8$  K are shown in (c), (d) and (e), respectively. The spectrum measured after the subsequent heating period at  $T = 291$  K is shown in (f) (black), together with that measured at the beginning at the same temperature (blue) as shown in (a). The symbols \* and # indicate the signals of desorbed and adsorbed NO, where the signal of the latter was cut. The symbol  $\sim$  indicates the signal of  $\text{Cr}^{3+}$  or  $\text{Cr}^{5+}$  impurities. Simulation parameters are given in Table D.1.

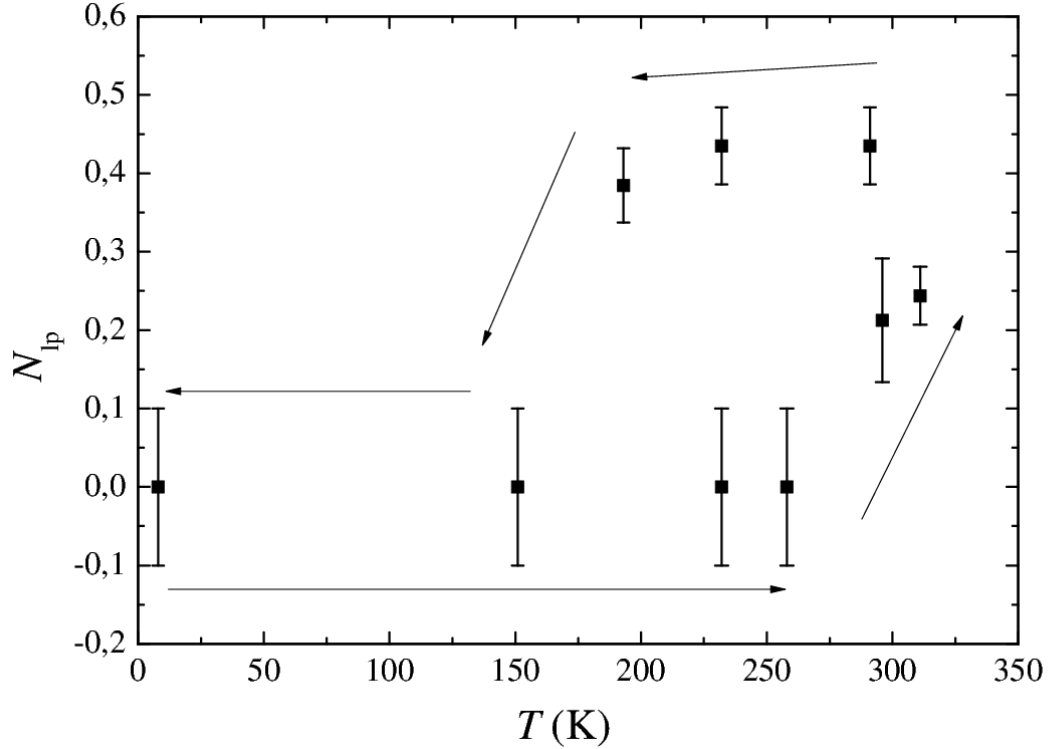


Figure D.3: Relative fraction  $N_{lp}$  of the lp phase as determined by the simulations of the lp and np  $\text{Cr}^{3+}$  EPR signals measured for the NO loaded sample Al/Cr-MIL-53 during a full temperature cycle.

$\text{Cr}^{5+}$  impurities.

The first spectrum of the test series shows EPR signals which are characteristic for both the lp and np phase of MIL-53 (Figure D.2a). This assignment is strongly indicated by their simulation derived spin Hamiltonian parameters which are summarized in Table D.1.<sup>[110,111]</sup> The corresponding simulated lp and np signals are also shown in Figure D.2a. The attribution of their spectral features to the corresponding EPR transitions is described elsewhere.<sup>[111]</sup> Most prominent are their lines between  $100 \text{ mT} < B_0 < 200 \text{ mT}$ , which correspond to the  $\theta = 90^\circ$  powder edges singularities of the transition between the first and second energy level. For the np phase this line is split into two lines, reflecting the orthorhombicity of the  $\text{Cr}^{3+}$  zfi tensor.

The spin Hamilton parameters as well as the linewidth parameters of the lp and np  $\text{Cr}^{3+}$  signals have been determined by simulation for each EPR spectrum of the measurement series. Selective EPR spectra and the corresponding simulations of the  $\text{Cr}^{3+}$  EPR signals are shown in Figure D.2 and the corresponding parameters as determined by simulation are summarized in Table D.1. The relative fraction  $N_{lp} = \frac{I_{lp}}{I_{lp} + I_{np}}$  of the lp phase was derived from the lp and np simulations according to their contribution to the experimental spectrum. Here, the overall simulated signal  $S_{\text{sum}} = I_{lp} \cdot S_{lp} + I_{np} \cdot S_{np}$  is the weighted sum of the lp and np simulations  $S_{lp}$  and  $S_{np}$ . The temperature-dependent fraction  $N_{lp}$  is shown in Figure D.3 and shows a strong hysteresis as it is typical for this material.<sup>[1,110]</sup> This parameter was chosen for the quantification of the lp phase, since previous results

have indicated that the sum amount of the lp and np phases stays constant during a full temperature cycle.<sup>[110]</sup> Furthermore, the equivalence of the first and last spectrum in the present test series proves that the transformations between the lp and np phases are completely reversible (see Figure D.2f).

After these methodological and preliminary explanations, the  $\text{Cr}^{3+}$  signals and their meaning for an understanding of the NO adsorption will be analyzed in more detail. First, the problem will be sketched out.

The NO might adsorbed only on the lp, only on the np or on both phases. One has to consider that the transitions between the lp and the np phases might complicate the problem. Such transitions might be triggered either by the NO adsorption and desorption, by the temperature variation or both of them. Are the  $\text{Cr}^{3+}$  and NO gas EPR data conclusive enough to pin down all possibilities to one scenario?

At this point the major characteristics of the temperature dependency of the lp and np  $\text{Cr}^{3+}$  signals will be outlined.

As shown in Figure D.2a,b, by heating sample Al/Cr-MIL-53 in hot water ( $T \approx 370$  K) at the beginning of the test series, the fraction of the lp phase EPR signal increases from  $N_{\text{lp}} \approx 25$  percent to  $N_{\text{lp}} \approx 45$  percent. Such an increase of the lp fraction induced by heating is typically for MIL-53.<sup>[1,110]</sup> But this fraction becomes not larger during the full temperature cycle. This small maximal value of the lp fraction differs from results measured for the dehydrated calcined MIL-53(Al/Cr), where  $N_{\text{lp}} \approx 90$  percent of the lp phase were present at room temperature after heating the sample in hot water ( $T \approx 370$  K). This difference in the high temperature phase composition might be related to slightly different synthesis conditions. Those might alter the flexibility of the MOF tremendously due to different amount and kind of defects and sizes of the crystallites as it was indicated for the MOF DUT-8(Ni).<sup>[224,241]</sup> Alternatively, it might be related to the presence of NO. But a systematic investigation of this issue is not an objective of the present study.

During cooling, the fraction of the lp phase signal decreases only slightly up to the temperature  $T = 193$  K, where it approaches  $N_{\text{lp}} \approx 38$  percent. Simultaneously, the lp  $\text{Cr}^{3+}$  signal broadens significantly, which can be simulated by an increase of its isotropic convolutional Lorentzian peak-to-peak linewidth from  $\delta B = 1.5 \pm 1.5$  mT at  $T = 291$  K to  $\delta B = 7 \pm 3$  mT at  $T = 193$  K (Table D.1). Such a large line broadening was not observed for the dehydrated and calcined MIL-53(Al/Cr),<sup>[110]</sup> which indicates a relation of this behavior to the presence of NO.

During the cooling from  $T = 193$  K to  $T = 151$  K, the lp  $\text{Cr}^{3+}$  signal vanishes completely. This observation also differs from the analogous study of the activated MIL-53(Al/Cr) material, where the lp signal was always visible and  $N_{\text{lp}} \gtrsim 15$  percent holds at all temperatures.<sup>[110]</sup> The disappearance of the lp signal indicates either an almost complete transformation from the lp to the np phase at temperatures  $151 \text{ K} < T < 193 \text{ K}$  or such a large broadening of the lp phase signal that it could not be resolved anymore by EPR. To make it more precise, one has to note that the present  $\text{Cr}^{3+}$  EPR spectroscopy has a detection limit for the lp phase of about  $N_{\text{lp}} \approx 10$  percent as estimated by simulations, assuming broad lp EPR signal linewidths as measured at  $T = 193$  K in the cooling

period.

During the subsequent cooling to  $T = 8$  K, the  $\text{Cr}^{3+}$  signal of the lp phase remains undetectable and that of the np phase shows no significant spectral changes. In the following heating period, no signal of the lp phase was observed up to the temperature  $T = 232$  K. At  $T = 258$  K a small EPR signal of the lp phase occurs (Figure D.1). Its relative fraction increases in the following experiments reaching  $N_{\text{lp}} \approx 25$  percent at room temperature (Figure D.3). Both spectra, the first and the last of this test series, are identical, verifying the full reversibility of the temperature driven structural phase transformation of MIL-53(Al/Cr) in the presence of some NO gas (see Figure D.2f).

To simplify the further discussion, it will be assumed first that almost all of the the lp phase has transformed to the np phase below  $T = 193$  K, as suggested by the EPR data. Finally, the possibility will be discussed that a fraction of the lp phase remains at low temperatures but was not observed by EPR due to the large line width and small intensity of the  $\text{Cr}^{3+}$  signal.

First, the heating period where the desorption of NO occurs, will be examined. As indicated by the temperature dependence of the NO gas EPR signal intensity (Figure 24a), this desorption was almost finished at temperatures above  $T = 193$  K. Thus, it follows that NO desorbs almost solely from the np phase, since here it is assumed that this is the only phase which is present at temperatures  $T < 193$  K. In the case of an exclusive NO desorption from the np phase, the np to lp transformation at temperatures  $T > 258$  K should be triggered primarily by the temperature, as it is typical for this MOF.<sup>[110]</sup> The corresponding transition temperature  $T = 285 \pm 25$  K seems to be smaller than that for the dehydrated MIL-53(Al/Cr), which has been determined by EPR to  $T = 352 \pm 23$  K. This might be related to the presence of NO gas in the sample tube. But further dependences of this transition temperature, like from the domain or crystal sizes, which are indicated by the broad temperature range where this transition occur, or from the presence of defects, might complicate an understanding of this matter.<sup>[224,241]</sup>

Now, the  $\text{Cr}^{3+}$  EPR signals measured during the cooling period shall be examined. One should note two relevant observations: First, a pronounced lp to np transition occurred during cooling between  $151 \text{ K} < T < 193 \text{ K}$ . Second, the linewidth of the lp phase EPR signal distinctly broadened with decreasing temperature. Considering the first issue, it might be possible that the observed lp to np transition is mainly triggered by the temperature and not by the NO adsorption, as it is typically for the MIL-53.<sup>[1,110]</sup> The corresponding temperature range is different to that  $60 \text{ K} < T < 150 \text{ K}$  of the activated MIL-53,<sup>[1,110]</sup> but this might be a consequence of the presence of NO in the gas phase or different characteristics of the samples with respect to defects or the particle size.<sup>[224,241]</sup> It might be also possible that the NO gas adsorption on the lp phase triggers its transformation to the np phase as the adsorption of  $\text{CO}_2$  does.<sup>[111]</sup> This might explain the more effective lp to np turnover than it was observed for the temperature triggered lp to np transition for the activated MIL-53(Al/Cr).<sup>[110]</sup> Indeed, the HYSORE results of the present thesis in chapter 4 indicate an NO adsorption in the middle of the narrow pore of MIL-53(Al/Cr), interacting with two opposite  $\mu_2$ -(OH) protons. This interaction might

pull both  $\mu_2$ -(OH) groups toward each other as it was observed likewise for CO<sub>2</sub> in MIL-53(Cr)<sup>[260]</sup>, shifting the lp to np transition temperature to higher values. However, both triggers, the temperature and the NO gas adsorption, might affect the lp to np transformation simultaneously. Consequently, it must be admitted that the only detection of the lp to np transition by Cr<sup>3+</sup>EPR does not allow for distinct conclusions about the kind of phase, NO adsorbs primarily on.

For the present objective the observation of a line broadening of the lp phase Cr<sup>3+</sup>EPR signal seems to be reasonable. This line broadening might indicate structural disorder induced by the adsorption of NO, which seems reasonable for a flexible MOF material. It might also indicate magnetic dipole-dipole interactions between the electron spins of the Cr<sup>3+</sup> ions and weakly physisorbed NO molecules. Both scenarios involve the adsorption of NO on the lp phase, which is therefore strongly indicated by the observed broadening of the lp phase Cr<sup>3+</sup> signal. But on the other hand, one cannot fully exclude the possibility that the observed line broadening results from structural disorder, which is determined solely by the temperature. Although such a temperature triggered broadening effect was not observed for the activated MIL-53(Al/Cr) material, the presence of NO in the sample tube might modulate the temperature-dependent occurrence of structural disorder. One concludes that the observed line broadening is an interesting effect and indicates most probably the adsorption of NO on the lp phase. But further studies are necessary to confirm this conclusion, to work out in detail the origin of the observed line broadening and to figure out on what phase NO primarily adsorbs, if both lp and np phases are present.

As announced, this subsection ends with the discussion of the possibility that NO adsorbs on the lp phase, prevents its transformation to the np phase at low temperatures and leads to such large structural disorder that the Cr<sup>3+</sup> EPR signal of the lp phase becomes too broad for a detection by EPR. One can make this consideration short. If this possibility would be true, one would expect similar signals of the lp phase during the heating period, as one has observed during the cooling period at temperatures, where the NO adsorption has happened. This is not the case. Signals of the lp phase were observed during the heating period at higher temperatures than they were observed during the cooling period (Figure D.1). At these temperatures the NO desorption was almost completed as proven by NO gas EPR. This observation strongly indicates that NO does not desorb from the lp phase and that the lp phase has transformed completely to the np phase during the cooling period within the resolution of Cr<sup>3+</sup> EPR. Thus, all conclusions, based on this assumption, should hold.

## E Supplementary material for chapter four

This subsection collects HYSORE spectra measured for sample Al-MIL-53 at  $T = 6$  K at different magnetic field positions. Each figure comprises the whole EPR spectrum and two enlargements, one of the signal of distant  $^{27}\text{Al}$  nuclei and one of the proton signals. The Latin letter on the top right of each figure corresponds to the respective field position indicated in Figure 28. Sum projections are shown on the top and right. The captions list the applied magnetic field and values for the time delay  $\tau$  between the first two pulses. Either two values  $\tau_{1,2}$  or three values  $\tau_{1,2,3}$  are given, meaning that the respective HYSORE spectrum is a sum of two or three HYSORE spectra, each measured with the respective  $\tau = \tau_{1,2,3}$  value.

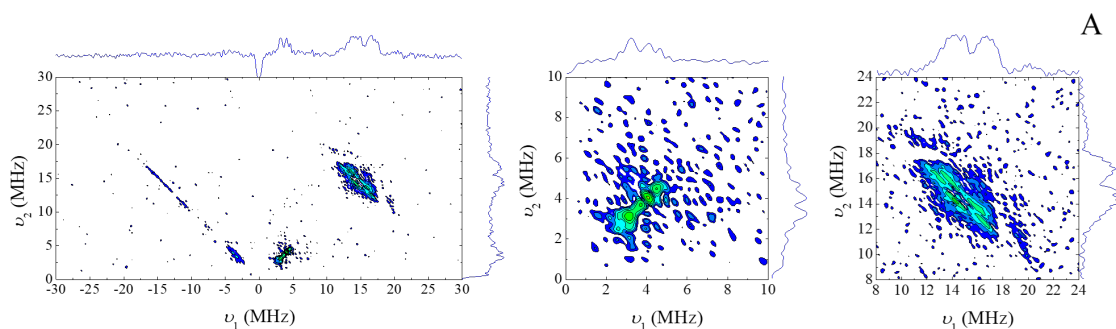


Figure E.1:  $B = 346.8$  mT,  $\tau_1 = 102$  ns,  $\tau_2 = 136$  ns

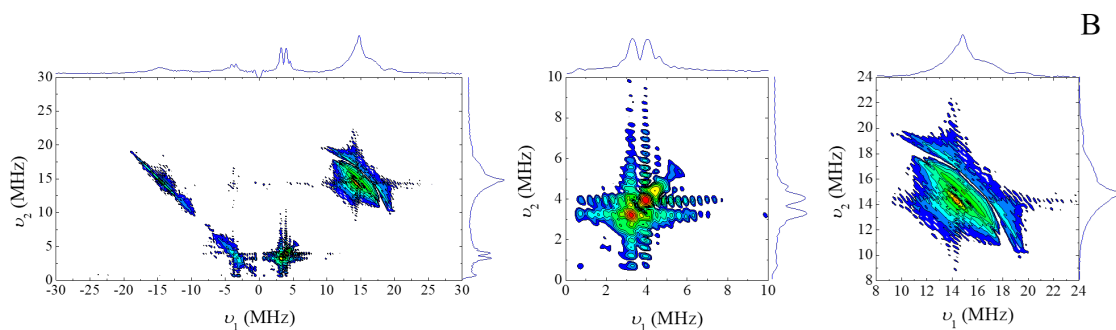


Figure E.2:  $B = 348.6$  mT,  $\tau_1 = 102$  ns,  $\tau_2 = 134$  ns

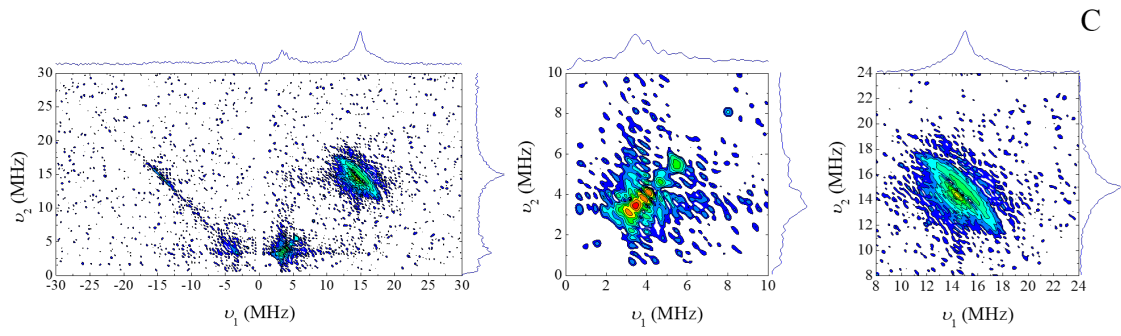


Figure E.3:  $B = 350.2$  mT,  $\tau_1 = 94$  ns,  $\tau_2 = 132$  ns

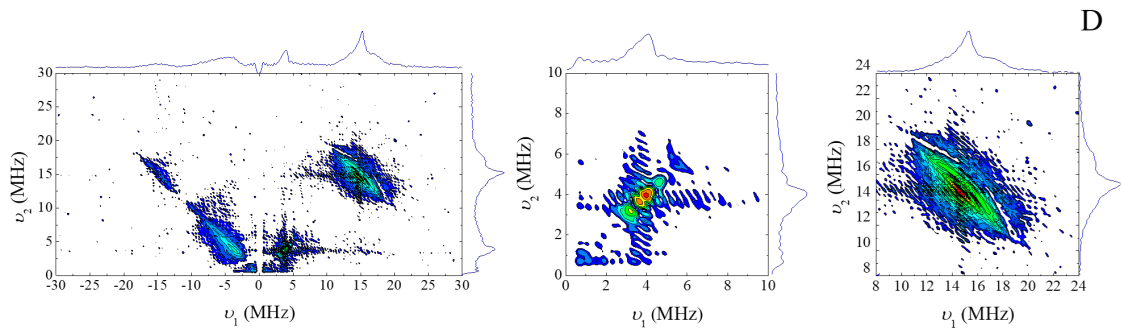


Figure E.4:  $B = 356.0$  mT,  $\tau_1 = 98$  ns,  $\tau_2 = 132$  ns

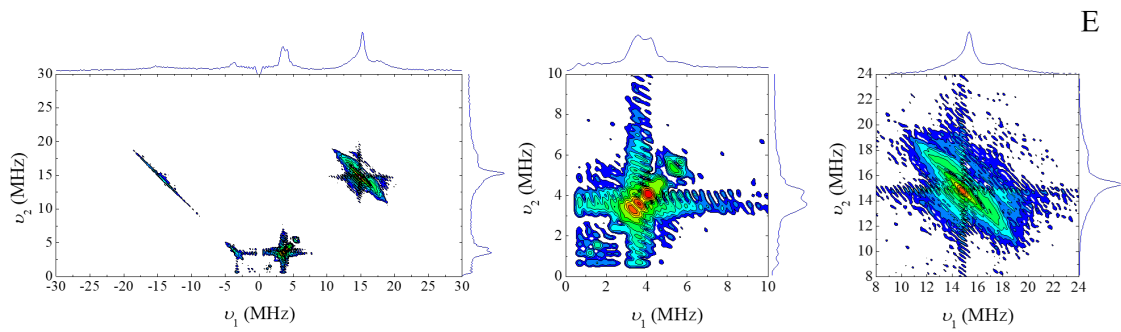


Figure E.5:  $B = 360.0$  mT,  $\tau_1 = 98$  ns,  $\tau_2 = 102$  ns,  $\tau_3 = 136$  ns

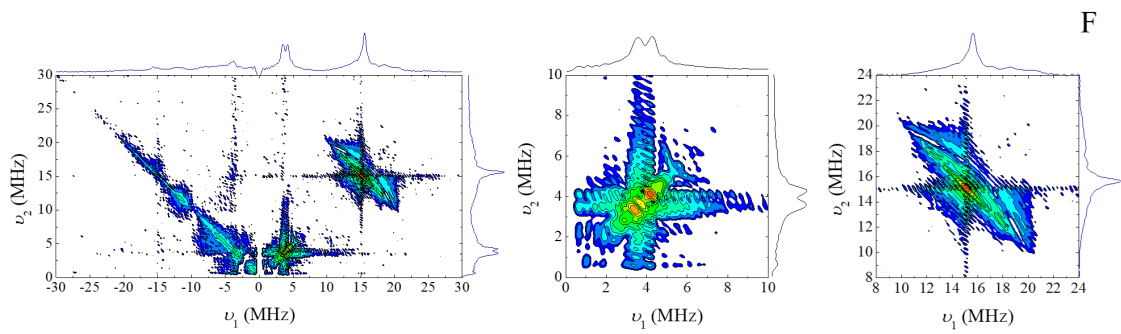


Figure E.6:  $B = 367.0$  mT,  $\tau_1 = 96$  ns,  $\tau_2 = 128$  ns

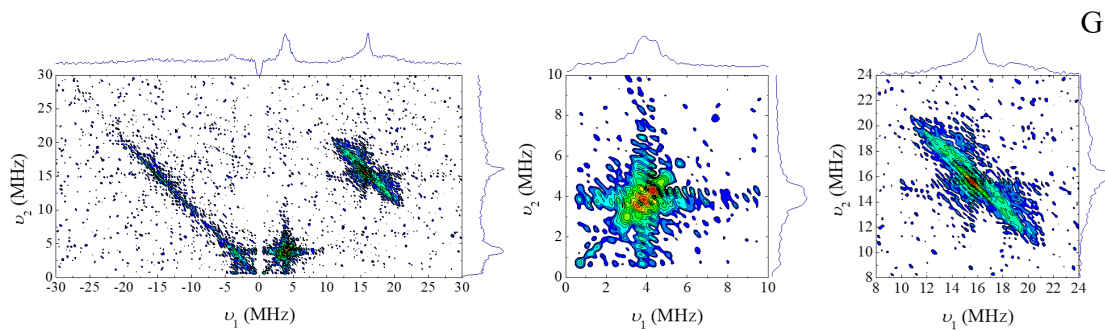


Figure E.7:  $B = 378.8$  mT,  $\tau_1 = 94$  ns,  $\tau_2 = 124$  ns,  $\tau_3 = 130$  ns

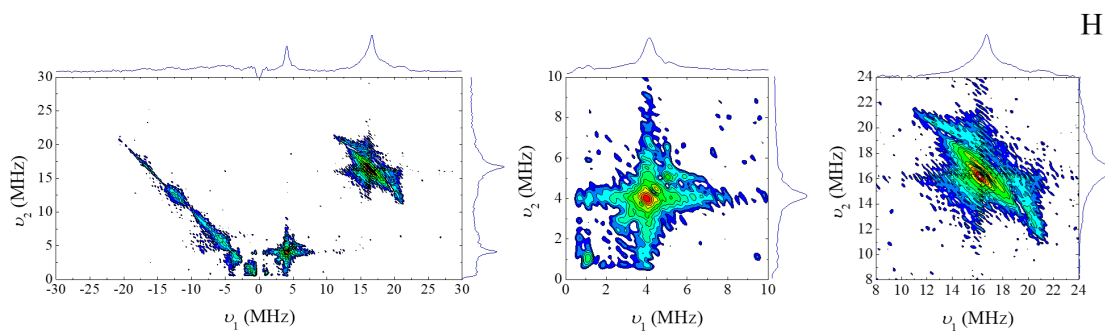


Figure E.8:  $B = 393.6$  mT,  $\tau_1 = 90$  ns,  $\tau_2 = 120$  ns

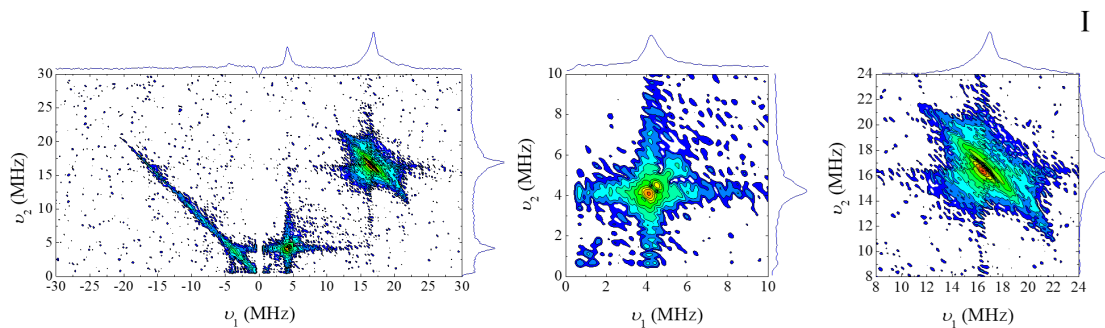


Figure E.9:  $B = 398.8$  mT,  $\tau_1 = 88$  ns,  $\tau_2 = 118$  ns

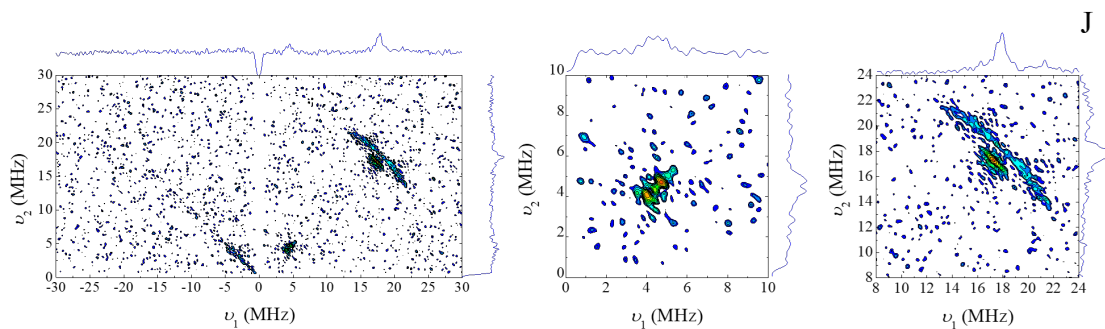


Figure E.10:  $B = 420.0$  mT,  $\tau_1 = 84$  ns,  $\tau_2 = 112$  ns



## F Supplementary material for chapter five

### F.1 HYSCORE spectra of sample Al-MIL-100

In this subsection HYSCORE spectra are collected that were measured at  $T = 6$  K and different magnetic field positions. The Latin letter in the top left corner corresponds to the respective fields indicated in Figure 38a. Below each experimental HYSCORE spectrum the respective simulated HYSCORE signal of species NO2a is shown in red. Sum projections are shown on the top and right of each spectrum. The figure captions listed the applied magnetic field, the time delay  $\tau$  between the first two pulses and the time increment  $\Delta t$  if it deviates from the value  $\Delta t = 24$ .

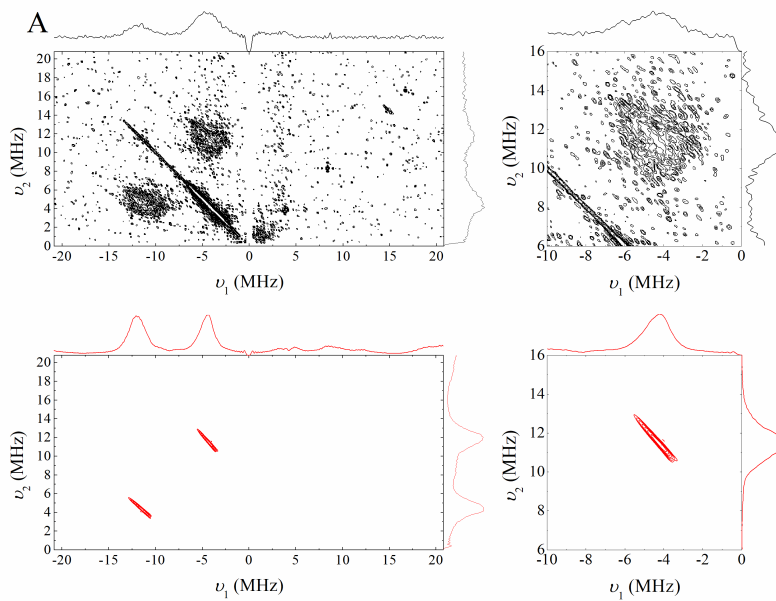


Figure F.1:  $B_0 = 344.3$  mT,  $\tau = 130$  ns

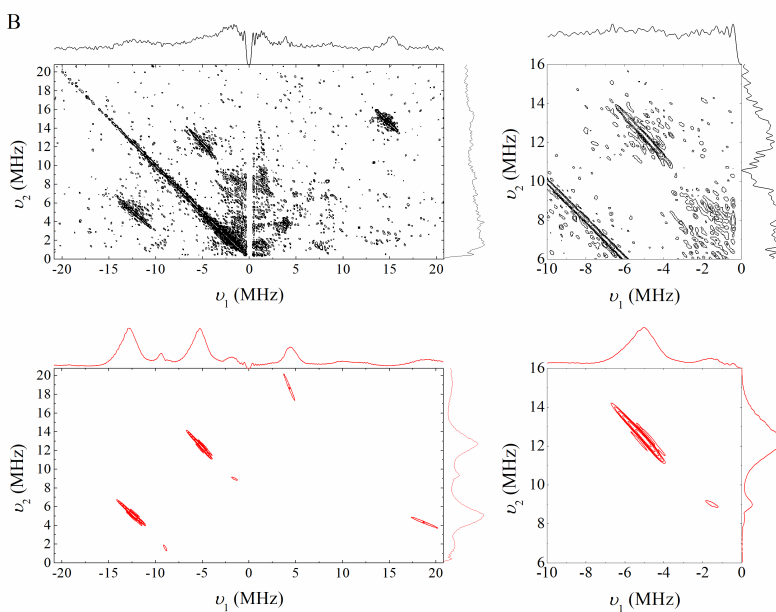


Figure F.2:  $B_0 = 345.0$  mT,  $\tau = 102$  ns

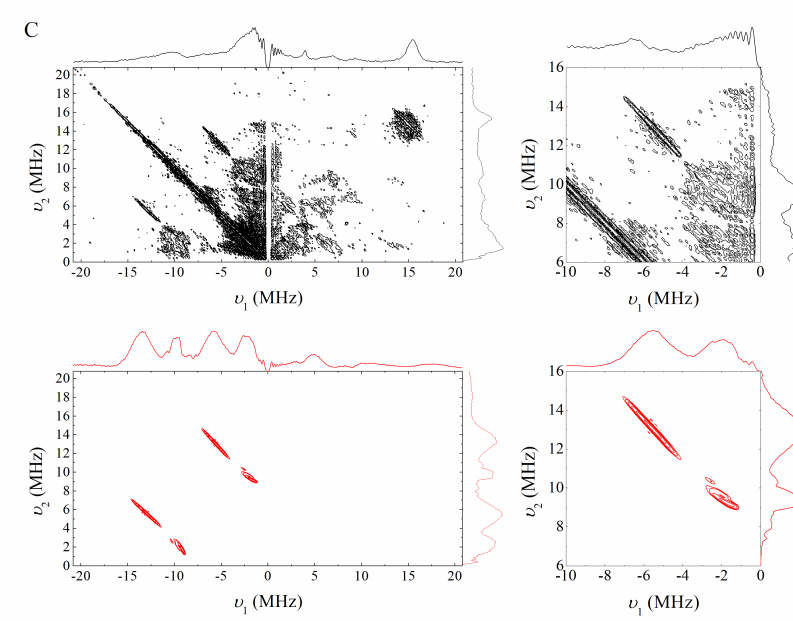


Figure F.3:  $B_0 = 348.0$  mT,  $\tau = 92$  ns

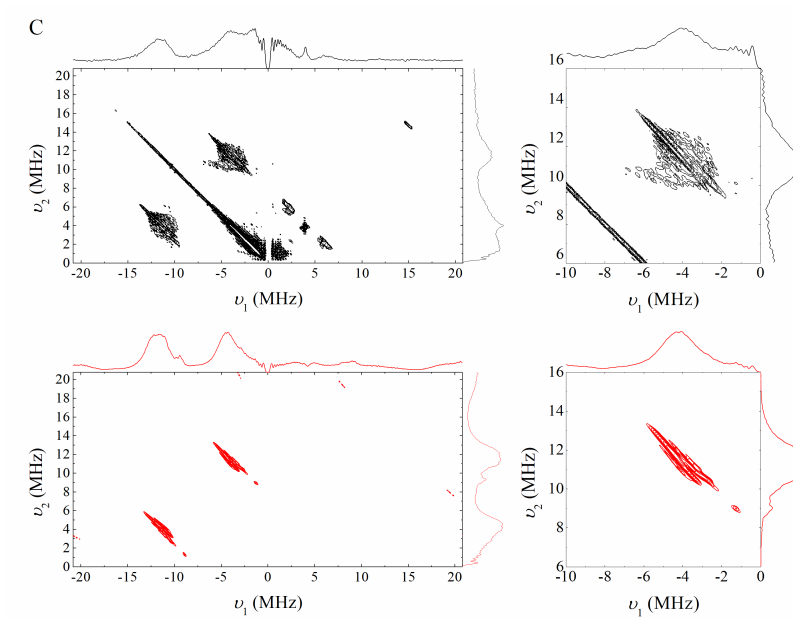


Figure F.4:  $B_0 = 348.0$  mT,  $\tau = 130$  ns

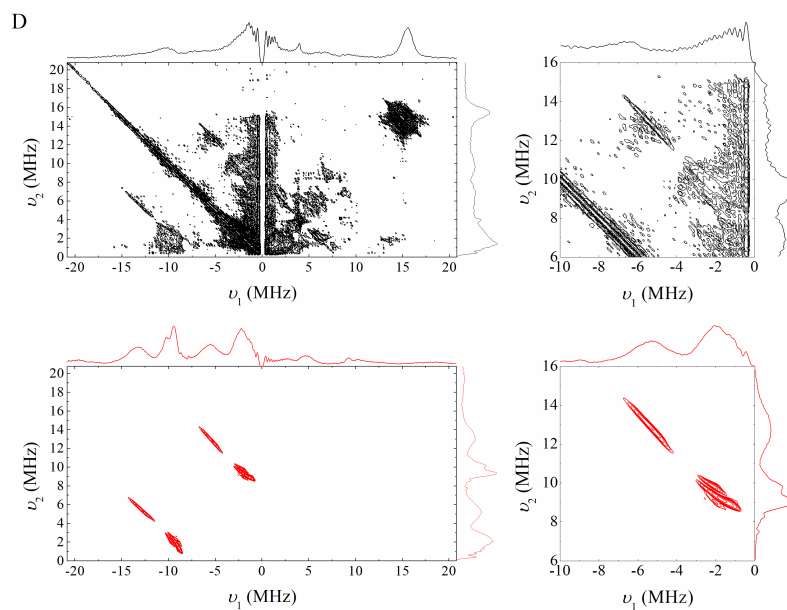


Figure F.5:  $B_0 = 350.0$  mT,  $\tau = 92$  ns

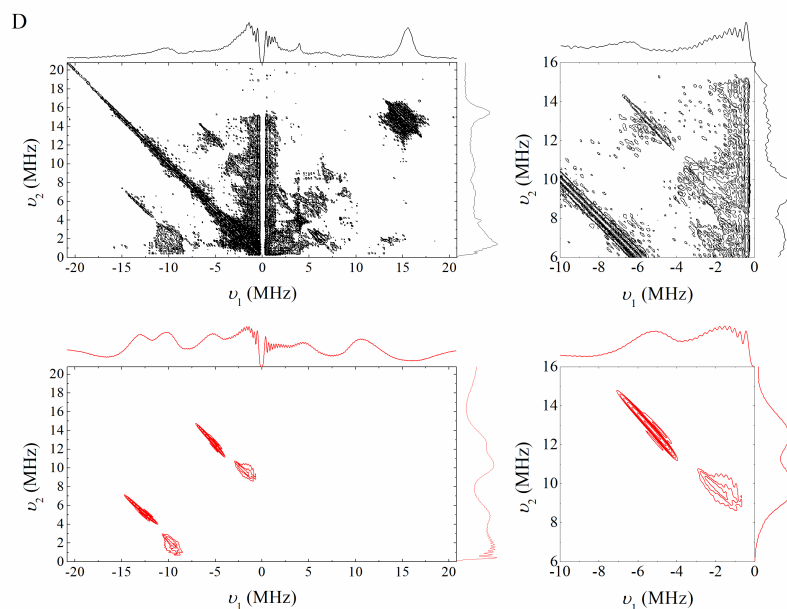
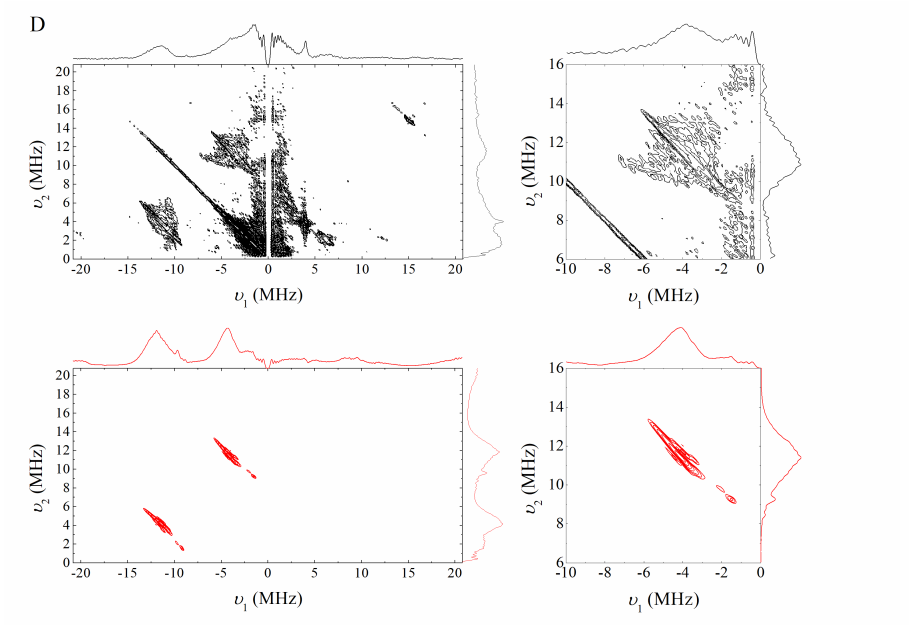
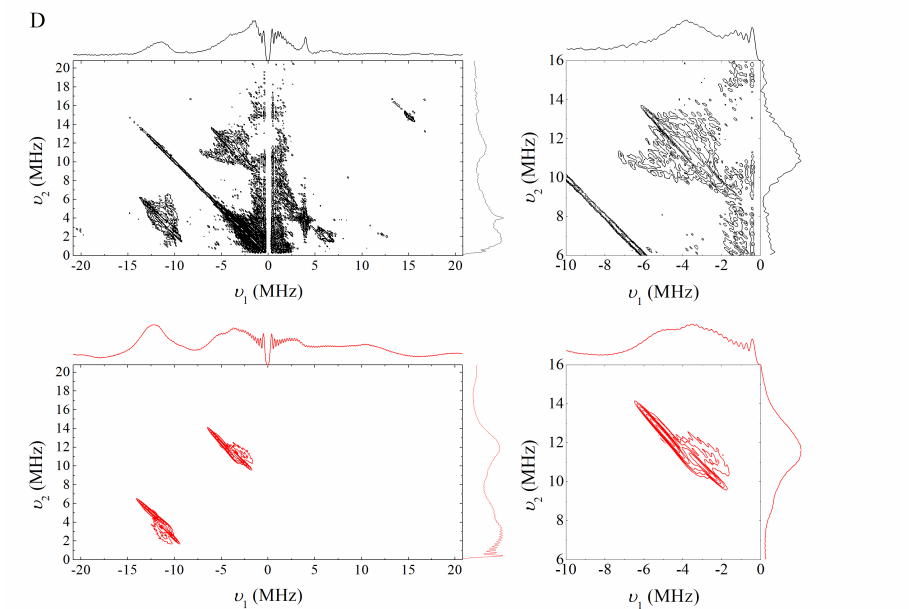


Figure F.6:  $B_0 = 350.0$  mT,  $\tau = 92$  ns. For simulations a  $^{27}\text{Al}$  nqi was assumed with  $C_Q = 5.53$  MHz and  $\eta = 0.3$ .<sup>[201]</sup> Both values were assumed to be Gaussian distributed with standard deviations  $\Delta C_Q = 1.1$  MHz and  $\Delta\eta = 0.06$ .


 Figure F.7:  $B_0 = 350.0$  mT,  $\tau = 128$  ns

 Figure F.8:  $B_0 = 350.0$  mT,  $\tau = 128$  ns. For simulations a  $^{27}\text{Al}$  nqi was assumed with  $C_Q = 5.53$  MHz and  $\eta = 0.3$ .<sup>[201]</sup> Both values were assumed to be Gaussian distributed with standard deviations  $\Delta C_Q = 1.1$  MHz and  $\Delta\eta = 0.06$ .

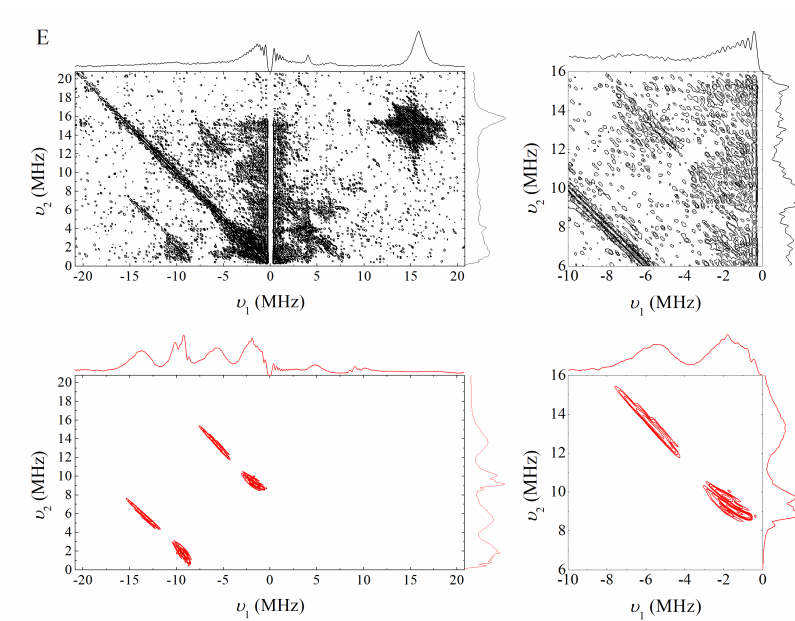


Figure F.9:  $B_0 = 357.0$  mT,  $\tau = 90$  ns

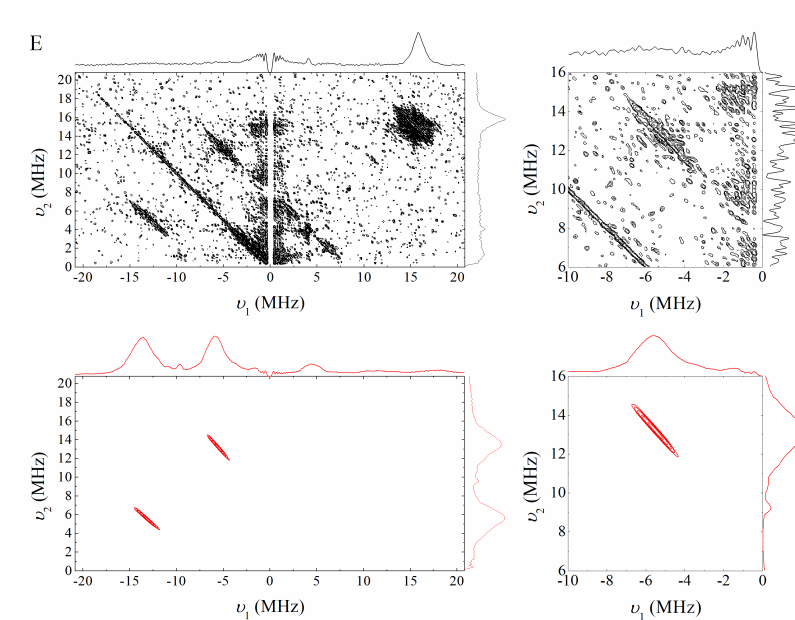


Figure F.10:  $B_0 = 357.0$  mT,  $\tau = 100$  ns

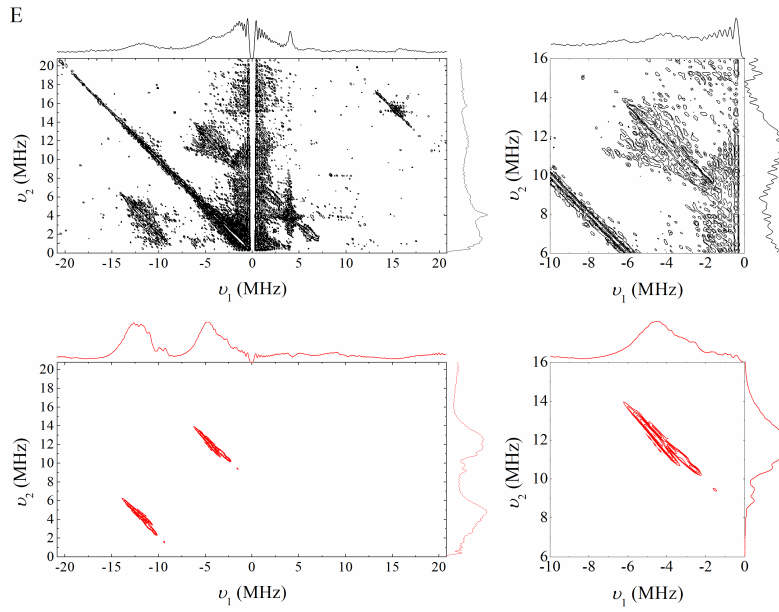


Figure F.11:  $B_0 = 357.0$  mT,  $\tau = 126$  ns

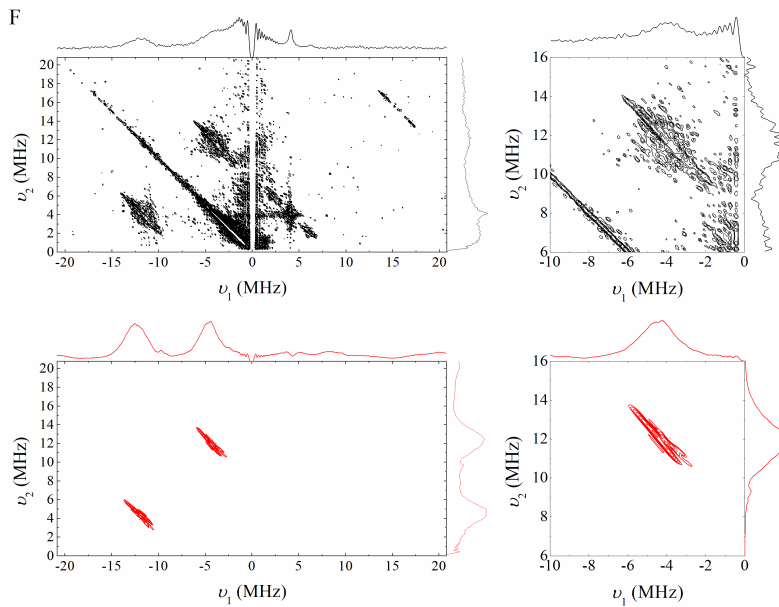


Figure F.12:  $B_0 = 360.5$  mT,  $\tau = 126$  ns

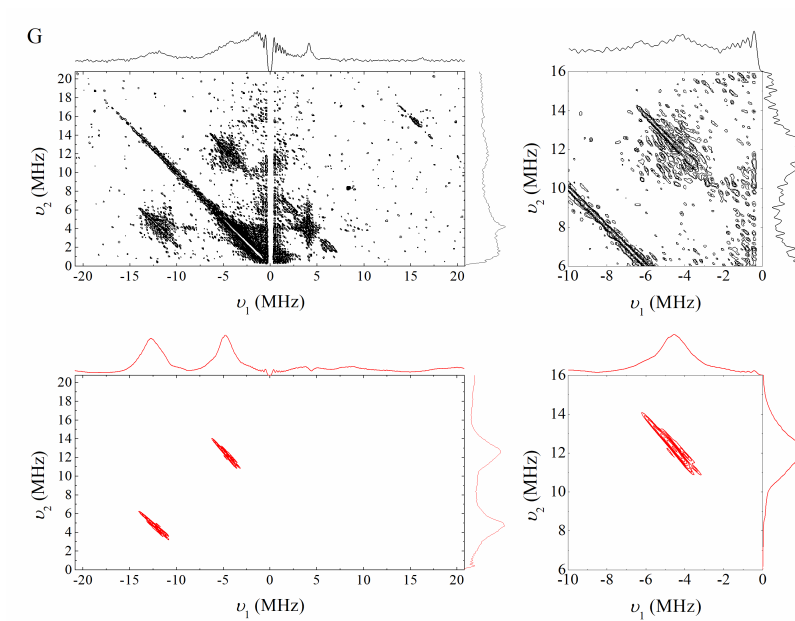


Figure F.13:  $B_0 = 362.0$  mT,  $\tau = 124$  ns

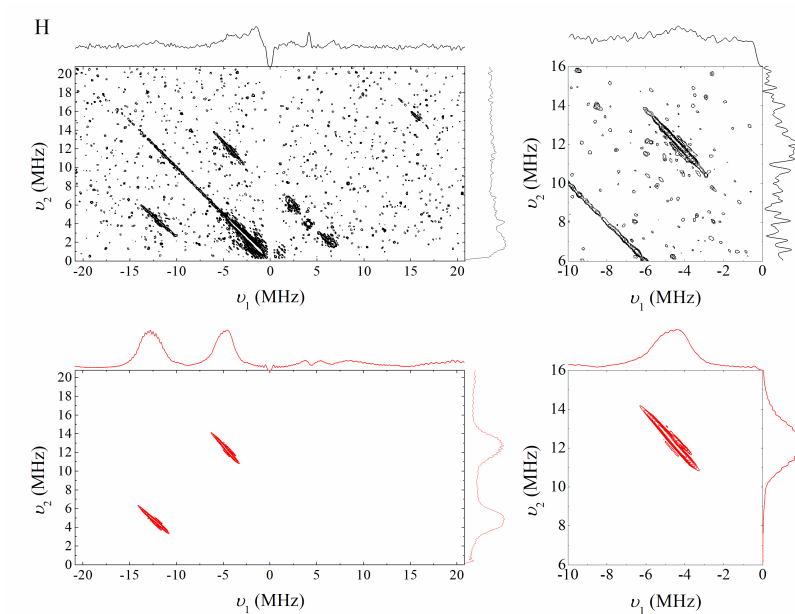


Figure F.14:  $B_0 = 364.0$  mT,  $\tau = 124$  ns



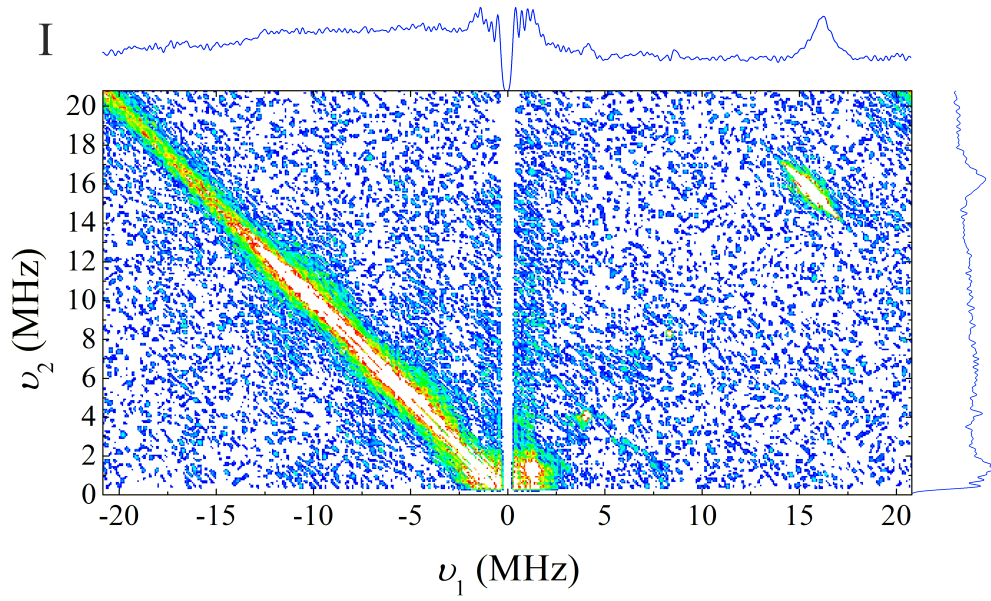


Figure F.15:  $B_0 = 366.0$  mT,  $\tau = 88$  ns

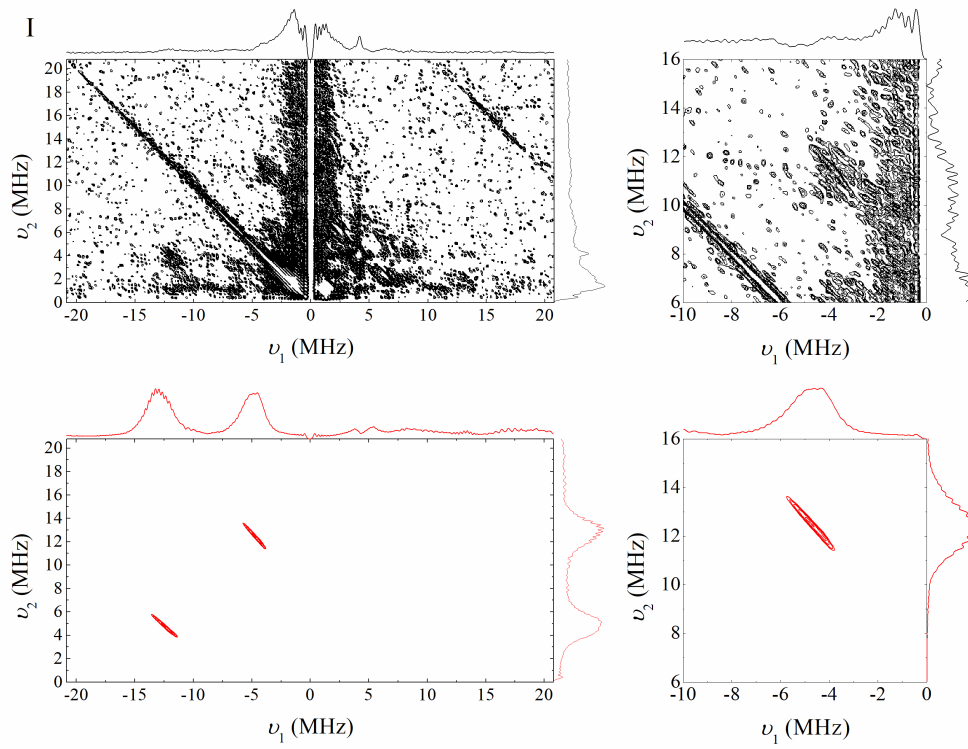


Figure F.16:  $B_0 = 366.0$  mT,  $\tau = 124$  ns

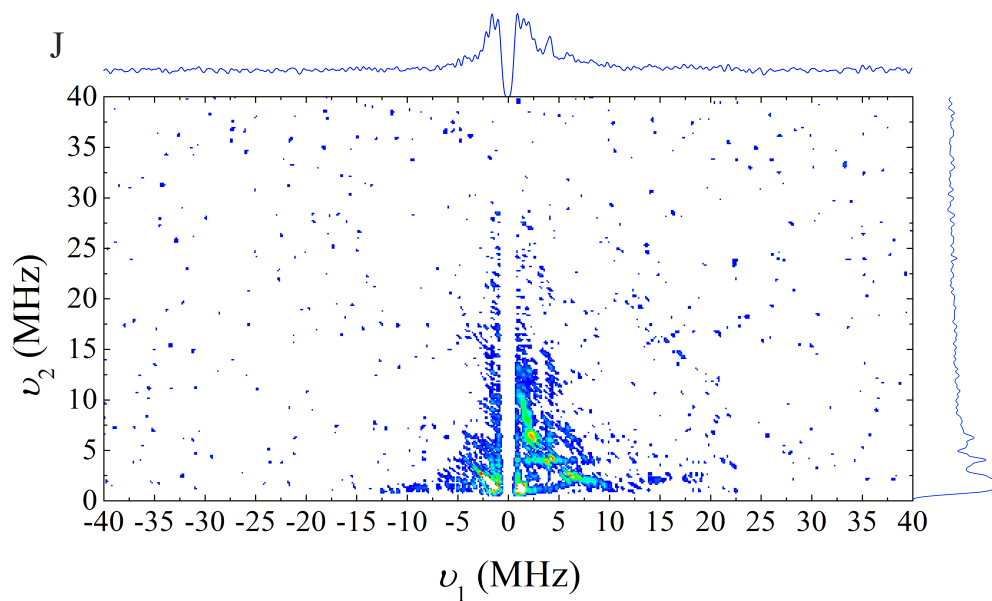


Figure F.17:  $B_0 = 368.1$  mT,  $\tau = 122$  ns,  $\Delta t = 12$  ns

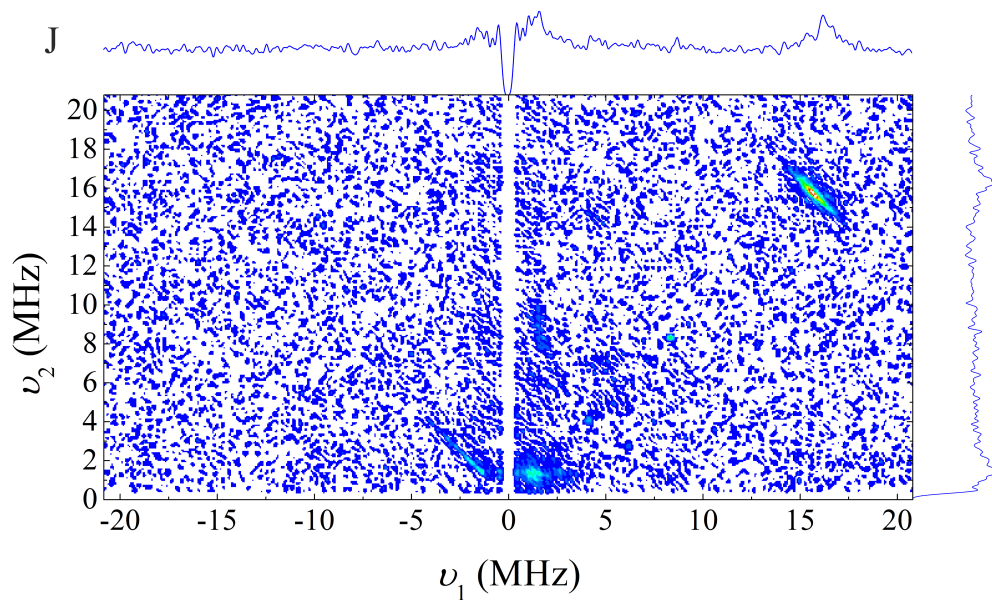


Figure F.18:  $B_0 = 368.2$  mT,  $\tau = 100$  ns

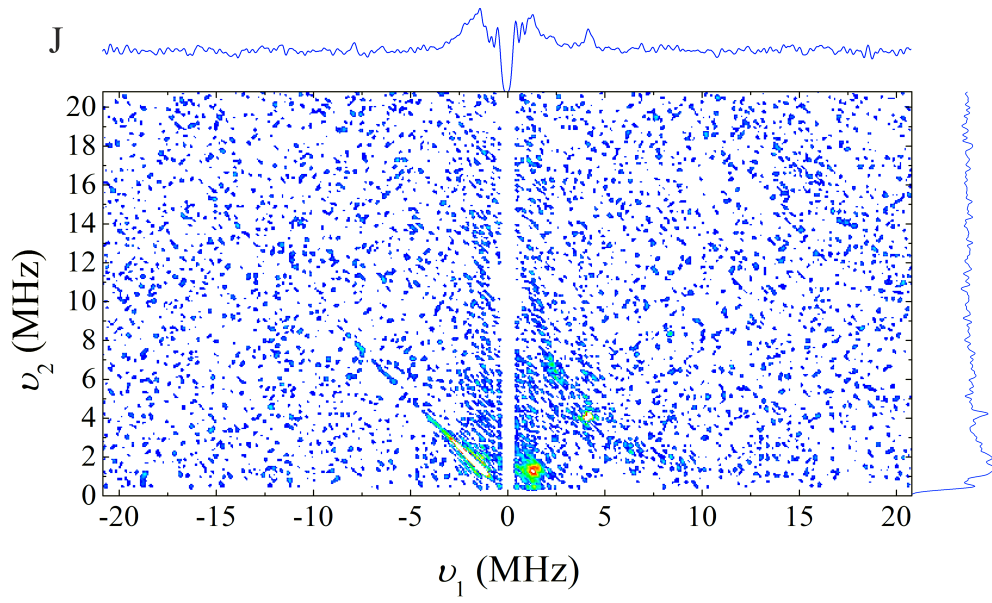


Figure F.19:  $B_0 = 368.2$  mT,  $\tau = 122$  ns

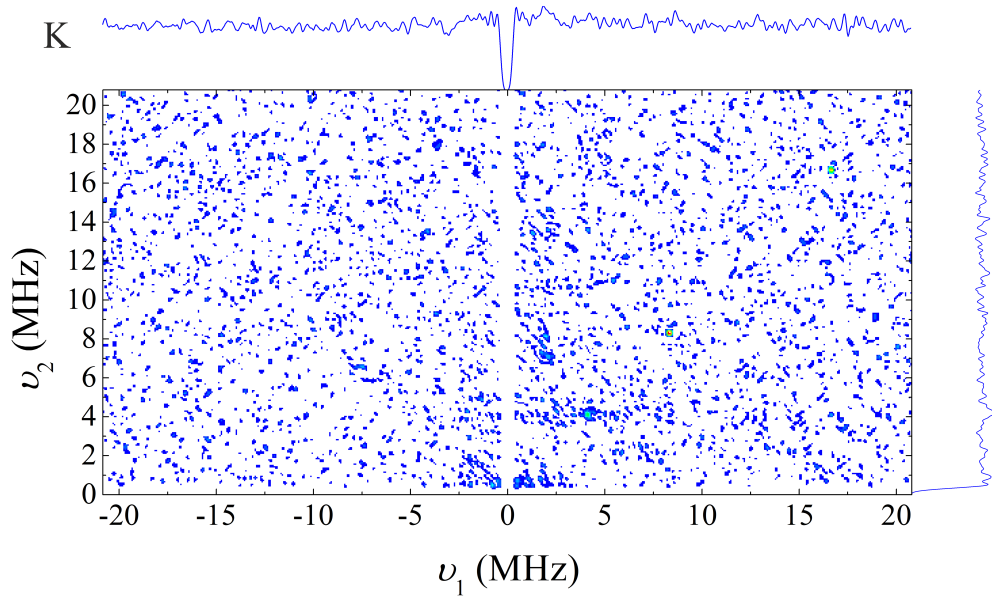


Figure F.20:  $B_0 = 371.2$  mT,  $\tau = 122$  ns

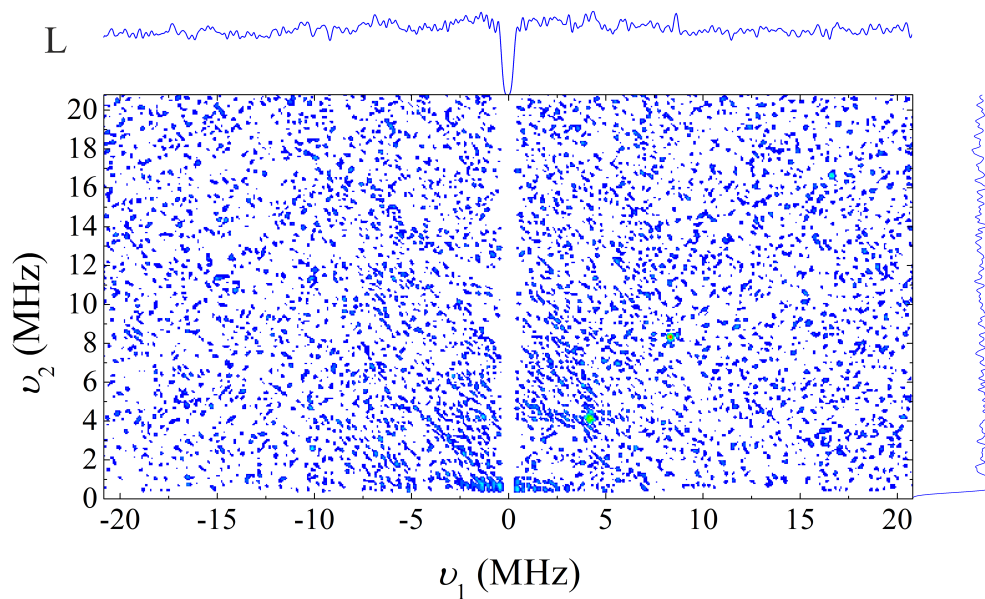


Figure F.21:  $B_0 = 374.1$  mT,  $\tau = 120$  ns

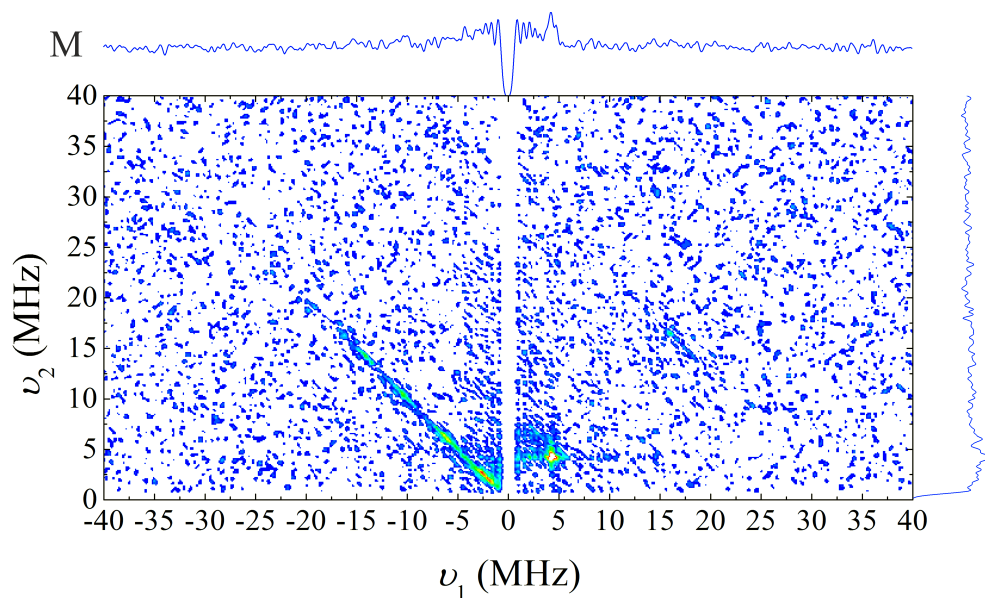


Figure F.22:  $B_0 = 378.0$  mT,  $\tau = 118$  ns,  $\Delta t = 12$  ns

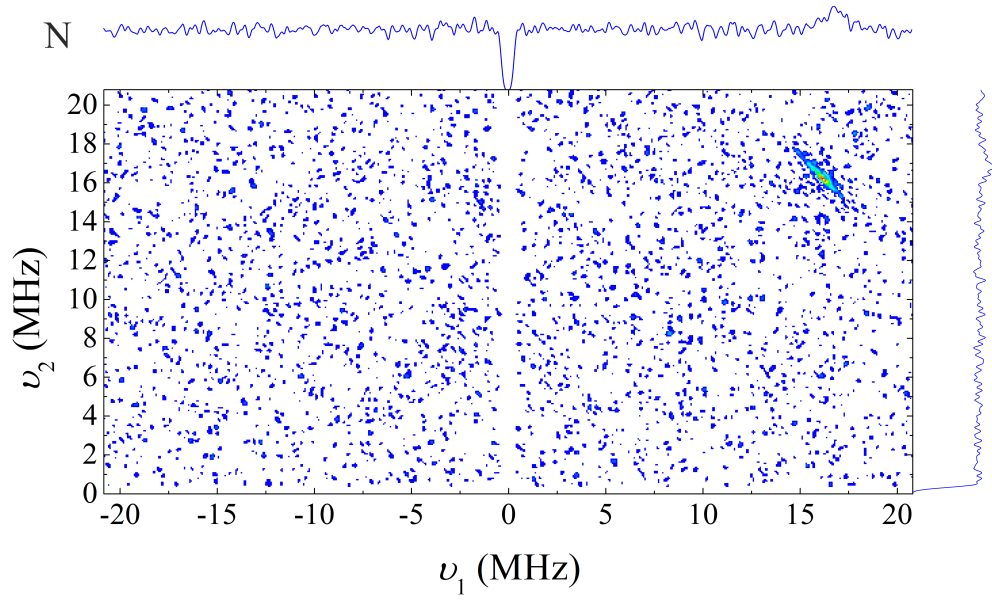


Figure F.23:  $B_0 = 380.0$  mT,  $\tau = 92$  ns

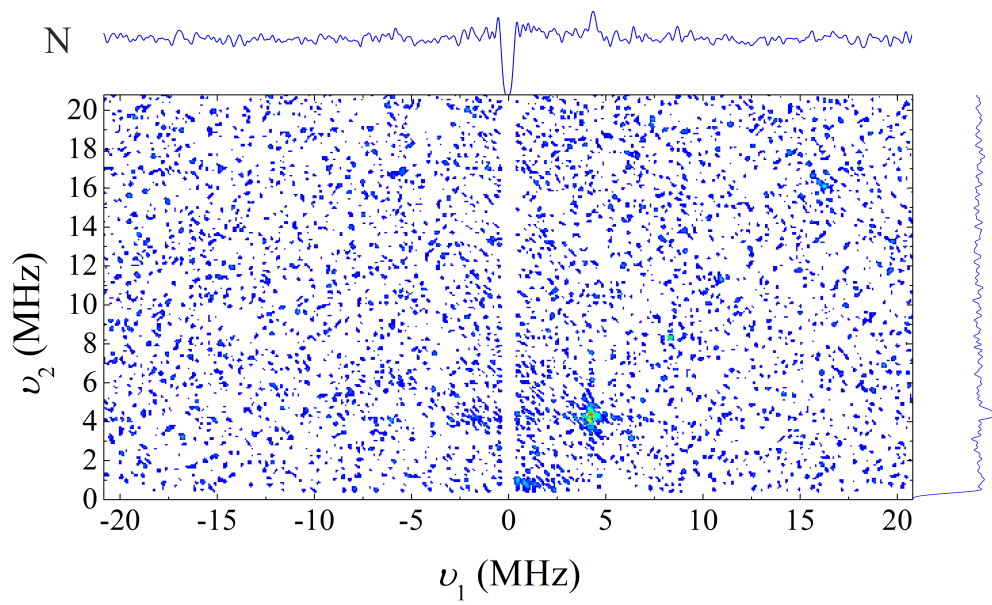


Figure F.24:  $B_0 = 380.0$  mT,  $\tau = 118$  ns

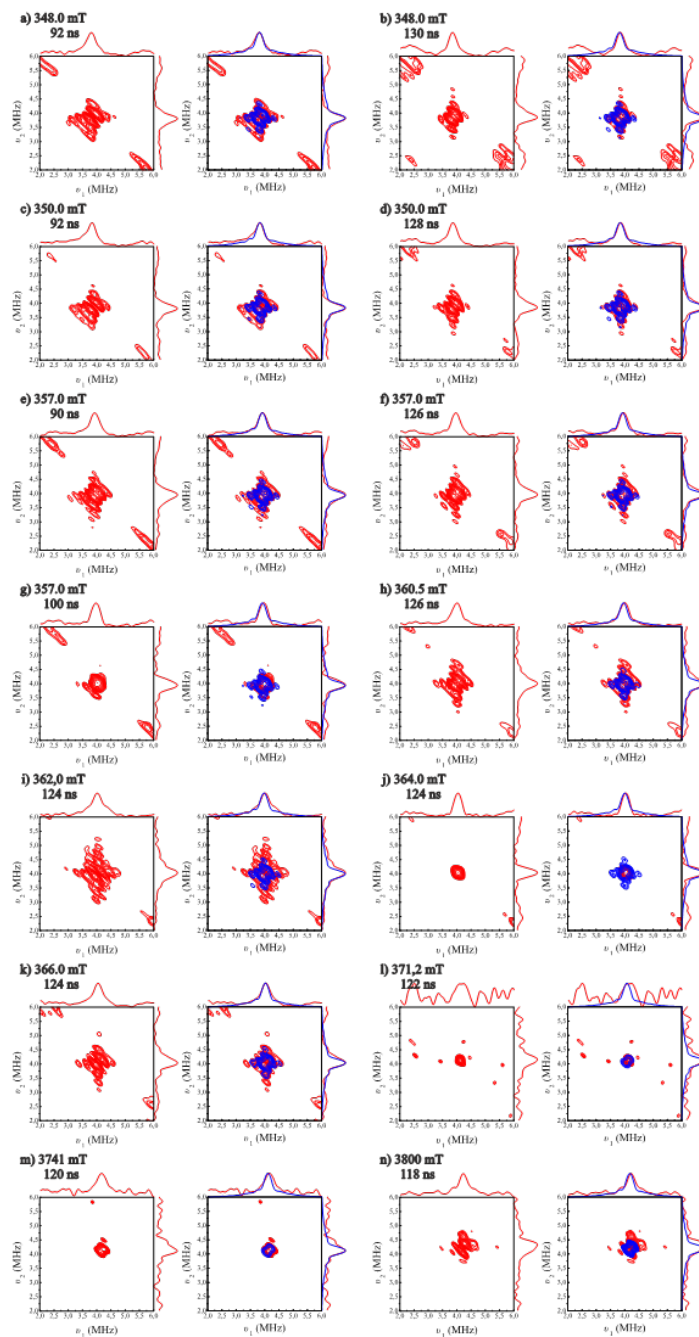


Figure F.25: HSCORE spectra measured at  $T = 6$  K at magnetic field positions and with  $\tau$  values as given on the top left of each subfigure. They show the experimental (red) and simulated (blue) signal of the distant  $^{27}\text{Al}$  nuclear species A12c

## F.2 Details of the DFT calculations and further calculated structural and magnetic parameters

For all DFT calculations the ORCA 3.0.0 program package<sup>[317]</sup> was used. Cluster models with spin multiplicity 1 were treated with the restricted Kohn-Sham formalism whereas for those with spin multiplicity 2 the unrestricted Kohn-Sham formalism was applied.<sup>[317]</sup> To obtain reasonable structures for the **ML** and **M** cluster models, first the corresponding clusters without NO and H<sub>2</sub>O ligands were geometry optimized. Then, the H<sub>2</sub>O ligand was added and the structures were optimized again. For this preliminary calculations different starting geometries for the OH<sup>-</sup> and H<sub>2</sub>O ligands were chosen and the structures were optimized using the B3LYP functional<sup>[342,343]</sup> and the def2-TZVP<sup>[344,387]</sup> basis set. The resulting structures with the smallest energy were selected as inputs for the clusters **ML** and **M**, adding an NO molecule at the remaining CUS. In a next step, relaxed surface scans were performed for both clusters **ML** and **M**, using the B3LYP functional. Here, the dihedral angle  $\varphi$  between the plane containing the N, Al1 and Al2 atoms and the plain containing the Al<sup>3+</sup>-N-O complex was constrained to different values, covering the full circle in steps  $\Delta\varphi = 10^\circ$ . For those scans the [Al<sub>3</sub>( $\mu_3$ -O)(OOC)<sub>6</sub>]<sup>+</sup> core and the OH<sup>-</sup>, H<sub>2</sub>O and NO ligands were treated with the def2-TZVP basis set. All other atoms were treated with the cheaper def2-SV(P)<sup>[344]</sup> basis set. The structures with  $\varphi = \varphi_{\min}$ , where the resulting energies are smallest, were used for further geometry optimizations on B3LYP/def2-TZVP and PBE0/def-TZVP<sup>[345-347]</sup> levels of theory, obtaining the final cluster models **ML** and **M**. Both models of theory show a good performance for the calculation of interactions energies between the [Al<sub>3</sub>( $\mu_3$ -O)(OOC)<sub>6</sub>]<sup>+</sup> core and various ligand molecules as published by Mavrantoukakis et al.<sup>[236]</sup>

In all calculations dispersion forces were included using Grimme's atom-pairwise dispersion correction with the Becke-Johnson damping.<sup>[388,389]</sup> The integration grid parameters were always set by the keywords Grid7 and NoFinalGrid. Except for the model clusters with water but without NO and for the relaxed surface scans further parameters IntAcc = 6.0 and AngularGrid = 7 were set. In all calculations the self-consistent field method (SCF) convergence tolerance was set to an energy of  $\Delta E = 1e - 8 E_h$  by the keyword TightSCF. The RI or RIJCOSX approximations were always applied for non-hybrid or hybrid functions, respectively, to speed up the calculations. They comprise the 'resolution-of-the-identity' (RI) and 'chain-of-spheres exchange' (COSX). In all cases the COSX integration grid was set with the keyword GridX9. Furthermore, the def2-SVP/J and def2-TZVP/J auxiliary basis sets for the Coulomb fitting were always set explicitly, when the def2-SV(P) or def2-TZVP basis sets were used.

Magnetic parameters like the g-tensor, the electric field gradient at the Al and N sites as well as the Fermi-contact and dipolar contributions to the hfi tensors of the <sup>1</sup>H, <sup>14</sup>N and <sup>27</sup>Al nuclei were calculated for the **ML** model using the EPR/NMR module of the ORCA 3.0.0 package. Here, the IGLO-III<sup>[348]</sup> basis set was used for the next neighbored oxygens of all Al atoms, for the whole NO molecule as well as for the oxygens of the OH<sup>-</sup> and H<sub>2</sub>O ligands. The EPR-II<sup>[349]</sup> basis set was used for all other non-metallic atoms. For different calculations the different basis sets aug-cc-pVTZ<sup>[350]</sup>, aug-cc-pVTZ-J<sup>[350,390,391]</sup> and IGLO-

Table F.1: Certain structural parameters of the  $\text{OH}^-$  and  $\text{H}_2\text{O}$  adsorption complexes of the **ML** and **M** model clusters derived by DFT using the B3LYP or PBE0 functional. The length  $r_{\text{Al-OH}}$  is the distance between the Al3 atom and the oxygen of the  $\text{OH}^-$  group, whereas  $r_{\text{H}_2\text{O-Al}}$  is the distance between the Al2 atom and the oxygen of the water molecule. The angles  $\theta_{\text{Al-O-H}}$  and  $\theta_{\text{H}_2\text{-O-Al}}$  are the Al3-O-H bond angle of the  $\text{OH}^-$  ligand and the angle between the waters Al2-O bond and the averaged vector sum of both water O-H bonds, respectively. The parameters  $\varphi_{\text{A-AlOH}}$  and  $\varphi_{\text{H}_2\text{OAl-A}}$  are the angle between the plane A containing all three Al atoms and the plane containing the Al3-OH complex as well as the angle between the plane A and the plane, spanned by the Al2-O bond of the water complex and the waters averaged sum of both water O-H bonds, respectively.

| Parameter                              | <b>ML</b> /B3LYP | <b>ML</b> /PBE0 | <b>M</b> /B3LYP | <b>M</b> /PBE0 |
|--|------------------|-----------------|-----------------|----------------|
| $r_{\text{Al-OH}}$ (Å)                 | 1.748            | 1.742           | 1.748           | 1.744          |
| $\theta_{\text{Al-O-H}}$ (°)           | 117.54           | 116.83          | 115.98          | 115.16         |
| $\varphi_{\text{A-AlOH}}$ (°)          | 89.91            | 90.26           | 110.86          | 113.87         |
| $r_{\text{H}_2\text{O-Al}}$ (Å)        | 2.068            | 2.046           | 2.053           | 2.039          |
| $\theta_{\text{H}_2\text{-O-Al}}$ (°)  | 119.87           | 118.25          | 115.79          | 114.39         |
| $\varphi_{\text{H}_2\text{OAl-A}}$ (°) | 1.66             | 1.26            | 6.23            | 9.27           |

III were used for the Al atoms.<sup>[242]</sup> Since the performance of different functionals for the calculation of the isotropic hfi is discussed controversially in the literature,<sup>[231,233,242,362]</sup> magnetic parameters were calculated with a variety of functionals including generalized gradient correction GGA functionals (BP86,<sup>[353]</sup> OLYP,<sup>[356]</sup> PBE,<sup>[351,352]</sup> PW91,<sup>[357]</sup> PWP), hybrid functionals (PBE0, B3LYP, O3LYP<sup>[355]</sup>), the meta-GGA functional TPSS<sup>[360]</sup> and its hybrid version TPSSh.<sup>[360]</sup> In all cases, for the calculation of the spin-orbit-coupling operator an accurate variant was chosen by the keyword SOMF(1X). The orbital contribution to the hfi of the Al1 atom was always neglected since exemplary calculations showed that it is less than 0.05 MHz.

For the calculation of the binding energy<sup>[236]</sup> the counterpoise correction of the basis set superposition error<sup>[363]</sup> was considered. For the analysis of the calculated wave function the program Chemissian version 4.43 was used.



Table F.2: DFT derived hfi and nqi parameters of all three  $^{27}\text{Al}$  nuclei of the cluster model **ML** that are calculated with the B3LYP functional setting the basis set for the Al atoms to either aug-cc-pVTZ, aug-cc-pVTZ-J or IGLO-III. The Euler angles describe the orientation relative to the g-tensor.

| Parameter                            | aug-cc-pVTZ |        |        | aug-cc-pVTZ-J |        |        | IGLO-III |        |        |
|--------------------------------------|-------------|--------|--------|---------------|--------|--------|----------|--------|--------|
|                                      | Al1         | Al2    | Al3    | Al1           | Al2    | Al3    | Al1      | Al2    | Al3    |
| $a_{\text{iso}}$ (MHz)               | 21.67       | 0.08   | 0.12   | 23.81         | 0.08   | 0.13   | 23.71    | 0.07   | 0.13   |
| $T$ (MHz)                            | 3.59        | 0.13   | 0.13   | 3.61          | 0.13   | 0.13   | 3.62     | 0.13   | 0.13   |
| $\rho$                               | 0.029       | 0.002  | 0.002  | 0.030         | 0.001  | 0.002  | 0.030    | 0.001  | 0.002  |
| $\alpha_{\text{hfi}}$ ( $^{\circ}$ ) | 89.22       | 93.91  | 87.34  | 89.24         | 93.93  | 87.38  | 89.28    | 93.96  | 87.38  |
| $\beta_{\text{hfi}}$ ( $^{\circ}$ )  | 47.95       | 29.34  | 62.62  | 47.96         | 29.42  | 62.68  | 47.97    | 29.40  | 62.68  |
| $\gamma_{\text{hfi}}$ ( $^{\circ}$ ) | 89.71       | 86.63  | 85.71  | 89.22         | 84.99  | 86.23  | 89.43    | 84.63  | 86.37  |
| $C_Q$ (MHz)                          | 4.28        | 2.08   | -20.56 | 2.80          | 1.40   | -19.36 | 2.96     | 1.52   | -18.84 |
| $\eta$                               | 0.326       | 0.181  | 0.047  | 0.104         | 0.399  | 0.051  | 0.204    | 0.301  | 0.062  |
| $\alpha_{\text{nqi}}$ ( $^{\circ}$ ) | 95.56       | -106.7 | 85.36  | 83.83         | -106.2 | 85.72  | 93.96    | -106.6 | 85.68  |
| $\beta_{\text{nqi}}$ ( $^{\circ}$ )  | 73.00       | 35.47  | 110.40 | 90.14         | 41.95  | 110.57 | 29.40    | 37.98  | 110.56 |
| $\gamma_{\text{nqi}}$ ( $^{\circ}$ ) | 85.77       | -156.9 | 79.35  | 101.53        | -165.2 | 82.32  | 84.32    | -162.9 | 82.76  |

## Bibliography

- [1] Y. Liu, J.-H. Her, A. Dailly, A. J. Ramirez-Cuesta, D. A. Neumann, and C. M. Brown. *Journal of the American Chemical Society* **130**, 11813–11818 (2008).
- [2] S. Kitagawa and M. Kondo. *Bulletin of the Chemical Society of Japan* **71**, 1739–1753 (1998).
- [3] S. Kitagawa, R. Kitaura, and S.-i. Noro. *Angewandte Chemie International Edition* **43**, 2334–2375 (2004).
- [4] B. F. Hoskins and R. Robson. *Journal of the American Chemical Society* **111**, 5962–5964 (1989).
- [5] B. F. Hoskins and R. Robson. *Journal of the American Chemical Society* **112**, 1546–1554 (1990).
- [6] D. Venkataraman, G. B. Gardner, S. Lee, and J. S. Moore. *Journal of the American Chemical Society* **117**, 11600–11601 (1995).
- [7] G. B. Gardner, D. Venkataraman, J. S. Moore, and S. Lee. *Nature* **374**, 792–795 (1995).
- [8] O. M. Yaghi, G. Li, and H. Li. *Nature* **378**, 703–706 (1995).
- [9] S. Subramanian and M. J. Zaworotko. *Angewandte Chemie International Edition in English* **34**, 2127–2129 (1995).
- [10] W. Li. *Progress in Materials Science* **100**, 21–63 (2019).
- [11] J. Caro. *Chemie Ingenieur Technik* **90**, 1759–1768 (2018).
- [12] V. Bon. *Current Opinion in Green and Sustainable Chemistry* **4**, 44–49 (2017).
- [13] Z. Liang, C. Qu, W. Guo, R. Zou, and Q. Xu. *Advanced Materials* **30**, 1702891 (2017).
- [14] B. Li, M. Chrzanowski, Y. Zhang, and S. Ma. *Coordination Chemistry Reviews* **307**, 106–129 (2016).
- [15] M. I. Nandasiri, S. R. Jambovane, B. P. McGrail, H. T. Schaefer, and S. K. Nune. *Coordination Chemistry Reviews* **311**, 38–52 (2016).
- [16] R. J. Kuppler, D. J. Timmons, Q.-R. Fang, J.-R. Li, T. A. Makal, M. D. Young, D. Yuan, D. Zhao, W. Zhuang, and H.-C. Zhou. *Coordination Chemistry Reviews* **253**, 3042–3066 (2009).
- [17] U. Mueller, M. Schubert, F. Teich, H. Puetter, K. Schierle-Arndt, and J. Pastré. *Journal of Materials Chemistry* **16**, 626 (2006).

- 
- [18] H. Montes-Andrés, G. Orcajo, C. Mellot-Draznieks, C. Martos, J. A. Botas, and G. Calleja. *The Journal of Physical Chemistry C* **122**, 28123–28132 (2018).
- [19] S. E. Bambalaza, H. W. Langmi, R. Mokaya, N. M. Musyoka, J. Ren, and L. E. Khotseng. *Journal of Materials Chemistry A* **6**, 23569–23577 (2018).
- [20] M. Beckner and A. Dailly. *International Journal of Energy Research* **40**, 91–99 (2016).
- [21] N. A. Qasem, R. Ben-Mansour, and M. A. Habib. *Applied Energy* **210**, 317–326 (2018).
- [22] M. Younas, M. Sohail, L. K. Leong, M. J. K. Bashir, and S. Sumathi. *International Journal of Environmental Science and Technology* **13**, 1839–1860 (2016).
- [23] H. Wang, W. Meng, J. Wu, J. Ding, H. Hou, and Y. Fan. *Coordination Chemistry Reviews* **307**, 130–146 (2016).
- [24] K. C. Stylianou and W. L. Queen. *Chimia* **69**, 274–283 (2015).
- [25] J. H. Lee and J. Kim. *Membrane Journal* **25**, 465–477 (2015).
- [26] G. Liu, V. Chernikova, Y. Liu, K. Zhang, Y. Belmabkhout, O. Shekhah, C. Zhang, S. Yi, M. Eddaoudi, and W. J. Koros. *Nature Materials* **17**, 283–289 (2018).
- [27] B. Ghalei, K. Sakurai, Y. Kinoshita, K. Wakimoto, A. P. Isfahani, Q. Song, K. Doitomi, S. Furukawa, H. Hirao, H. Kusuda, S. Kitagawa, and E. Sivaniah. *Nature Energy* **2**, 17086 (2017).
- [28] K. Adil, Y. Belmabkhout, R. S. Pillai, A. Cadiau, P. M. Bhatt, A. H. Assen, G. Maurin, and M. Eddaoudi. *Chemical Society Reviews* **46**, 3402–3430 (2017).
- [29] X. Li, Y. Liu, J. Wang, J. Gascon, J. Li, and B. V. der Bruggen. *Chemical Society Reviews* **46**, 7124–7144 (2017).
- [30] Y. Zhang, X. Feng, S. Yuan, J. Zhou, and B. Wang. *Physical Chemistry Chemical Physics* **3**, 896–909 (2016).
- [31] S. R. Venna and M. A. Carreon. *Chemical Engineering Science* **124**, 3–19 (2015).
- [32] D. Cao, H. Huang, Y. Lan, X. Chen, Q. Yang, D. Liu, Y. Gong, C. Xiao, C. Zhong, and S. Peng. *Journal of Materials Chemistry A* **6**, 19954–19959 (2018).
- [33] G. Han, Y. Gong, H. Huang, D. Cao, X. Chen, D. Liu, and C. Zhong. *ACS Applied Materials & Interfaces* **10**, 32128–32132 (2018).
- [34] H. Oh, I. Savchenko, A. Mavrandonakis, T. Heine, and M. Hirscher. *ACS Nano* **8**, 761–770 (2013).
- [35] P.-Q. Liao, J.-Q. Shen, and J.-P. Zhang. *Coordination Chemistry Reviews* **373**, 22–48 (2018).

- [36] L. Jiao, Y. Wang, H.-L. Jiang, and Q. Xu. *Advanced Materials* **30**, 1703663 (2017).
- [37] Y. Liu, A. J. Howarth, N. A. Vermeulen, S.-Y. Moon, J. T. Hupp, and O. K. Farha. *Coordination Chemistry Reviews* **346**, 101–111 (2017).
- [38] Y. Chen and S. Ma. *Dalton transactions (Cambridge, England : 2003)* **45**, 9744–9753 (2016).
- [39] D. Bhattacharjee, B. K. Mishra, A. K. Chakrabartty, and R. C. DeKa. *New Journal of Chemistry* **39**, 2209–2216 (2015).
- [40] A. H. Chughtai, N. Ahmad, H. A. Younus, A. Laypkov, and F. Verpoort. *Chemical Society Reviews* **44**, 6804–6849 (2015).
- [41] A. C. Kathalikkattil, R. Babu, J. Tharun, R. Roshan, and D.-W. Park. *Catalysis Surveys from Asia* **19**, 223–235 (2015).
- [42] X. Fang, Q. Shang, Y. Wang, L. Jiao, T. Yao, Y. Li, Q. Zhang, Y. Luo, and H.-L. Jiang. *Advanced Materials* **30**, 1705112 (2018).
- [43] C.-C. Wang, Y.-Q. Zhang, J. Li, and P. Wang. *Journal of Molecular Structure* **1083**, 127–136 (2015).
- [44] M. Marszewski, S. Cao, J. Yu, and M. Jaroniec. *Materials Horizons* **2**, 261–278 (2015).
- [45] L. Shen, R. Liang, and L. Wu. *Chinese Journal of Catalysis* **36**, 2071–2088 (2015).
- [46] S. Wu, Y. Lin, J. Liu, W. Shi, G. Yang, and P. Cheng. *Advanced Functional Materials* **28**, 1707169 (2018).
- [47] Y. Li, A.-S. Xiao, B. Zou, H.-X. Zhang, K.-L. Yan, and Y. Lin. *Polyhedron* **154**, 83–97 (2018).
- [48] W. P. Lustig, S. Mukherjee, N. D. Rudd, A. V. Desai, J. Li, and S. K. Ghosh. *Chemical Society Reviews* **46**, 3242–3285 (2017).
- [49] R.-B. Lin, S.-Y. Liu, J.-W. Ye, X.-Y. Li, and J.-P. Zhang. *Advanced Science* **3**, 1500434 (2016).
- [50] P. Kumar, A. Deep, and K.-H. Kim. *TrAC Trends in Analytical Chemistry* **73**, 39–53 (2015).
- [51] A. Indra, T. Song, and U. Paik. *Advanced Materials* **30**, 1705146 (2018).
- [52] L. Wang, Y. Han, X. Feng, J. Zhou, P. Qi, and B. Wang. *Coordination Chemistry Reviews* **307**, 361–381 (2016).
- [53] W. Kaveevivitchai and A. J. Jacobson. *Journal of Power Sources* **278**, 265–273 (2015).

- 
- [54] F.-S. Ke, Y.-S. Wu, and H. Deng. *Journal of Solid State Chemistry* **223**, 109–121 (2015).
- [55] L. Tian, X. Yang, Q. Liu, F. Qu, and H. Tang. *Applied Surface Science* **455**, 403–409 (2018).
- [56] R. Kaur, K.-H. Kim, A. K. Paul, and A. Deep. *Journal of Materials Chemistry A* **4**, 3991–4002 (2016).
- [57] P. Kumar, V. Bansal, A. Deep, and K.-H. Kim. *Journal of Porous Materials* **22**, 413–424 (2015).
- [58] S. Wang and X. Wang. *Small* **11**, 3097–3112 (2015).
- [59] X. Zhang, W. Wang, Z. Hu, G. Wang, and K. Uvdal. *Coordination Chemistry Reviews* **284**, 206–235 (2015).
- [60] M. C. So, G. P. Wiederrecht, J. E. Mondloch, J. T. Hupp, and O. K. Farha. *Chem. Commun.* **51**, 3501–3510 (2015).
- [61] Y. Tang, T. Xia, T. Song, Y. Cui, Y. Yang, and G. Qian. *Advanced Optical Materials* **6**, 1800968 (2018).
- [62] Y. Cui, B. Chen, and G. Qian. *Coordination Chemistry Reviews* **273-274**, 76–86 (2014).
- [63] J. Li, X. Wang, G. Zhao, C. Chen, Z. Chai, A. Alsaedi, T. Hayat, and X. Wang. *Chemical Society Reviews* **47**, 2322–2356 (2018).
- [64] A. A. Alqadami, M. Naushad, Z. A. Alothman, and A. A. Ghfar. *ACS Applied Materials & Interfaces* **9**, 36026–36037 (2017).
- [65] S. Li, Y. Chen, X. Pei, S. Zhang, X. Feng, J. Zhou, and B. Wang. *Chinese Journal of Chemistry* **34**, 175–185 (2016).
- [66] N. Nicomel, K. Leus, K. Folens, P. van der Voort, and G. Du Laing. *International Journal of Environmental Research and Public Health* **13**, 62 (2016).
- [67] P. Kumar, K.-H. Kim, E. E. Kwon, and J. E. Szulejko. *Journal of Materials Chemistry A* **4**, 345–361 (2016).
- [68] M. Solovyeva, L. Gordeeva, T. Krieger, and Y. Aristov. *Energy Conversion and Management* **174**, 356–363 (2018).
- [69] H. W. B. Teo, A. Chakraborty, and S. Kayal. *Microporous and Mesoporous Materials* **272**, 109–116 (2018).
- [70] W. Cai, J. Wang, C. Chu, W. Chen, C. Wu, and G. Liu. *Advanced Science* **6**, 1801526 (2018).

- [71] M. H. Teplensky, M. Fantham, P. Li, T. C. Wang, J. P. Mehta, L. J. Young, P. Z. Moghadam, J. T. Hupp, O. K. Farha, C. F. Kaminski, and D. Fairen-Jimenez. *Journal of the American Chemical Society* **139**, 7522–7532 (2017).
- [72] M.-X. Wu and Y.-W. Yang. *Advanced Materials* **29**, 1606134 (2017).
- [73] R. Liu, T. Yu, Z. Shi, and Z. Wang. *International journal of nanomedicine* **11**, 1187–1200 (2016).
- [74] C.-Y. Sun, C. Qin, X.-L. Wang, and Z.-M. Su. *Expert Opinion on Drug Delivery* **10**, 89–101 (2013).
- [75] R. C. Huxford, J. Della Rocca, and W. Lin. *Biocatalysis and Biotransformation/Bioinorganic Chemistry* **14**, 262–268 (2010).
- [76] S. Kaskel. *The chemistry of metal-organic frameworks: Synthesis, characterization, and applications*. Wiley-VCH, Weinheim (2016).
- [77] A. J. Howarth, A. W. Peters, N. A. Vermeulen, T. C. Wang, J. T. Hupp, and O. K. Farha. *Chemistry of Materials* **29**, 26–39 (2016).
- [78] F. Rouquerol. *Adsorption by powders and porous solids: Principles, methodology and applications*. Academic Press, Kidlington, Oxford, second edition ed. (2014).
- [79] M. Mazaj, V. Kaučič, and N. Z. Logar. *Acta Chimica Slovenica* pp. 440–458 (2016).
- [80] F. Gándara and T. D. Bennett. *IUCrJ* **1**, 563–570 (2014).
- [81] E. J. Carrington, I. J. Vitorica-Yrezabal, and L. Brammer. *Acta crystallographica Section B, Structural science, crystal engineering and materials* **70**, 404–422 (2014).
- [82] F. L. Morel, S. Pin, T. Huthwelker, M. Ranocchiari, and J. A. van Bokhoven. *Physical Chemistry Chemical Physics* **17**, 3326–3331 (2015).
- [83] N. Nijem and Y. J. Chabal. *Comments on Inorganic Chemistry* **34**, 78–102 (2014).
- [84] W. Chen, Y. nan Wu, and F. Li. *Journal of Chemistry* **2016**, 1–11 (2016).
- [85] E. Weiland, M.-A. Springuel-Huet, A. Nossou, and A. Gédéon. *Microporous and Mesoporous Materials* **225**, 41–65 (2016).
- [86] H. Hoffmann, M. Debowski, P. Müller, S. Paasch, I. Senkowska, S. Kaskel, and E. Brunner. *Materials* **5**, 2537–2572 (2012).
- [87] P. Decyk, A. Więckowski, L. Najder-Kozdrowska, I. Bilkova, and M. Ziółek. *Acta Physica Polonica A* **132**, 38–44 (2017).
- [88] A. Godiksen, P. N. R. Vennestrøm, S. B. Rasmussen, and S. Mossin. *Topics in Catalysis* **60**, 13–29 (2016).

- 
- [89] B. Weckhuysen, R. Heidler, and R. Schoonheydt. In H. Karge and J. Weitkamp (Eds.), *Characterization I*, vol. 4 of *Molecular Sieves – Science and Technology*, pp. 295–335. Springer Berlin Heidelberg (2004).
- [90] L. Kevan. *Accounts of Chemical Research* **20**, 1–7 (1987).
- [91] L. Kevan. *Reviews of Chemical Intermediates* **8**, 53–85 (1987).
- [92] M. Chiesa, E. Giamello, and M. Che. *Chemical Reviews* **110**, 1320–1347 (2009).
- [93] M. Chiesa, M. C. Paganini, and E. Giamello. *Applied Magnetic Resonance* **37**, 605–618 (2009).
- [94] D. M. Murphy. In S. D. Jackson and J. S. J. Hargreaves (Eds.), *Metal oxide catalysis*, pp. 1–50. Wiley-VCH, Weinheim (©2009).
- [95] K. Dyrek and M. Che. *Chemical Reviews* **97**, 305–332 (1997).
- [96] Z. Sojka and M. Che. *Colloids and Surfaces A: Physicochemical and Engineering Aspects* **158**, 165–178 (1999).
- [97] S. van Doorslaer and D. Murphy. In M. Drescher and G. Jeschke (Eds.), *EPR Spectroscopy*, vol. 321 of *Topics in Current Chemistry*, pp. 1–39. Springer Berlin Heidelberg (2012).
- [98] Z. Sojka and M. Che. *Applied Magnetic Resonance* **20**, 433–456 (2001).
- [99] D. M. Murphy and C. C. Rowlands. *Current Opinion in Solid State and Materials Science* **5**, 97–104 (2001).
- [100] B. Jee, K. Eisinger, F. Gul-E-Noor, M. Bertmer, M. Hartmann, D. Himsl, and A. Pöpl. *Journal of Physical Chemistry C* **114**, 16630–16639 (2010).
- [101] A. Kul'taeva, T. Biktagirov, J. Bergmann, L. Hensel, H. Krautscheid, and A. Pöpl. *Physical Chemistry Chemical Physics* **19**, 31030–31038 (2017).
- [102] M. Šimėnas, A. Kul'taeva, S. Balčiūnas, M. Trzebiatowska, D. Klose, G. Jeschke, M. Mączka, J. Banys, and A. Pöpl. *The Journal of Physical Chemistry C* **121**, 16533–16540 (2017).
- [103] I. Nevjestic, H. Depauw, K. Leus, V. Kalendra, I. Caretti, G. Jeschke, S. van Doorslaer, F. Callens, P. van der Voort, and H. Vrielinck. In *European Federation of Electron Paramagnetic Resonance Groups, 9th Conference, Abstracts* (2014).
- [104] I. Nevjestic, H. Depauw, K. Leus, V. Kalendra, I. Caretti, G. Jeschke, S. van Doorslaer, F. Callens, P. van der Voort, and H. Vrielinck. *ChemPhysChem* **16**, 3118 (2015).
- [105] B. Jee, P. St. Petkov, G. N. Vayssilov, T. Heine, M. Hartmann, and A. Pöpl. *Journal of Physical Chemistry C* **117**, 8231–8240 (2013).

- [106] B. Jee, M. Hartmann, and A. Pöpl. *Molecular Physics* **111**, 2950–2966 (2013).
- [107] M. Šimėnas, B. Jee, M. Hartmann, J. Banys, and A. Pöpl. *The Journal of Physical Chemistry C* **119**, 28530–28535 (2015).
- [108] S. Friedländer, P. St. Petkov, F. Bolling, A. Kultaeva, W. Böhlmann, O. Ovchar, A. G. Belous, T. Heine, and A. Pöpl. *Journal of Physical Chemistry C* **120**, 27399–27411 (2016).
- [109] A. S. Poryvaev, A. M. Sheveleva, P. A. Demakov, S. S. Arzumanov, A. G. Stepanov, D. N. Dybtsev, and M. V. Fedin. *Applied Magnetic Resonance* **49**, 255–264 (2018).
- [110] M. Mendt, B. Jee, N. Stock, T. Ahnfeldt, M. Hartmann, D. Himsl, and A. Pöpl. *The Journal of Physical Chemistry C* **114**, 19443–19451 (2010).
- [111] M. Mendt, B. Jee, D. Himsl, L. Moschkowitz, T. Ahnfeldt, N. Stock, M. Hartmann, and A. Pöpl. *Applied Magnetic Resonance* **45**, 269–285 (2014).
- [112] I. Nevjstić, H. Depauw, K. Leus, G. Rampelberg, C. A. Murray, C. Detavernier, P. van der Voort, F. Callens, and H. Vrielinck. *Journal of Physical Chemistry C* **120**, 17400–17407 (2016).
- [113] I. Nevjstić, H. Depauw, P. Gast, P. Tack, D. Deduytsche, K. Leus, M. V. Landeghem, E. Goovaerts, L. Vincze, C. Detavernier, P. V. D. Voort, F. Callens, and H. Vrielinck. *Physical Chemistry Chemical Physics* **19**, 24545–24554 (2017).
- [114] M. Mendt, P. Vervoorts, A. Schneemann, R. A. Fischer, and A. Pöpl. *The Journal of Physical Chemistry C* (2019).
- [115] A. Kultaeva, V. Bon, M. S. Weiss, A. Pöpl, and S. Kaskel. *Inorganic Chemistry* **57**, 11920–11929 (2018).
- [116] A. M. Sheveleva, D. I. Kolokolov, A. A. Gabrienko, A. G. Stepanov, S. A. Gromilov, I. K. Shundrina, R. Z. Sagdeev, M. V. Fedin, and E. G. Bagryanskaya. *The Journal of Physical Chemistry Letters* **5**, 20–24 (2014).
- [117] A. S. Poryvaev, A. M. Sheveleva, D. I. Kolokolov, A. G. Stepanov, E. G. Bagryanskaya, and M. V. Fedin. *The Journal of Physical Chemistry C* **120**, 10698–10704 (2016).
- [118] B. Jee, K. Koch, L. Moschkowitz, D. Himsl, M. Hartman, and A. Pöpl. *Journal of Physical Chemistry Letters* **2**, 357–361 (2011).
- [119] M. N. Timofeeva, V. N. Panchenko, A. A. Abel, N. A. Khan, I. Ahmed, A. B. Ayupov, K. P. Volcho, and S. H. Jung. *Journal of Catalysis* **311**, 114–120 (2014).
- [120] A. M. Sheveleva, A. V. Anikeenko, A. S. Poryvaev, D. L. Kuzmina, I. K. Shundrina, D. I. Kolokolov, A. G. Stepanov, and M. V. Fedin. *Journal of Physical Chemistry C* **121**, 19880–19886 (2017).



- 
- [121] M. Dan-Hardi, C. Serre, T. Frot, L. Rozes, G. Maurin, C. Sanchez, and G. Férey. *Journal of the American Chemical Society* **131**, 10857–10859 (2009).
- [122] D. Sun, W. Liu, Y. Fu, Z. Fang, F. Sun, X. Fu, Y. Zhang, and Z. Li. *Chemistry – A European Journal* **20**, 4780–4788 (2014).
- [123] J. Long, S. Wang, Z. Ding, S. Wang, Y. Zhou, L. Huang, and X. Wang. *Chemical Communications* **48**, 11656–11658 (2012).
- [124] M. J. Beier, W. Kleist, M. T. Wharmby, R. Kissner, B. Kimmerle, P. A. Wright, J.-D. Grunwaldt, and A. Baiker. *Chemistry – A European Journal* **18**, 887–898 (2012).
- [125] H. R. Zeller and W. Känzig. *Helvetica Physica Acta* p. 845 (1967).
- [126] R. T. Shuey and H. R. Zeller. *Helvetica Physica Acta* (1967).
- [127] C. J. Rhodes. *Chemical Papers* **70** (2016).
- [128] D. Biglino, H. Li, R. Erickson, A. Lund, H. Yahiro, and M. Shiotani. *Physical Chemistry Chemical Physics* **1**, 2887–2896 (1999).
- [129] A. Godiksen, O. L. Isaksen, S. B. Rasmussen, P. N. R. Vennestrøm, and S. Mossin. *ChemCatChem* **10**, 366–370 (2017).
- [130] N. Hogg. *Free Radical Biology and Medicine* **49**, 122–129 (2010).
- [131] Y. A. Henry, A. Guissani, and B. Ducastel. *Nitric oxide research from chemistry to biology: EPR spectroscopy of nitrosylated compounds*. Molecular biology intelligence unit. Springer and Landes, New York and Berlin and Heidelberg and London and Paris and Tokyo and Hong Kong and Barcelona and Budapest and Austin (1997).
- [132] A. L. Kleschyov, P. Wenzel, and T. Munzel. *Journal of Chromatography B* **851**, 12–20 (2007).
- [133] M. R. Kumar, T. Clover, A. D. Olaitan, C. Becker, T. Solouki, and P. J. Farmer. *Nitric Oxide* **77**, 96–105 (2018).
- [134] A. H. Khan, K. Peikert, M. Fröba, and M. Bertmer. *Microporous and Mesoporous Materials* **216**, 111–117 (2015).
- [135] A. H. Khan, B. Barth, M. Hartmann, J. Haase, and M. Bertmer. *Journal of Physical Chemistry C* **122**, 12723–12730 (2018).
- [136] L. J. Ignarro, G. M. Buga, K. S. Wood, R. E. Byrns, and G. Chaudhuri. *Proceedings of the National Academy of Sciences* **84**, 9265–9269 (1987).
- [137] R. F. Furchgott, M. T. Khan, and D. Jothianandan. *Federation Proceedings* **46**, 385 (1987).
- [138] W. P. Arnold, C. K. Mittal, S. Katsuki, and F. Murad. *Proc. Natl. Acad. Sci. U. S. A.* **74**, 3203–3207 (1977).

- [139] A. W. Carpenter and M. H. Schoenfisch. *Chemical Society Reviews* **41**, 3742 (2012).
- [140] G. Walford and J. Loscalzo. *Journal of Thrombosis and Haemostasis* **1**, 2112–2118 (2003).
- [141] L. J. Ignarro and F. Murad. *Nitric oxide: Biochemistry, molecular biology, and therapeutic implications*. Academic Press, San Diego (1995).
- [142] F. J. Corpas and J. B. Barroso. *Nitric oxide : biology and chemistry / official journal of the Nitric Oxide Society* **45**, 15–19 (2015).
- [143] A. B. Seabra, M. Rai, and N. Durán. *Journal of Plant Biochemistry and Biotechnology* **23**, 1–10 (2014).
- [144] C. J. Lowenstein. *Annals of Internal Medicine* **120**, 227 (1994).
- [145] F. C. Fang. *Journal of Clinical Investigation* **99**, 2818–2825 (1997).
- [146] A. R. Butler and D. L. H. Williams. *Chemical Society Reviews* **22**, 233 (1993).
- [147] J.-d. Luo and A. F. Chen. *Acta Pharmacologica Sinica* **26**, 259–264 (2005).
- [148] P. Vallance. *Fundamental and Clinical Pharmacology* **17**, 1–10 (2003).
- [149] J. P. Maia-de Oliveira, C. Trzesniak, I. R. Oliveira, M. J. Kempton, T. M. N. d. Rezende, S. Iego, G. B. Baker, S. M. Dursun, J. P. Machado-de Sousa, and J. E. C. Hallak. *Revista Brasileira de Psiquiatria* **34**, **Supplement 2**, 149–162 (2012).
- [150] S. Huerta, S. Chilka, and B. Bonavida. *International Journal of Oncology* **33**, 909–927 (2008).
- [151] C. Yang, S. Jeong, S. Ku, K. Lee, and M. H. Park. *Journal of Controlled Release* **279**, 157–170 (2018).
- [152] Z. Li, X. Xu, L. Deng, R. Liao, R. Liang, B. Zhang, and L. Zhang. *Bioorganic & Medicinal Chemistry* **26**, 3947–3952 (2018).
- [153] G. Li, S. Yu, W. Xue, D. Ma, and W. Zhang. *Chemical Engineering Journal* **347**, 923–931 (2018).
- [154] S. Vimalraj, S. Pichu, T. Pankajam, K. Dharanibalan, V. Djonov, and S. Chatterjee. *Nitric Oxide* **82**, 48–58 (2019).
- [155] K. Fontana, L. Ventimiglia, and B. Mutus. *Journal of Chemical Technology & Biotechnology* **93**, 2093–2101 (2018).
- [156] A. B. Seabra and N. Durán. *European Journal of Pharmacology* **826**, 158–168 (2018).
- [157] S. Panthi, S. Manandhar, and K. Gautam. *Translational Neurodegeneration* **7** (2018).
- [158] A. Seabra, R. Lima, and M. Calderón. *Current Topics in Medicinal Chemistry* **15**, 298–308 (2015).

- 
- [159] H. Zhu, B. Ka, and F. Murad. *World Journal of Surgery* **31**, 624–631 (2007).
- [160] M. R. Miller and I. L. Megson. *British Journal of Pharmacology* **151**, 305–321 (2007).
- [161] P. G. Parzuchowski, M. C. Frost, and M. E. Meyerhoff. *Journal of the American Chemical Society* **124**, 12182–12191 (2002).
- [162] F. DeRosa, M. R. Kibbe, S. F. Najjar, M. L. Citro, L. K. Keefer, and J. A. Hrabie. *Journal of the American Chemical Society* **129**, 3786–3787 (2007).
- [163] A. B. Seabra and N. Duran. *Mini-Reviews in Medicinal Chemistry* **17**, 216–223 (2017).
- [164] J. Gehring, B. Trepka, N. Klinkenberg, H. Bronner, D. Schleheck, and S. Polarz. *Journal of the American Chemical Society* **138**, 3076–3084 (2016).
- [165] J. H. Shin and M. H. Schoenfish. *Chemistry of Materials* **20**, 239–249 (2008).
- [166] J. H. Shin, S. K. Metzger, and M. H. Schoenfish. *Journal of the American Chemical Society* **129**, 4612–4619 (2007).
- [167] D. A. Riccio and M. H. Schoenfish. *Chemical Society Reviews* **41**, 3731 (2012).
- [168] G. Narin, Ç. B. Albayrak, and S. Ülkü. *Applied Clay Science* **50**, 560–568 (2010).
- [169] P. S. Wheatley, A. C. McKinlay, and R. E. Morris. In *Zeolites and related materials: Trends, targets and challenges, Proceedings of the 4th International FEZA Conference*, vol. 174 of *Studies in Surface Science and Catalysis*, pp. 441–446. Elsevier (2008).
- [170] M. Mowbray, X. Tan, P. S. Wheatley, R. E. Morris, and R. B. Weller. *Journal of Investigative Dermatology* **128**, 352–360 (2007).
- [171] P. S. Wheatley, A. R. Butler, M. S. Crane, S. Fox, B. Xiao, A. G. Rossi, I. L. Megson, and R. E. Morris. *Journal of the American Chemical Society* **128**, 502–509 (2006).
- [172] P. S. Wheatley, A. R. Butler, M. S. Crane, A. G. Rossi, I. L. Megson, and R. E. Morris. In N. Ž. J. Čejka and P. Nachtigall (Eds.), *Studies in Surface Science and Catalysis : Molecular Sieves: From Basic Research to Industrial Applications Proceedings of the 3rd International Zeolite Symposium (3rd FEZA)*, vol. 158, pp. 2033–2040. Elsevier (2005).
- [173] R. R. Haikal, C. Hua, J. J. Perry, D. O’Nolan, I. Syed, A. Kumar, A. H. Chester, M. J. Zaworotko, M. H. Yacoub, and M. H. Alkordi. *ACS Applied Materials & Interfaces* **9**, 43520–43528 (2017).
- [174] T. Li, K. Taylor-Edinbyrd, and R. Kumar. *Physical Chemistry Chemical Physics* **17**, 23403–23412 (2015).

- [175] E. D. Bloch, W. L. Queen, S. Chavan, P. S. Wheatley, J. M. Zadrozny, R. Morris, C. M. Brown, C. Lamberti, S. Bordiga, and J. R. Long. *Journal of the American Chemical Society* **137**, 3466–3469 (2015).
- [176] K. Peikert, L. J. McCormick, D. Cattaneo, M. J. Duncan, F. Hoffmann, A. H. Khan, M. Bertmer, R. E. Morris, and M. Fröba. *Microporous and Mesoporous Materials* **216**, 118–126 (2015).
- [177] C. Kim, S. Diring, S. Furukawa, and S. Kitagawa. *Dalton transactions (Cambridge, England : 2003)* **44**, 15324–15333 (2015).
- [178] J. F. Eubank, P. S. Wheatley, G. Lebars, A. C. McKinlay, H. Leclerc, P. Horcajada, M. Daturi, A. Vimont, R. E. Morris, and C. Serre. *APL Materials* **2**, 124112 (2014).
- [179] A. C. McKinlay, J. F. Eubank, S. Wuttke, B. Xiao, P. S. Wheatley, P. Bazin, J.-C. Lavalley, M. Daturi, A. Vimont, G. de Weireld, P. Horcajada, C. Serre, and R. E. Morris. *Chemistry of Materials* **25**, 1592–1599 (2013).
- [180] N. J. Hinks, A. C. McKinlay, B. Xiao, P. S. Wheatley, and R. E. Morris. *Microporous and Mesoporous Materials* **129**, 330–334 (2010).
- [181] M. J. Ingleson, R. Heck, J. A. Gould, and M. J. Rosseinsky. *Inorganic Chemistry* **48**, 9986–9988 (2009).
- [182] F. Bonino, S. Chavan, J. G. Vitillo, E. Groppo, G. Agostini, C. Lamberti, P. D. C. Dietzel, C. Prestipino, and S. Bordiga. *Chemistry of Materials* **20**, 4957–4968 (2008).
- [183] S. T. Gregg, Q. Yuan, R. E. Morris, and B. Xiao. *Materials Today Communications* **12**, 95–105 (2017).
- [184] A. C. McKinlay, B. Xiao, D. S. Wragg, P. S. Wheatley, I. L. Megson, and R. E. Morris. *Journal of the American Chemical Society* **130**, 10440–10444 (2008).
- [185] B. Xiao, P. S. Wheatley, X. Zhao, A. J. Fletcher, S. Fox, A. G. Rossi, I. L. Megson, S. Bordiga, L. Regli, K. M. Thomas, and R. E. Morris. *Journal of the American Chemical Society* **129**, 1203–1209 (2007).
- [186] D. Cattaneo, S. J. Warrender, M. J. Duncan, C. J. Kelsall, M. K. Doherty, P. D. Whitfield, I. L. Megson, and R. E. Morris. *RSC advances* **6**, 14059–14067 (2016).
- [187] K. A. Mocniak, I. Kubajewska, D. E. M. Spillane, G. R. Williams, and R. E. Morris. *RSC Advances* **5**, 83648–83656 (2015).
- [188] J. G. Nguyen, K. K. Tanabe, and S. M. Cohen. *CrystEngComm* **12**, 2335 (2010).
- [189] H. Zhang, X.-T. Tian, Y. Shang, Y.-H. Li, and X.-B. Yin. *ACS Applied Materials & Interfaces* **10**, 28390–28398 (2018).
- [190] R. V. Pinto, F. Antunes, J. Pires, V. Graça, P. Brandão, and M. L. Pinto. *Acta Biomaterialia* **51**, 66–74 (2017).

- 
- [191] J. L. Harding and M. M. Reynolds. *Journal of Materials Chemistry B* **2**, 2530–2536 (2014).
- [192] M. J. Neufeld, J. L. Harding, and M. M. Reynolds. *ACS Applied Materials & Interfaces* **7**, 26742–26750 (2015).
- [193] D. Cattaneo, S. J. Warrender, M. J. Duncan, R. Castledine, N. Parkinson, I. Haley, and R. E. Morris. *Dalton transactions (Cambridge, England : 2003)* **45**, 618–629 (2016).
- [194] A. V. Desai, P. Samanta, B. Manna, and S. K. Ghosh. *Chemical communications (Cambridge, England)* **51**, 6111–6114 (2015).
- [195] J. L. Harding and M. M. Reynolds. *Journal of the American Chemical Society* **134**, 3330–3333 (2012).
- [196] T. Rudolf, A. Pöpl, W. Brunner, and D. Michel. *Magnetic Resonance in Chemistry* **37**, S93–S99 (1999).
- [197] T. Rudolf, A. Pöpl, W. Hofbauer, and D. Michel. *Physical Chemistry Chemical Physics* **3**, 2167–2173 (2001).
- [198] T. Rudolf, W. Böhlmann, and A. Pöpl. *Journal of Magnetic Resonance* **155**, 45–56 (2002).
- [199] A. Pöpl, M. Hartmann, W. Böhlmann, and R. Böttcher. *The Journal of Physical Chemistry A* **102**, 3599–3606 (1998).
- [200] A. Pöpl, T. Rudolf, P. Manikandan, and D. Goldfarb. *Journal of the American Chemical Society* **122**, 10194–10200 (2000).
- [201] M. Haouas, C. Volkringer, T. Loiseau, G. Férey, and F. Taulelle. *The Journal of Physical Chemistry C* **115**, 17934–17944 (2011).
- [202] L. Mitchell, P. Williamson, B. Ehrlichova, A. E. Anderson, V. R. Seymour, S. E. Ashbrook, N. Acerbi, L. M. Daniels, R. I. Walton, M. L. Clarke, and P. A. Wright. *Chemistry (Weinheim an der Bergstrasse, Germany)* **20**, 17185–17197 (2014).
- [203] V. N. Panchenko, M. M. Matrosova, J. Jeon, J. W. Jun, M. N. Timofeeva, and S. H. Jung. *Journal of Catalysis* **316**, 251–259 (2014).
- [204] Z. Hu and D. Zhao. *CrystEngComm* **19**, 4066–4081 (2017).
- [205] C. Volkringer, H. Leclerc, J.-C. Lavalley, T. Loiseau, G. Férey, M. Daturi, and A. Vimont. *Journal of Physical Chemistry C* **116**, 5710–5719 (2012).
- [206] H. Leclerc, A. Vimont, J.-C. Lavalley, M. Daturi, A. D. Wiersum, P. L. Llewellyn, P. Horcajada, G. Férey, and C. Serre. *Physical Chemistry Chemical Physics* **13**, 11748–11756 (2011).

- [207] A. Vimont, J.-M. Goupil, J.-C. Lavalley, M. Daturi, S. Surble, C. Serre, F. Millange, G. Férey, and N. Audebrand. *Journal of the American Chemical Society* **128**, 3218–3227 (2006).
- [208] L. Yuan, M. Tian, J. Lan, X. Cao, X. Wang, Z. Chai, J. K. Gibson, and W. Shi. *Chemical Communications* **54**, 370–373 (2018).
- [209] R. E. Morris and L. Brammer. *Chemical Society Reviews* **46**, 5444–5462 (2017).
- [210] L. S. Xie, L. Sun, R. Wan, S. S. Park, J. A. DeGayner, C. H. Hendon, and M. Dincă. *Journal of the American Chemical Society* **140**, 7411–7414 (2018).
- [211] S. Yuan, L. Zou, J.-S. Qin, J. Li, L. Huang, L. Feng, X. Wang, M. Bosch, A. Alsalme, T. Cagin, and H.-C. Zhou. *Nature Communications* **8**, 15356 (2017).
- [212] J. Canivet, M. Vandichel, and D. Farrusseng. *Dalton Transactions* **45**, 4090–4099 (2016).
- [213] K. Wang, C. Li, Y. Liang, T. Han, H. Huang, Q. Yang, D. Liu, and C. Zhong. *Chemical Engineering Journal* **289**, 486–493 (2016).
- [214] A. K. Cheetham, T. D. Bennett, F.-X. Coudert, and A. L. Goodwin. *Dalton Transactions* **45**, 4113–4126 (2016).
- [215] Z. Fang, B. Bueken, D. E. de Vos, and R. A. Fischer. *Angewandte Chemie (International Ed. in English)* **54**, 7234–7254 (2015).
- [216] H. Furukawa, U. Müller, and O. M. Yaghi. *Angewandte Chemie International Edition* **54**, 3417–3430 (2015).
- [217] S. K. Elsaïdi, M. H. Mohamed, D. Banerjee, and P. K. Thallapally. *Coordination Chemistry Reviews* **358**, 125–152 (2018).
- [218] Z. Chang, D.-H. Yang, J. Xu, T.-L. Hu, and X.-H. Bu. *Advanced materials (Deerfield Beach, Fla.)* **27**, 5432–5441 (2015).
- [219] A. Schneemann, V. Bon, I. Schwedler, I. Senkowska, S. Kaskel, and R. A. Fischer. *Chemical Society reviews* **43**, 6062–6096 (2014).
- [220] M. Alhamami, H. Doan, and C.-H. Cheng. *Materials* **7**, 3198–3250 (2014).
- [221] A. J. Fletcher, K. M. Thomas, and M. J. Rosseinsky. *Journal of Solid State Chemistry* **178**, 2491–2510 (2005).
- [222] M. Mendt and A. Pöpl. *Applied Magnetic Resonance* **46**, 1249–1263 (2015).
- [223] B. Barth, M. Mendt, A. Pöpl, and M. Hartmann. *Microporous and Mesoporous Materials* **216**, 97–110 (2015).
- [224] M. Mendt, F. Gutt, N. Kavoosi, V. Bon, I. Senkowska, S. Kaskel, and A. Pöpl. *The Journal of Physical Chemistry C* **120**, 14246–14259 (2016).

- 
- [225] M. Danilczuk and A. Lund. *Chemical Physics Letters* **490**, 205–209 (2010).
- [226] M. Miletic, J. L. Gland, K. C. Hass, and W. F. Schneider. *Journal of Physical Chemistry B* **107**, 157–163 (2002).
- [227] K. M. Neyman, D. I. Ganyushin, V. A. Nasluzov, N. Rösch, A. Pöpl, and M. Hartmann. *Physical Chemistry Chemical Physics* **5**, 2429–2434 (2003).
- [228] G. Periyasamy, M. Sundararajan, I. H. Hillier, N. A. Burton, and J. J. W. McDouall. *Physical Chemistry Chemical Physics* **9**, 2498–2506 (2007).
- [229] P. Pietrzyk and Z. Sojka. *Journal of Physical Chemistry A* **109**, 10571–10581 (2005).
- [230] M. Radoul, M. Sundararajan, A. Potapov, C. Riplinger, F. Neese, and D. Goldfarb. *Physical Chemistry Chemical Physics* **12**, 7276–7289 (2010).
- [231] M. Sundararajan and F. Neese. *Journal of Chemical Theory and Computation* **8**, 563–574 (2011).
- [232] N. C. Tomson, M. R. Crimmin, T. Petrenko, L. E. Rosebrugh, S. Sproules, W. C. Boyd, R. G. Bergman, S. DeBeer, F. D. Toste, and K. Wieghardt. *Journal of the American Chemical Society* **133**, 18785–18801 (2011).
- [233] L. Hermosilla, P. Calle, Garcia de la Vega, J M, and C. Sieiro. *The Journal of Physical Chemistry A* **109**, 1114–1124 (2005).
- [234] M. L. Pinto, J. Rocha, J. R. B. Gomes, and J. Pires. *Journal of the American Chemical Society* **133**, 6396–6402 (2011).
- [235] M. A. Addicoat, N. Vankova, I. F. Akter, and T. Heine. *Journal of Chemical Theory and Computation* **10**, 880–891 (2014).
- [236] A. Mavrandonakis, K. D. Vogiatzis, A. D. Boese, K. Fink, T. Heine, and W. Klopper. *Inorganic Chemistry* **54**, 8251–8263 (2015).
- [237] T. A. Maark and S. Pal. *International Journal of Hydrogen Energy* **35**, 12846–12857 (2010).
- [238] T. Loiseau, C. Serre, C. Huguenard, G. Fink, F. Taulelle, M. Henry, T. Bataille, and G. Férey. *Chemistry - A European Journal* **10**, 1373–1382 (2004).
- [239] C. Volkringer, D. Popov, T. Loiseau, G. Férey, M. Burghammer, C. Riekel, M. Haouas, and F. Taulelle. *Chemistry of Materials* **21**, 5695–5697 (2009).
- [240] V. Bon, N. Klein, I. Senkovska, A. Heerwig, J. Getzschmann, D. Wallacher, I. Zizak, M. Brzhezinskaya, U. Mueller, and S. Kaskel. *Physical Chemistry Chemical Physics* **17**, 17471–17479 (2015).
- [241] N. Kavooosi, V. Bon, I. Senkovska, S. Krause, C. Atzori, F. Bonino, J. Pallmann, S. Paasch, E. Brunner, and S. Kaskel. *Dalton Transactions (Cambridge, England : 2003)* **46**, 4685–4695 (2017).

- [242] M. Mendt, B. Barth, M. Hartmann, and A. Pöpl. *The Journal of Chemical Physics* **147**, 224701 (2017).
- [243] N. Klein, C. Herzog, M. Sabo, I. Senkovska, J. Getzschmann, S. Paasch, M. R. Lohe, E. Brunner, and S. Kaskel. *Physical Chemistry Chemical Physics* **12**, 11778 (2010).
- [244] N. Klein, H. C. Hoffmann, A. Cadiou, J. Getzschmann, M. R. Lohe, S. Paasch, T. Heydenreich, K. Adil, I. Senkovska, E. Brunner, and S. Kaskel. *Journal of Materials Chemistry* **22**, 10303–10312 (2012).
- [245] H. C. Hoffmann, B. Assfour, F. Epperlein, N. Klein, S. Paasch, I. Senkovska, S. Kaskel, G. Seifert, and E. Brunner. *Journal of the American Chemical Society* **133**, 8681–8690 (2011).
- [246] J. Y. Lee, L. Pan, X. Huang, T. J. Emge, and J. Li. *Advanced Functional Materials* **21**, 993–998 (2011).
- [247] S. R. Batten, N. R. Champness, X.-M. Chen, J. Garcia-Martinez, S. Kitagawa, L. Öhrström, M. O’Keeffe, M. Paik Suh, and J. Reedijk. *Pure and Applied Chemistry* **85** (2013).
- [248] L. Öhrström. *Crystals* **5**, 154–162 (2015).
- [249] W. Lu, Z. Wei, Z.-Y. Gu, T.-F. Liu, J. Park, J. Park, J. Tian, M. Zhang, Q. Zhang, T. r. Gentle, M. Bosch, and H.-C. Zhou. *Chemical Society Reviews* **43**, 5561–5593 (2014).
- [250] Di Li and K. Kaneko. *Chemical Physics Letters* **335**, 50–56 (2001).
- [251] K. Uemura, S. Kitagawa, M. Kondo, K. Fukui, R. Kitaura, H.-C. Chang, and T. Mizutani. *Chemistry – A European Journal* **8**, 3586–3600 (2002).
- [252] N. Kavoosi, T. Savchenko, I. Senkovska, M. Maliuta, V. Bon, A. Eychmüller, and S. Kaskel. *Microporous and Mesoporous Materials* **271**, 169–174 (2018).
- [253] A. Krylov, A. Vtyurin, P. Petkov, I. Senkovska, M. Maliuta, V. Bon, T. Heine, S. Kaskel, and E. Slyusareva. *Physical chemistry chemical physics : PCCP* **19**, 32099–32104 (2017).
- [254] H. Miura, V. Bon, I. Senkovska, S. Ehrling, S. Watanabe, M. Ohba, and S. Kaskel. *Dalton transactions (Cambridge, England : 2003)* **46**, 14002–14011 (2017).
- [255] C. Serre, F. Millange, C. Thouvenot, M. Noguès, G. Marsolier, D. Louër, and G. Férey. *Journal of the American Chemical Society* **124**, 13519–13526 (2002).
- [256] F. Millange, C. Serre, and G. Férey. *Chemical Communications* **0**, 822–823 (2002).
- [257] T. R. Whitfield, X. Wang, L. Liu, and A. J. Jacobson. *Solid State Sciences* **7**, 1096–1103 (2005).



- 
- [258] E. V. Anokhina, M. Vougo-Zanda, X. Wang, and A. J. Jacobson. *Journal of the American Chemical Society* **127**, 15000–15001 (2005).
- [259] M. Vougo-Zanda, J. Huang, E. Anokhina, X. Wang, and A. J. Jacobson. *Inorganic Chemistry* **47**, 11535–11542 (2008).
- [260] C. Serre, S. Bourrelly, A. Vimont, N. A. Ramsahye, G. Maurin, P. L. Llewellyn, M. Daturi, Y. Filinchuk, O. Leynaud, P. Barnes, and G. Férey. *Advanced Materials* **19**, 2246–2251 (2007).
- [261] L. Hamon, C. Serre, T. Devic, T. Loiseau, F. Millange, G. Férey, and G. de Weireld. *Journal of the American Chemical Society* **131**, 8775–8777 (2009).
- [262] A. Boutin, M.-A. Springuel-Huet, A. Nossou, A. Gedeon, T. Loiseau, C. Volkringer, G. Férey, F.-X. Coudert, and A. H. Fuchs. *Angewandte Chemie (International ed. in English)* **48**, 8314–8317 (2009).
- [263] P. L. Llewellyn, P. Horcajada, G. Maurin, T. Devic, N. Rosenbach, S. Bourrelly, C. Serre, D. Vincent, S. Loera-Serna, Y. Filinchuk, and G. Férey. *Journal of the American Chemical Society* **131**, 13002–13008 (2009).
- [264] T. K. Trung, P. Trens, N. Tanchoux, S. Bourrelly, P. L. Llewellyn, S. Loera-Serna, C. Serre, T. Loiseau, F. Fajula, and G. Férey. *Journal of the American Chemical Society* **130**, 16926–16932 (2008).
- [265] V. Finsky, L. Ma, L. Alaerts, D. E. de Vos, G. V. Baron, and J. F. M. Denayer. *Microporous and Mesoporous Materials* **120**, 221–227 (2009).
- [266] D. Kolokolov, H. Jovic, A. Stepanov, M. Plazanet, M. Zbiri, J. Ollivier, V. Guillermin, T. Devic, C. Serre, and G. Férey. *The European Physical Journal Special Topics* **189**, 263–271 (2010).
- [267] J. L. Schlenker, F. G. Dwyer, E. E. Jenkins, W. J. Rohrbaugh, G. T. Kokotailo, and W. M. Meier. *Nature* **294**, 340–342 (1981).
- [268] A. Schweiger and G. Jeschke. *Principles of Pulse Electron Paramagnetic Resonance*. Oxford University Press, Oxford and UK, New York (2001).
- [269] A. Abragam and M. H. L. Pryce. *Proceedings of the Royal Society A: Mathematical, Physical and Engineering Sciences* **205**, 135–153 (1951).
- [270] R. McWeeny. *The Journal of Chemical Physics* **42**, 1717 (1965).
- [271] J. R. Pilbrow. *Transition Ion Electron Paramagnetic Resonance*. Clarendon Press and Oxford University Press, Oxford, New York (1990).
- [272] M. H. Levitt. *Spin Dynamics: Basics of Nuclear Magnetic Resonance*. Second edition. ed. (2008).

- [273] S. A. Dikanov, A. A. Shubin, and V. N. Parmon. *Journal of Magnetic Resonance (1969)* **42**, 474–487 (1981).
- [274] S. Dikanov and M. Bowman. *Journal of Magnetic Resonance, Series A* **116**, 125–128 (1995).
- [275] J. E. Wertz and J. R. Bolton. *Electron spin resonance: Elementary theory and practical applications*. Chapman and Hall, New York (1986).
- [276] G. Schultz. *Magnetic resonance imaging with nonlinear gradient fields: Signal encoding and image reconstruction*. Springer Spektrum, Wiesbaden (2013).
- [277] P. Höfer, A. Grupp, H. Nebenführ, and M. Mehring. *Chemical Physics Letters* **132**, 279–282 (1986).
- [278] S. A. Dikanov, A. M. Tyryshkin, and M. K. Bowman. *Journal of Magnetic Resonance* **144**, 228–242 (2000).
- [279] R. I. Samoilova, S. A. Dikanov, A. V. Fionov, A. M. Tyryshkin, E. V. Lunina, and M. K. Bowman. *The Journal of Physical Chemistry* **100**, 17621–17629 (1996).
- [280] P. Hofer. *Journal of Magnetic Resonance, Series A* **111**, 77–86 (1994).
- [281] G. Herzberg and J. W. T. Spinks. *Spectra of diatomic molecules*. D. Van Nostrand Company, New York [etc.] (1950).
- [282] E. Cartmell and G. Fowles. *Valency and Molecular Structure*. Butterworths, London, second edition ed. (1961).
- [283] R. P. Orenha and S. E. Galembeck. *Journal of Chemical Education* **91**, 1064–1069 (2014).
- [284] H. Brion, C. Moser, and M. Yamazaki. *The Journal of Chemical Physics* **30**, 673 (1959).
- [285] G. Dousmanis. *Physical Review* **97**, 967–970 (1955).
- [286] T. C. James and R. J. Thibault. *The Journal of Chemical Physics* **41**, 2806 (1964).
- [287] H. Margenau and A. Henry. *Physical Review* **78**, 587–592 (1950).
- [288] R. Beringer and J. Castle. *Physical Review* **78**, 581–586 (1950).
- [289] M. Jinguji, Y. Ohokubo, and I. Tanaka. *Chem. Phys. Lett.* **54**, 136–138 (1978).
- [290] C. C. Lin and M. Mizushima. *Phys. Rev.* **100**, 1726–1730 (1955).
- [291] R. L. Brown and H. E. Radford. *Physical Review* **147**, 6–12 (1966).
- [292] C. K. Jen. *Physical Review* **76**, 1494–1501 (1949).
- [293] E. L. Hill. *Physical Review* **34**, 1507–1516 (1929).

- 
- [294] S. Stoll and A. Schweiger. *Journal of Magnetic Resonance* **178**, 42–55 (2006).
- [295] G. R. Hanson, K. E. Gates, C. J. Noble, M. Griffin, A. Mitchell, and S. Benson. *Contributions from the 11th International Conference on Biological Inorganic Chemistry* **98**, 903–916 (2004).
- [296] J. W. Whittaker. *Journal of Chemical Education* **68**, 421 (1991).
- [297] R. Beringer, E. B. Rawson, and A. F. Henry. *Physical Review* **94**, 343–349 (1954).
- [298] J. H. van Vleck. *Reviews of Modern Physics* **23**, 213–227 (1951).
- [299] J. H. Lunsford. *The Journal of Chemical Physics* **46**, 4347–4351 (1967).
- [300] J. H. Lunsford. *Journal of Physical Chemistry* **72**, 2141–2144 (1968).
- [301] C. L. Gardner and M. A. Weinberger. *Canadian Journal of Chemistry* **48**, 1317–1322 (1970).
- [302] H. Yahiro, A. Lund, and M. Shiotani. *Spectrochimica Acta, Part A: Molecular and Biomolecular Spectroscopy* **60**, 1267–1278 (2004).
- [303] V. Umamaheswari, M. Hartmann, and A. Pöpl. *Journal of Physical Chemistry B* **109**, 19723–19731 (2005).
- [304] V. Umamaheswari, M. Hartmann, and A. Pöpl. *Journal of Physical Chemistry B* **109**, 1537–1546 (2005).
- [305] E. van Faassen and A. F. Vanin (Eds.). *Radicals for Life: The Various Forms of Nitric Oxide*. Elsevier, Amsterdam and Oxford (2007).
- [306] P. Fiscaro, E. Giamello, G. Berlier, and C. Lamberti. *Research on Chemical Intermediates* **29**, 805–816 (2003).
- [307] C. Naccache and Y. B. Taarit. *Journal of the Chemical Society, Faraday Transactions 1: Physical Chemistry in Condensed Phases* **69**, 1475 (1973).
- [308] E. Garbowski and J. C. Vedrine. *Chemical Physics Letters* **48**, 551–554 (1977).
- [309] M. Chiesa, M. C. Paganini, E. Giamello, C. Di Valentin, and G. Pacchioni. *Journal of Molecular Catalysis A: Chemical* **204–205**, 779–786 (2003).
- [310] Z. Sojka, P. Pietrzyk, G. Martra, M. Kermarec, and M. Che. *Nano-Structured Materials for Catalysis* **114**, 154–161 (2006).
- [311] A. Abragam and B. Bleaney. *Electron Paramagnetic Resonance of Transition Ions*. International series of monographs on physics. Clarendon P (1970).
- [312] W. Hayes and J. Wilkens. *Proceedings of the Royal Society A: Mathematical, Physical and Engineering Sciences* **281**, 340–365 (1964).

- [313] T. A. Ivanova, I. Jacyna-Onyszkiewicz, J. Mroziński, R. Troć, Y. Yablokov, and V. V. Zelentsov. *Physica B: Condensed Matter* **304**, 246–255 (2001).
- [314] F. Jensen. *Introduction to Computational Chemistry*. John Wiley & Sons, Chichester, England and Hoboken, NJ, 2nd ed. ed. (2007).
- [315] P. Hohenberg and W. Kohn. *Physical Review* **136**, B864–B871 (1964).
- [316] W. Kohn and L. J. Sham. *Physical Review* **140**, A1133–A1138 (1965).
- [317] F. Neese. *Wiley Interdisciplinary Reviews: Computational Molecular Science* **2**, 73–78 (2012).
- [318] M. Kaupp, M. Bühl, and V. G. Malkin. *Calculation of NMR and EPR parameters: Theory and applications*. Wiley-VCH, Weinheim (2004).
- [319] A. A. Westenberg and N. deHaas. *Journal of Chemical Physics* **51**, 5215–5225 (1969).
- [320] M. Ruzzi, E. Sartori, A. Moscatelli, I. V. Khudyakov, and N. J. Turro. *J. Phys. Chem. A* **117**, 5232–5240 (2013).
- [321] T. J. Cook and T. A. Miller. *Journal of Chemical Physics* **59**, 1352–1361 (1973).
- [322] H.-J. Bauer and K. F. Sahm. *Journal of Chemical Physics* **42**, 3400–3404 (1965).
- [323] J. O. Hirschfelder, C. F. Curtiss, and R. B. Bird. *Molecular Theory of Gases and Liquids*. Structure of matter series. Wiley, New York and London (1954).
- [324] W. V. Smith and R. Howard. *Physical Review* **79**, 132–136 (1950).
- [325] C. J. Jameson, A. K. Jameson, and J. K. Hwang. *Journal of Chemical Physics* **89**, 4074–4081 (1988).
- [326] C. J. Jameson, A. K. Jameson, J. K. Hwang, and D. Dabkowski. *Journal of Physical Chemistry* **92**, 5937–5941 (1988).
- [327] C. J. Jameson, A. K. Jameson, and J. K. Hwang. *Journal of Chemical Physics* **94**, 172–178 (1991).
- [328] L. D. Landau, E. M. Lifshitz, L. P. PitaevskiĀ, J. B. Sykes, and M. J. Kearsley. *Statistical Physics*, vol. 5 of *Course of Theoretical Physics*. Elsevier Butterworth Heinemann, Amsterdam and London, 3 ed. (1980).
- [329] <https://encyclopedia.airliquide.com/nitric-oxide> (2018).
- [330] M. W. Anderson and L. Kevan. *Journal of Physical Chemistry* **91**, 2926–2930 (1987).
- [331] A. Pöppl and L. Kevan. *Journal of Physical Chemistry* **100**, 3387–3394 (1996).
- [332] P. S. Petkov, V. Bon, C. L. Hobday, A. B. Kuc, P. Melix, S. Kaskel, T. DÄCeren, and T. Heine. *Physical Chemistry Chemical Physics* **21**, 674–680 (2019).

- 
- [333] A. V. Astashkin, L. Chen, B. O. Elmore, D. Kunwar, Y. Miao, H. Li, T. L. Poulos, L. J. Roman, and C. Feng. *The Journal of Physical Chemistry. A* **119**, 6641–6649 (2015).
- [334] E. Alvarez, N. Guillou, C. Martineau, B. Bueken, B. van de Voorde, C. Le Guillouzer, P. Fabry, F. Nouar, F. Taulelle, D. de Vos, J.-S. Chang, K. H. Cho, N. Ramsahye, T. Devic, M. Daturi, G. Maurin, and C. Serre. *Angewandte Chemie International Edition* **54**, 3664–3668 (2015).
- [335] M. Gaab, N. Trukhan, S. Maurer, R. Gummaraju, and U. Müller. *Microporous and Mesoporous Materials* **157**, 131–136 (2012).
- [336] A. Aijaz, T. Akita, H. Yang, and Q. Xu. *Chemical Communications (Cambridge, England)* **50**, 6498–6501 (2014).
- [337] Y. Chen, B. Fan, N. Lu, and R. Li. *Catalysis Communications* **64**, 91–95 (2015).
- [338] R. Grall, T. Hidalgo, J. Delic, A. Garcia-Marquez, S. Chevillard, and P. Horcajada. *Journal of Materials Chemistry B* **3**, 8279–8292 (2015).
- [339] M. Mito, T. Tatano, Y. Komorida, T. Tajiri, H. Deguchi, S. Takagi, S. Kohiki, M. Ohba, R. Matsuda, and S. Kitagawa. *Microporous and Mesoporous Materials* **132**, 464–469 (2010).
- [340] C. Gemperle and A. Schweiger. *Chemical Reviews* **91**, 1481–1505 (1991).
- [341] D. H. Whiffen. *Molecular Physics* **10**, 595–596 (1966).
- [342] C. Lee, W. Yang, and R. G. Parr. *Physical Review B* **37**, 785–789 (1988).
- [343] A. D. Becke. *The Journal of Chemical Physics* **98**, 5648 (1993).
- [344] A. Schäfer, H. Horn, and R. Ahlrichs. *The Journal of Chemical Physics* **97**, 2571 (1992).
- [345] M. Ernzerhof and G. E. Scuseria. *The Journal of Chemical Physics* **110**, 5029 (1999).
- [346] C. Adamo, M. Cossi, and V. Barone. *Journal of Molecular Structure: THEOCHEM* **493**, 145–157 (1999).
- [347] C. Adamo and V. Barone. *The Journal of Chemical Physics* **110**, 6158 (1999).
- [348] W. Kutzelnigg, U. Fleischer, and M. Schindler. In U. Fleischer, W. Kutzelnigg, H.-H. Limbach, G. J. Martin, M. L. Martin, and M. Schindler (Eds.), *Deuterium and Shift Calculation*, pp. 165–262. Springer Berlin Heidelberg, Berlin, Heidelberg (1991).
- [349] V. Barone. In D. P. Chong (Ed.), *Recent Advances In Density Functional Methods, Part I*. World Scientific (1995).
- [350] D. E. Woon and T. H. Dunning. *The Journal of Chemical Physics* **98**, 1358 (1993).

- [351] J. P. Perdew, K. Burke, and M. Ernzerhof. *Physical Review Letters* **77**, 3865–3868 (1996).
- [352] J. P. Perdew, K. Burke, and M. Ernzerhof. *Physical Review Letters* **78**, 1396 (1997).
- [353] A. D. Becke. *Physical Review A* **38**, 3098–3100 (1988).
- [354] J. P. Perdew and W. Yue. *Physical Review B* **33**, 8800–8802 (1986).
- [355] A. J. Cohen and N. C. Handy. *Molecular Physics* **99**, 607–615 (2001).
- [356] N. C. Handy and A. J. Cohen. *Molecular Physics* **99**, 403–412 (2001).
- [357] J. P. Perdew, J. A. Chevary, S. H. Vosko, K. A. Jackson, M. R. Pederson, D. J. Singh, and C. Fiolhais. *Physical Review B* **46**, 6671–6687 (1992).
- [358] J. P. Perdew. *Physical Review B* **33**, 8822–8824 (1986).
- [359] J. P. Perdew. *Physical Review B* **34**, 7406 (1986).
- [360] J. Tao, J. P. Perdew, V. N. Staroverov, and G. E. Scuseria. *Physical Review Letters* **91**, 146401 (2003).
- [361] R. Li, Z. Li, and Y. Pan. *Physics and Chemistry of Minerals* **39**, 491–501 (2012).
- [362] A. C. Saladino and S. C. Larsen. *The Journal of Physical Chemistry A* **107**, 1872–1878 (2003).
- [363] S. F. Boys and F. Bernardi. *Molecular Physics* **19**, 553–566 (2006).
- [364] J. R. Morton and K. F. Preston. *Journal of Magnetic Resonance (1969)* **30**, 577–582 (1978).
- [365] J. Enemark and R. Feltham. *Coordination Chemistry Reviews* **13**, 339–406 (1974).
- [366] C. E. Dinerman and G. E. Ewing. *The Journal of Chemical Physics* **53**, 626–631 (1970).
- [367] C.-D. Wu, A. Hu, L. Zhang, and W. Lin. *Journal of the American Chemical Society* **127**, 8940–8941 (2005).
- [368] S. Stoll, C. Calle, G. Mitrikas, and A. Schweiger. *Journal of Magnetic Resonance* **177**, 93–101 (2005).
- [369] V. Bon, J. Pallmann, E. Eisbein, H. C. Hoffmann, I. Senkowska, I. Schwedler, A. Schneemann, S. Henke, D. Wallacher, R. A. Fischer, G. Seifert, E. Brunner, and S. Kaskel. *Microporous Mesoporous Mater.* **216**, 64–74 (2015).
- [370] K. Treppe, S. Schwalbe, and G. Seifert. *Physical Chemistry Chemical Physics* **17**, 17122–17129 (2015).
- [371] P. J. Chmielewski and L. Latos-Grażyński. *Inorganic Chemistry* **36**, 840–845 (1997).

- 
- [372] G. A. Bowmaker, P. D. W. Boyd, and G. K. Campbell. *Inorganic Chemistry* **21**, 2403–2412 (1982).
- [373] V. V. Saraev, P. B. Kraikovskii, D. A. Matveev, S. N. Zelinskii, and K. Lammertsma. *Inorganica Chimica Acta* **359**, 2314–2320 (2006).
- [374] P. H. Kasai and R. J. Bishop. *Journal of the American Chemical Society* **94**, 5560–5566 (1972).
- [375] A. Abragam and B. Bleaney. *Electron Paramagnetic Resonance of Transition Ions*. Dover Publications, New York (1986).
- [376] N. M. Atherton. *Principles of Electron Spin Resonance*. Ellis Horwood Series in Physical Chemistry. Ellis Horwood and PTR Prentice Hall, New York (1993).
- [377] S. Friedländer, M. Šimėnas, M. Kobalz, P. Eckold, O. Ovchar, A. G. Belous, J. Banys, H. Krautscheid, and A. Pöpl. *The Journal of Physical Chemistry C* **119**, 19171–19179 (2015).
- [378] R. R. Urbano, A. Garcia, E. Granado, J. A. Sanjurjo, I. Torriani, C. Rettori, S. B. Oseroff, A. Hassan, G. B. Martins, Z. Fisk, P. G. Pagliuso, J. L. Sarrao, R. Caciuffo, and R. M. Ibberson. *Physical Review B* **62**, 9593–9598 (2000).
- [379] L. Laskowski, A. Kassiba, M. Makowska-Janusik, A. Mehdi, A. Gibaud, N. Errien, and J. Swiatek. *Journal of Physics. Condensed Matter : an Institute of Physics Journal* **21**, 076004 (2009).
- [380] H.-I. Lee, P. E. Doan, and B. M. Hoffman. *Journal of Magnetic Resonance* **140**, 91–107 (1999).
- [381] P. Horcajada, S. Surble, C. Serre, D.-Y. Hong, Y.-K. Seo, J.-S. Chang, J.-M. Greneche, I. Margiolaki, and G. Férey. *Chemical Communications* **0**, 2820–2822 (2007).
- [382] Y.-L. Zhao, M. D. Bartberger, K. Goto, K. Shimada, T. Kawashima, and K. N. Houk. *Journal of the American Chemical Society* **127**, 7964–7965 (2005).
- [383] C. Volkringer, H. Leclerc, J.-C. Lavalley, T. Loiseau, G. Férey, M. Daturi, and A. Vimont. *Journal of Physical Chemistry C* **116**, 5710–5719 (2012).
- [384] S. Dissegna, K. Epp, W. R. Heinz, G. Kieslich, and R. A. Fischer. *Advanced Materials* **30**, 1704501 (2018).
- [385] M. Haouas, C. Volkringer, T. Loiseau, G. Férey, and F. Taulelle. *Chemistry of Materials* **24**, 2462–2471 (2012).
- [386] Y.-K. Seo, J. W. Yoon, J. S. Lee, U.-H. Lee, Y. K. Hwang, C.-H. Jun, P. Horcajada, C. Serre, and J.-S. Chang. *Metal Organic Frameworks* **157**, 137–145 (2012).

- [387] F. Weigend and R. Ahlrichs. *Physical Chemistry Chemical Physics* **7**, 3297–3305 (2005).
- [388] S. Grimme, J. Antony, S. Ehrlich, and H. Krieg. *The Journal of Chemical Physics* **132**, 154104 (2010).
- [389] S. Grimme, S. Ehrlich, and L. Goerigk. *Journal of Computational Chemistry* **32**, 1456–1465 (2011).
- [390] P. F. Provasi and S. P. A. Sauer. *The Journal of Chemical Physics* **133**, 054308 (2010).
- [391] E. D. Hedegard, J. Kongsted, and S. P. A. Sauer. *Physical Chemistry Chemical Physics* **14**, 10669–10676 (2012).